ISBN 978-82-326-7654-5 (printed ver.)
ISBN 978-82-326-7653-8 (electronic ver.)
ISSN 1503-8181 (printed ver.)
ISSN 2703-8084 (electronic ver.)

NTNU
Norwegian University of
Science and Technology

Doctoral thesis

George Katsikogiannis

Doctoral theses at NTNU, 2024:26

NTNU
Norwegian University of
Science and Technology
Thesis for the degree of
Philosophiae Doctor
Faculty of Engineering
Department of Marine Technology

NTNU

Doctoral theses at NTNU, 2024:26

George Katsikogiannis

Estimation of Long-Term Fatigue and Extreme Responses of Large-Diameter Monopiles for Offshore Wind Turbines

NTNU
Norwegian University of
Science and Technology

George Katsikogiannis

Estimation of Long-Term Fatigue and Extreme Responses of Large-Diameter Monopiles for Offshore Wind Turbines

Thesis for the degree of Philosophiae Doctor

Trondheim, February 2024

Norwegian University of Science and Technology
Faculty of Engineering
Department of Marine Technology

NTNU
Norwegian University of
Science and Technology

NTNU
Norwegian University of Science and Technology

Thesis for the degree of Philosophiae Doctor

Faculty of Engineering
Department of Marine Technology

ISBN 978-82-326-7654-5 (printed ver.)
ISBN 978-82-326-7653-8 (electronic ver.)
ISSN 1503-8181 (printed ver.)
ISSN 2703-8084 (electronic ver.)

Doctoral theses at NTNU, 2024:26

PRINTED IN
NORWAY
NO - 1598

NORDIC SWAN ECOLABEL
Printed matter
2041 0731

Printed by Skipnes Kommunikasjon AS

Abstract

Offshore wind energy is a crucial part of the global effort to transition towards a decarbonized energy system. In this context, the foundations used to support offshore wind turbines (OWTs) play a significant role in determining the feasibility of offshore wind projects, as they represent a substantial portion of the total capital expenditure. Currently, the most widely used type of foundation for OWTs is the monopile, due to its simple fabrication process, extensive installation experience, and proven reliability. However, as the offshore wind sector develops, employing larger turbines in size and capacity in deeper water depths, larger monopiles are required to withstand the increased loads, imposing challenges that need to be addressed.

The design of foundations for OWTs requires incorporating several engineering disciplines, considering various environmental and operational conditions, load scenarios, and design criteria to ensure the structural integrity of the foundation its operational lifetime. The behaviour of large-diameter monopiles differs notably from the smaller ones used in earlier offshore wind developments or the long, slender piles commonly used in i.e. the oil & gas industry. The thesis aims to further develop computationally efficient design methods and evaluate the impact of state-of-the-art physical load models compared to widely used approaches for long-term responses, ensuring that monopiles remain a reliable and cost-effective option in offshore wind energy.

OWTs are complex systems with nonlinearities and strong coupling between environmental loads and structural responses. Full long-term fatigue assessment (FLTA) using time-domain simulations is the most accurate approach, but requires extensive computational effort due to the large number of load cases involved. To reduce the computational burden, environmental lumping can be employed to select a representative set of sea states for fatigue design. The thesis introduces an environmental lumping method which considers the wind-wave environment and the dynamics of the OWT to ensure

fatigue damage prediction along the support structure with accuracy above 90%, while reducing computational effort more than 95% compared to FLTA. The method is extended to consistently account for wind-sea and swell components, with similar levels of accuracy and effort.

The design of OWTs should also ensure their integrity under extreme conditions. The full long-term analysis that considers all sea states and response variability is commonly proposed, but it is computationally intensive. The environmental contour method (ECM) is a widely used alternative, approximating extreme responses by analyzing short-term conditions along the contour. However, directly applying the ECM to OWTs poses challenges due to non-monotonic wind loads, which become more critical for larger turbines and, when combined with waves near the OWT's natural period, can cause extreme responses even in non-extreme wind speeds. Furthermore, neglecting metocean variables important for responses in the establishment of contours may affect the estimated extremes. The uncertainty associated with extreme responses using the ECM at representative wind speeds is investigated, highlighting their sensitivity to the probabilistic models used for the wave parameters and the stochastic variation due to seed variability.

Additionally to the methods applied for design purposes, numerical models used for global analysis are essential for the estimated dynamic behaviour and responses. Specifically, the widely used $p-y$ approach for modelling pile behaviour in OWTs reveals several limitations when applied to large-diameter monopiles, arising from omitting critical aspects of soil behaviour, differences in loading conditions (e.g., dominant bending moments), and their relatively rigid behaviour, which contrast with the $p-y$ assumptions. Fatigue and extreme responses using $p-y$ curves are compared to an elasto-plastic model, which captures the non-linear load-displacement response, hysteretic damping, and soil resistance components, depicting the importance of soil damping, particularly when aerodynamic damping is negligible.

Finally, current engineering models cannot account for diffraction effects when higher-order wave kinematic theories are used, as MacCamy and Fuchs's approach only applies to linear waves. As diffraction becomes increasingly important for larger diameters, a new load model was developed, which combines the conventional Morison's formulation with a frequency-dependent mass coefficient from MacCamy and Fuchs theory. The conventional Morison's load model is compared to the new load model using 2^{nd}-order wave kinematics for extreme loads and responses.

Acknowledgments

This PhD study was conducted at the Department of Marine Technology at the Norwegian University of Science and Technology (NTNU). The research was made possible through financial support from the Norwegian Research Council (Grant No. 268182) as part of the WAS-XL (Wave loads and Soil support for eXtra Large monopiles) project. The project involved collaboration between SINTEF Ocean, NTNU, Norwegian Geotechnical Institute (NGI), Equinor, Innogy, EDF (Électricité de France) Dept. Research & Development, Vattenfall, and Multiconsult. Additionally, part of the work was carried out at the Centre for Autonomous Marine Operations and Systems (AMOS), which is sponsored by the Norwegian Research Council as part of the Centres of Excellence funding scheme (project number 223254 - AMOS).

Firstly, I would like to express my gratitude to my supervisor, Professor Erin E. Bachynski-Polić. I am grateful for your technical assistance, guidance, and the faith you put in me during the past years. From our weekly meetings to my e-mails at 2 a.m. on a Saturday, which I knew you would respond to at the first chance, I sincerely thank you for always being there for me. Your expertise and focus on detail helped me improve my critical thinking and shaped the way I approach questions and problems. Lastly, being a great supervisor requires technical expertise and being present for your student, understanding his needs, thoughts, and life matters that may occur during the Ph.D. period. And you are a great supervisor, Erin! I wish you a bright future, with only beautiful moments with Moira and Drazen!

Sincere appreciation also goes to my co-supervisor Professor Sverre Haver. I still remember when I first met you in your guest lecture in one of my Ph.D. courses. I was genuinely fascinated by the condensed combination of your academic knowledge, practical experience, energy, and passion. Despite of you being located permanently at Stavanger, our meetings and your profound knowledge, were always eye openers for my way of thinking and approach to tackle a problem. I still remember one of our phone calls during the summer vacation, where I was at the beach in my hometown, you were preparing pizza for your dinner, and we were discussing about using the Gumbel distribution for paper review I just had received! Although we did not have a weekly contact, you have truly been a mentor for me. Thank you for all your interest in my work and your kind advises, in all aspects.

The Ph.D. journey would have been far less interesting if I could not share in a daily basis moments with other candidates and friends. Their importance became significantly profound during the Coronavirus pandemic, where we had to comply with the rules of social distancing. From interesting discussions during coffee and lunch breaks, to evenings trying forget Ph.D. struggles. Thomas, Haris, Carlos, John Marius, Stian, Irene, Henrik, Sepideh, Vincent, Davide, Balazs, Mihalis^2, Andreas, Spiros, Artemis, I wish you all a bright future. I thank you for all the memories during those years.

Special thanks go to my colleague Stian Høegh Sørum for the great collaboration we had during our PhD, and Ana Page from Norwegian Geotechnical Institute (NGI) for her continuous cooperation and support related to the soil model used in the thesis. Finally, I would like to thank Bjørn Tore Bach and Mostafa Jalali for their technical assistance at the Department of Marine Technology, and all the partners from WAS-XL project for the constructive discussions and their useful feedback during our yearly meetings.

In conclusion, I would like to express my gratitude to my parents. Strato and Markela, nothing would have been possible without your lifelong encouragement and support for my decisions and your faith in me from my early years. Thank you for all your love. I love you unconditionally! Finally, to my companion in life, Kaia. I sincerely thank you for always being there for me, for your support, and your patience during the past four years; they would be significantly more difficult without your smile and positive energy. I am looking forward to our future moments!

In memory of Πέτρος (1936-2018) and Τάσος (1963-2022)

George Katsikogiannis
February - 2024
Trondheim, Norway

Publication List

In the framework of the thesis, a collection of papers has been published in different scientific journals and international conferences. The papers are listed below, and a declaration of authorship is provided.

List of Papers

Paper 1 (P1):
Katsikogiannis, G., Bachynski, E.E., Page, A.M. Fatigue sensitivity to foundation modelling in different operational states for the DTU 10MW monopile-based offshore wind turbine. *Journal of Physics: Conference Series* 2019; 1356: 012019. **2**(3):138-145. `https://dx.doi.org/10.1088/1742-6596/1356/1/012019`

Paper 2 (P2):
Katsikogiannis, G., Sørum, S.H., Bachynski, E.E., Amdahl, J. Environmental lumping for efficient fatigue assessment of large-diameter monopile wind turbines. *Marine Structures* 2021; **77**, 102939. `https://doi.org/10.1016/j.marstruc.2021.102939`

Paper 3 (P3):
Katsikogiannis, G., Hegseth, J.M., Bachynski, E.E. Application of a lumping method for fatigue design of monopile-based wind turbines using fully coupled and simplified models *Applied Ocean Research* 2022; **120**, 102998. `https://doi.org/10.1016/j.apor.2021.102998`

Paper 4 (P4):
Katsikogiannis, G., Haver, Sverre, K., Bachynski, E.E. Assessing some statistical and physical modelling uncertainties of extreme responses for monopile-based offshore wind turbines, using metocean contours *Applied Ocean Research* 2024; **143**, 103880. `https://doi.org/10.1016/j.apor.2024.103880`

Paper 5 (P5):
Sørum, S.H., Katsikogiannis, G. Bachynski, E.E., Amdahl, J., Page, A.M., Klinkvort, R. T. Fatigue design sensitivities of large monopile offshore wind turbines *Wind Energy* 2022;**25**, 1095-4244. `https://onlinelibrary.wiley.com/doi/abs/10.1002/we.2755`

Declaration of authorship

Table 1 summarizes the author contributions for the papers included in the thesis, following the definition from Allen et al.[1]. The author's initials are capitalized where the author has had a leading role towards the contribution of the paper, and lower case where the author has made a contribution.

Table 1: Author contributions for the papers included in thesis

	P1	**P2**	**P3**	**P4**	**P5**
CO	GK	GK,shs	GK	GK	SHS,gk,ebp
ME	GK	GK,SHS	GK	GK	SHS,gk,ebp
SO	GK	GK,shs	GK,jmh	GK	GK,shs
VA	GK	GK,shs	GK	GK	SHS
FA	GK	GK,SHS	GK	GK	SHS, GK
IN	GK	GK,SHS	GK	GK	SHS, gk
DC	GK	GK	GK	GK	SHS, gk
$\mathbf{W}_{od}$	GK	GK,shs	GK	GK	SHS, gk
$\mathbf{W}_{r\&e}$	EBP,AMP	GK,shs	EBP,AMP	EBP,SH	SHS, gk
VI	GK	GK,shs	GK	GK	SHS, gk
SU	EBP	EBP,JA	EBP	EBP,SH	EBP,JA
PA	GK	GK	GK	GK	SHS
FAC	EBP	EBP,JA	EBP	EBP	EBP,JA

- Abbreviations of authors: **GK:** George Katiskogiannis, **SHS:** Stian Høegh Sørum, **EBP:** Erin Bachynski-Polić, **SH:** Sverre Haver, **JA:** Jørgen Amdahl, **JMH:** John Marius Hegseth, **AMP:** Ana M. Page, **RTK:** Rasmus T. Klinkvort.

- Abbreviations of contributions: **CO:** Conceptualization, **ME:** Methodology, **SO:** Software, **VA:** Validation, **FA:** Formal Analysis, **IN:** Investigation, **DC:** Data Curation, $\mathbf{W}_{od}$**:** Writing (original draft), $\mathbf{W}_{r\&e}$**:** Writing (review & editing), **VI:** Visualization, **SU:** Supervision, **PA:** Project administration, **FAc:** Funding acquisition.

Contents

Nomenclature

List of Abbreviations

ALS	Accidental Limit State
BEM	Blade Element Momentum
CAPEX	Capital Expenditure
DLC	Design Load Case (set of load cases in design standards)
DLL	Dynamic Link Library
ECM	Environmental Contour Method
FEA	Finite Element Analysis
FLS	Fatigue Limit State
IFORM	Inverse First Order Reliability Method
IPCC	Intergovernmental Panel on Climate Change
IRENA	International Renewable Energy Agency
LCOE	Levelised Cost of Energy
LC	Load Case (load case analyzed in the simulation tool)
MECM	Modified Environmental Contour Method
NTM	Normal Turbulence Model
O&M	Operation and Maintenance
OPEX	Operation and Maintenance costs
OWT	Offshore Wind Turbine
PSD	Power Spectral Density

RNA	Rotor-Nacelle Assembly
SLS	Serviceability Limit State
SWL	Still Water Level
ULS	Ultimate Limit State

Chapter 2

λ	Wavelength
ρ	Sea water density
C_α	Added mass coefficient
C_d	Drag coefficient
C_m	Inertia coefficient
D_p	Monopile diameter
dF	Total hydrodynamic force per unit length
H_s	Significant wave height
T_p	Peak period
u_r	Relative horizontal fluid particle velocity
U_w	Wind speed
$\dot{u}_s$	Structure acceleration normal to the member
$\dot{u}_w$	Flow acceleration normal to the member

Chapter 3

$\boldsymbol{C_\chi}$	Generalized damping matrix
$\boldsymbol{F(t)}$	Generalized load vector
$\boldsymbol{F_W}$	Generalized wave load vector
$\boldsymbol{H_{\zeta F}}$	Transfer function from wave amplitude to modal excitation forces
$\boldsymbol{H_{\zeta F}^{H}}$	Conjugate transpose
$\boldsymbol{K_\chi}$	Generalized stiffness matrix
$\boldsymbol{M_\chi}$	Generalized mass matrix

$\boldsymbol{M_d}$	Discrete mass matrix
$\boldsymbol{M_{el}}$	Elemental mass matrix
$\boldsymbol{M_G}$	Global mass matrix
$\boldsymbol{S_\zeta}$	Wave spectrum
$\boldsymbol{K_G}$	Global stiffness matrix
$\boldsymbol{K_{el,b}}$	Elemental bending stiffness matrix
$\boldsymbol{K_{el,g}}$	Elemental geometric stiffness matrix
$\boldsymbol{K_s}$	Soil stiffness matrix
$\boldsymbol{S_{F_{wave}}}$	Wave load cross spectral density matrix
$\boldsymbol{S_{F_{wind}}}$	Wind load cross spectral density matrix
$\boldsymbol{S_u}$	Total load cross spectral density matrix
$\boldsymbol{S_y}$	Cross spectral density matrix of response y
$\chi(t)$	Modal coordinate (position)
η_κ	Gain-scheduling parameter
ω_c	Corner frequency
$\psi(z)$	Mode shapes
σ_u	Variance velocity
σ_x	Axial stress on the outer surface of a tubular cross section
θ	Angular position at the circumference tubular cross section
θ_{pa}	Blade pitch angle
ζ	Wave elevation
ζ_A	Wave amplitude
A	Cross-sectional area
d	Water depth
$D_{t,i}$	Diameter of tower section i
$dF_D(z,\omega)$	Viscous excitation force

$dF_M(z,\omega)$	First order wave excitation from MacCamy-Fuchs theory
F_T	Aerodynamic thrust
g	Gravitational acceleration
I_D	Rotor and drivetrain inertia
I_y	Second moment of area computed about the y axis
I_z	Second moment of area computed about the z axis
I_{xx}, I_{yy}	RNA inertias
k	Wave number
K_g	Generator torque constant
k_i	Integral gain of the PI controller
k_p	Proportional gain of the PI controller
L_p	Monopile embedded length
$L_{t,i}$	Length of tower section i
M_T	Tilting moment
M_y	Bending moment about the y axis
M_z	Bending moment about the x axis
M_{RNA}	RNA mass
N_x	Axial force
N_{gear}	Gear ratio
P_0	Rated power
Q_A	Aerodynamic torque
Q_G	Generator torque
r	Outer radius of a tubular cross section
t_p	Monopile thickness
$t_{t,i}$	Thickness of tower section i
$\dot{\chi}(t)$	Modal coordinate (velocity)

$\dot{\phi}_0$	Reference rotor speed
$\dot{\varphi}$	Rotor speed
$\dot{\phi}_{lp}$	Filtered rotor speed

Chapter 4

β	Irregularity factor
δ	Bandwidth parameter
$\Gamma(\cdot)$	Gamma function
ν_0	i^{th} mean zero up-crossing rate
σ_{eq}	Equivalent stress range
θ_u	Wind direction
θ_w^{sw}	Wave direction (swell component)
θ_w^{ws}	Wave direction (wind-sea component)
d_{ST}^{FD}	Unit fatigue damage obtained using $S_{\sigma_{i,j}}$
d_{LT}^{TD}	Long-term damage
d_{ST}^{TD}	Short-term damage obtained from a time-domain simulation
$D_{LT,SD}^{lumped}$	Long-term fatigue calculated from a lumped load case in time-domain
$D_{LT,target}$	Target fatigue damage
$D_{U,scale}$	Scaled unit fatigue damage
H_s^{LC}, T_p^{LC}	Sea-state parameters of a lumped load case
$H_{\zeta\sigma}$	Stress transfer function of wave elevation to stress response
$H_{s,i}^{lb}, H_{s,i}^{ub}$	Lower and upper bounds of a H_s class i
m	S-N curve fatigue strength exponent
m_i	i^{th} spectral moment
N	Total number of observations within the dataset
n_k	Number observations $U \in [U_k^{lb}, U_k^{ub})$
N_y	Specified design life

N_{θ_u}	Number of wind directional sectors
N_{θ_w}	Number of wave directional sectors
N_{H_s}	Number of H_s classes within a scatter diagram
$n_{i,j}$	Number observations with $H_s \in [H_{s,i}^{lb}, H_{s,i}^{ub})$ and $T_p \in [T_{p,j}^{lb}, T_{p,j}^{ub})$
$n_{k,i,j}$	Number observations with $H_s \in [H_{s,i}^{lb}, H_{s,i}^{ub})$ and $T_p \in [T_{p,j}^{lb}, T_{p,j}^{ub})$, under the condition that $U \in [U_k^{lb}, U_k^{ub})$
N_{T_p}	Number of T_p classes within a scatter diagram
$P(\cdot)$	Probability of occurrence of an event
$P^{sw}_{SD_{k,\theta_u,\theta_{ws},\theta_{sw}}}$	Total probability of a swell scatter diagram wind speed, wind direction, wind-sea direction, swell direction
$P^{ws}_{SD_{k,\theta_u,\theta_{ws}}}$	Total probability of a wind-sea scatter diagram conditioned on wind speed, wind direction, wind-sea direction
P_{SD_k}	Total probability of a scatter diagram (combined sea) conditioned on wind speed
$S_{\sigma\sigma}$	Power spectral density of the stress response
$S_{\sigma_{i,j}}$	Stress spectrum representative for a sea-state class $H_{s,i}$–$T_{p,j}$ within a scatter diagram
$S_{\zeta\zeta}$	Incident white noise wave spectrum
$T_{p,j}^{lb}, T_{p,j}^{ub}$	Lower and upper bounds of a T_p class j
U_k^{lb}, U_k^{ub}	Lower and upper bounds of a U class k
U_{hub}	Wind speed at hub height

Chapter 6

β_d	Damping factor for stiffness proportional damping
δ	Logarithmic decrement
ξ	Global damping ratio
A_i, A_{i+1}	Successive amplitudes in motion decay test

Chapter 7

α	Monopile radius

α_g and β_g	Parameters of Gumbel distribution
β	Reliability index
η	Transition point between Lognormal and Weibull models in LonoWe distribution
κ_h^{2p}, A_h^{2p}	2-parameter Weibull shape, scale parameters of f_{H_s}
κ_h^{3p}, A_h^{3p}, γ_h^{3p}	3-parameter Weibull shape, scale location parameters of f_{H_s}
κ_t, A_t, γ_t	Weibull shape, scale, location parameters of f_{T_p}
κ_u, A_u, γ_u	3-parameter Weibull shape, scale location parameters of $f_{U_{hub}}$
λ_p	Wave length, calculated based on peak period
μ_t, σ_t^2	Log-normal mean and variance of $\ln(t)$ in f_{T_p}
μ_M	Mean of Gumbel distributed variable
$\Phi^{-1}(\cdot)$	Inverse standard cumulative distribution function
σ_M	Standard deviation of Gumbel distributed variable
τ	Duration of sea state
c_i, d_i, e_i	Parameters used in the dependence structure of Weibull models for environmental contours with $i = 1, 2, 3$
C_{m_n}	Frequency-dependent mass coefficient estimated from MacCamy-Fuchs diffraction theory
$dF_{inertia}$	Inertia force per unit length, as a linear composition of N Fourier components from the nonlinear acceleration signal
$F_X^{LT}(\cdot)$	Long-term cumulative distribution function of response X
$F_X^{ST}(\cdot)$	Short-term cumulative distribution function of response X
f_{H_s}	Conditional distribution for H_s for given U_{hub}
$F_M(\cdot)$	Gumbel distribution for short-term global maxima of fore-aft bending moment at the mudline
f_{T_p}	Conditional distribution for T_p for given U_{hub} and H_s
f_{U_{hub},H_s,T_p}	Joint environmental probability density function
$f_{U_{hub}}$	Marginal distribution for wind speed at hub height

h	Water depth
$J_1'(\cdot)$, $Y_1'(\cdot)$	First and second kind Bessel functions of first order. Prime denotes the derivative with respect to the argument.
k_n	Wave number corresponding to a Fourier component at frequency ω_n
m_i, s_i	Parameters used in the dependence structure of Log-normal models for environmental contours with $i = 1, 2, 3$
$M_{90\%}$	90^{th} percentile of global maxima of fore-aft bending moment at the mudline
$P_f(\xi)$	Failure probability for level ξ
p_g	Percentile of the 1-hour extreme value distribution
r_k	Radius of a circle in contour sphere for a wind class u_k in Gaussian space
S_p	Wave steepness limit
T_N	Target return period of N years
u_1, u_2, u_3	Uncorrelated normally distributed variables
$\dot{u}_n$	n^{th} Fourier component of the acceleration signal

List of Figures

List of Tables

Chapter 1

Introduction

The chapter gives an overview of offshore wind as a part of the energy sector, its current status, and future projections. The reader is introduced to the substructures of offshore wind turbines, focusing on monopile foundations. The design challenges of large-diameter monopiles are shortly outlined, and finally, the objectives, contributions, and organization of the thesis are given.

1.1 Background

Global warming has become a major concern internationally, having observable effects on human and natural systems. Its causes, potential impacts, and mitigation measures have been extensively investigated by the Intergovernmental Panel on Climate Change (IPCC) [2]. The Paris Agreement [3], which reflects the commitment to global climate action, aims to limit global warming to 1.5°C compared to pre-industrial levels. However, achieving this goal requires a profound transformation in the global energy landscape [4]. In particular, due to the strong correlation between global carbon dioxide (CO_2) and global temperature variations [5], a significant reduction of CO_2 emissions is needed. This relationship is evident in the warming projections for different scenarios up to the year 2100, see e.g., Figure 1.1 [6].

Decarbonization of the energy sector is a key component of the global energy transformation through the continuous deployment of renewable energy sources. Amongst others, wind power has been a pioneering renewable technology in the last decades. As shown in Figure 1.2 [7], according to International Renewable Energy Agency (IRENA), onshore and offshore wind together are expected to generate more than one-third of total electricity needs by 2050, becoming the leading source of energy.

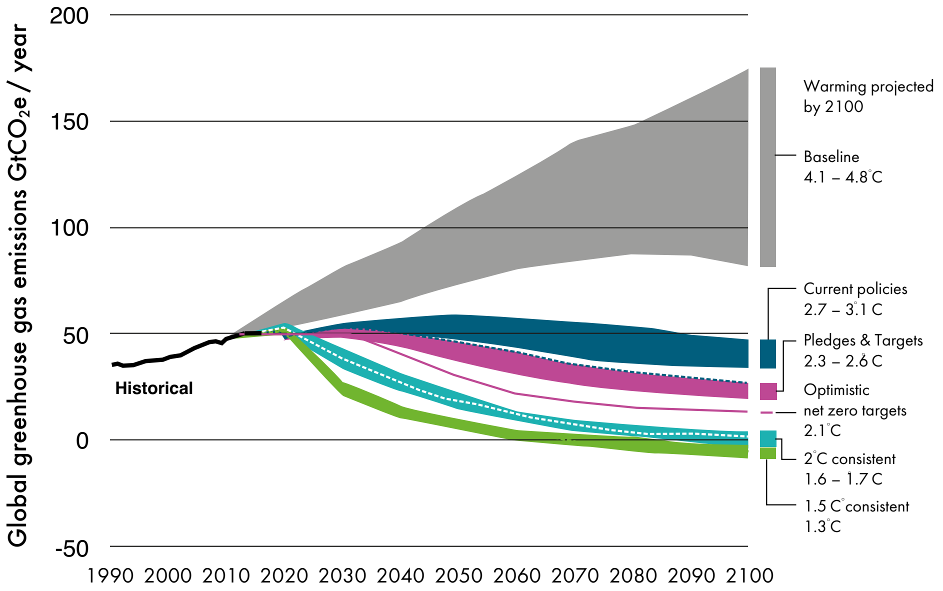

Figure 1.1: Emissions and expected warming based on pledges and current policies. Source: Global Wind Report 2021 [6] (GWEC)

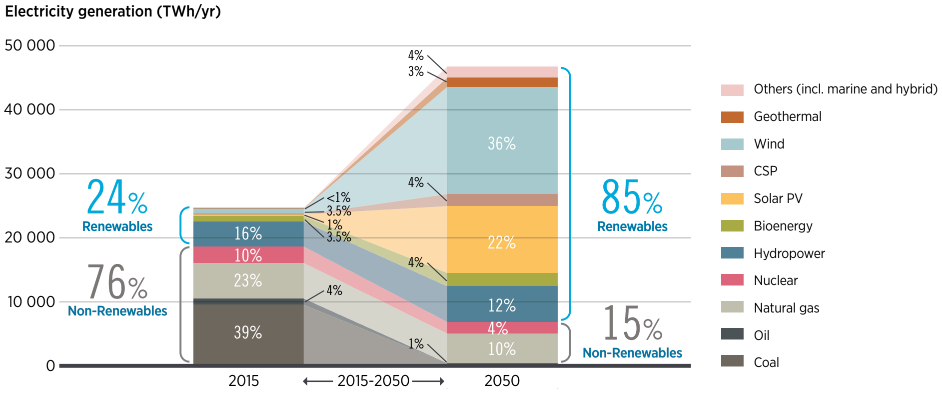

Figure 1.2: Breakdown of electricity generation, by source (TWh/yr). Source: IRENA [7]

Offshore wind power has significant potential compared to onshore wind due to the high energy density, lower wind shear and turbulence, and minimum visual impact [8]. However, offshore wind farms impose significant economic and technical challenges in terms of design, installation, operation, and maintenance (O&M) due to the harsh marine environment. Despite being a relatively new technology in the early 2000s, offshore wind has become a reliable and cost-effective energy source thanks to continuous technological innovations. Nevertheless, for further development of offshore wind energy, substantial cost reductions are needed to decrease the levelised cost of energy (LCOE), mainly originating either from technological advances that can lead to more efficient designs of offshore wind turbines (OWTs), or by improvements in the supply chain to meet the growing market needs.

The foundation is a crucial element in offshore wind deployments as it provides support to the turbine and shall withstand operational and environmental loads over its design life of 20-25 years. Currently, the dominant foundation type for offshore wind farms is the monopile, accounting for nearly 82% of all installed substructures in Europe [9]. It is anticipated that monopiles will continue to be the preferred choice for future developments due to their simplicity, fabrication speed, and installation experience [10].

With larger and heavier wind turbines being installed in deeper waters, the diameter of monopiles needs to increase to resist the significantly larger dynamic loads. These large-diameter monopiles, often referred to as XL or XXL monopiles, push the limits of technical and economic feasibility. Typically, the natural frequencies of the structure decrease as the rated power of the turbine increases, bringing them closer to the primary wave frequencies and making them more susceptible to wave loads. Furthermore, the applicability and level of accuracy of soil-structure interaction and hydrodynamic models commonly used for small-diameter monopiles need to be critically examined when used to estimate long-term fatigue and extreme responses of large-diameter monopiles.

The economic viability of large-diameter monopiles is influenced by the substantial contribution of OWT foundations to the total capital costs. As a result, any potential cost reductions can significantly impact their feasibility. To achieve this, a comprehensive evaluation and improvement of design methods and models from various engineering disciplines is essential. These methods and models should effectively address the complexities that arise with increasing monopile dimensions, including factors such as wave loads, soil-structure interaction, and long-term fatigue and extreme responses. By employing advanced design methods and refined models, designers can gain a deeper understanding of large-diameter monopile behaviour, thereby ensuring the reliability and efficiency of their designs.

1.2 Scaling up of offshore wind

Offshore wind development began in the 1980s, initially focused on studying the potential of offshore wind resources [11]. The first commercial offshore wind farm, Vindeby, was deployed in 1991 off the coast of Denmark, with a capacity of 5 MW. In the following decade, more projects were completed in countries like Denmark, Sweden, the Netherlands, and the UK. These early offshore wind farms used relatively simple designs, with onshore turbines supported on concrete foundations in shallow waters, while the emphasis was on assessing technical feasibility rather than cost considerations [12].

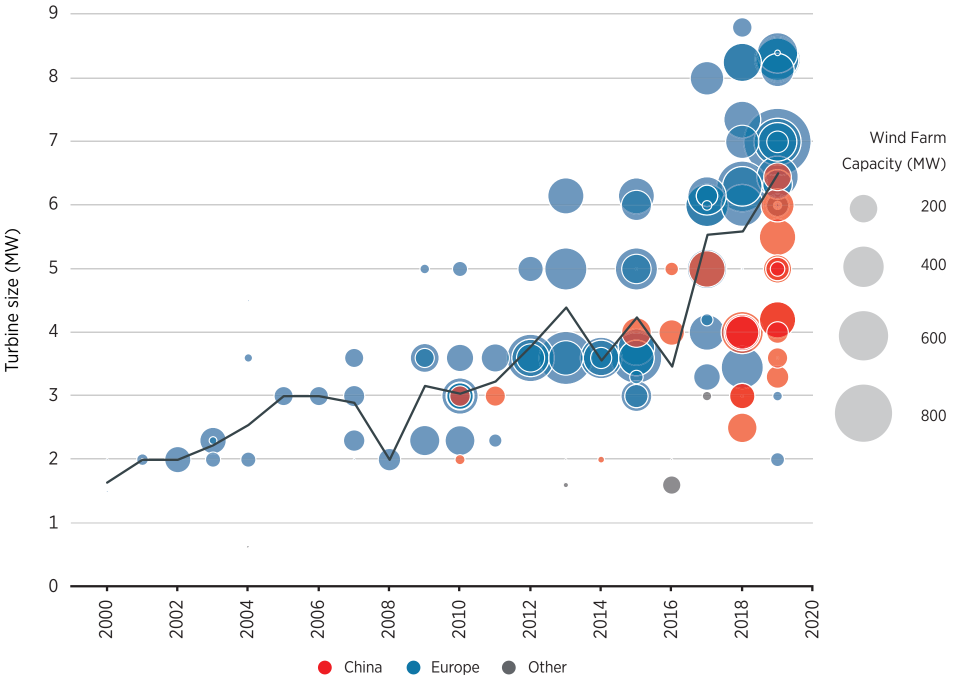

Figure 1.3: Project turbine size and global average turbine size and wind farm capacity for offshore wind, 2000-2019. Source: IRENA [13]

After 2000, offshore wind technology underwent significant advances. Turbines with larger capacities were installed, new foundation types were introduced, and specialized vessels were developed for efficient operation and maintenance activities. The commissioning of Horns Rev 1 in the North Sea in 2002 marked a crucial milestone, as it was the first wind farm to use steel monopile foundations. This transition from pilot projects to commercial development demonstrated the need for further advances in offshore wind technology. As a result, offshore wind power targets were raised, leading to the scaling up of projects and the adoption of larger turbines and wind farms, as illustrated in Figure 1.3 [13].

At the time of writing, the total installed capacity of global offshore wind exceeds 35 GW. Europe has been the leading region, accounting for 25 GW by the end of 2020, with the rest being concentrated in China. Deployment is set to broaden to North America, while pilot and commercial projects have been conducted in Asia-Pacific [8, 14, 15]. Projections indicate that the total installed capacity is expected to reach around 230 GW by 2030 and nearly 1000 GW by 2050 [16, 17]. This continuous progression over the years requires harnessing stronger winds in deeper waters, also in response to public demand for reduced visual impact. Figure 1.4 reflects this trend, showing that bottom-fixed OWTs installed in 2019 had an average distance to shore of 60 km and a water depth of 32 m, while turbines installed in 2001 were situated at averagely 5 km from the shore, at merely 7 m depth [13].

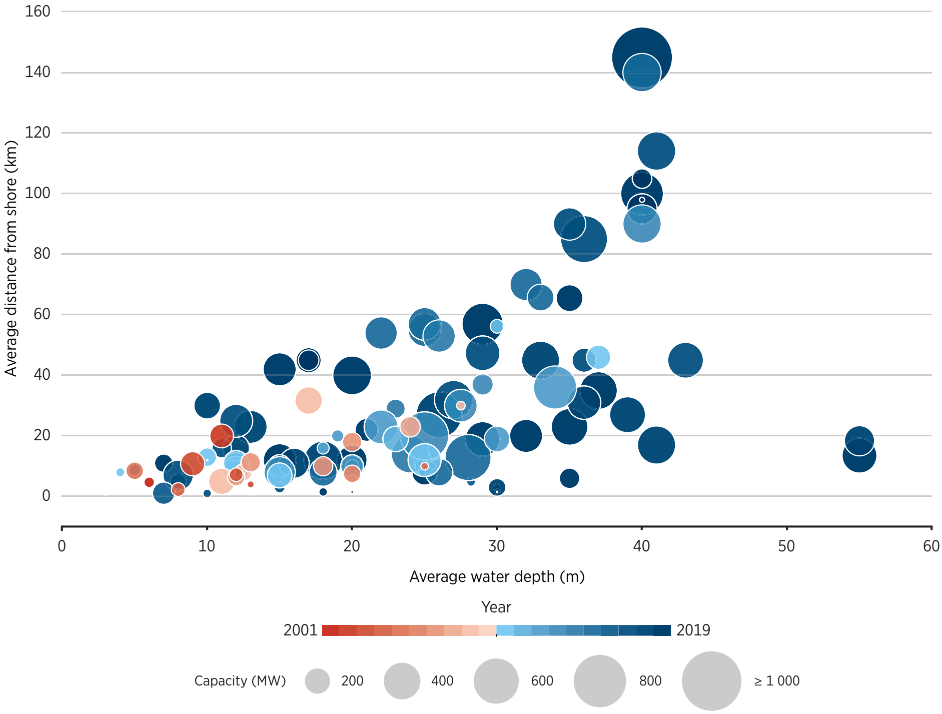

Figure 1.4: Average distance from shore and water depth for offshore wind, 2000-2019. Source: IRENA [13]

These developments signify the progress in expanding offshore wind capacity, and as Figure 1.5 illustrates, this continuous growth is also reflected in the growth of rotor diameters, hub heights, and tower sizes within the industry, pushing the boundaries of technological, economical and logistical capabilities.

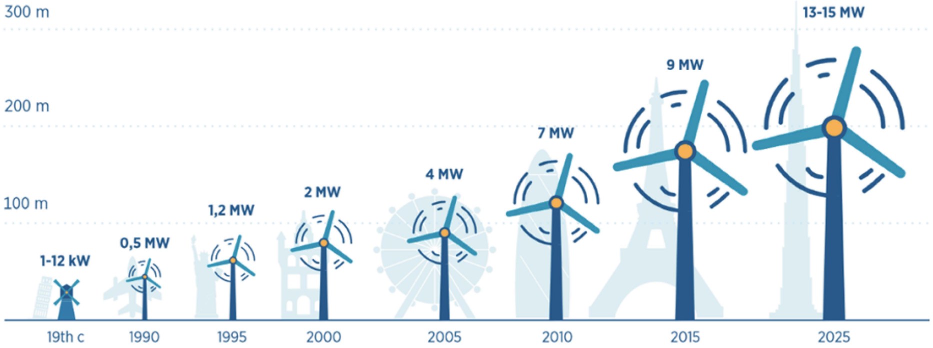

Figure 1.5: Growth in size of typical commercial wind turbines. Source: IRENA [18]

1.3 Offshore wind costs

In response to the increasing complexity and size of offshore wind projects, and the growing demands of the supply chain, continuous improvements in design, fabrication, installation, and O&M were necessary. The focus shifted towards cost reduction to unleash the full potential of offshore wind and ensure its competitiveness in the market.

In the past decade, joint projects combining research and innovation played a significant role in addressing industry challenges [12]. Turbine manufacturers introduced higher-output turbines, with some reaching up to 14 MW, increasing power production while reducing costs per megawatt-hour (MWh) due to fewer installations, foundations, and units to service. Moreover, manufacturing, transportation, and installation processes have been streamlined, components have been standardized, and remote monitoring and simulation technologies have been implemented. The introduction of specialized vessels for maintenance also contributed to lower O&M costs.

Figure 1.6 provides an overview of the LCOE for offshore wind between 2000 and 2023 [13], clearly indicating that these advances have gradually led to cost reductions over the past decade, making offshore wind a more competitive energy source.

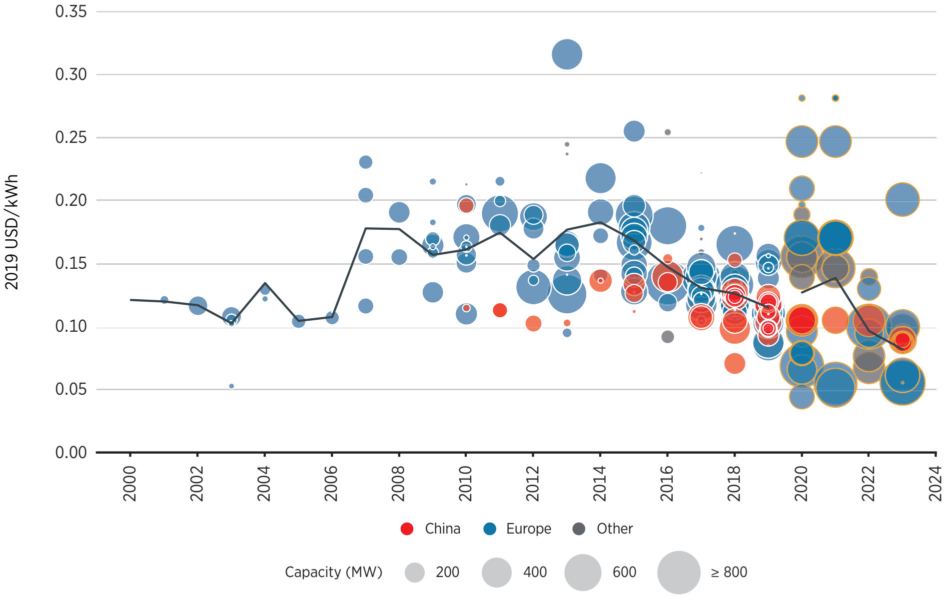

Figure 1.6: Offshore wind project and global weighted average LCOE, 2000-2023. Source: IRENA [13]

The deployment of an offshore wind farm requires high capital expenditure (CAPEX) and operation and maintenance costs (OPEX). CAPEX primarily includes the costs associated with infrastructure, construction, and the installation of key components such as the rotor-nacelle assembly (RNA), support structure, and electrical components. OPEX includes expenses related to the operation, planned-unplanned maintenance, and transmission charges. While costs can vary considerably among different offshore wind projects [19], BVG Associates provides a comprehensive guide to the typical cost breakdown of various elements involved in an offshore wind farm, spanning from project development to decommissioning [20]. Figure 1.7 shows their breakdown of the major costs, estimated assuming a UK 1 GW project of 100 10 MW monopile-based turbines, located 60 km from shore in 30 m water depth and commencing in operation in 2022 [20].

Several aspects affect the final costs of offshore wind farm projects. Projects located in deeper waters with heavier and more expensive foundations, increase costs for steel and installation. Soil conditions also play a role, with

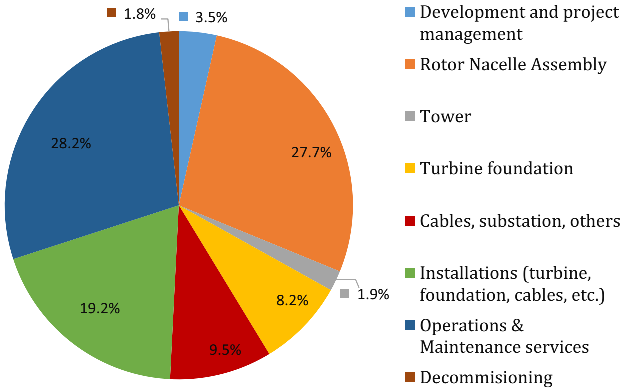

Figure 1.7: Contribution of major cost elements of an offshore wind farm to LCOE. Source: BVG Associates [20]

certain conditions, e.g., dense sand or stiff clay, offering cost benefits through simpler installation methods (e.g., piling), while others, e.g., rock can significantly raise costs due to the need for alternative designs and installation techniques such as drilling. Due to the soil-structure interaction, soil conditions also can affect the amount of steel which is required to achieve the desirable stiffness for the whole OWT. In some markets such as Asia or North America, seismic considerations or typhoon winds may dominate the final design, while tidal ranges can add to costs due to the minimum clearance required from sea level to blade tip throughout the turbine's design life. Finally, projects located further from the shore face longer access times, which can reduce the accessibility for installation and maintenance activities and impact energy production.

Since 2012, several studies have been conducted evaluating pathways for potential cost reductions for offshore wind farms [21–29]. These studies highlight the need for technological innovation and improvements in the supply chain to address future challenges. Improvements in turbine technology, such as higher rated power and capacity factors, are expected to have the greatest impact on the cost-effectiveness of wind power. Furthermore, optimization of wind farm layout, advances in blade materials, design, and manufacturing, and innovations in support structure design, are also identified as key factors to further reduce LCOE. Regarding O&M, the introduction of condition-based maintenance, remote inspections, and improved personnel access are expected to considerably impact projects located far from shore, which involve greater transit distances and harsh sea conditions [26].

1.4 Offshore wind support structures

In accordance with IEC 61400-3-1 [30], the support structure of an offshore wind turbine (OWT) consists of the tower, the foundation - the part below the seabed, which transfers the loads acting on the support structure into the seabed - and the substructure, which refers to the part of the support structure that extends upwards from the seabed and connects the foundation to the tower. Figure 1.8 provides simplified illustrations of these different bottom-fixed support structures along with their foundations.

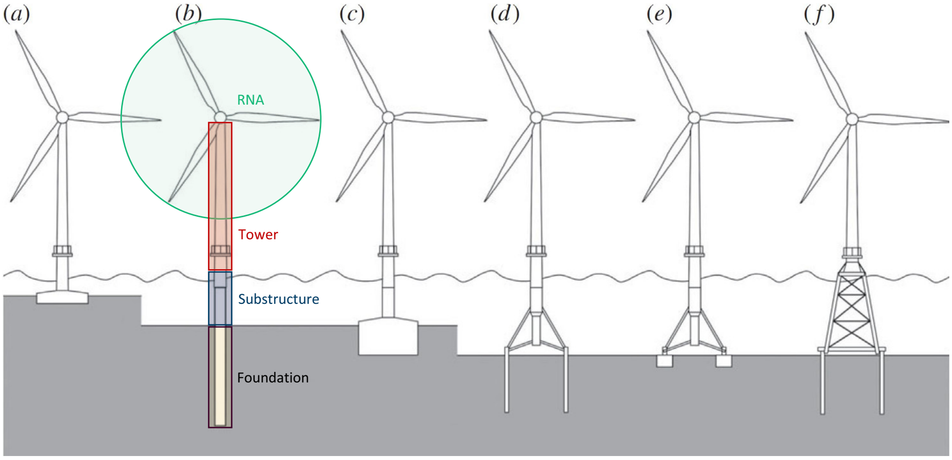

Figure 1.8: Typical bottom-fixed substructures used for offshore wind turbines (a) gravity-based (b) monopile (c) bucket (d)-(e) tripod (f) jacket. Source: Kallehave et al. [31]

The substructures used for OWTs typically account for 15% to 20% of the total capital expenditure (CAPEX), including installation costs [8, 20]. There are different types of substructures, including gravity-based structures, monopiles, and jackets. To date, monopile foundations have supported over 80% of the installed offshore wind capacity, while jackets account for approximately 10% of installations [9]. Gravity-based OWTs were primarily deployed in early offshore wind farms located in shallow water depths and contribute to around 5% of the installed substructures. Other concepts, such as tripods, are less commonly used. Several studies discuss the technical aspects, challenges, current status, and future prospects for various substructure concepts [8, 32, 33].

The primary function of the foundation is to provide support to the turbine, ensuring safety and reliability within its entire design life. The selection of the foundation type depends on various factors, including technical considerations such as water depth and seabed profile, as well as economic aspects like the availability of infrastructure for fabrication and transportation [34]. The design of the foundation is dependent on the RNA characteristics, and site-specific metocean and soil conditions. It is worth noting that different foundation designs can be adapted even for the individual locations within the wind farm, which can affect the economic feasibility of the project [35].

1.4.1 Design process and requirements

Foundation design is a multidisciplinary complex task due to many uncertain input parameters from various engineering fields, the complexity of the numerical models, and the extensive computational effort required. Generally, the design process typically consists of different phases, ranging from the preliminary phase with site metocean assessments, environmental surveys (e.g., geological, hydrographical), and conceptual design studies, to the detailed design phase that includes the final design of the foundation, tower, secondary structures, controller, and other aspects. An overview of various design phases and their objectives is given by Passon et al. [36].

Various parties are involved in the design process, primarily the wind turbine manufacturer and the foundation designer, with several technical and commercial interfaces [37]. The wind turbine manufacturer is responsible for designing the tower, modelling of turbine controller and aerodynamics, and performing the aero-elastic simulations using the integrated OWT model. The foundation designer focuses on the foundation design, considering hydrodynamic loads, soil modelling, and metocean assessment [38]. Finally, an independent certification body certifies the models, computational procedures, and the final design of the support structure.

Design standards such as IEC 61400-3 [30] and DNVGL-ST-0126 [39] provide engineering and technical requirements for the design of bottom-fixed support structures for offshore wind turbines. The design is based on different limit state criteria, which include requirements regarding material failure due to cumulative damage caused by repetitive loading (Fatigue Limit State - FLS), exceedance of the structural resistance (Ultimate Limit State - ULS), tolerance criteria, e.g., verticality, over its lifetime (Serviceability Limit State - SLS), and exceedance of maximum load-carrying capacity for (rare) accidental loads (Accidental Limit State - ALS). This thesis focuses on aspects related to FLS and ULS design.

To evaluate the design for the different design criteria, an extensive number of simulations are performed under different loading scenarios. Those scenarios are represented by design load cases (DLCs), which represent different combinations of design situations (e.g., power production, parked turbine, shutdown) and environmental conditions.

Typically, for the load calculations, industry adopts approaches where the support structure and wind turbine are simulated separately, using superimposed or semi-integrated load calculation approaches [36, 40]. The main reasons for applying these approaches are protection of confidential data, e.g. related to the RNA, individual design responsibilities with particular fields of expertise of the involved parties, and sophisticated simulation tools for individual design tasks, which cannot be easily shared [38]. Nevertheless, to estimate OWT load effects, fully integrated time-domain simulations are required [30]. In these simulations, the entire OWT system - RNA, support structure - is subjected to simultaneous aerodynamic and hydrodynamic loads, typically including the control system and soil-structure interaction modelling. The simultaneous consideration of these effects is essential for capturing the tightly coupled interaction between the various loads and structural characteristics of the OWT dynamic response. The importance of integrated load analysis in the design process for the accuracy of load calculations, and for the optimized design of the support structures has been highlighted in the literature [36, 38, 41].

Fully integrated simulations that consider all relevant loads and subsystems of the wind turbine system rely on advanced modelling tools. While commercial software packages exist for this purpose [42–44], they require a comprehensive technical background to use effectively. Furthermore, they are computationally expensive, especially when analyzing thousands of load cases for design purposes. Therefore, suitable simplified models, combined with applied design methods, are of interest, especially during the preliminary design phases. These models can provide valuable insights into the behaviour of the wind turbine system and support the design process.

1.4.2 Monopile foundation

The monopile foundation consists of tubular sections of rolled steel plates that are welded together to form a single pile. The monopile is connected to the OWT tower through a transition piece. The transition piece serves as an intermediary component between the monopile and the OWT tower. It is attached to the monopile either through a grouted connection, a flanged connection or other type of connections, e.g. slip joint [45]. The transition piece typically includes boat landing features that provide access for personnel from vessels, as well as ladders and other ancillary components. It also has a flange that allows for connection to the wind turbine tower. During installation, the monopile is driven, drilled, or vibrated into the seabed. The specific installation method depends on the soil and site conditions. Depending on the soil or current conditions, scour protection may be required around the base of the monopile to prevent erosion. Figure 1.9 shows a simplified illustration of a monopile foundation with the transition piece, and scour protection.

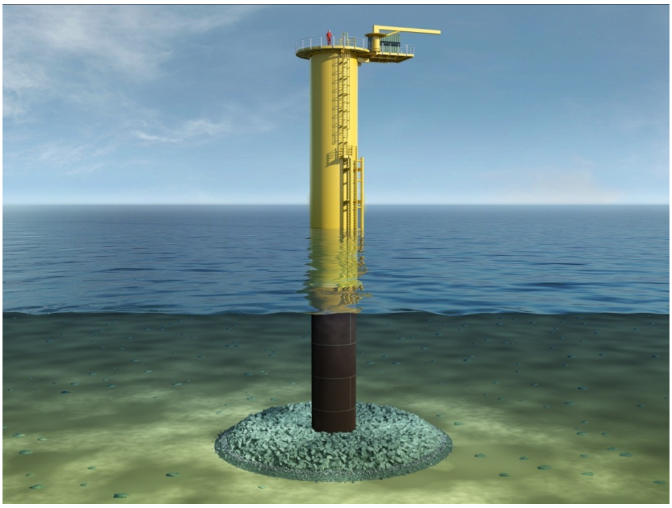

Figure 1.9: Monopile foundation with the transition piece [46]

Despite the initial predictions that monopiles would not be economically feasible for water depths over 20-25 m (and potentially only for turbines up to 3 MW) [47], it is still unclear at which water depth they become too expensive [32]. However, it is expected that monopiles will remain the preferred choice in the coming years [10], with the supply chain being continuously updated to meet the market needs. Fabrication processes have been optimized, with a focus on continuous and efficient production. Innovations in welding technology and equipment upgrades have allowed for the handling of larger dimensions and heavier monopiles. Furthermore, installation vessels with high payload capacity, deck space, and large cranes have been developed to operate in deeper waters, installing larger turbines and heavier support structures. Finally, the proven track record of monopiles as a reliable technology has also given confidence in investments [47].

Monopile design is typically adapted for site-specific environmental conditions. Environmental loads are mainly transferred as shear forces and bending moments through the structure, and then as lateral loads into the seabed. Axial loads due to RNA and tower weight are mainly relevant for buckling considerations. Torsion loads exist but are generally less significant from a design perspective. The key design parameters of a monopile foundation are the diameter, embedded length, and wall thickness. The diameter and embedded length contribute to the required stiffness of the foundation and are determined based on the magnitude of applied loads. Embedded length shall ensure vertical stability and limit horizontal deflection and rotation over the design lifetime [48]. The wall thickness of the monopile should be sufficient to meet criteria related to buckling resistance and fatigue during installation and operational design life.

1.4.3 Design considerations for large-diameter monopiles

As the capacity and size of offshore wind turbines increase, larger monopiles are required to withstand the increased aerodynamic and hydrodynamic loads. One of the primary objectives during the design of OWTs is to avoid the occurrence of resonance phenomena, which implicate rapidly accumulated fatigue damage (FLS) and can lead to stresses exceeding the structural capacity (ULS) [39]. To mitigate these issues, it is crucial to ensure that the natural frequency of the overall structure (particularly the first bending mode) does not coincide with the excitation frequencies experienced by the turbine. This becomes particularly challenging for monopile-based offshore wind turbines because they are subjected to a wide range of dynamic loads with different excitation frequencies.

These loads include aerodynamic and hydrodynamic loads due to wind and waves, loads associated with the rotor rotational frequency (1P) such as aerodynamic and imbalance loads, and loads at the blade passing frequency range (3P for three-bladed turbines) due to tower shadow and turbulence sampling [49–52]. Figure 1.10 [53] illustrates the main excitation loads acting on an OWT, and Figure 1.11 shows an example of typical stress time series and spectra at mudline (seabed level) for an OWT, where the stress response is influenced by various processes depending on the environmental condition and whether the turbine is in operational or parked state.

The design of OWTs aims to ensure that the first natural frequency of the structure lies within one of three possible ranges: soft-soft, soft-stiff, or stiff-stiff. These ranges are determined based on the relationship between the

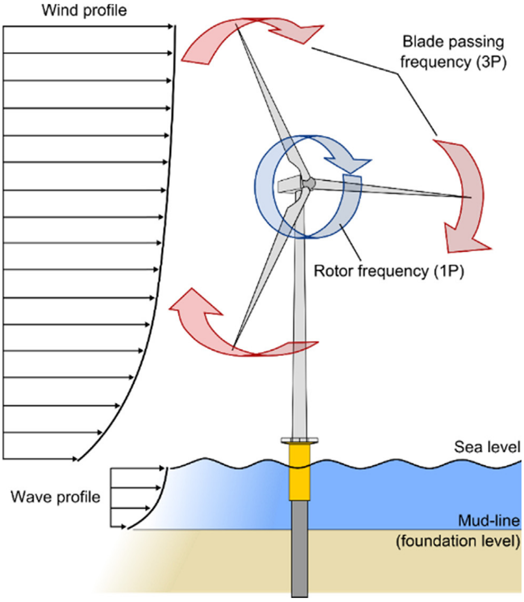

Figure 1.10: Excitation loads acting on an offshore wind turbine [53]

natural frequency and the rotor excitation frequencies experienced by the turbine. If the natural frequency is lower than the 1P frequency (soft-soft zone), the overall structure is typically too flexible and lacks structural integrity [54]. Such designs can lead to excessive deflections, vibrations, and potential structural failures. OWTs with natural frequency higher than the upper bound of 3P frequency (stiff-stiff zone) are economically unfeasible as their weight becomes excessively large, leading to higher material, transportation, and installation costs [48, 51, 55]. The common practice is for the natural frequency of the OWT to be within the soft-stiff range, as those designs can provide the required structural stiffness in the most economical manner. Variable-speed turbines, which are commonly used in offshore wind farms, further reduce the allowable frequency range for design.

The use of higher capacity wind turbines introduces several challenges related to the increased mass and size of the turbine components. The larger mass at the top of the structure, combined with longer blades to capture more wind energy, results in higher hub heights to maintain proper blade tip clearance above still water level (SWL). These factors lead to more slender structures with lower natural frequencies that are subjected to higher loads and exhibit pronounced dynamic responses.

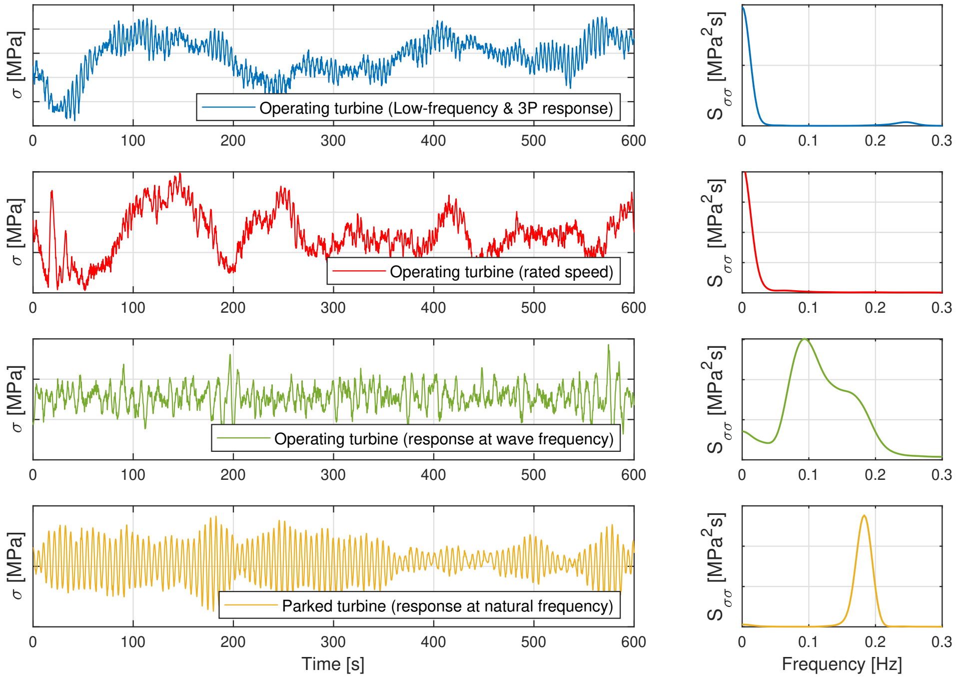

Figure 1.11: Typical response stress time series and spectra for a monopile-based OWT at mudline for different environmental and operational conditions.

Furthermore, the longer rotor blades also lead to higher blade tip speeds, which can cause issues such as increased turbulence in the wake, blade dynamics, and operational noise. To mitigate these effects, lower rotational speeds are often required for higher capacity turbines. As wind turbines increase in rated power, the allowable soft-stiff design range is shifted towards the typical wave excitation frequencies, imposing challenges for long-term fatigue and extreme responses. This shift is illustrated in Figure 1.12, where the 1P and 3P frequency content is shown for three different turbines (5 MW, 10 MW, and 15 MW) in relation to the site-specific 60-year cumulative distribution of peak frequency of sea states from NORA10 dataset [56, 57].

Fatigue assessment is a critical aspect of foundation design, becoming increasingly important for large-diameter monopiles. However, performing full fatigue assessments in the time domain, considering wind and wave loads,

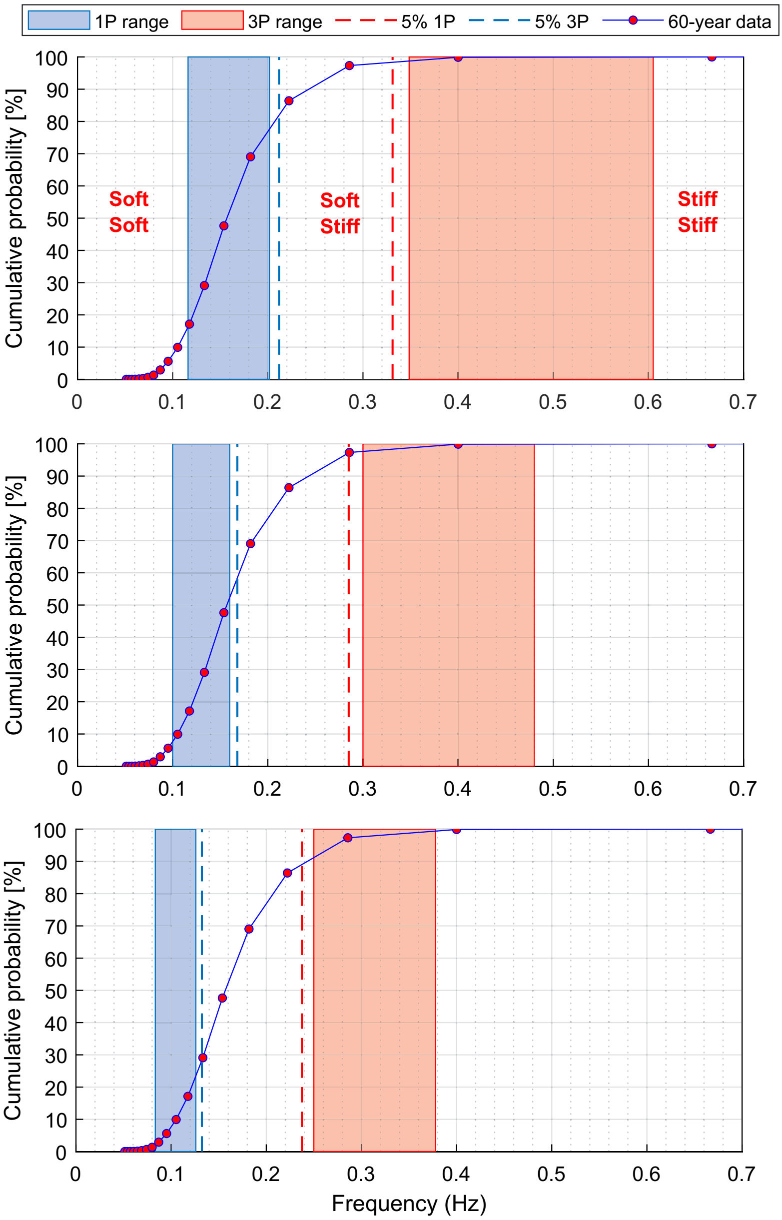

Figure 1.12: Excitation frequency content for the three OWTs considered in the thesis, and the wave peak frequency cumulative distribution function of the site-specific sea states. Top: 5 MW - Middle:10 MW - Bottom:15 MW

control system effects, and soil-structure interaction, can be computationally intensive. Therefore, there is a need for computationally efficient methods that account for wind- and wave-induced responses in an integrated manner, while considering long-term environment and OWT dynamics. Such methods can be beneficial in all design phases: both for preliminary assessment of less conservative designs or evaluating e.g. different positions within a wind farm. Furthermore, although fully integrated analyses carried out with time-domain numerical tools are the most accurate approach for load calculations, in practice, simplified models are often used during design (Sec. 1.4.1).

Another crucial aspect of OWT design is to ensure adequate structural resistance against extreme environmental loads. A proposed method to estimate long-term extreme responses of offshore structures is the full long-term analysis [58], but its use is typically prohibitive due to the high computational costs. An alternative approach to calculate the extremes is the environmental contour method (ECM), which is a simplification of the inverse first-order reliability method (IFORM). ECM is widely used in the offshore industry and recommended in design standards [30, 59, 60]. However, its direct applicability to OWTs poses various challenges compared to other types of offshore structures. Particularly, their non-monotonic response behaviour with respect to wind loads, can lead to extreme responses during operational states with non-extreme environmental conditions. Additionally, as shown, the continuous growth of monopile-based OWT dimensions brings their natural periods closer to primary wave periods, resulting in high dynamic responses that demand thorough consideration of the impact of statistical modelling on several metocean parameters, such as the wave peak period. The thesis uses ECM to establish multiple contours within the operational wind speed range and further explores the impact of statistical modelling of metocean conditions on environmental contours and extreme responses.

For monopile-based offshore wind turbines, achieving the required structural stiffness for the foundation can be accomplished by increasing the monopile diameter or, to a lesser extent, increasing the wall thickness [61]. However, larger-diameter monopiles introduce challenges related to increased wave loads and increase the necessity for accurate hydrodynamic and soil-structure interaction models in dynamic analyses, as they can reduce the conservatism in the OWT design, due to their impact on the dynamic response. Therefore, the impact of hydrodynamic and soil-structure interaction models commonly used for long (small-diameter) slender piles needs to be thoroughly assessed and compared to state-of-the-art models representative for large-diameter monopiles for long-term fatigue and extreme responses of large-diameter monopiles.

1.5 Thesis Objectives & Outline

This thesis focuses on FLS/ULS design challenges imposed by the growing dimensions of monopile foundations. The aim is to improve design methods and to investigate the impact of state-of-the-art numerical models for global responses on long-term fatigue and extreme responses of large-diameter monopiles.

The first of the research objectives of this thesis is to develop an accurate and computationally efficient method for FLS design as alternative to the conventional long-term fatigue assessment, accounting for wind-sea and swell components. The second objective is to compare the performance of state-of-the-art foundation models with commonly employed modelling methods and to assess their impact on fatigue estimates under varying metocean conditions and operational states. The third objective is to assess various statistical and physical load modelling uncertainties of extreme responses for monopile-based OWTs, using environmental contour method, providing a more thorough understanding of their relative importance for ULS design. The thesis is divided into the following chapters, summarized below:

Chapter 2 provides a detailed literature review to establish the background and scope of the thesis. The focus is on design methods for long-term fatigue and extreme responses of large-diameter monopiles, soil-structure interaction, and hydrodynamic modelling.

Chapter 3 provides a comprehensive overview of the numerical models employed for the analyses in the thesis. It includes details about the site-specific metocean conditions, wind turbines, fully coupled time-domain models, and reduced order state-space frequency-domain models.

Chapter 4 describes the environmental lumping method using fully coupled and reduced order models. The method is initially described for one wave component and then extended to bimodal sea states, i.e., combining wind-sea and swell components.

Chapter 5 presents the results of the lumping method. Its performance is compared to a full long-term fatigue assessment in terms of accuracy and computational time, and its sensitivity to various parameters is evaluated.

Chapter 6 investigates the effect of foundation modelling on fatigue damage estimates. A macro-element approach is compared to the $p - y$ curves modelling approach. The effect of nonlinear soil damping formulation on fatigue estimates is investigated, with focus on conditions when aerodynamic damping is negligible in the response direction, such as parked states and wind-wave misalignment conditions.

Chapter 7 focuses on the extreme responses of monopile-based OWTs using the environmental contour method. The chapter assesses the relative impact of different statistical and load models on extreme responses. Different probabilistic models for the metocean variables are used, and their effect on the resulting contours is shown. Then, the importance of soil and hydrodynamic models on extreme responses is identified under different conditions.

Chapter 8 summarizes the main findings and contributions of the thesis and serves as a conclusion chapter, providing recommendations for further research of related topics.

1.6 Thesis Contributions

The research carried out in this PhD develops an accurate and computationally efficient method for FLS design of monopile-based OWTs; improves the understanding of the impact of state-of-the-art physical load models compared to widely used approaches on fatigue estimates; and provides more comprehensive insights of the relative importance between statistical and physical load modelling uncertainties when characteristic design responses are estimated using the environmental contour method. More specifically, the following outcomes resulted from this work:

- **Environmental lumping for FLS design**
  A novel lumping method was developed as an alternative to full long-term fatigue assessment for the FLS design of monopile-based OWTs. This method integrates the metocean conditions and OWT dynamics to extract representative DLCs to predict long-term fatigue estimates along the support structure. Moreover, the method is further developed to incorporate wind-sea and swell components in an integrated

and consistent manner.

The proposed method addresses several challenges and limitations of existing methods. Furthermore, it provides a remarkable reduction of computational effort for fatigue assessment compared to the conventional approach using scatter diagrams, which is proposed in the design standards, while maintaining comparable levels of accuracy throughout the support structure. This significant reduction in computational requirements makes the lumping method an efficient tool for fatigue design and sensitivity studies, enabling practitioners to achieve accurate fatigue predictions with notably reduced computational resources from early design phases, enhancing the feasibility and efficiency of the design process.

Finally, to the author's knowledge, there is no method available in the literature incorporating wind-sea and swell components, and no recommendations in the design standards. The proposed lumping method is extended to consistently consider wind-sea and swell components in fatigue assessment. Validation against hindcast data assessment provided similar levels of accuracy and reduction of computational effort, revealing a great potential for the method to be used in FLS design.

- **Effect of foundation modelling on fatigue**
  The thesis investigates the influence of foundation modelling on the dynamic behaviour and fatigue estimates of monopiles, focusing on comparing the widely used $p-y$ curve approach with a macro-element model that incorporates hysteretic damping and varying stiffness after load reversals.

  The thesis contributes to a more thorough understanding of how foundation modelling impacts the estimated dynamic behaviour and fatigue of monopiles. It highlights the importance of considering hysteretic damping and varying stiffness after load reversals, especially in parked states or conditions with large wind-wave misalignment, with negligible aerodynamic damping.

- **Environmental contours and extreme responses**
  The focus of the research lies in the comprehensive evaluation and comparison of some uncertainties originating from statistical and physical load modelling aspects, when estimating extreme responses for large-diameter monopile foundations, using environmental contour method.

The results enhance the understanding of how different probabilistic models and estimation methods for distribution parameters impact the resultant contours and corresponding extreme responses for monopile-based OWTs. Furthermore, the study depicts the increasing significance of load cases at the rated speed, as wind turbine sizes and natural periods increase.

The variations in extreme responses due to foundation modelling underscore its impact in the absence of aerodynamic damping. Diffraction effects are seen to be increasingly important for larger diameters and shorter period sea states. Nevertheless, for the cases analyzed in the thesis, variations on extreme responses caused by contours established from different statistical models of the metocean parameters or stochastic variation due to seed variability can be larger than variations caused by different physical load models.

Chapter 2

Design challenges of large-diameter monopiles

This chapter focuses on the challenges related to long-term fatigue and extreme responses of large-diameter monopiles. The reader is given a detailed literature review of state-of-the-art design methods and physical load models commonly used for FLS and ULS design. The chapter aims to identify research gaps and current limitations, extracting the topics of this thesis.

2.1 Design methods for long-term responses

2.1.1 Long-term fatigue responses

Different approaches can be used to estimate the accumulated fatigue damage of offshore structures. These include deterministic, spectral-based, simplified, and time-domain methods [62, 63]. Deterministic methods utilize a regular wave to represent a sea state, ignoring its stochastic characteristics. Spectral-based approaches consider the stochastic nature of the sea state, but they cannot correctly handle nonlinearities in the system. Simplified fatigue assessment based on a closed-form formulation is an alternative approach to estimate the long-term fatigue damage and can be found in various design guidelines [62–64].

The time-domain method typically incorporates time-domain simulations for the dynamic analysis of the structural model, combined with the rainflow counting technique [65] to estimate the fatigue damage. Although the time-domain method is considered the most accurate approach, it requires significant computational effort.

2.1.1.1 Full long-term fatigue assessment

OWTs are complex systems with multiple sources of nonlinearities, including aerodynamic and hydrodynamic loads, soil-structure interaction, and control system effects. Moreover, there is a strong coupling between the applied loads and the response characteristics of the wind turbine. For example, aerodynamic damping depends on the wind speed and operation of the turbine, and soil damping depends on the mean thrust force resulting from wind loading for different wind speeds.

Due to the nonlinear effects and the strong coupling between environmental loads and structural responses, fully integrated time-domain simulations combined with rainflow counting are considered the most accurate approach for OWTs. In the context of OWT fatigue assessment, the common approach is to analyze all sea states that have a non-zero probability of occurrence in the wave scatter diagrams, as recommended by design standards such as the IEC 61400-3 [30]. This procedure, referred to as a full long-term fatigue assessment, requires analyzing a significant number of load cases, considering all relevant combinations of environmental parameters and operational conditions. Seidel et al. [66] highlighted that, when considering directional information on wave conditions as a function of wind speed and wind direction, up to 30,000 time series simulations may be necessary during the basic design phase to capture the fatigue load cases according to IEC 61400-3 [30]. This emphasizes the need for computationally efficient yet accurate methods for simulating and analyzing the long-term fatigue behaviour of OWTs.

2.1.1.2 Environmental lumping for fatigue design

Reducing the computational effort of long-term time-domain fatigue assessment for OWTs can be achieved through simplifications such as omitting simulations for opposite wind-wave directions and combining occurrences in post-processing [66]. Reducing the number of environmental conditions, also referred to as environmental lumping, is another efficient method to reduce the computational effort. Environmental lumping involves selecting a reduced set of representative sea states to replace the full set of load cases used in full long-term fatigue assessment. The challenge is to select the reduced set of load cases that accurately predicts the accumulated fatigue damage along the OWT structure, considering its dynamic properties and the long-term metocean conditions simultaneously.

Various methods have been developed for selecting representative sea states in the context of fatigue life assessment for offshore applications such as mooring and riser systems [67, 68], fish cages [69, 70], OWTs [47, 71–74], fixed and floating platforms [75–77]. A common practice involves lumping the sea states within a wave scatter diagram into a smaller number of blocks, as shown in Figure 2.1. Representative sea states (blue markers) within each block are adopted to replace original sea states in the fatigue assessment. As outlined in standards like DNV-RP-F204 [78], it is important to ensure that the fatigue damage from the representative sea states is not smaller than that from the original sea states in the lumping block.

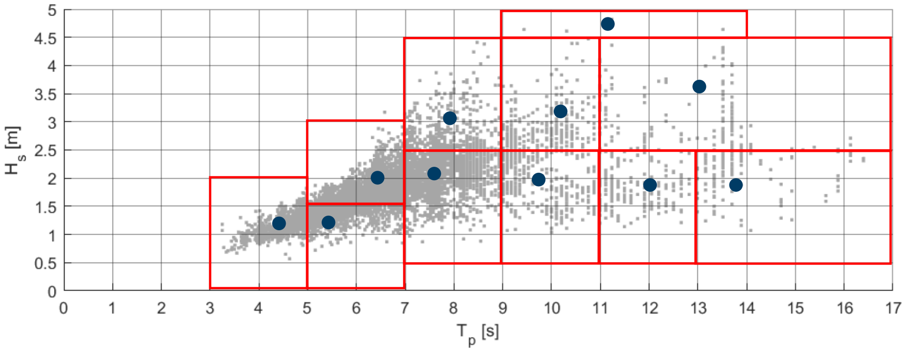

Figure 2.1: Example of lumping of a wave scatter diagram in blocks (red rectangles), represented by on lumped load cases (blue markers).

Different approaches have been proposed for selecting representative sea state parameters within lumping blocks. For example, Sheehan et al. [67] applied a conservative approach for selecting representative sea state parameters for riser fatigue assessment, using the largest significant wave height (H_s) and the weighted average of the peak period (T_p). However, this method resulted in significant overestimation of fatigue damage. Furthermore, the study highlighted the importance of the choice of peak period and the number of lumping blocks.

Jia [77] applied a block lumping method for calculating wave-induced damage on jacket structures, using the assumption of a proportional relationship between fatigue damage and the m^{th} power of the wave height, where m corresponds to the S-N fatigue curve slope. In his approach, similar to Burton et al. [79], the representative H_s of each block was estimated based on this assumption, and T_p was estimated using a weighted average principle. However, the applicability of this method to a two-segment S-N curve is questionable. The study depicted that the number of the lumping blocks, as well as the representative sea states within those blocks are critical aspects for the accuracy of the method, as important sea states that may contribute notably to fatigue damage may be disregarded. Sensitivity studies, such as investigating the influence of the number of lumping blocks, were recommended to ensure the accuracy and reliability of the fatigue assessment.

Song et al. [75] introduced a lumping block method based on spectral moments equivalence to select representative sea states. The method demonstrated accurate results for both fixed and floating offshore structures. However, it was observed that the method had a strong dependency on the number of blocks used. To address this limitation, Song et al. further developed the method in a subsequent study [76] by incorporating fatigue equivalence, which offered significant advantages compared to conventional block methods. Hou et al. [70] proposed an improved lumping block method for the fatigue assessment of a mooring system for a fish cage. Their method involved selecting a more severe significant wave height outperformed other block lumping methods in terms of accuracy.

Low and Cheung [68] proposed a lumping method based on fatigue equivalence by establishing a fatigue damage function over sea state parameters for the long-term fatigue assessment of mooring and riser systems. Although the method proved to be robust and accurate within engineering expectations, it is considered rather complicated for practical purposes [75]. Du et al. [69] simplified and further evaluated the lumping method proposed by Low and Cheung [68] for the fatigue assessment of a mooring system.

Lumping for OWTs should account for the influence of wind loading and the correlation between wind and waves in the offshore environment, which are essential for accurately predicting the response of OWTs considering factors like aerodynamic damping and soil-structure interaction. In the literature, various methods for environmental lumping in OWTs have been proposed. Kühn [71] introduced an iterative, damage-equivalent approach where the initial H_s is estimated based on the assumption of proportionality between fatigue damage and the m^{th} power of wave height [79], and the reciprocal of the wave period is defined in terms of the probabilistic average of wave frequencies. The sea state parameters are then refined iteratively to achieve a target damage level based on the full wave climate. Seidel [47, 72] proposed an approach that uses an equivalent spectral energy representative of the entire scatter diagram, calculated from the weighted spectral values of the original sea states at the first natural frequency. A representative T_p is obtained based on the equivalent spectral energy, while the representative H_s is calculated using quasi-static considerations. Passon [73, 74] developed a damage-equivalent contour lines method, where the sea state parameters of the lumped load cases are defined based on the equivalence of a pseudo fatigue damage matrix over wave height and period. This method resulted in more accurate preservation of fatigue damage at different locations along the support structure compared to Seidel's and Kühn's methods [74], although it involved several simplifications.

The methods discussed above have certain limitations. For example, many block lumping methods are sensitive to how the blocks are partitioned, and some lack a solid theoretical foundation for selecting equivalent wave parameters, leading to significant overestimation of fatigue damage. Additionally, some existing methods are overly complex for practical use, and most approaches do not consider the dynamic characteristics of the structure. Finally, it is important to note that design standards for OWTs [80, 81] do not provide clear recommendations on how lumping should be performed, while recommendations from other offshore applications [78] have been found to be overly conservative.

To address these shortcomings, the thesis presents an environmental lumping method (Chapter 4), specifically developed for the extraction and analysis of representative load cases for FLS design of monopile-based OWTs. This method considers the wind-wave climate and the dynamics of the OWT in an integrated manner. It ensures that similar levels of accuracy in predicting fatigue damage are maintained throughout the support structure, while significantly reducing the computational effort required.

2.1.1.3 Lumping of wind-sea and swell

During the design process, wave hindcast data are typically provided for the combined sea state as well as for the wind-sea and swell components separately. The wind-sea component is predominantly influenced by the wind direction, while the swell component can come from any direction and is unrelated to the wind. Assuming that swell is co-directional with the wind-sea can lead to either overestimation or underestimation of fatigue damage for specific locations around the circumference of the monopile.

Considering the misalignment between wind and waves is crucial because there is negligible aerodynamic damping in the direction of wave loading. Therefore, it is essential to consistently account for the individual contributions of wind-sea and swell components during the FLS design to ensure a safe approach without excessive conservatism in fatigue damage predictions.

However, incorporating wind-sea and swell components into a full long-term fatigue assessment poses significant challenges due to the computational effort involved. Moreover, to the author's knowledge, there is no lumping method available in the literature to address the issue. In the thesis, the environmental lumping method is extended to consider wind-sea and swell components in a consistent manner.

2.1.2 Long-term extreme responses

In the design process for OWTs, ensuring structural integrity against extreme environmental conditions is a critical task. To perform design checks for ULS, long-term extreme responses are considered. These responses are typically characterized by specific annual exceedance probabilities or N-year target return periods [30, 59]. In principle, the long-term cumulative distribution function (CDF) of the extreme response should be determined to accurately estimate the characteristic N-year value. Then the response level at which the computed long-term probability matches the target exceedance probability is the desired characteristic N-year value [82]. An approach typically proposed for estimating long-term extreme responses of offshore structures is the full long-term analysis [58]. However, its use is typically prohibitive due to high computational costs, while, it does not account for serial correlation in environmental conditions, resulting in positive bias in estimated extreme responses [83, 84]. Therefore, alternative methods are used in practice.

2.1.2.1 Full long-term analysis

Full long-term analysis (FLTA), also known as *all sea states approach*, considers all site-specific environmental conditions to estimate long-term extreme responses [85]. The method takes into account both the variability in environmental conditions (such as waves and wind) and the short-term variability of the response. The FLTA involves computing the long-term CDF of the extreme response by integrating the joint probability density function of a specific environmental condition with the corresponding short-term response probability distribution.

To perform FLTA, several steps are involved. First, the site-specific joint distribution of the environmental parameters needs to be established. Then, a multidimensional integral is solved, which considers the contribution of all short-term conditions to the long-term response, to obtain the long-term CDF of the extreme response. However, performing FLTA can be computationally intensive, as it often requires time-domain simulations or model tests to capture the stochastic nature of the relevant response quantities. As a result, FLTA becomes impractical for many offshore applications [86]. For OWTs, the complexity is further increased as the integration domain expands to include both wind and wave conditions, resulting in a larger number of short-term conditions that need to be analyzed [82, 87, 88].

FLTA results are often used as a benchmark to assess the accuracy and calibrate approximate long-term analysis methods [87] used for predicting extreme responses of offshore structures. For example, Li et al. [87] compared a modified environmental contour method with FLTA to estimate extreme responses of bottom-founded offshore wind turbines. Similarly, Baarholm et al. [86] used FLTA results as a reference to estimate the target percentile for the environmental contour method in their investigation of the ringing phenomenon in the *Troll A Platform*. Haselsteiner et al. [89] provide a summary of examples of FLTA methods used in various studies in the literature.

To improve the computational efficiency of FLTA, researchers have explored different approaches. These include reducing the number of required short-term response calculations or developing more efficient methods to compute the short-term quantities [90]. However, in practical offshore design, the environmental contour method is commonly applied as an alternative to FLTA for defining extreme conditions and responses. The environmental contour method is widely used to estimate extreme responses and is preferred due to its computational efficiency compared to FLTA.

2.1.2.2 Environmental contour method (ECM)

For ULS design requirements, the focus is on low exceedance probabilities, such as loads and responses with a 50-year or higher return period. It has been observed that only a small portion of the joint distribution of environmental parameters, specifically the tail part, significantly contributes to long-term extreme responses, while the majority of environmental conditions have negligible effects on the results [91]. Consequently, it is sufficient to check a limited set of load cases to ensure adequate structural capacity.

One approach to limit the number of load cases assumes that the maximum response for a specific return period is approximated for a sea state with similar return period. For example, to estimate 50-year responses, one can analyze a sea state with a 50-year significant wave height (H_s) and representative values of other variables, such as peak period (T_p), for that H_s level. Empirical evidence supports this assumption for structures where the response is primarily driven by H_s. However, it may be misleading for dynamically sensitive structures, where critical conditions can occur for moderate sea states near the natural period of the structure [92, 93]. This is particularly relevant for offshore wind turbines that exhibit resonant behaviour, leading to critical responses, especially in parked conditions when aerodynamic damping is negligible or for conditions with moderate sea states combined with maximum wind loads. This motivates the concept of environmental contours, which represent combinations of environmental variables with a specified return period.

The Environmental Contour Method (ECM) further simplifies general inverse reliability approaches, which include the response conditional on the environment as an additional variable, and thus identifies a limited number of short term conditions. Besides its computational efficiency, the method is appealing since it decouples the probabilistic description of the environment from the structural design. This can be particularly beneficial for evaluating different design options under site-specific environmental conditions.

Establishing environmental contours involves three steps, as illustrated in Figure 2.2. First, a statistical model is constructed to describe the joint distribution of metocean parameters. This model is then used to establish the N-year contours, which represent combinations of parameters with a specific return period. Finally, the response of interest is calculated for various conditions along the N-year contour.

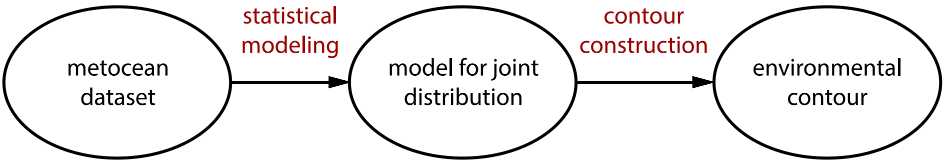

Figure 2.2: Steps to establish contours from a metocean dataset [94]

Figure 2.3 shows an example of an $H_s - T_p$ environmental contour for different probabilistic models, along with the metocean data and simulated combinations along the contour. Typically, to identify the most severe sea state, multiple stochastic time-domain simulations are performed for different conditions along the contour, and the largest response is calculated. Then, having defined the most severe sea state, to establish the N-year characteristic response that represents the extreme response for the N-year return period, different approaches can be used. One common method is to calculate the median (50th percentile) of the largest response values obtained from the simulations. Alternatively, a higher percentile, such as 85% to 95%, can be selected to indirectly account for the short-term variability [86, 95–97]. Other approaches include using a contour with a higher return period, a correction factor to refine the design loads [98], or applying an additional safety factor multiplied by the characteristic load [99]. A combination of these methods can be employed, as proposed by Derbanne et al. [100].

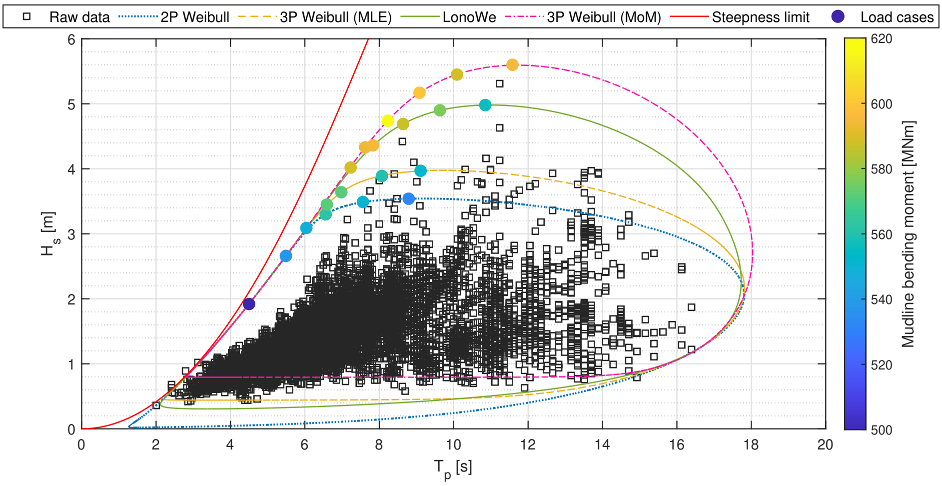

Figure 2.3: Simulated combinations along the contours, to identify the most severe sea state for the extremes of a selected response quantity.

Various approaches exist for establishing the joint distribution of metocean variables and establishing environmental contours. These methods include global hierarchical models [101–116], copula models [117–120], kernel density estimates [121–123], block-resampling methods [124], and conditional extreme value models [125, 126]. The global hierarchical model that is used in the thesis is widely used and also recommended by the design standards, however it poses several challenges. Firstly, selecting specific statistical models for the metocean parameters and the way in which those are related (dependence structure) in a model is mostly based on experience, rather than solid theoretical principles. In particular, the dependence functions typically used in literature and recommended in the design standards [30, 59] do not provide any physical interpretation as noted by Haselsteiner et al. [127] who presented recent work on the topic. Furthermore, fitting a statistical model to all observations does not guarantee a representative fit to the tail of the distribution, which is the range of most interest for estimating extremes, while serial in the data is ignored, resulting in positive bias in extreme estimates [83, 84].

Similarly, different methods exist for establishing metocean contours, based on different concepts of exceedance probability. For the inverse first-order reliability method (IFORM) that is widely used in the offshore industry [90, 92, 128], and direct sampling method [129–131], the contour exceedance probability is defined as a marginal exceedance probability. In contrast, for recent methods such as inverse second-order reliability method (ISORM) [132, 133], and highest density contour method (HDC) [123], contours are defined in terms of the total exceedance probability, being significantly more conservative [134]. Other approaches are the Nataf transformation [135], or the Direct-IFORM, which replaces the multi-dimensional joint distribution by a series of univariate fits, allowing to be applied in higher dimensions for arbitrary numbers of variables, without loss in performance. The method was firstly introduced by Derbanne et al. [136] and further presented by Mackay et al. [137], where its applicability to the design of OWTs is discussed.

Ross et al. [138] presented a survey of the metocean user community regarding environmental contours, providing recommendations on when and how to use them. Studies have compared different environmental contour methods and investigated the impact of statistical uncertainties on the contour lines and resulting extreme responses [139, 140]. Notably, Mackay and Haselsteiner [134] studied the impact of the choice of contour on simple structural reliability problems, highlighting that some understanding about the shape of a structure's failure surface is required, to choose an appropriate contour method. Haselsteiner et al. [94] conducted a benchmarking exercise comparing contours obtained using different methods, revealing large variations in the contours and no clear conclusions on which contours provide the most accurate response estimates or how the contour establishment steps contribute to these variations. Hautecloque et al. [83] extended the study by quantifying the accuracy of extreme responses using various contour methods for different types of structures, such as ships and a tension leg platform. The study highlighted the importance of ensuring that the statistical model fits the data well to obtain accurate response estimates. Contours based on IFORM were found to exhibit better accuracy, but further evaluation for different offshore applications was recommended. It was also depicted that neglecting serial correlation in the data can lead to a positive bias in response estimates, while methods that account for serial correlation showed closer agreement with reference results. A method to reduce the influence of serial correlation in metocean data and environmental contours for prediction of extreme return levels was also presented by Coe et al. [141].

These studies highlight the ongoing research and discussion around the selection and accuracy of different environmental contour methods, as well as the importance of considering statistical uncertainties and serial correlation in the data to obtain reliable extreme response estimates.

2.1.2.3 Challenges of ECM for offshore wind turbines

Applying the environmental contour method (ECM) directly to offshore wind turbines (OWTs) can be challenging. According to the IEC 61400-3-1 standard, a 2-dimensional contour of wind speed (U_w) and significant wave height (H_s) should be established, with the peak period (T_p) chosen deterministically as the value that results in the highest response for a given U_w-H_s combination. However, for dynamically sensitive structures like OWTs, neglecting the stochastic nature of the wave period in establishing the contours can lead to non-conservative extreme response estimates.

Valamanesh et al. [142] found that higher mudline bending moments were observed for moderate sea states near the natural period compared to cases where T_p was chosen for the most severe wind and wave combination. Similarly, Velarde et al. [85] demonstrated that resonant loads during parked or idling conditions under operational wind speeds could dominate the design loads for monopile-bases OWTs.

To account for the three dominant variables (U_w, H_s, and T_p) in a probabilistic manner, it is necessary to establish a three-dimensional contour surface. Li et al. [143] proposed estimating the response for a set of points on this surface to consider the combined effect of the three metocean variables on the extreme response of OWTs. Horn and Winterstein [144] used multiple 2D contours, both $U_w - H_s$ and $H_s - T_p$, to deal with the three-dimensional variable space. Other studies focused on using H_s-T_p contours representative of different wind speeds [87]. It is still uncertain which approach is best suited to address the environmental variables relevant to OWT design [89]. However, as emphasized by Ross et al. [138], it is essential to include all dominant environmental variables associated with the response quantity of interest in the establishment of the contour. Otherwise, it is likely that the contour will result in an inadequate estimation of the N-year response.

Another challenge using the ECM for OWTs is their non-monotonic behaviour with respect to wind loads due to the controller. The control system is designed so the OWT extracts the maximum possible power from wind, until its rated capacity, at the rated wind speed, where mean responses reach their maximum due to wind loads. Above rated speed, the blades are pitched to keep constant power output, such that mean loads due to wind gradually decrease until the cut-out speed. Finally, blades are fully pitched to minimize loads above cut-out wind speed while the turbine is parked, i.e., not producing power, and wind loads as well as fore-aft aerodynamic damping abruptly drop. As a result, OWT responses, e.g., overturning moment, can be higher during operational conditions, particularly close to the rated speed. The importance of evaluating both operational and parked conditions to derive design loads has been highlighted in the literature, see e.g., Saranyasoontorn and Manuel [145]. Due to this behaviour, extreme responses can be governed by the non-extreme operating wind conditions due to wind loads instead of an extreme condition where the turbine is parked.

Various studies have indicated that the ECM is not directly applicable to OWTs, and it is recommended to use the complete IFORM that accounts for response variability [82]. Li et al. [87] proposed a modified version of the ECM specifically for OWTs. They established multiple H_s-T_p environmental contours for different wind speeds ranging from the rated wind speed to the cut-out wind speed, to identify the largest response value. This modified ECM has been successfully applied to various OWT configurations, including bottom-founded [87] or semi-submersible [146] OWTs, a two-rotor floating OWT concept [147], and integrated offshore renewable energy devices [88], yielding reasonable accuracy compared to results obtained from FLTA.

In this thesis, some statistical and physical load modelling uncertainties of extreme responses for monopile-based OWTs are assessed, using environmental contours. ECM using the global hierarchical approach and IFORM was used to establish contours for representative wind classes. The focus is on investigating the impact of different conditional probability distributions for significant wave height and peak period, as well as methods for estimating distribution parameters on the resulting contours. Additionally the relative importance compared to the impact of foundation and hydrodynamic load models on extreme responses is evaluated for different design scenarios.

2.2 Physical load models for design purposes

2.2.1 Soil-structure interaction

Soil-structure interaction refers to the interaction between the foundation of an OWT and the surrounding soil, and it plays a crucial role in the overall dynamic behaviour of the wind turbine system.

Several important aspects of soil behaviour should be considered in the analysis. These include the variation in soil stiffness under cyclic loading, the increase in soil damping with higher shear strain caused by larger loads, and the accurate representation of the load-transfer mechanism from the foundation to the soil. These factors have a significant impact on the long-term performance of OWTs and should be carefully accounted for when assessing the response of the system. It should be highlighted that the study does not address the long-term behaviour of the soil, i.e., soil degradation over time, but rather considers the long-term behaviour of the structure based on short-term assessment with different soil-structure interaction models.

2.2.1.1 The $p-y$ approach: applicability and limitations

The design standards for offshore structures, such as OWTs [30, 39], typically use the $p-y$ method to model laterally loaded piles. In this approach, the pile is represented as a beam, and the resistance of the soil to lateral displacement is modeled using a series of discrete, uncoupled, nonlinear elastic springs along the pile.

The $p-y$ method was originally introduced by Reese & Matlcock [148] for slender piles in the oil and gas industry, where axial loads are dominant and the piles have high embedded length-to-diameter (L/D) ratios. It has been widely accepted in the industry due to its successful track record in designing flexible piles over many years [48, 149]. However, the loading conditions for monopile foundations in OWTs are significantly different from those in the oil and gas industry. The magnitude and character of the loads, as well as the failure modes and cyclic loading effects, are distinct [51, 149, 150].

The loading of monopile foundations in OWTs is characterized by horizontal loads, which, combined with the height of the structure, lead to dominant bending moments at the seabed. The vertical loads, due to the relatively low weight of the structure, are unimportant compared to the overturning moments from wind and waves [48, 151]. Furthermore, the flexibility of the pile plays a significant role in the soil-structure interaction and failure mechanism [150], and therefore a distinction shall be made between a pile with rigid behaviour and one that is relatively flexible [149]. Large-diameter monopiles are characterized by slenderness ratios (L/D) below 5, which leads to relatively rigid behaviour compared to the slenderness ratios of 15-20 assumed in the development of the $p - y$ method [152]. The difference in geometry and loading conditions between monopile-based OWTs and piles of jacket structures is illustrated in Figure 2.4, adopted from Bhattachary [153].

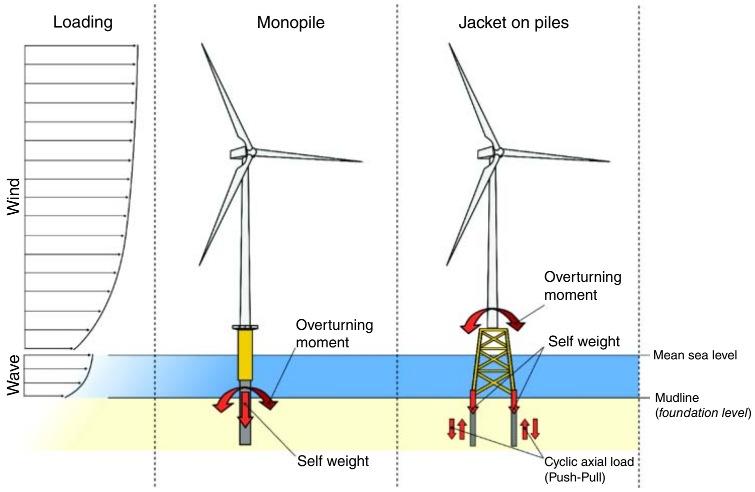

Figure 2.4: Load transfer for an OWT supported on a monopile and a jacket with multiple pile foundations [153]

The stiffness of the OWT system is significantly influenced by the stiffness of the surrounding soil. Soil stiffness can be classified as strain-hardening or strain-softening based on how it changes under repeated strains [153]. When the soil stiffness increases or decreases, the foundation becomes stiffer or softer, respectively, directly affecting the natural frequency of the system.

Nonlinear response of foundations has been observed through various full-scale measurements, indicating that the natural frequency of monopile-based OWTs decreases as displacement or acceleration levels increase [154, 155]. Studies conducted by Arany et al. [156] on monopile-based OWTs have demonstrated that rotational stiffness, which represents the moment required for unit rotation of the pile at the mudline, is the dominant factor influencing the natural frequency of the system. Figure 2.5 illustrates the relationship between natural frequency and rotational stiffness for 12 operating wind turbines. The curves clearly indicate that any change in soil stiffness can alter the dynamic characteristics of the system. Similar observations regarding the dynamic soil-structure interaction have been made through scaled model tests [50, 157, 158], which showed that the dynamic characteristics of OWTs can change over time, or monitoring of operational wind farms, such as the measurements from the Lely wind farm that revealed change of natural frequency after six years of operation [71].

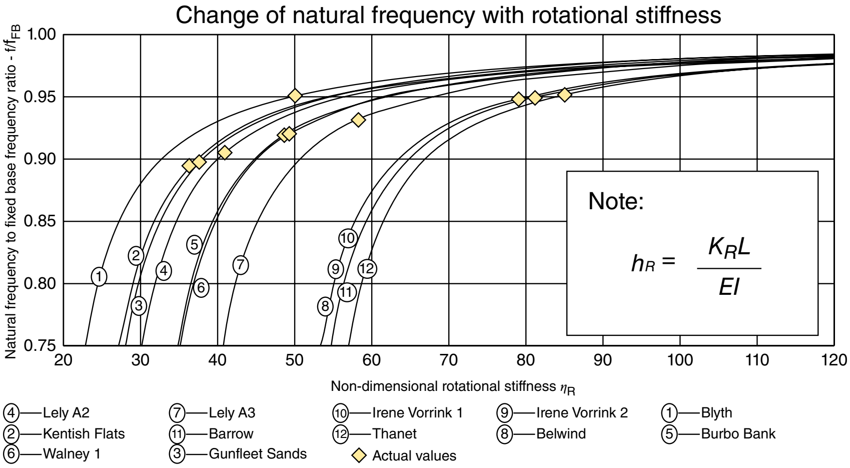

Figure 2.5: Change in natural frequency with non-dimensional rotational stiffness, h_R. K_R: foundation rotational stiffness, EI: bending stiffness, L: superstructure length [152]

Soils exhibit nonlinear responses during load reversals, resulting in varying soil stiffness during loading, unloading, and reloading cycles. These variations in stiffness can bring the natural frequency of the OWT closer to the excitation frequencies, leading to increased dynamic responses and potentially compromising the structural integrity due to resonance. Therefore, it is crucial to accurately represent the cyclic loading-induced variations in foundation stiffness to estimate fatigue damage more realistically.

Another essential aspect in the foundation modelling is the accurate representation of soil damping, particularly in situations where aerodynamic damping, which contributes the most to overall damping, is negligible. In those conditions, such as parked state and wind-wave misalignment situations, the relative importance of soil damping increases. Soil damping in soil-structure interaction consists of radiation damping resulting from geometric spreading of waves, hysteretic damping due to material plastic deformations, and to a lesser extent, damping induced by pore fluid [153, 159]. Wave radiation damping and pore fluid-induced damping are generally negligible for frequencies below 1 Hz [153, 160], and hysteretic damping becomes the main contributor in the analysis of monopile foundations.

While the $p-y$ method is widely employed for OWTs and can be easily integrated into simulation tools, it cannot entirely capture effects such as hysteretic damping or stiffness variation after load reversals. Therefore, alternative numerical foundation models have been proposed for fully integrated analyses of monopile-based OWTs [159], including modified $p-y$ curves, $p-y$ curves derived from finite element analysis, discrete lateral and rotational springs, and macro-element models.

2.2.1.2 Macro-element models

An approach that can accurately capture both the foundation stiffness and damping is macro-element modelling. Macro-element models were initially introduced in geotechnics by Roscoe and Schofield [161] and have been widely applied in various offshore applications [162–166]. Unlike $p-y$ curves, macro-element models condense the response of the foundation and surrounding soil into a force-displacement relationship at a single point, typically located at the mudline [163], as illustrated in Figure 2.6. The response at this point is derived from the interaction between the soil and the structure below the mudline, but the explicit representation of these interactions is not included in the model.

In the macro-element model, the relationship between horizontal forces, moments, and displacements, as well as rotations, is described using the framework of multi-surface plasticity, which was originally proposed by Iwan [167]. The model assumes linear elastic responses for vertical and torsional cyclic loading, which are decoupled from the horizontal responses. The nonlinear behaviour of the surrounding soil is incorporated into the macro-element formulation through various input parameters, including coefficients of the elastic stiffness at the mudline, two load-displacement curves, and a few numerical parameters.

A macro-element was developed as part of the REDWIN (REDucing cost of offshore WINd by integrated structural and geotechnical design) project [168], specifically for predicting the response of monopile-based offshore wind turbines. The mathematical formulation and detailed characteristics of the

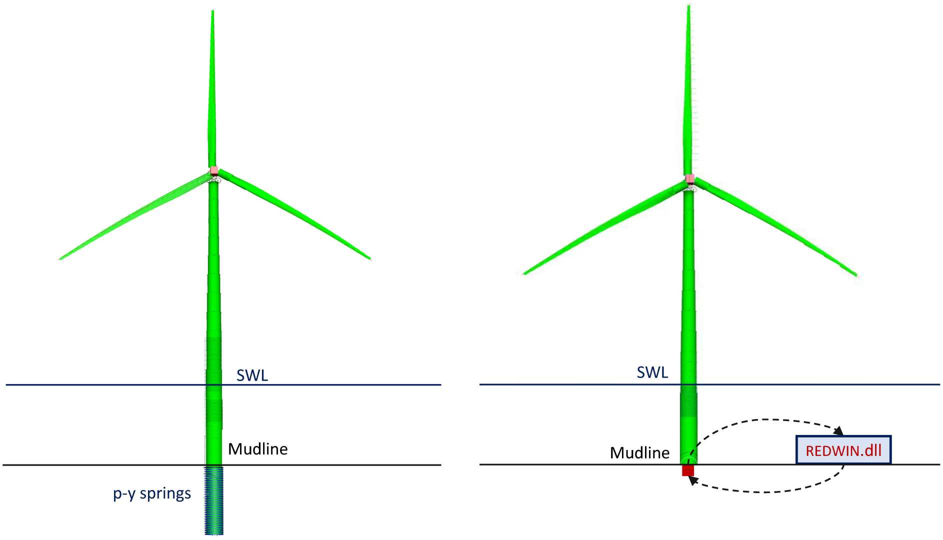

Figure 2.6: Illustration of foundation modelling using $p-y$ curves (left) and macro-element (right) in the simulation tool

macro-element model have been published in a series of journal papers [160, 169–171]. This macro-element model incorporates soil resistance components, including base and side shear. Furthermore, unlike the traditional $p-y$ formulation, it is capable of reproducing the change in overall stiffness due to nonlinear hysteretic behaviour and the hysteretic damping observed in monopile-based OWTs in integrated time-domain analyses. The model also accounts for the influence of multi-directional loading, which has been observed to affect the foundation stiffness and hysteretic damping [170].

The model's behaviour was compared against results from large-scale pile tests, full-scale field measurements, and FEA simulations conducted on monopile foundations of an OWT installed in the North Sea [169–171]. Particularly, its performance has been validated against field test measurements and FEA results for three piled foundations, demonstrating its capability to accurately reproduce the nonlinear load-displacement response and observed hysteretic behaviour in monopiles [169]. Furthermore, comparisons to full-scale field data from an offshore wind turbine in the North Sea, depicted that with appropriate calibration, the model can match the measured natural frequency and accurately predict fatigue loads [171].

2.2.1.3 Effect of soil modelling on OWT responses

Several studies have investigated the effect of soil stiffness and damping on the long-term responses of monopile-based OWTs. Schafhirt et al. [172] examined the impact of soil stiffness variations on the damage equivalent loads using $p - y$ curves. They found that a 50% reduction in soil stiffness increased the damage equivalent loads at the mudline by 7%. This result was consistent with the findings of Damgaard et al. [173], who studied the effects of soil stiffness and damping changes on fatigue loads using a lumped-parameter foundation model. They observed that a 50% reduction in soil Young's modulus increased the fatigue equivalent moment at the mudline by approximately 12%, while a 50% reduction in soil damping properties increased the fatigue damage equivalent moment by 25%.

Aasen et al. [174] compared different soil-foundation models and highlighted the influence of both stiffness and damping on fatigue damage. They considered four models: (1) $p - y$ curves, (2) linear elastic stiffness matrix at the mudline, (3) linear elastic stiffness matrix with soil damping, and (4) a nonlinear 1-D elasto-plastic model, which can capture the nonlinear stiffness and damping due to hysteresis. The last model, which provided the most realistic representation, reduced long-term fatigue damage by 11% to 22% compared to the other models. Furthermore, Carswell et al. [175] investigated the effect of hysteretic damping on extreme responses of monopiles subjected to storm loading. They found that soil damping reduced both the maximum and standard deviation of the mudline bending moment by 7-9%.

Considering these findings, it becomes evident that commonly used soil-structure interaction models like $p - y$ curves may not accurately capture the behaviour of large-diameter monopiles in OWTs, due to the different geometry and nature of loading. Furthermore, neglecting important aspects such as unloading on different stiffness after load reversals and damping due to hysteresis can affect fatigue and extreme estimates. Hence, further research and comparison of more realistic foundation models are necessary to better understand and predict the fatigue responses of large-diameter monopile foundations in OWTs.

2.2.2 Hydrodynamic modelling

Different models have been developed to calculate hydrodynamic loads on circular cylinders that are partially submerged, such as those used in monopile-based OWTs. Among the models for hydrodynamic loads, Morison's equation [176] is recommended by design standards like the International Electrotechnical Commission (IEC) [30] and Det Norske Veritas (DNV) [59], and it is commonly used in practice.

2.2.2.1 Morison's equation

Morison's equation is a semi-empirical formulation based on the assumption that the cylinder is slender, meaning its diameter is small compared to the wavelength of the incident waves. This assumption implies that the cylinder does not generate a significant diffracted wave field. Morison's equation combines viscous drag and inertia load components, and it can be expressed as follows,

$$dF = \frac{1}{2}C_d \rho D_p |u_r| u_r + C_m \pi \rho \frac{D_p^2}{4}(\dot{u}_w - \dot{u}_s) - \rho \frac{D_p^2}{4}\dot{u}_s \tag{2.1}$$

where dF is the force per unit length, C_d, C_m are the drag and inertia coefficients respectively, ρ is the water density, and D_p is the pile diameter. u_r is the relative horizontal fluid particle velocity normal to the member, and $\dot{u}_w, \dot{u}_s$ are the flow and structure accelerations normal to the member, respectively. The inertia coefficient can be split in two contributions

$$C_m = 1 + C_a \tag{2.2}$$

where C_a is the added mass coefficient. The first term represents the *Froude-Krylov* force from the pressure of the undisturbed wave, and the second term represents the diffraction effects. Morison's equation assumes a slender structure, i.e. the cylinder diameter is small compared to the wavelength of the incident wave.

The drag and inertia coefficients, C_d and C_m, vary with different parameters such as Reynolds number, Keulegan-Carpenter number, surface roughness, and the ratio of current or wave velocity to the cylinder velocity. Experimental studies have shown significant variations in these coefficients even under similar conditions [30]. In design calculations, it is common practice to assume constant values of 0.9 for C_d and 2.0 for C_m [59]. However, it is important to note that these values are simplifications and may not capture the true variations in coefficients for specific conditions.

2.2.2.2 MacCamy-Fuchs model

When the dimensions of a structure are large compared to the wavelength, λ, of the incident waves, i.e., typically when $D_p > 0.2\lambda$, diffraction effects become important. In such cases, Morison's equation is no longer sufficient, and alternative approaches are needed. Design standards [30], recommend using the MacCamy and Fuchs [177] analytical solution for the diffraction of long-crested waves incident on vertical piles. This approach considers the superposition of incident and scattered wave potentials to determine the wave field. While Morison's equation can still be used for the drag force component in this approach, the inertia force component varies depending on the size of the pile and the frequency of the incoming waves.

The MacCamy and Fuchs model is particularly relevant for larger monopile foundations, where diffraction is significant. As Figure 2.7 shows, the inertia load coefficient C_m reduces significantly for short waves and larger diameters, leading to a decrease in the total horizontal force. It is important to note that the MacCamy and Fuchs model is applicable only for linear waves, while Morison's equation can be used with wave kinematics derived from different theories.

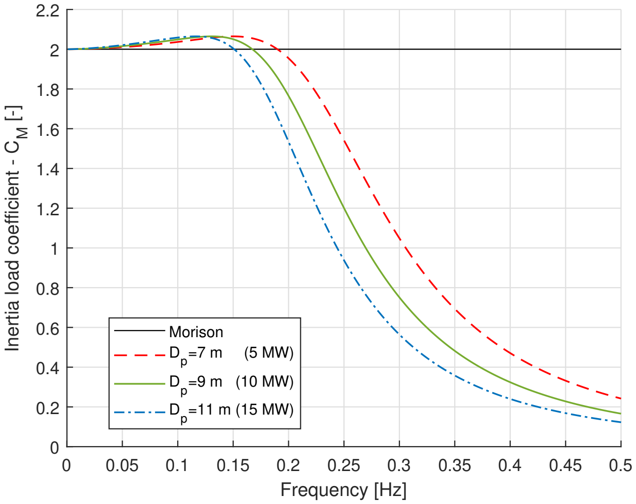

Figure 2.7: Comparison of inertia load coefficient for different monopile diameters at 30 m depth

2.2.2.3 Challenges related to hydrodynamic load models

The choice of wave kinematics and wave load models depends on the specific purpose of the study and the wave conditions being considered. For fatigue analysis of OWTs, which is primarily dominated by moderate sea states, the Airy linear theory is often sufficient. However, second-order effects from nonlinear waves can become important during parked states or when wind and waves are misaligned, as aerodynamic damping in the wave force direction is negligible. Researchers have discussed these aspects in the literature [178, 179], and it has been noted that although higher peaks may be observed when considering second-order waves, the overall fatigue lifetime is not significantly affected, especially considering that severe sea states have a low probability of occurrence. Therefore, for fatigue analysis, linear wave kinematics can generally be used without compromising accuracy. Diffraction effects, which are crucial for fatigue lifetime estimation, can then be incorporated using the MacCamy and Fuchs model [180].

In the context of ULS design, where the focus is on extreme loads and subsequent responses, steep waves become more relevant. Under these conditions, the nonlinear effects caused by wave steepness cannot be neglected, particularly in intermediate and shallow water depths. Therefore, higher-order wave kinematics and wave load models are typically required.

One commonly used approach in simulation tools is to use 2^{nd}-order directional Stokes waves [59], which incorporate second-order correction terms, including sum- and difference-frequency wave components. The difference frequency components are not significant for monopiles, but the sum-frequency components affect the wave shape, making them steeper with higher crests and flatter troughs. The wave kinematics obtained 2^{nd} second-order irregular wave theory can be used as input in Morison's equation to compute hydrodynamic loads. An alternative to 2^{nd}-order waves, is using wave kinematics from a fully nonlinear potential flow solver, which is considerably more computationally intensive. The challenge of both models is to accurately capture wave breaking, which typically requires numerical filters.

Other methods to compute extreme loads from nonlinear waves include the constrained wave approach, where a regular stream function wave is embedded into a background irregular linear wave realization, or fully nonlinear computations. However, these methods have limitations in terms of accuracy or computational time [181, 182]. Several higher-order theories have been developed, such as Rainey's model [183], Faltinsen et al. [184], Malenica and Molin [185], and Kristiansen and Faltinsen [186]. Comparisons of these higher-order models for extreme responses of monopile foundations can be found in the literature [182, 187] but are not discussed further in the thesis.

Current engineering models cannot account for diffraction effects when higher order wave kinematic theories are used, as MacCamy and Fuchs's approach only applies to linear waves. As diffraction becomes increasingly important with increasing diameter, a new load model has been developed during the WAS-XL project. The model combines the conventional Morison's formulation for slender bodies with a frequency-dependent mass coefficient based on formulation from MacCamy and Fuchs. Conventional Morison's equation with constant and frequency-dependent mass coefficient, using 2^{nd}-order Stokes waves, are evaluated to compute extreme loads. The importance of diffraction effects in hydrodynamic load models is compared to other modelling aspects (soil modelling, statistical modelling of metocean conditions) for estimating extreme responses (Chapter 7).

Chapter 3

Numerical models

This chapter describes the site conditions, the wind turbines, and the features of the numerical models used in the thesis. It summarizes the structural formulation and environmental load models for the fully coupled time-domain models and the simplified state-space frequency-domain models.

3.1 Site-specific information

This section provides a detailed summary of the site-specific metocean and soil conditions for an hypothetical location at the North Sea with coordinates (55.11°N, 3.47°E) and a water depth of 30 meters. These conditions served as the basis for conducting long-term fatigue and extreme response studies, and the soil conditions were the basis for calibrating the soil models used for the thesis. Figure 3.1 indicates approximately the location of the site (blue marker), along with areas of wind farm development in Europe.

3.1.1 Metocean conditions

Two site-specific metocean datasets were used, for the thesis and relevant scientific papers. The first dataset was obtained from the National Kapodistrian University of Athens (NKUA) and was generated using a numerical hindcast model for the Marina Platform project [143]. This dataset covers a 10-year period from 2001 to 2010 and provides metocean parameters for various locations. The second hindcast dataset, known as NORA10 [56, 57], is from the Norwegian Reanalysis Archive. It is a regional dataset, developed by the Norwegian Meteorological Institute [188], specifically designed for the northeast Atlantic and offers 3-hour resolution data. The NORA10 hindcast spans a longer time period, from 1957 to 2017. Both datasets in-

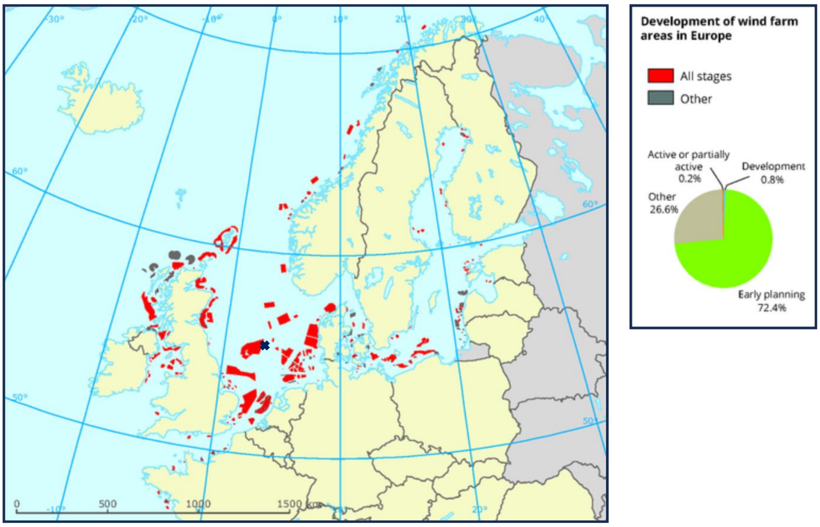

Figure 3.1: Site location (blue marker) used in the thesis. Original figure (without the marker) taken from European Environment Agency website.

clude information on mean wind speed at 10 meters above still water level (SWL), significant wave height (H_s), wave peak period (T_p), and wind-wave directionality for both wind-driven and swell components, as well as combined sea conditions.

The 10-year hindcast data from NKUA were compared to the NORA10 dataset for the same location and period (2001-2010). The NKUA data, which were originally provided at a different time resolution, were averaged over 3-hour intervals to match the resolution of the NORA10 data. The comparison did not consider spatial resolution effects. The agreement between the two datasets was evaluated using q-q plots for H_s and T_p, shown in Figure 3.2.

The figure indicates a good agreement between the two datasets, with correlation coefficients of 0.93 for H_s and 0.90 for T_p. It is noted that the NKUA data exhibited slightly higher values for H_s in the range of 6-7 meters compared to the NORA10 data. The minimum value of peak frequency in NKUA data was 0.061 Hz, resulting maximum T_p slightly above 16 s, explaining partly the difference with NORA10 data. Overall, the level of agreement between the datasets was acceptable for the purposes of the study, and no further comprehensive data comparison was conducted.

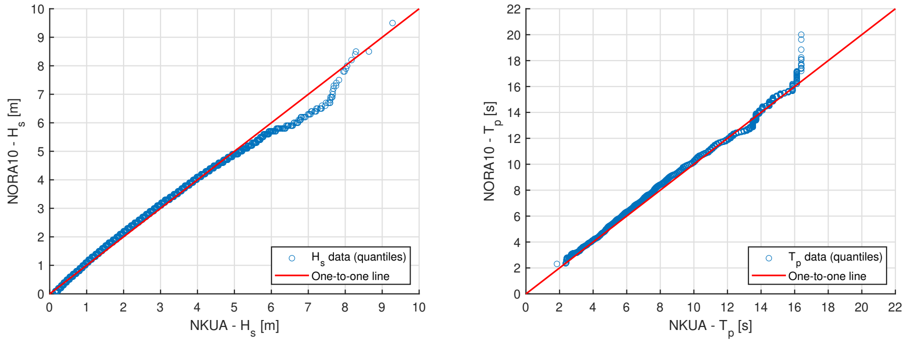

(a) H_s

(b) T_p

Figure 3.2: q-q plots for H_s and T_p 10-year wave data comparison between NKUA and NORA10 hindcast datasets

Figure 3.3 presents scatter density plots for the main metocean parameters from NKUA hindcast data, illustrating the joint distribution of variables. Figure 3.4 displays wind and wave roses, providing a graphical representation of wind and wave directionality for the combined sea component.

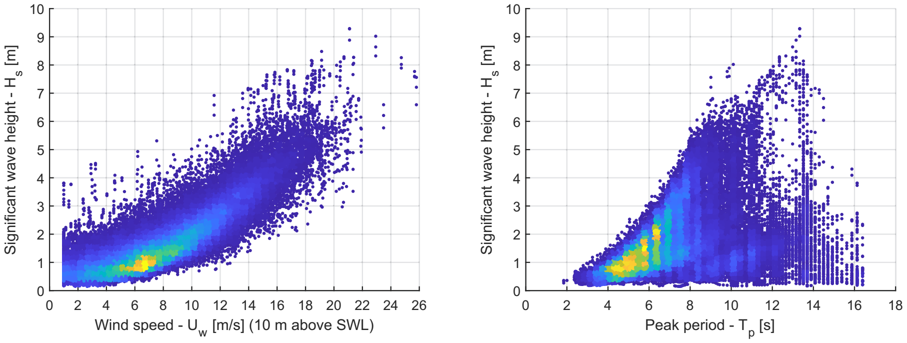

(a) $U_w - H_s$

(b) $T_p - H_s$

Figure 3.3: Scatter density plots of metocean parameters based on NKUA hindcast data

3.1.2 Soil conditions

The soil conditions defined for the hypothetical site consisted of a 3-meter layer of sand followed by clay layers below. The undrained shear strength of the soil increased linearly with depth, while the shear modulus exhibited

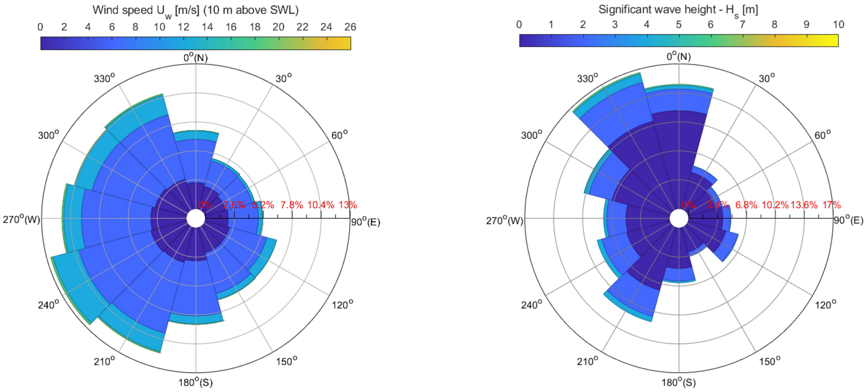

(a) Wind (b) Combined sea

Figure 3.4: Wind and wave roses based on NKUA hindcast data

a parabolic variation. The specific properties of each layer used for the calibration are summarized in Table 3.1 and Table 3.2.

Table 3.1: FEA soil parameters for sand layer (0-3 m)

Parameter	Notation	Value	Unit
Drainage type	-	Drained	-
Submerged weight	γ'	10	kN/m^3
Secant stiffness in standard drained triaxial test	E_{50}^{ref}	3.0E+04	kPa
Tangent stiffness for primary oedometer loading	E_{oed}^{ref}	3.0E+04	kPa
Unloading and reloading stiffness	E_{ur}^{ref}	9.1E+04	kPa
Power for stress-level dependency of stiffness	m	0.54	-
Effective cohesion	C'_{ref}	1	kPa
Effective angle of internal friction	ϕ'_{ref}	34.25	deg
Angle of dilatancy	ψ	4.25	deg
Reference shear modulus at very small strains	G_0^{ref}	9.4E+04	kPa
Threshold shear strain at which $G_s = 0.722 \cdot G_0$	$\gamma_{0.7}$	0.015	%

The foundation models used in the thesis and described in Sec. 3.3.1.2, were calibrated to Finite Element Analysis (FEA) results from the Norwegian Geotechnical Institute (NGI). NGI conducted full 3D continuum modelling of the soil volume with the monopile foundations, and calibrated the macro-element and $p-y$ curves models. The behaviour of the clay layers was represented by the NGI-ADP soil model [189], which describes the elasto-plastic,

Table 3.2: FEA soil parameters for clay layers (3-100 m)

Parameter	Unit	Depth [m] 3 - 9	9 - 18	18 - 36	36 - 72	72 - 100
γ'	kN/m^3	10	10	10	10	10
$G_{ur}/S_{u,A}$	-	1252	782.2	553.1	391.1	299.5
$\gamma_{f,C}$	%	10	10	10	10	10
$\gamma_{f,E}$	%	15	15	15	15	15
$\gamma_{f,DSS}$	%	15	15	15	15	15
$S_{u,ref}$	kPa	30	90	180	360	720
$S_{u,inc}$	kPa/m	10	10	10	10	10
$S_{u,P}/S_{u,A}$	-	0.48	0.48	0.48	0.48	0.48
$S_{u,DSS}/S_{u,A}$	-	0.67	0.67	0.67	0.67	0.67

- $G_{ur}/S_{u,A}$: Ratio of unloading/reloading shear modulus over active shear strength
- $\gamma_{f,C}$, $\gamma_{f,E}$, $\gamma_{f,DSS}$: Shear strain at failure in compression, extension, and direct simple shear (DSS) respectively
- $S_{u,ref}$, $S_{u,inc}$: Active undrained shear strength at the top of each clay layer, and increase per meter
- $S_{u,P}/S_{u,A}$: Ratio of passive shear strength over active shear strength
- $S_{u,DSS}/S_{u,A}$: Ratio of DSS shear strength over active shear strength

non-linear stress behaviour of saturated clays under undrained monotonic loading conditions. It's important to note that the focus of the thesis is not to investigate the constitutive models used for the soil, but instead on using calibrated foundation models based on FEA results provided by the NGI.

3.2 Wind turbine models

The thesis considers three representative utility-scale multi-megawatt wind turbine models: the NREL 5 MW [190], the DTU 10 MW [191], and the IEA 15 MW [192] reference wind turbines. All three turbines are three-bladed upwind variable-speed turbines, and their key parameters are summarized in Table 3.3. The corresponding generator-torque and blade-pitch control systems were based on specific controller models. For the NREL 5 MW turbine, the NREL Baseline Wind Turbine Controller [190] was employed. The DTU 10 MW turbine used the Basic DTU Wind Energy Controller [193], while the IEA 15 MW [194] turbine employed NREL's Reference OpenSource Controller. Figure 3.5 illustrates their main response characteristics for steady wind speeds ranging from 1 m/s to 25 m/s.

Table 3.3: Main parameters of the turbines used in the thesis

Parameter	Unit	NREL	DTU	IEA
Power rating	MW	5	10	15
Rotor orientation	-	Upwind	Upwind	Upwind
Number of blades	-	3	3	3
Cut-in wind speed	m/s	4	4	3
Rated wind speed	m/s	11.4	11.4	10.6
Cut-out wind speed	m/s	25	25	25
Minimum rotor speed	rpm	4.9	6.0	5.0
Maximum (Rated) rotor speed	rpm	12.1	9.6	7.56
Maximum tip speed	m/s	79.9	90	95
Design tip speed ratio	m/s		7.5	9.0
Hub height	m	90	119	150
Hub diameter	m	4.24	5.6	7.94
Rotor diameter	m	126	178.3	240
Blade mass	tonnes	17.7	41	65.3
RNA mass	tonnes	350	674	1017

The tower of each wind turbine model was represented by sections with specified lengths ($L_{t,i}$), diameters ($D_{t,i}$), and wall thicknesses ($t_{t,i}$). The dimensions of these sections, summarized in Table 3.4, vary along the height of the tower, as illustrated in Figure 3.6.

For the NREL 5 MW turbine, the sectional properties of the tower are similar to the original land-based tower design, as documented in the NREL 5 MW reference [190]. However, the thickness of the sections was increased by 30% to ensure that the first fore-aft and side-to-side frequencies of the tower fall within the 1P-3P range of the wind turbine when installed on the monopile designed for the hypothetical location.

The sectional properties of the tower for the DTU 10 MW turbine followed a preliminary design presented by Velarde (Chapter 5) [195]. The tower dimensions were modified to meet the fundamental frequency requirement of the entire system, considering a monopile with a 9 m diameter and a 0.11 m thickness at a water depth of 30 m.

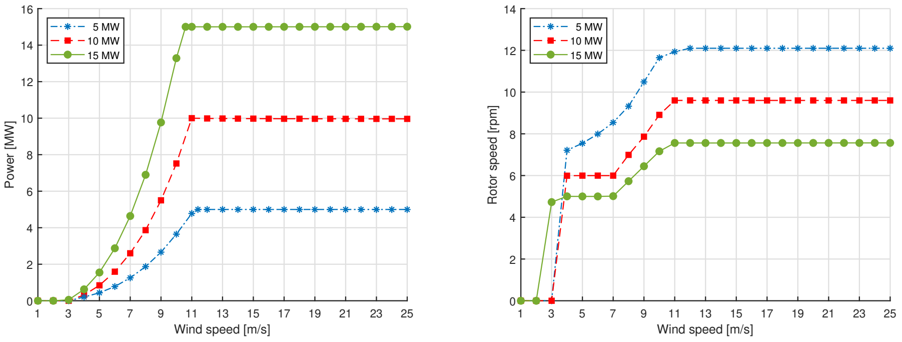

(a) Power (b) Rotational speed

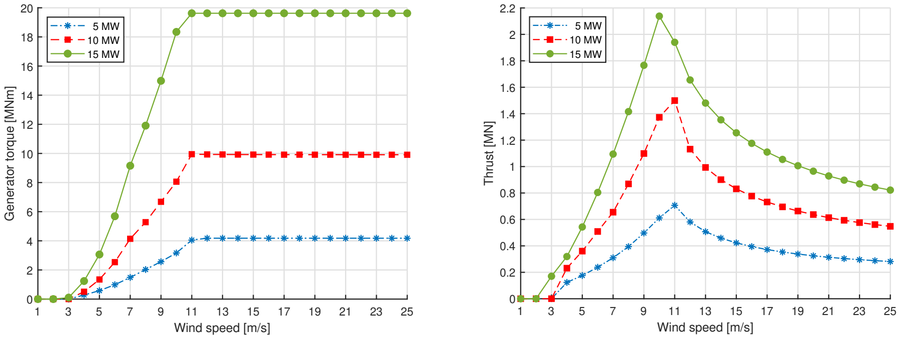

(c) Torque (d) Aerodynamic thrust

Figure 3.5: Response characteristics for steady wind

The tower design for the IEA 15 MW turbine was based on the original design specifications provided in the IEA 15 MW reference [192].

All wind turbines are supported on monopile-based support structures, separated into two parts. The first part is the substructure, which extends from SWL to the mudline, and the second is the foundation, which extends from the mudline to the monopile tip. Constant diameter (D_p) and wall thickness (t_p) along the monopile structure were considered for all OWTs. The 5 MW monopile dimensions were based on the OC3 monopile [196], modified to achieve a desired natural frequency ∼0.25 Hz, which is in the middle of the soft-stiff frequency range of the 5 MW OWT (Figure 1.12). The dimensions of the base-case 10 MW monopile were based on Velarde and Bachynski [197], for water depth 30 m and a diameter-to-thickness ratio

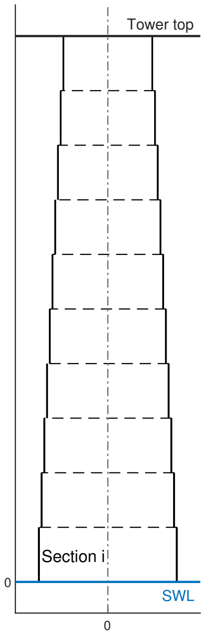

Figure 3.6: Representation of tower sections for the three OWT models

Table 3.4: Tower sectional properties [m] for the three OWT turbines with the accumulated length of each section.

Section	NREL 5 MW			DTU 10 MW			IEA 15 MW		
i	$L_{t,i}$	$D_{t,i}$	$t_{t,i}$	$L_{t,i}$	$D_{t,i}$	$t_{t,i}$	$L_{t,i}$	$D_{t,i}$	$t_{t,i}$
1	8.76	6.00	0.0351	11.56	9.34	0.0665	15.00	11.00	0.1100
2	17.52	5.76	0.0339	23.13	9.01	0.0630	28.00	10.00	0.0395
3	26.28	5.53	0.0328	34.69	8.69	0.0595	41.00	9.96	0.0365
4	35.04	5.29	0.0316	46.25	8.36	0.0560	54.00	9.68	0.0338
5	43.8	5.05	0.0305	57.82	8.04	0.0525	67.00	9.14	0.0322
6	52.56	4.82	0.0293	69.38	7.71	0.0490	80.00	8.49	0.0307
7	61.32	4.58	0.0282	80.94	7.39	0.0455	93.00	7.77	0.0291
8	70.08	4.34	0.0270	92.50	7.06	0.0420	106.00	7.15	0.0272
9	78.84	4.11	0.0259	104.07	6.74	0.0385	119.00	6.83	0.0240
10	87.6	3.87	0.0247	115.63	6.41	0.0350	132.00	6.66	0.0208
11	-	-	-	-	-	-	144.58	6.54	0.0240

$\sim$80. The base-case embedded length was 36 m. The monopile supporting the 15 MW turbine was designed for a target natural frequency around 0.18 Hz - 0.19 Hz. For the 5 MW and 15 MW monopiles, the embedded length is chosen to have a length-to-diameter ratio ($L_p : D_p$) equal to 4, as the 10 MW case. The diameter-to-thickness ratio ($D_p : t_p$) is below the limits required by design standards. The Young's and shear modulus for steel were taken as 210 MPa, and 80.8 MPa, respectively. The density was taken as 8.5 t/kgm^3 to account for secondary components. Figure 3.7 illustrates the OWTs.

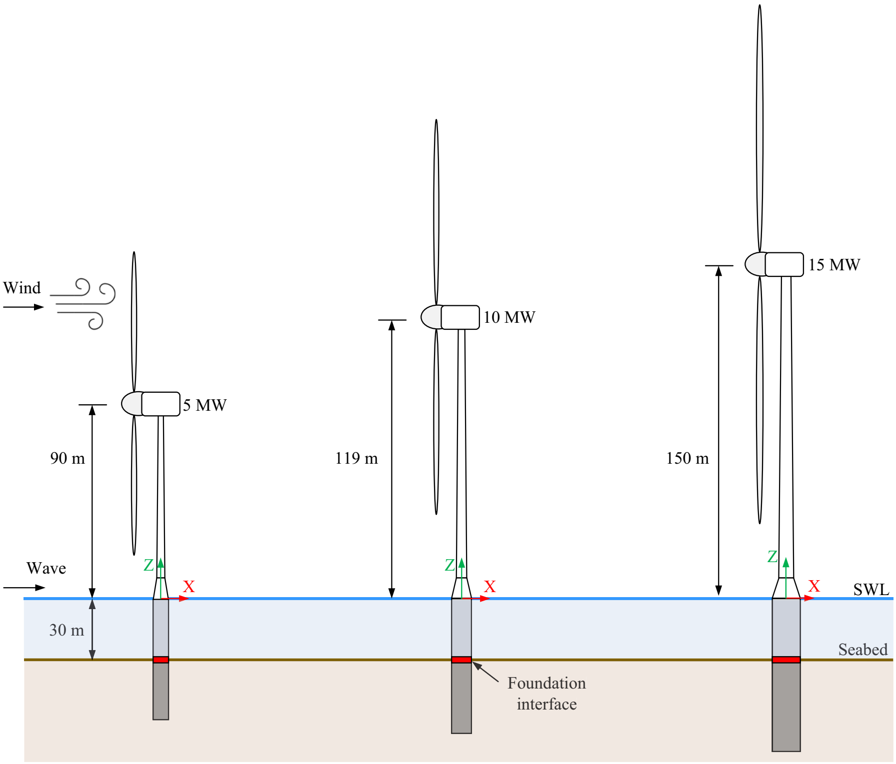

Figure 3.7: Illustration of the three OWT models

Table 3.5: Main monopile dimensions for the three OWTs

Parameter	Notation	Unit	NREL 5 MW	DTU 10 MW	IEA 15 MW
Diameter	D_p	m	7	9	11
Thickness	t_p	m	0.07	0.11	0.11
Embedded length	L_p	m	28	36	44
Length-to-Diameter	$L_p : D_p$	-	4	4	4
Diameter-to-Thickness	$D_p : t_p$	-	100	80	100

3.3 Simulation models

The thesis used two different simulation models to represent the OWTs. The first is a fully coupled nonlinear aero-hydro-servo-elastic time-domain model, described in Sec. 3.3.1. The second model is a simplified state-space frequency-domain model, discussed in Sec. 3.3.2.

3.3.1 Fully coupled models

3.3.1.1 RNA, tower and substructure

In the fully coupled time-domain models, the simulation tool SIMA [198, 199] was used to model the rotor-nacelle assembly (RNA), tower, and monopile above the seabed. SIMA is an aero-hydro-servo-elastic simulation tool developed by SINTEF Ocean. The tool has undergone verification through experimental studies and code-to-code comparisons with other analysis tools for both floating and bottom-fixed offshore wind turbines, see e.g. [42–44, 200].

The RNA was represented by a rigid body, which was replaced by a nodal mass and inertia at the top of the tower, given in Table 3.6. The properties, geometry, and characteristics of the airfoils used to model the blades were obtained from the relevant reference turbine documents [190–192]. The tower and substructure components were modeled as axisymmetric beam elements, using nonlinear beam element theory that allows for large rotational deformations, incorporated in SIMA. A circular hollow cross-section was used, with the diameter and thickness being specified according to the design requirements.

Table 3.6: RNA masses and inertias of the OWTs

Parameter	Unit	NREL	DTU	IEA
Mass (M_{RNA})	tonnes	350	674	1017
Inertia (I_{xx})*	tonnes m^2	4.38E+07	1.60E+08	3.19E+08
Inertia (I_{yy})	tonnes m^2	2.22E+03	7.81E+04	2.78E+05

* I_{xx} values include drivetrain inertia

3.3.1.2 Foundation modelling

Three different modelling approaches were employed to represent the foundation, i.e., the monopile below the mudline, in the simulations. These include a linear stiffness matrix, $p-y$ curves, and a macro-element. All models were calibrated using the same FEA results obtained from full 3D continuum modelling of the soil volume. The soil properties used in the simulations can be found in Tables 3.1 and 3.2, and the dimensions of the foundations are provided in Table 3.5.

In the first approach, a linear elastic stiffness matrix was applied at the mudline to represent the foundation. This stiffness matrix was considered as the linear elastic stiffness part from the macro-element models, which were used to capture the monopile-foundation response at representative load levels. It is noted that this approach was used only in the first paper of the thesis. The second approach involved the use of $p-y$ curves. In this method, the pile was modeled as a beam, and the resistance of the soil to lateral displacement of the pile was represented by a series of discrete, uncoupled, axisymmetric nonlinear elastic springs along the pile. An illustration of the $p-y$ springs modeled in SIMA is shown in Figure 3.8.

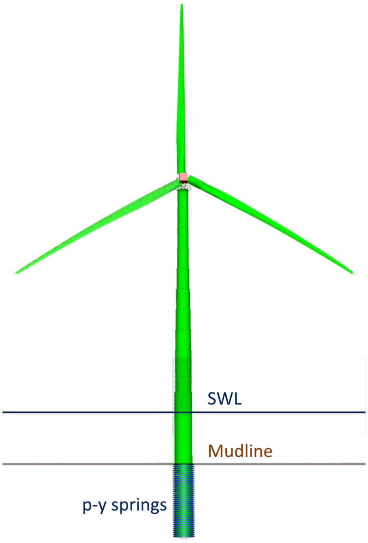

Figure 3.8: OWT modelled in SIMA using $p-y$ springs

The third approach used a nonlinear elasto-plastic model based on the macro-element concept, which was developed as part of the REDWIN project. The model condenses the soil-foundation system into a single node located at the mudline, representing the interface between the foundation and the rest of the structure, as shown in Figure 2.6. By using this model, the complete nonlinear response of the soil-foundation system is captured through load-displacement curves obtained from nonlinear analyses conducted in FEA.

The macro-element model interacts with SIMA through a dynamic link library (DLL). This DLL serves as an interface between the macro-element model and SIMA. At the beginning of each calculation time step, the DLL retrieves the nodal displacement (u_i) and rotation fields (r_i) at the mudline from SIMA to estimate the external forces (F_i, M_i) acting on the macro-element model. These external forces are then computed by the macro-element model and returned to SIMA. This iterative process continues until specific convergence criteria are satisfied. The interface between SIMA and the REDWIN DLL is depicted in Figure 3.9. To calculate the forces along the monopile below the seabed, a separate post-processing numerical tool is employed. This tool adopts a beam on spring model, where the springs are calibrated based on the results obtained from FEA. The calibration methodology used for the springs is described by Klinkvort et al. 2020 [201].

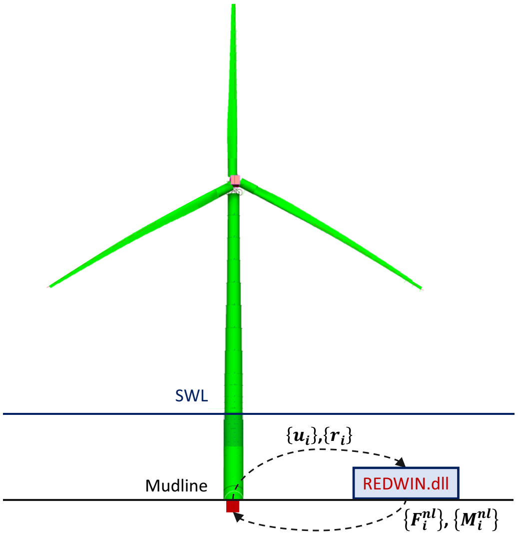

Figure 3.9: Interaction between macro-element and SIMA

3.3.1.3 Stochastic wind field & aerodynamic loads

TurbSim, developed by the National Renewable Energy Laboratory (NREL), was used in the thesis to generate turbulent wind time series for the aeroelastic simulations. TurbSim is a stochastic turbulence simulation tool that generates time series of three-component wind-speed vectors at specific points in a two-dimensional vertical rectangular grid fixed in space, as shown in Figure 3.10 [202]. For each OWT, the center grid point was located at the hub height, and the grid dimensions (height and width) were equal and chosen to cover the rotor diameter. The tool utilizes a numerical simulation approach to generate realistic turbulent wind conditions.

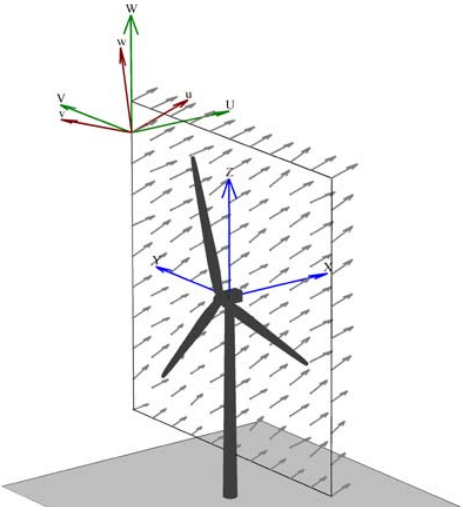

Figure 3.10: TurbSim wind field example. Definitions of coordinate systems, can be found in TurbSim's user guide [202]

In the thesis, only the longitudinal wind component has a nonzero mean value, while all three components include a fluctuating component. The desired mean wind speed at the hub height of the wind turbine was provided as input to TurbSim. The velocity spectra and spatial coherence, which describe the distribution of turbulence energy in the frequency domain and the correlation between different points in space, respectively, were also specified as inputs. TurbSim employs an inverse Fourier transform with a random seed to produce time series of wind output, compatible with SIMA.

For the simulations conducted in the thesis, the Kaimal spectrum with exponential coherence, referred to as the "Kaimal turbulence model", was used, which assumes exponential coherence only in the longitudinal direction. This choice aligns with the recommendations for design load calculations outlined in the IEC 61400-1 4^{th} Edition [30]. The Kaimal turbulence model provides a reasonable representation of the turbulence characteristics typically observed in the atmosphere, allowing for realistic and accurate simulations of wind turbine behaviour under turbulent wind conditions.

In the absence of detailed wind data for the location under consideration, the turbulence intensity in TurbSim simulations was defined based on the normal turbulence model (NTM) for IEC Class C [30]. Wind shear, which characterizes the change in mean wind speed with altitude above the SWL due to the effects of the viscous boundary layer, was represented using a power-law formulation [59]. In the thesis, a value of $\alpha = 0.14$ was used for the power-law exponent. This value is commonly recommended for offshore environments according to design guidelines.

To calculate the aerodynamic loads from the wind speed time series, SIMA employed blade element momentum (BEM) theory. BEM theory assumes that the normal and tangential forces on the rotor plane can be derived from the blade element theory and momentum theory for each blade element of the turbine. Engineering corrections were applied to account for various factors. For instance, the Prandtl tip-correction factor was considered to address the assumption made by momentum theory that blade loads are evenly distributed over the azimuth of an annular section, while in practice, the loads are concentrated at a finite number of blades. The Glauert correction was applied when the axial induction factors exceeded or equaled 0.5, as the validity of axial momentum theory diminishes in such cases. Furthermore, dynamic stall and dynamic wake corrections were incorporated to refine the calculations and improve the accuracy of the simulations [203].

3.3.1.4 Wave kinematics & hydrodynamic loads

The time-domain simulations in the thesis used stochastic irregular waves with random seeds as the wave input. Two wave kinematic theories were employed: the Airy linear wave theory with constant extrapolation of the wave potential up to the instantaneous free surface, and Stokes' 2^{nd} order waves. The wave kinematics time series were generated using the Fast Fourier Transform (FFT) within SIMA, based on specified significant wave height (H_s) and spectral peak period (T_p), using commonly used wave design spectra such as JONSWAP and Pierson-Moskowitz. Long-crested waves were considered. The number and duration of the time-domain stochastic simulations were selected to minimize statistical variability and ensure a reasonable basis for comparisons of the quantities of interest.

Different hydrodynamic models were employed to calculate wave loads and responses of the OWTs. For fatigue-related studies, the Morison equation was utilized with both linear and 2^{nd} order wave theories. To account for diffraction effects, the MacCamy & Fuchs hydrodynamic model was used. The drag coefficient (C_d) and inertia coefficient (C_m) were assumed to be 0.9 and 2.0, respectively, according to DNV guidelines [59] for the Morison equation. The added mass coefficient was assumed to be constant and equal to 1.0 for the MacCamy & Fuchs model. For extreme response analyses, the Morison equation with 2^{nd} order waves was employed and compared to a novel hydrodynamic load model. This new model combines the conventional Morison equation with a frequency-dependent mass coefficient based on the first-order MacCamy & Fuchs solution.

3.3.1.5 Fatigue damage from time-domain simulations

The time-domain simulations provide a time history of loads at different cross sections along the monopile, denoted as N_x (axial force), M_y (bending moment about the y-axis), and M_z (bending moment about the z-axis). Based on the coordinate system in Figure 3.11, the axial stress σ_x at a specific point (r, θ) on the outer surface of the tubular cross section, with an outer radius of r, is estimated using the following equation:

$$\sigma_x = \frac{N_x}{A} - \frac{M_y}{I_y} r \sin(\theta) + \frac{M_z}{I_z} r \cos(\theta). \tag{3.1}$$

Here, A is the cross-sectional area, I_y and I_z are the second moment of area for the cross section computed about the y and z axes, respectively.

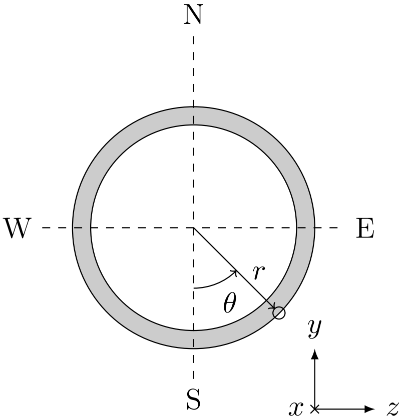

Figure 3.11: Tubular cross-section local coordinate system with compass directions

The shear stress and its resultant fatigue damage were not considered due to their negligible effect compared to the axial stress. The number of load cycles for different stress levels was calculated using the rainflow counting method [65], implemented using the WAFO Toolbox [204]. Representative bi-linear S-N curves were selected based on design standards. Curve “D” [63] was chosen for steel in seawater with cathodic protection, while air was considered for the monopile and the tower, respectively. The S-N curves for girth welds were used since fatigue damage is more prominent in welds. A reference thickness of 25 mm and a thickness exponent of 0.2 for fatigue strength were used based on DNV recommended practice [63]. Stress concentration factors were not taken into account in the analysis.

3.3.2 State-space models

The development of simplified models that accurately represent the response characteristics of OWTs is an important aspect. These simplified models provide quick insights into the system’s properties, making them valuable in the design process. As part of this effort, a linear state-space representation for the OWT models was developed and solved in the frequency domain. This model was based on the work of J.M. Hegseth, as presented in his PhD thesis [205], which focused on floating offshore wind turbines.

The simplified model was utilized in the thesis for two primary purposes. Firstly, it was employed to assess the accuracy of response calculations compared to the fully coupled models. This evaluation aimed to determine how well the simplified model captured the essential characteristics of the OWT response when compared to fully coupled models. Secondly, the potential integration of the simplified model into the design process was explored. This involved investigating how the simplified model could be combined with the developed environmental lumping method.

Overall, the development and evaluation of the simplified OWT model in this thesis aimed to enhance the understanding of its accuracy and applicability, with the ultimate goal of integrating it effectively into the design process for offshore wind turbines.

3.3.2.1 OWT system formulation

The tower and substructure (monopile above the seabed) were modeled as slender flexible beams, following Euler–Bernoulli beam theory, which assumes small deflections. Each beam element was represented by an elemental mass and stiffness matrix. The elemental mass matrix accounted for the structural mass of the beam element, as well as the added mass and enclosed water mass (only for the monopile section). The blades of the model were considered rigid, and the discrete masses, such as the RNA and transition piece, were represented separately. The global mass matrix of the entire OWT system, denoted as $[\mathbf{M_G}]$, was obtained by summing the elemental mass matrix $[\mathbf{M_{el}}]$ and the discrete mass matrix $[\mathbf{M_d}]$, given in Eq. 3.2,

$$[\mathbf{M_G}] = [\mathbf{M_{el}}] + [\mathbf{M_d}]. \tag{3.2}$$

Similarly, the global stiffness matrix, denoted as $[\mathbf{K_G}]$, was composed of the elemental stiffness and the soil stiffness. The elemental stiffness matrix consisted of the bending stiffness and the geometric stiffness, following the definition for an Euler-Bernoulli straight beam element. The soil stiffness at the mudline was represented by a linear stiffness matrix, which was taken as the linear stiffness part of the macro-element models. The global stiffness matrix of the OWT system, $[\mathbf{K_G}]$, was calculated as the sum of the bending stiffness matrix $[\mathbf{K_{el,b}}]$, the geometric stiffness matrix $[\mathbf{K_{el,g}}]$, and the soil stiffness matrix $[\mathbf{K_s}]$, as in Eq. 3.3,

$$[\mathbf{K_G}] = [\mathbf{K_{el,b}}] + [\mathbf{K_{el,g}}] + [\mathbf{K_s}]. \tag{3.3}$$

Figure 3.12 shows an illustration of the OWT simplified response model. The dynamic response of the support structure in the OWT simplified model was estimated using modal superposition. The mode shapes of the OWT system, denoted as $\psi(z)$, were obtained by solving the eigenvalue problem based on the global mass and stiffness matrices. For each OWT, the first four fore-aft and side-side modes were considered.

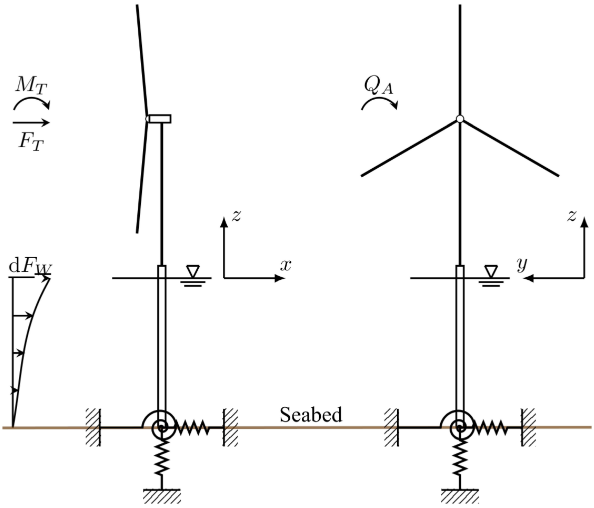

Figure 3.12: Representation of the OWT simplified response model

Figure 3.13 illustrates the fore-aft mode shapes for the three OWT models. These mode shapes represent the spatial distribution of displacements along the support structure. The nodal displacement, $u(z,t)$, at a specific position z along the support structure and at a given time t can be expressed as a superposition of the mode shapes, $\psi(z)$, multiplied by their corresponding modal coordinates, $\chi(t)$, given in Eq. 3.4

$$w(z,t) = \sum_{i=1}^{4} \psi_i(z)\chi_i(t) = \boldsymbol{\psi}(z)^\top \boldsymbol{\chi}(t). \tag{3.4}$$

Here, $\psi_i(z)$ is the i-th mode shape, and $\chi_i(t)$ is the modal coordinate corresponding to the i-th mode. The modal coordinates were assumed to be harmonic with a complex amplitude χ_0 and a frequency ω, represented as $\chi(t) = \chi_0 \mathrm{e}^{i\omega t}$. The generalized equations of motion for the OWT system can be expressed as Eq. 3.5:

$$\mathbf{M}_\chi \ddot{\chi}(t) + \mathbf{C}_\chi \dot{\chi}(t) + \mathbf{K}_\chi \chi(t) = \mathbf{F}(\mathbf{t}) \tag{3.5}$$

where $\boldsymbol{M_\chi}$, $\boldsymbol{C_\chi}$, $\boldsymbol{K_\chi}$ describe the generalized mass, stiffness and damping matrices, respectively, and $\boldsymbol{F(t)}$ is the generalized load vector. The formulation of the generalized system matrices of the structural system is given in Appendix A.

The state variables included the position, $\chi(t)$, and velocity, $\dot{\chi}(t)$, of the structure in modal coordinates. The third state variable was the rotor speed, $\dot{\varphi}$, described by a single degree of freedom drivetrain model, considering only the rigid body dynamics (Eq. 3.6).

$$I_D\,\ddot{\varphi} = Q_A - N_{gear} Q_G \tag{3.6}$$

where I_D is the rotor and drivetrain inertia, Q_A is the aerodynamic torque, N_{gear} is the gear ratio, and Q_G is the generator torque. Q_A is a function of relative wind speed between mean wind speed and horizontal RNA velocity, rotor speed $\dot{\varphi}$, and blade pitch angle θ_{pa}, and Q_G is a function of $\dot{\varphi}$. It should be noted that θ_{pa} and Q_G were defined from the control system.

The control system consisted of a generator-torque and a collective blade-pitch controller, which were applied independently below-rated and above-rated wind speeds, respectively. For both ranges, the rotor speed was low-pass filtered to avoid high-frequency actuation, based on Eq. 3.7,

$$\ddot{\phi}_{lp} + \omega_c \dot{\phi}_{lp} = \omega_c \dot{\phi} \tag{3.7}$$

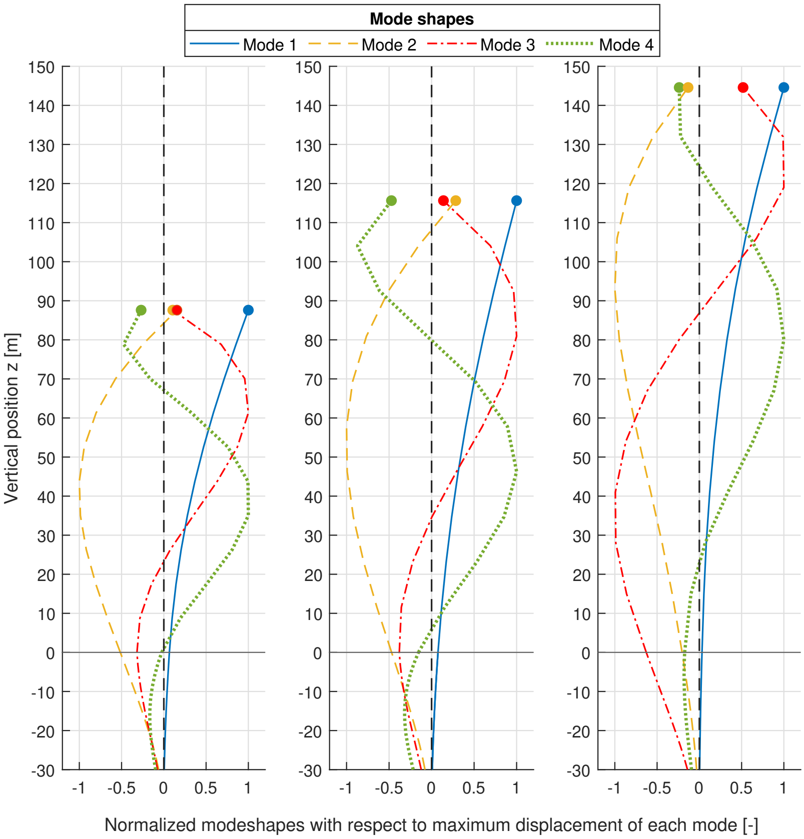

Figure 3.13: First four fore-aft mode-shapes, $\psi(z)$, as obtained by the eigenvalue analysis of the simplified state-space models

where ω_c is the corner frequency, and $\dot{\phi}_{lp}$ is the filtered rotor speed. Below rated wind speed, the generator torque was set proportional to the square of the rotor speed to balance the aerodynamic torque and thus maintain the optimal tip-speed ratio at the mean wind speed. For a rotor speed deviation $\ddot{\phi}_{lp}$ from the reference rotor speed $\dot{\phi}_0$, the updated generator torque was found from Eq. 3.8,

$$Q_G = 2K_g\dot{\phi}_0\dot{\phi}_{lp} \tag{3.8}$$

where K_g is the generator torque constant, and η_κ is the gain-scheduling parameter. Above rated wind speed, a gain-scheduled PI controller is used to modify the collective blade pitch angle, which is found from Eq. 3.9, as follows,

$$\theta_{pa} = \eta_\kappa k_i \phi_{lp} + \eta_\kappa k_p \dot{\phi}_{lp} \tag{3.9}$$

where k_i and k_p are the integral and proportional gains of the PI controller, respectively. Above rated speed, the generator torque is kept constant at the rated torque, and using a first-order Taylor series expansion following [190], it can be expressed by Eq. 3.10,

$$Q_G = \frac{P_0}{N_{gear}\dot{\phi}_0} - \frac{P_0}{N_{gear}\dot{\phi}_0^2}\dot{\phi}_{lp} \tag{3.10}$$

where P_0 is the rated power.

3.3.2.2 Hydrodynamic and aerodynamic loads

The generalized load vector consisted of the hydrodynamic and aerodynamic loads. Wave loads were expressed by the load vector, $\mathbf{F}_W$, which contains the generalized wave excitation force for each nodal position along the substructure. The hydrodynamic loads include first order wave excitation, $dF_M(z,\omega)$, from MacCamy-Fuchs theory [177] to account for diffraction effects, and viscous excitation force, $dF_D(z,\omega)$ based on stochastic linearization of the quadratic drag term in Morison's equation [206] for a fixed cylinder. Eq. 3.11 shows the net force, $dF_M(z,\omega)$, in the direction of wave propagation per unit axial length for a regular wave of amplitude ζ_A acting on a cylinder of radius r,

$$dF_M(z,\omega) = \frac{4\rho g \zeta_A}{k}\frac{\cosh k(z+d)}{\cosh kd}\frac{1}{\sqrt{A(kr)}}e^{i[\omega t - \alpha(kr)]} \tag{3.11}$$

where g is the gravitational acceleration, k is the wave number, d is the water depth, and parameters $A(kr)$, $\alpha(kr)$ can be found in design standards [30]. Eq. 3.12 gives the viscous excitation force,

$$dF_D(z,\omega) = \frac{1}{2}\rho C_d D_p u|u| \approx \frac{1}{2}\rho C_d D_p \sqrt{\frac{8}{\pi}}\sigma_u u \tag{3.12}$$

where C_d is the drag coefficient. From linear wave kinematics, the undisturbed wave particle velocity u for a wave elevation ζ

$$u(z,t) = \omega\frac{\cosh k(z+d)}{\sinh kd}\zeta \quad \text{with} \quad \zeta = \zeta_A \cos\omega t \tag{3.13}$$

with the variance of the velocity, σ_u^2, found from

$$\sigma_u^2 = \left[\frac{\cosh k(z+d)}{\sinh kd}\zeta\right]^2 \int_0^\infty \omega^2 S_\zeta \mathrm{d}\omega \tag{3.14}$$

where S_ζ is the wave spectrum. The total generalized wave load vector is given in Eq. 3.15.

$$F_W(\omega) = \int_{-d}^{0} \left[dF_M(z,\omega) + dF_D(z,\omega)\right] \psi(z)\mathrm{d}z \tag{3.15}$$

The wave load cross spectral density matrix can be calculated from Eq. 3.16,

$$\mathbf{S}_{F_{wave}}(\omega) = \mathbf{H}_{\zeta F}(\omega)\mathbf{S}_\zeta(\omega)(\mathbf{H}_{\zeta F}(\omega))^H, \tag{3.16}$$

$\mathbf{H}_{\zeta F}$ represents the transfer function from wave amplitude to total wave excitation forces, and $(\cdot)^H$ denotes the conjugate transpose [58].

The aerodynamic loads on the rotor were estimated using linearized blade element momentum theory. The incoming wind field is described by the Kaimal spectrum and an exponential coherence function in the longitudinal wind velocity component, as specified by the IEC standard [80].

The calculation of axial and tangential induction factors for each OWT follows the procedure proposed by Ning [207]. The BEM equations are parameterized to a single variable, the local inflow angle. An iterative procedure is then employed to estimate the induction factors for each blade element, considering various blade pitch angles and tip speed ratios. The Prandtl and Glauert corrections for tip loss and hub loss are included in the procedure [79], while dynamic wake and dynamic stall effects are neglected. Considering that the rotor design and blade geometry for each OWT model do not change in the course of the thesis, the pre-calculated induction factors, which remain constant throughout the thesis, are stored and used in the subsequent response analyses. It is worth noting that the dynamic response of the blades and their impact on the support structure response were not considered in this study.

The aerodynamic forces on a blade element are nonlinear functions of the relative wind speed, rotor speed, and blade angle [79]. A first-order Taylor expansion was used to approximate the tangential (F_t) and normal (F_n) blade element forces relative to the rotor plane at a distance r from the blade root [205]. By integrating the loads along the blade radius R, the blade root loads were estimated, including the flapwise shear force, the flapwise bending moment, and the edgewise bending moment. Finally, the resultant rotor loads, which consist of the aerodynamic thrust F_T, tilting moment M_T, and aerodynamic torque Q_A, were calculated by summing the blade root forces. Figure 3.14 provides a simplified illustration of an OWT rotor with the relevant resultant loads, demonstrating the interaction between the aerodynamic forces and the rotor structure.

$$F_T(v_{rel}, \dot{\varphi}, \theta) = \sum_{i=1}^{3} \int_0^R F_{n,i}(v_{rel}, \dot{\varphi}, \theta)\, dr \tag{3.17a}$$

$$M_T(v_{rel}, \dot{\varphi}, \theta) = \sum_{i=1}^{3} \int_0^R rF_{n,i}(v_{rel}, \dot{\varphi}, \theta)\, dr \tag{3.17b}$$

$$Q_A(v_{rel}, \dot{\varphi}, \theta) = \sum_{i=1}^{3} \int_0^R rF_{t,i}(v_{rel}, \dot{\varphi}, \theta)\, dr \tag{3.17c}$$

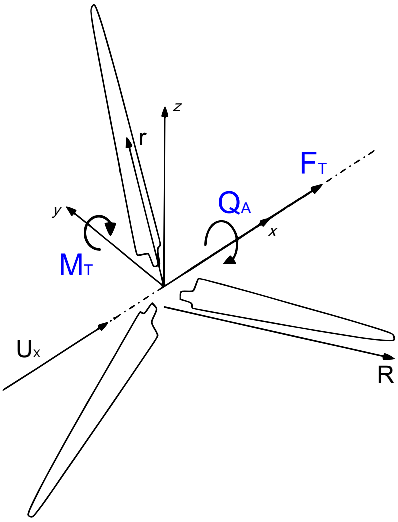

Figure 3.14: Horizontal axis rotor with the resultant loads indicated

In the OWT simplified model, the aerodynamic forces on the rotor were applied as resultant loads at the top of the tower. These loads were estimated based on the concept of rotor effective wind speed, which describes the incoming wind for each of the three forces (thrust, tilting moment, and aerodynamic torque) mentioned in Eq. 3.17.

The rotor effective wind speed is defined as a transfer function that relates the incoming wind speed at the hub height, associated with a specific blade pitch angle and rotor speed, to the rotor effective wind speed for a given resultant load. The rotor effective wind speed is chosen such that it produces identical loads as the full wind field over the rotor. This transfer function takes into account the interaction between the wind speed and the blade element loads. The rotor effective wind speed spectra are established by considering the incoming wind spectrum, the spatial coherence function, and the transfer functions between wind speed and blade element loads. These factors are combined in the wind load matrix $\mathbf{S}_{\mathbf{F}_{\mathbf{wind}}}(\omega)$. The detailed derivation of the rotor effective wind speed spectra is provided by Hegseth [205], building upon the work of Halfpenny [208].

By using the rotor effective wind speed spectra, the loads on the rotor can be accurately represented based on a simplified model, taking into account the relevant characteristics of the incoming wind field and the aerodynamic forces acting on the blades. This approach allows for efficient and accurate analysis of the OWT system response while considering the complexities of the aerodynamic loads.

3.3.2.3 State-space formulation

The ordinary differential equations that describe the dynamics of the system were transformed into a set of first-order differential equations in the state-space form, Eq. 3.18,

$$\dot{\mathbf{x}} = \mathbf{A}\mathbf{x} + \mathbf{B}\mathbf{u} \tag{3.18}$$

where $\mathbf{x}$ is a vector that contains the unknown state variables that describe the system's state at any time, and $\mathbf{A}$ contains the system characteristics. $\mathbf{B}$ is a locator matrix that relates any external input-excitation $\mathbf{u}$ to the states of the system. The state-space model consists of a structural and a control module, each with its state-space formulation, with representative inputs, outputs, and states. Their formulation follows the one described in detail by Hegseth [205, 209], and only an overview is given here.

For the structural system, based on Eq. 3.5 and Eq. 3.7, the state vector, $\mathbf{x}_s$, consists of the position and velocity in modal coordinates, $\chi(t)$, and the rotor speed, $\dot{\varphi}$. This was considered a minimal set of degrees of freedom that could give an accurate overview of the system dynamics. Similarly, for the control system, from Eq. 3.7, the state vector $\mathbf{x}_c$ consists of the low pass filtered angular position ϕ_{lp}, and velocity $\dot{\phi}_{lp}$, of the rotor, while the output is the generator torque, Q_G, and the blade pitch angle, θ. The output of the control state-space module was incorporated as input in the structural module with the environmental loads to obtain the coupled aero-hydro-servo-elastic model. The representation of the coupled structural-control system based on Eq. 3.18, is given by Eq. 3.19,

$$\begin{bmatrix} \dot{\mathbf{x}}_\mathbf{s} \\ \dot{\mathbf{x}}_\mathbf{c} \end{bmatrix} = \begin{bmatrix} \mathbf{A_s} & \mathbf{0} \\ \mathbf{0} & \mathbf{A_c} \end{bmatrix} \begin{bmatrix} \mathbf{x_s} \\ \mathbf{x_c} \end{bmatrix} + \begin{bmatrix} \mathbf{B_{sd}} & \mathbf{B_{sc}} \\ \mathbf{0} & \mathbf{B_c} \end{bmatrix} \begin{bmatrix} \mathbf{u_{sd}} \\ \mathbf{u_{sc}} \end{bmatrix} \tag{3.19}$$

where $\mathbf{A_s}$, $\mathbf{A_c}$ are the structure and control system characteristics respectively, $\mathbf{B_{sd}}$ relates the environmental input to the structure, $\mathbf{B_c}$ relates the control input to the controller, and $\mathbf{B_{sc}}$ couples the structural system to the control system. The closed-loop system is then transformed to the frequency domain, where the transfer matrix between input and output for a frequency ω is defined by Eq. 3.20,

$$\mathbf{H}(\omega) = \mathbf{C}\left(i\omega\mathbf{I} - \mathbf{A}\right)^{-1}\mathbf{B} \tag{3.20}$$

with $\mathbf{C}$ equal to the identity matrix. The cross spectral density matrix for the load processes, $\mathbf{S_u}(\omega)$, can be written by Eq. 3.21, and the response spectra of output $\mathbf{y}$ (Eq. 3.22) are then found along the diagonal of the cross spectral density matrix $\mathbf{S_y}(\omega)$.

$$\mathbf{S_u}(\omega) = \begin{bmatrix} \mathbf{S}_{F_{wind}}(\omega) & \mathbf{0} \\ \mathbf{0} & \mathbf{S}_{F_{wave}}(\omega) \end{bmatrix} \tag{3.21}$$

$$\mathbf{S_y}(\omega) = \mathbf{H}(\omega)\mathbf{S_u}(\omega)\left(\mathbf{H}(\omega)\right)^H. \tag{3.22}$$

To evaluate the validity of the simplified models, the fore-aft bending moment spectra were compared to spectra from time domain simulations of the fully coupled models. Results from comparisons are shown in publication P3 [210].

Chapter 4

Environmental lumping for fatigue design

This chapter describes the developed environmental lumping method to extract and analyze representative load cases for FLS design, as an alternative to the standard long-term fatigue assessment procedure. The detailed steps of the method are described, for co-directional scatter diagrams for one wave component, and multi-directional scatter diagrams for wind-sea and swell components.

4.1 Organization of metocean parameters

Fatigue design of OWTs is based on load calculations considering simultaneous wind and wave conditions. The domain of the variables that describes the metocean conditions is split into classes (bins) of constant size, typically defined by the design standards [30], and represented by scatter diagrams. Scatter diagrams describe the long-term variability of metocean conditions by defining the joint probability of occurrence of different sea states within the dataset, considering concurrent metocean conditions. To establish the scatter diagrams, the following metocean parameters are considered,

- Wind speed at hub height, U
- Wind direction, θ_u
- Significant wave height, H_s
- Peak period, T_p
- Wave direction, θ_w

Combining those parameters leads to a five-dimensional parameter space $\Omega = (U, \theta_u, H_s, T_p, \theta_w)$, which consists of all the observations N within the dataset. Below, some basic probability definitions are given, which will be used in the following sections. The marginal probability of a metocean parameter, e.g. U, to be within a class k, with lower and upper bounds U_k^{lb} and U_k^{ub} respectively, can be expressed by Eq. 4.1,

$$P\left(U_k\right) = P\left(U_k^{lb} \leq U_k < U_k^{ub}\right) = \frac{n_k}{N} \tag{4.1}$$

where n_k is the number of observations where $U \in [U_k^{lb}, U_k^{ub})$. Similarly, the joint probability of two metocean parameters, e.g., H_s and T_p to be within classes i, and j, respectively, i.e., $H_s \in [H_{s,i}^{lb}, H_{s,i}^{ub})$ and $T_p \in [T_{p,j}^{lb}, T_{p,j}^{ub})$ can be expressed by Eq. 4.2,

$$P\left(H_{s,i} \cap T_{p,j}\right) = P\left(H_{s,i}^{lb} \leq H_s < H_{s,i}^{ub} \cap T_{p,j}^{lb} \leq T_p < T_{p,j}^{ub}\right) = \frac{n_{i,j}}{N} \tag{4.2}$$

where $n_{i,j}$ is the number observations with $H_s \in [H_{s,i}^{lb}, H_{s,i}^{ub})$ and $T_p \in [T_{p,j}^{lb}, T_{p,j}^{ub})$. Finally, the conditional probability of a sea state $P(H_{s,i} \cap T_{p,j})$ for a given wind class U_k, where $U \in [U_k^{lb}, U_k^{ub})$ can be expressed by Eq. 4.3,

$$P\left(H_{s,i} \cap T_{p,j} | U_k\right) = P\left(H_{s,i} \cap T_{p,j} | U_k^{lb} \leq U < U_k^{ub}\right) = \frac{n_{k,i,j}}{N} \tag{4.3}$$

where $n_{k,i,j}$ is the number observations with $H_s \in [H_{s,i}^{lb}, H_{s,i}^{ub})$ and $T_p \in [T_{p,j}^{lb}, T_{p,j}^{ub})$, under the condition that $U \in [U_k^{lb}, U_k^{ub})$.

For the co-directional scatter diagrams, the wind (θ_u) and wave (θ_w) direction were not considered, and they are assumed equal, and 0°, i.e., facing the fore-aft direction of the OWT in the analyses. Wave data ($H_s - T_p$) were organized in scatter diagrams based on wind speed classes associated with the mean wind speed at hub height for each OWT. Each scatter diagram consists of $i = 1, ...N_{H_s}$ classes for the significant wave height and $j = 1, ..., N_{T_p}$ classes for the peak period, each one represented by the class midpoints $H_{s,i} - T_{p,j}$.

For a given wind class U_k, where $U \in [U_k^{lb}, U_k^{ub})$, the probability of occurrence of a wave class $H_{s,i} - T_{p,j}$ can be expressed by the conditional probability given by Eq. 4.3, and the total probability of the representative scatter diagram is given by Eq. 4.4,

$$P_{SD_k} = \sum_{i=1}^{N_{H_s}} \sum_{j=1}^{N_{T_p}} P\left(H_{s,i} \cap T_{p,j} | U_k\right). \tag{4.4}$$

4.2 Fatigue assessment using scatter diagrams

The conventional approach to assess OWT long-term fatigue damage is to analyze all sea states with a non-zero probability of occurrence in the wave scatter diagrams, as suggested by the design standards [30]. An example of this approach is illustrated in Figure 4.1, which shows a co-directional scatter diagram that represents the wave data within wind class $U_k \in [12, 14)$ m/s, divided into different classes.

To assess the short- and long-term damage, the data within each sea state class (i, j) are represented by the midpoint values of the class, $H_{s,i}$ and $T_{p,j}$, respectively, denoted by the coloured nodes in the scatter diagram. For each sea state, either one 1-hr or six 10-min realizations (known as *seeds*) should be simulated [30], assuming stationary environmental conditions. The first option is used in the thesis.

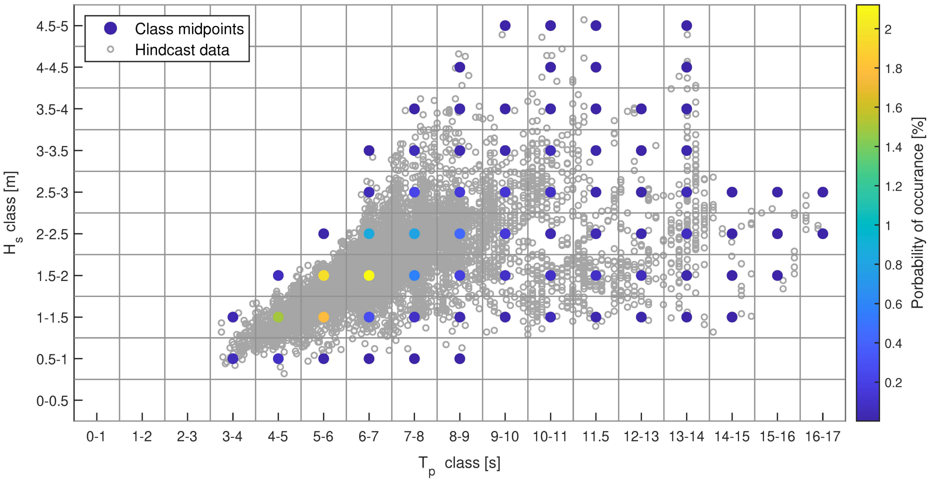

Figure 4.1: Illustration of hindcast data as classified in a wave scatter diagram. The nodes represent the class midpoint values, and their colour indicates the probability of occurrence of the class.

To estimate the short-term fatigue damage for each sea state within the scatter diagram, the stress time history obtained from each simulation is analyzed. The number of load cycles for different stress levels is computed using the rainflow counting method (RFC) [65]. Using characteristic bilinear S-N curves for steel, the short-term (1-hour) damage, denoted as $d_{ST}^{TD}(U_k, H_{s,i}, T_{p,j})$, is then estimated. Figure 4.2 illustrates this procedure.

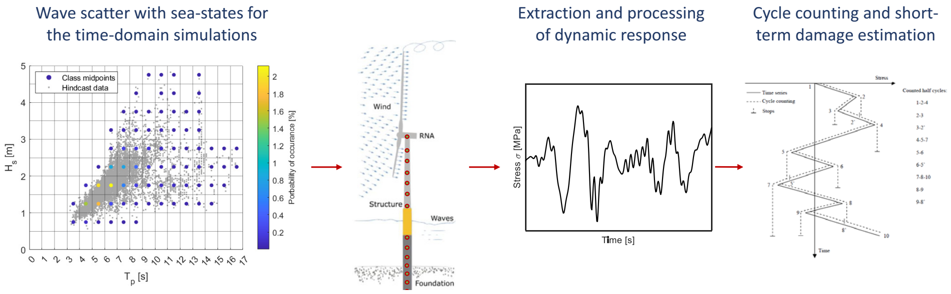

Figure 4.2: Procedure to estimate short-term fatigue damage for each sea state within a wave scatter diagram (RFC illustration [211]).

To estimate the long-term fatigue damage, the short-term damage of each sea-state class is multiplied by its representative probability of occurrence, denoted as $P(H_{s,i} \cap T_{p,j}|U_k)$, and the specified design lifetime N_y expressed in hours. This calculation is based on the assumption of Palmgren-Miner's linear damage accumulation hypothesis [62, 81], and is given in Eq. 4.5,

$$d_{LT}(U_k, H_{s,i}, T_{p,j}) = N_y \cdot P(H_{s,i} \cap T_{p,j}|U_k) \cdot d_{ST}^{TD}(U_k, H_{s,i}, T_{p,j}). \tag{4.5}$$

The procedure described above is referred to in the thesis as a full long-term fatigue assessment. Fatigue assessment based on the conventional full long-term approach requires analyzing a large number of load cases. For the hindcast data considered in this work, assuming a wind class size of 2 m/s, and a typical wave class with size 0.5 m for H_s and 1 s for T_p (as shown in Figure 4.1), results in 19 co-directional scatter diagrams, and a total number of approximately 1000 (U, H_s, T_p) combinations that need to be analyzed. If the wind speed class size is decreased to 1 m/s, the number of analyses is almost doubled. Moreover, considering seed variability and performing multiple analyses to reduce statistical uncertainty further increases the computational time.

4.3 Damage-equivalent lumping method

The damage-equivalent lumping method (DELM) derives one lumped load case to represent each scatter diagram within the long-term fatigue assessment. The lumped load case, denoted as $\left(H_s^{LC}, T_p^{LC}\right)$, has a probability of occurrence equal to the total probability of occurrence of the representative scatter diagram P_{SD_k} (Eq. 4.4), and it replaces all sea-state classes with individual probabilities of occurrence $P(H_{s,i} \cap T_{p,j}|U_k)$ in the scatter diagram.

This approach is illustrated in Figure 4.3. The use of the lumped load case aims to reduce the computational effort required for the fatigue assessment compared to the conventional approach. Instead of analyzing each individual sea state within the scatter diagram, only one load case needs to be analyzed, simplifying the analysis process and saving computational resources.

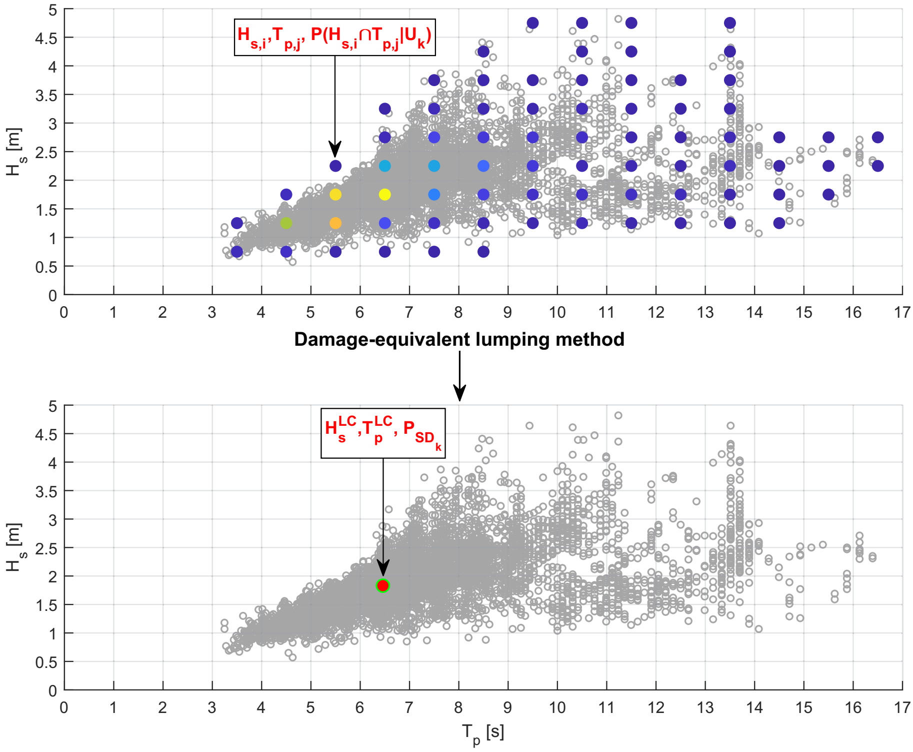

Figure 4.3: Illustration of damage-equivalent lumping method

The main objective of the method is to extract a lumped load case $\left(H_s^{LC}, T_p^{LC}\right)$ that can provide adequate long-term damage estimates throughout the support structure, by considering the following aspects in an integrated manner:

- The effect of wind loading, which is essential for the OWT response;
- The wind-wave correlation of offshore environment and the long-term distribution of the sea states within the wave scatter diagrams;
- The dynamic response characteristics of the OWT structure within the lumping process;
- Combination of wind-sea and swell components in a consistent way.

For each co-directional scatter diagram associated with a wind class, the lumped load case is defined by a concurrent mean wind speed at hub height, taken as the midpoint value of the wind class, and the sea state parameters $\left(H_s^{LC}, T_p^{LC}\right)$. For multi-directional scatter diagrams, the wind and wave directions are also considered, as discussed in Sec. 5.3.

The lumping method presented by Katsikogiannis et al. [210, 212] is based on the concept of damage-equivalent contour lines, also known to as contour lines [73, 74]. These contour lines represent $H_s - T_p$ combinations that result in similar long-term fatigue damage estimates at a specific location along the structure. The method applies to both fully integrated time-domain models (Sec. 3.3.1) and state-space frequency-domain models (Sec. 3.3.2).

The lumping method consists of two main steps. The first step is to derive the stress spectra along the support structure for each $H_{s,i} - T_{p,j}$ combination within the wave scatter diagrams (Sec. 4.3.1). The second step of the method is to determine the damage-equivalent contour lines, to obtain the lumped load cases (Sec. 4.3.2). The application of the method using the fully coupled and simplified models differs only in the derivation of the stress spectra, while the overall procedure to derive the lumped load cases is identical.

4.3.1 Derivation of stress spectrum

To derive the stress spectrum using fully-coupled models, a 3-hour white noise wave excitation and uniform wind are applied to the OWT model for each wind class. By conducting a time-domain simulation, the stress response along the OWT is obtained. To establish the relationship between wave elevation and stress response at different positions along the support structure, a linear stress transfer function, denoted as $H_{\zeta\sigma}$, is derived. This transfer function quantifies the relationship between the spectral densities of the wave input and the stress output given in Eq. 4.6,

$$|H_{\zeta\sigma}(f, z)| = \sqrt{\frac{S_{\sigma\sigma}(f, z)}{S_{\zeta\zeta}(f)}}, \tag{4.6}$$

where $S_{\sigma\sigma}(f, z)$ is the power spectral density of the stress response, $S_{\zeta\zeta}(f)$ is the incident white noise wave spectrum, and z is the vertical position along the support structure. Spectral densities from wave and response time series were estimated using WAFO toolbox [204], applying spectral smoothing. Figure 4.4 illustrates the procedure to derive stress transfer functions for different positions along the support structure for one wind speed class.

For monopile-based OWTs, the contour lines (and lumped load cases) could be extracted from two locations along the support structure [210]. One should be representative of the tower response (e.g., tower base), and one of the monopile response (e.g., mudline), to adequately capture the dynamic response due to wave loads. The exact locations chosen for extracting the contour lines have minimal influence on the derived $H_s^{LC} - T_p^{LC}$ values, as shown by Katsikogiannis et al. [210]. The variations in the derived lumped load cases were found to be negligible compared to the statistical uncertainty in the damage estimation. In the thesis, the tower base and the mudline were selected as representative locations along the OWT for the lumping process.

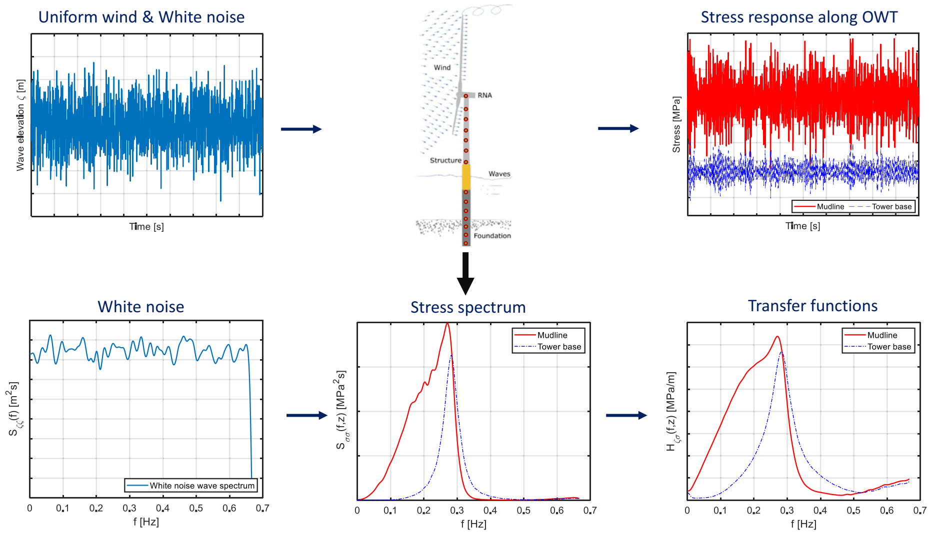

Figure 4.4: Procedure to determine stress transfer functions representative for each scatter diagram associated with a wind speed class, using fully integrated time-domain models (Figure 3.7).

As the spectral approach relates the wave input to the stress response, the response spectra should represent the OWT dynamic response caused only by wave loads. Therefore, the operational turbine was subjected to a constant, uniform wind field while disabling tower shadow effects. This approach assists to minimize the dynamic excitation caused by the wind while still capturing the influence of aerodynamic damping and mean thrust. Including the mean thrust is also essential for accurately representing the nonlinear soil properties, such as stiffness and damping, which are affected by the soil deflection resulting from the mean responses to the aerodynamic thrust. To ensure that the transfer functions adequately cover the entire frequency range within the scatter diagram, MacCamy & Fuchs' load model [177] was applied. This model accounts for diffraction effects that become important for frequencies higher than approximately 0.15-0.2 Hz, as shown in Figure 2.7. The frequency range between 0 Hz and 0.7 Hz was considered in the analysis to include all relevant response frequencies for the monopile-based OWT models considered in the thesis.

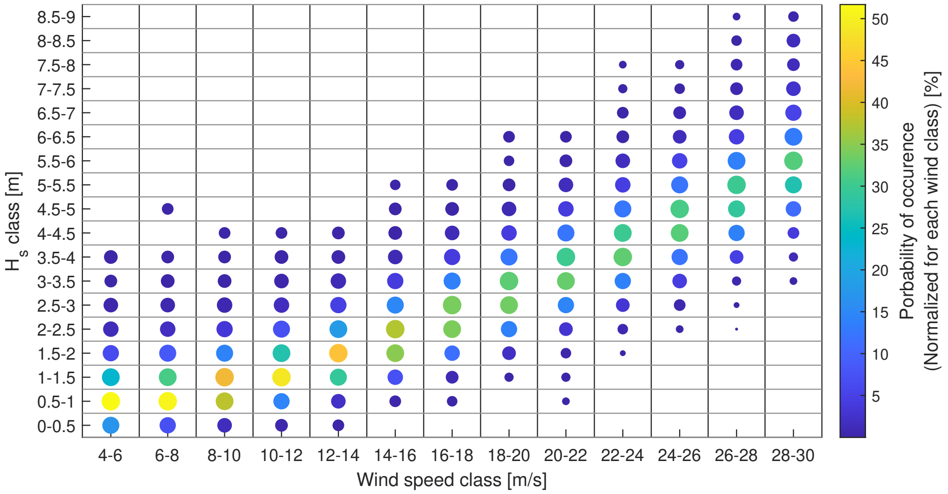

Figure 4.5: H_s classes probability of occurrence (colour) and contribution to the long-term damage (size) at mudline. Probabilities are scaled to the total wind class quantities

For the white noise excitation, the significant wave height was selected as the midpoint value of the most probable H_s class within the wave scatter diagram associated with the wind class. This choice relies on the results of the full long-term fatigue assessment, which depicted that for the monopile-based OWTs used in the study, long-term fatigue damage within a scatter diagram was generally dominated by the sea states with the highest probability of occurrence, as shown in Figure 4.5 for the 10 MW model. In Figure 4.5, each H_s class is represented by marker colour indicating its probability of occurrence, scaled to the total probability of the wind class. The marker size represents the contribution of each H_s class to the long-term fatigue damage within each wind class at the mudline position. The analysis shows that the probability of occurrence of different H_s classes is positively correlated with their contribution to long-term damage, with a correlation coefficient exceeding 0.95 for operational and approximately 0.9 for parked wind classes. Similar trends were observed for the 5 MW and 15 MW OWT models.

The transfer functions $H_{\zeta\sigma}(f,z)$ obtained for each wave scatter diagram, are combined with typical wave spectra, such as JONSWAP or Pierson-Moskowitz spectra, corresponding to each $(H_{s,i}, T_{p,j})$ class, resulting in a representative stress spectrum $S_{\sigma_{i,j}}(f,z)$ within the scatter diagram. The procedure to derive stress spectra is illustrated in Figure 4.6. $S_{\sigma_{i,j}}(f,z)$ is used in the subsequent step of establishing the damage-equivalent contour lines, which are used to determine the lumped load cases.

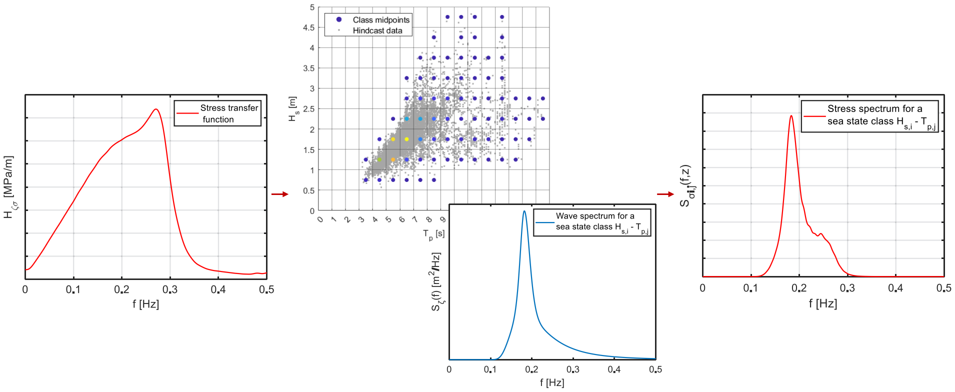

Figure 4.6: Derivation of stress spectrum $S_{\sigma_{i,j}}(f,z)$ for each $(H_{s,i}, T_{p,j})$ class within a scatter diagram, by combining $H_{\zeta\sigma}(f,z)$ and wave spectra

For the simplified state-space models (Sec. 3.3.2), the stress spectra $S_{\sigma_{i,j}}(f,z)$ along the support structure for each $H_{s,i} - T_{p,j}$ combination were derived directly as an output ($\mathbf{S}_{\mathbf{y}}(\omega)$ in Eq. 3.22) from the frequency-domain model.

4.3.2 Establishing damage-equivalent contour lines

Having defined the stress spectra, to establish the damage-equivalent contour lines, two main quantities are calculated: the *target*, and the *scaled unit* fatigue damage. These are derived based on the unit fatigue damage. The procedure for calculating these quantities is the same for the fully coupled and simplified models, and it is described in detail in the following sections.

4.3.2.1 Unit fatigue damage

To estimate the unit fatigue damage $d_{ST}^{FD}(U_k, H_{s,i}, T_{p,j})$ for a specified environmental condition $H_{s,i} - T_{p,j}$ within the scatter diagram associated with wind class U_k, the derived stress spectra $S_{\sigma_{i,j}}(f,z)$ are used. This unit fatigue damage represents the short-term damage over a specified time period, such as one hour. The irregularity factor β^1 is determined based on the stress spectrum, and it is calculated as $\beta = \sqrt{m_2^2/(m_0 \cdot m_4)}$, where m_i represents the i^{th} spectral moment. If $\beta \geq 0.96$, corresponding to a bandwidth parameter $\delta \leq 0.28$, the stress spectrum is considered narrow-banded. Otherwise, it is assumed to be wide-banded.

For a narrow-banded spectrum, the short-term stress ranges follow a Rayleigh distribution. The total number of cycles can be expressed using the mean zero up-crossing rate ν_0 and an equivalent stress range σ_{eq}. The equivalent stress range represents a constant stress range loading that is equivalent to the random loading. Assuming a single slope S-N curve with fatigue strength exponent m, for a narrow-banded Gaussian process with zero mean, the equivalent stress range σ_{eq} is calculated using Eq. 4.7 [58],

$$\sigma_{eq}^m = \left(2\sqrt{2m_0}\right)^m \cdot \Gamma(1 + m/2), \tag{4.7}$$

Here, m_0 is the zeroth spectral moment representing the variance of the stress spectrum $S_{\sigma_{i,j}}(f, z)$, and $\Gamma(\cdot)$ is the Gamma function. Finally, the short-term (1 hour) fatigue damage for the narrow-banded process associated with the environmental condition $H_{s,i} - T_{p,j}$ is calculated using Eq. 4.8,

$$d_{ST}^{FD}(U_k, H_{s,i}, T_{p,j}) = 3600 \cdot \nu_0 \cdot \sigma_{eq}^m / K, \tag{4.8}$$

where K is the material fatigue parameter. For a wide-banded process, empirical solutions have been proposed by several researchers since the 1980s. These include Wirching and Light [213], Zhao and Baker [214], Dirlik [215], Tovo-Benasciutti [216, 217], Gao-Moan [218]. Among these solutions, Dirlik's [215] and Benasciutti-Tovo's [217] empirical formulas have been found to be the most accurate approximations of the rainflow counting method [219]. Dirlik's formulation was used in the thesis. Dirlik's closed-form formulation is based on extensive numerical simulations using various spectral shapes. It approximates the probability density function of the stress range by combining one exponential and two Rayleigh distributions. Dirlik's solution has been widely used in estimating fatigue damage of offshore structures, and provides accurate results over a wide range of bandwidths for a stationary Gaussian process [218].

Dirlik's closed-form formulation requires a single slope parameter m. [215]. From the full long-term fatigue assessment, where bi-linear curves were used

---

[1] In Papers P2 & P3, β is called the bandwidth parameter. For the sake of completeness, $\beta = \sqrt{m_2^2/(m_0 \cdot m_4)}$, where m_i is the i^{th} spectral moment, is typically defined as the irregularity factor, while the bandwidth parameter is defined as $\delta = \sqrt{1 - \beta^2}$.

to calculate the damage, it was observed that the main contributor to the total damage is the high cycle region, above 10^6 cycles. Figure 4.7 shows the long-term fatigue damage distribution over the stress range for the three OWT models, at SWL and mudline. In the vicinity of SWL, the long-term damage occurs entirely in the high-cycle region, while at and close to the mudline, due to relatively larger responses, approximately 10% of the long-term damage is caused by stress ranges above the transition point. Therefore, to account for the significant contribution of the high-cycle region to the total damage, a single value $m = 5$ is used in Eq. 4.7.

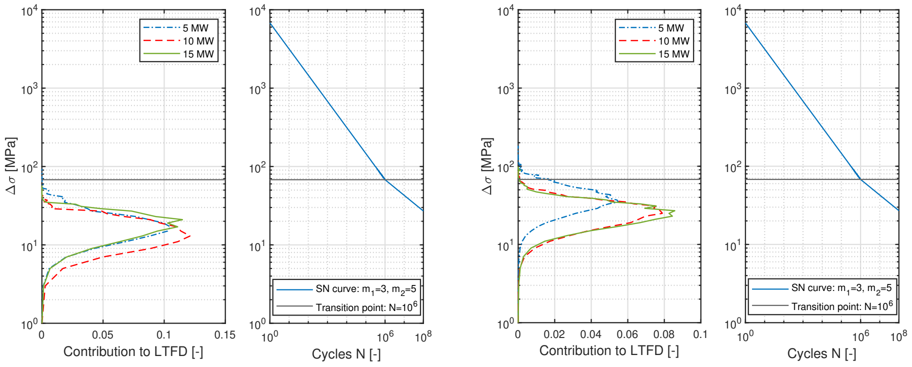

(a) Tower base (b) Mudline

Figure 4.7: Long-term damage distribution over the stress range, from full long-term fatigue assessment based on co-directional scatter diagrams

4.3.2.2 Target fatigue damage

Based on the unit fatigue damage d_{ST}^{FD}, the long-term damage of each class $(H_{s,i}, T_{p,j})$ can be calculated from Eq. 4.9 similarly to Eq. 4.5, as follows,

$$d_{LT}^{FD}(U_k, H_{s,i}, T_{p,j}) = N_y \cdot P(H_{s,i} \cap T_{p,j} | U_k) \cdot d_{ST}^{FD}(U_k, H_{s,i}, T_{p,j}). \tag{4.9}$$

The target fatigue damage $D_{LT,target}$, representative for a wave scatter diagram, is calculated by summing up the long-term damages d_{LT}^{FD} over all sea states in the scatter diagram. The summation is performed over the H_s and T_p classes in the scatter diagram, denoted by N_{H_s} and N_{T_p} respectively, given in Eq. 4.10,

$$D_{LT,target} = \sum_{i=1}^{N_{H_s}} \sum_{j=1}^{N_{T_p}} d_{LT}^{FD}(U_k, H_{s,i}, T_{p,j}). \tag{4.10}$$

4.3.2.3 Scaled unit fatigue damage

The scaled unit fatigue damage $D_{U,scale}$ is calculated using Eq. 4.11, by multiplying the unit fatigue damage $d_{ST}^{FD}(U_k, H_{s,i}, T_{p,j})$ by the total probability of occurrence P_{SD_k} of the representative wave scatter diagram (Eq. 4.4),

$$D_{U,scale}(U_k, H_{s,i}, T_{p,j}) = N_y \cdot d_{ST}^{FD}(U_k, H_{s,i}, T_{p,j}) \cdot P_{SD_k}. \tag{4.11}$$

$D_{U,scale}$ represents the long-term fatigue damage for a sea state $(H_{s,i}, T_{p,j})$, assuming that only the evaluated sea state class would be present in the wave scatter diagram. The surface plot shown in Figure 4.8 illustrates an example of the scaled unit fatigue damage $D_{U,scale}$ as a function of T_p and H_s at the mudline and tower base of a 10 MW offshore wind turbine. By calculating $D_{U,scale}$ for different sea state classes within the scatter diagram along the support structure, a surface is formed, which follows a behaviour similar to the dynamic amplification factor of a single-degree-of-freedom system.

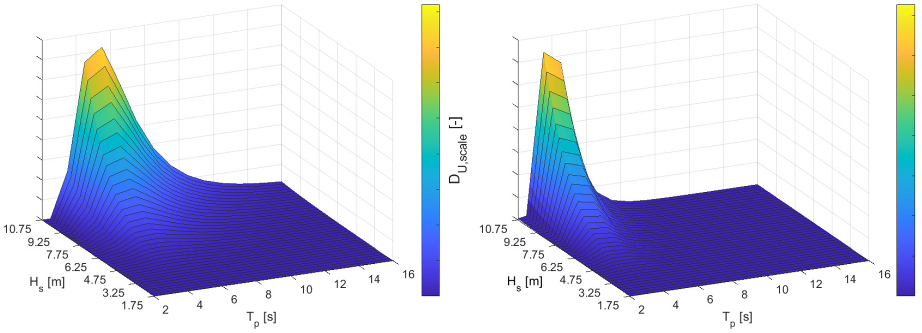

(a) Mudline (b) Tower base

Figure 4.8: Scaled unit fatigue damage surface over the $H_s - T_p$ space

The damage-equivalent contour line (DECL) represents all combinations of $H_{s,c}$ and $T_{p,c}$ for which the target long-term fatigue damage $D_{LT,target}$ (calculated using Eq. 4.10) is equal to the scaled unit fatigue damage $D_{U,scale}$ (calculated using Eq. 4.11), for a specific location along the OWT. The condition for the DECL is expressed in Eq. 4.12,

$$N_y \cdot D_{U,scale}(U_k, H_{s,c}, T_{p,c}) \cdot P_{SD_k} = D_{LT,target}. \tag{4.12}$$

Figure 4.9, the scaled unit fatigue damage $D_{U,scale}$ is represented by the multi-coloured surface, while the target long-term fatigue damage $D_{LT,target}$

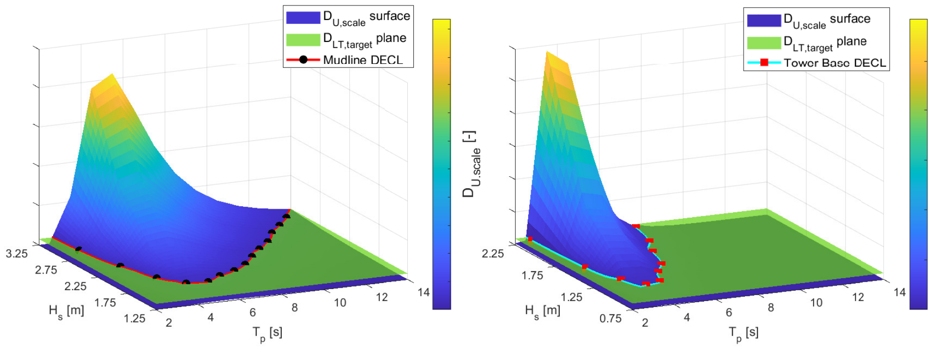

(a) Mudline

(b) Tower base

Figure 4.9: Scaled unit and target fatigue damage together with their intersection points, which form the DECL.

is shown as the green plane. The intersection points between these two represent the damage-equivalent contour lines (DECLs) for the mudline (Figure 4.9a) and tower base locations (Figure 4.9b). Only a small range of H_s and T_p is displayed for illustration purposes. Figure 4.10 shows the contour lines over the full H_s-T_p parameter space. Each contour line represents combinations of H_s and T_p that satisfy the condition in Eq. 4.12 for the specified location along the OWT. Their intersection point, indicated by a green marker, represents the lumped load case H_s^{LC}-T_p^{LC}, which satisfies Eq. 4.12 for both the mudline and tower base locations.

The shape of the contour lines reflects the dynamic behaviour of the structure and exhibits an approximately inverse relationship to the stress transfer functions, as shown in Figure 4.11 [210]. In the vicinity of the natural period, resonance effects cause a steep increase in fatigue damage, and as a result, small values of H_s are required to excite the structure to the target damage level $D_{LT,target}$. This leads to a local minimum in the contour lines. For longer wave periods, the stress transfer functions gradually decrease, indicating lower dynamic amplification, as expected for frequencies far below resonance. In this range, the number of load cycles also decreases, resulting in lower fatigue damage. Consequently, H_s gradually increases along the contour lines to excite the structure to the target damage level $D_{LT,target}$. For short wave periods, the dynamic amplification tends to zero as high-frequency external forces produce little response, resulting in low fatigue damage. In this range, a steep increase in H_s is observed in the contour lines. However, it is important to note that some of the sea state combina-

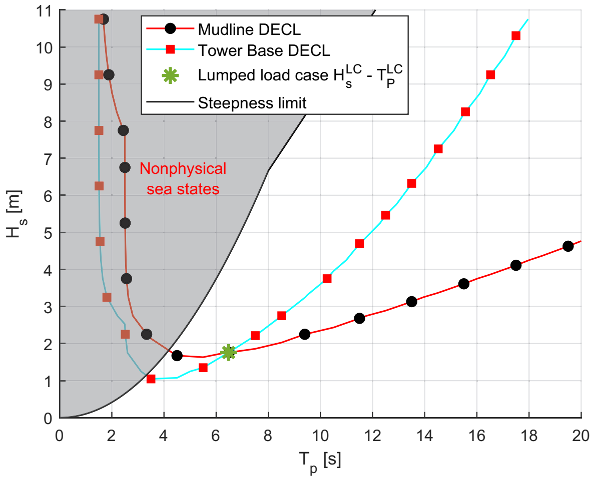

Figure 4.10: DECLs for the 10 MW model and the resultant lumped load case for wind class 12-14 m/s.

tions obtained in this range are nonphysical, exceeding the wave steepness limit [59]. The differences in the natural periods of OWTs are reflected in the contour lines, where the local minimum for the 5 MW and 10 MW models is observed close to 4 s, while for the 15 MW, it is approximately at 5.5 s.

4.3.3 Fatigue damage from the lumped load cases

Once a lumped load case H_s^{LC}-T_p^{LC} has been defined to represent a scatter diagram with a total probability of occurrence P_{SD_k}, the long-term fatigue damage can be calculated using Eq. 4.13:

$$D_{LT,SD}^{lumped} = N_y \cdot d_{ST}^{TD} \left(U_k, H_s^{LC}, T_p^{LC}\right) \cdot P_{SD_k}, \tag{4.13}$$

where d_{ST}^{TD} is the short-term fatigue damage obtained from 1-hour time-domain simulation and N_y is the specified design lifetime expressed in hours. Short-term damage estimates from time domain simulations strongly depend on wind and wave seed variability. Figure 4.12 illustrates this variability for damage estimates from 20 1-hour simulations with random seeds, for the same environmental condition. Variations up to ±20% from the average damage estimate (obtained from the 20 simulations) can be observed.

While the effect of seed variability is relatively low in full long-term fatigue assessments due to the large number of simulated sea states, it becomes more significant when a single load case is used to represent a scatter diagram.

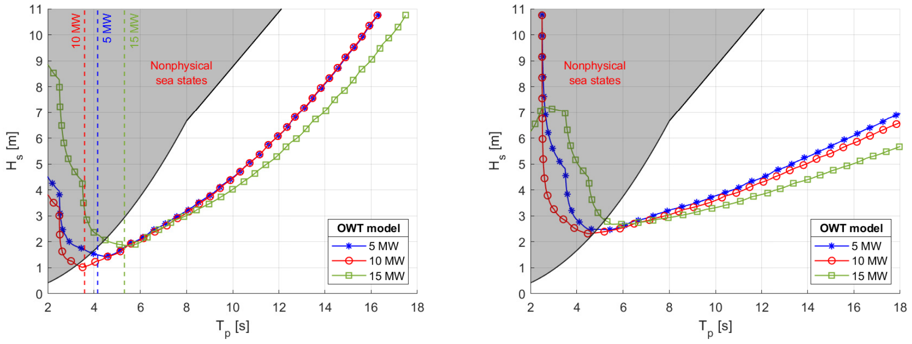

(a) Tower base contour lines (b) Mudline contour lines

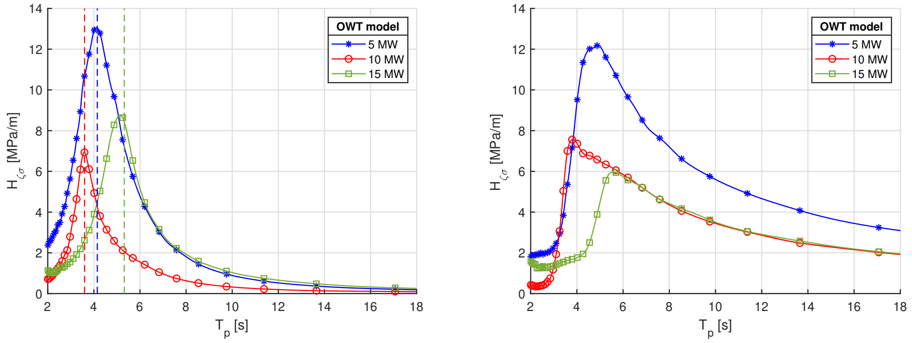

(c) Tower base stress transfer function (d) Mudline stress transfer function

Figure 4.11: DECLs and stress transfer at functions at tower base and mudline for the three OWT models. Wind class 18-20 m/s. [210]

In such cases, the statistical uncertainty is expected to increase. Therefore, several realizations of the lumped load case are required to obtain reasonable damage estimates [212].

To determine the number of simulations required to obtain reasonable fatigue damage estimates, the "modified coefficient of variation" (m.C.o.V) was used, by calculating the standard error over the mean for a given number of seeds. In this case, 20 1-hour simulations were conducted for the lumped load cases across various wind classes. Assuming that the true mean (μ_{20}) and standard deviation (σ_{20}) of the short-term damage can be estimated from the results of the 20 simulations, the standard error for a different number (n) of simulations (seeds) can be calculated as $\sigma_n = \sigma_{20}/\sqrt{n}$. The m.C.o.V is then defined as the ratio of σ_n to μ_{20}.

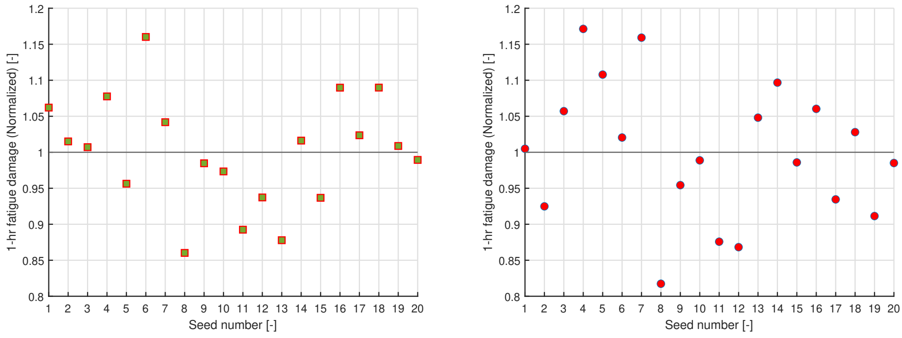

(a) Tower Base (b) Mudline

Figure 4.12: 1-hr damage from 20 simulations with random wind and wave seeds (U=17 m/s, H_s=2.78 m, T_p=7.32 s)

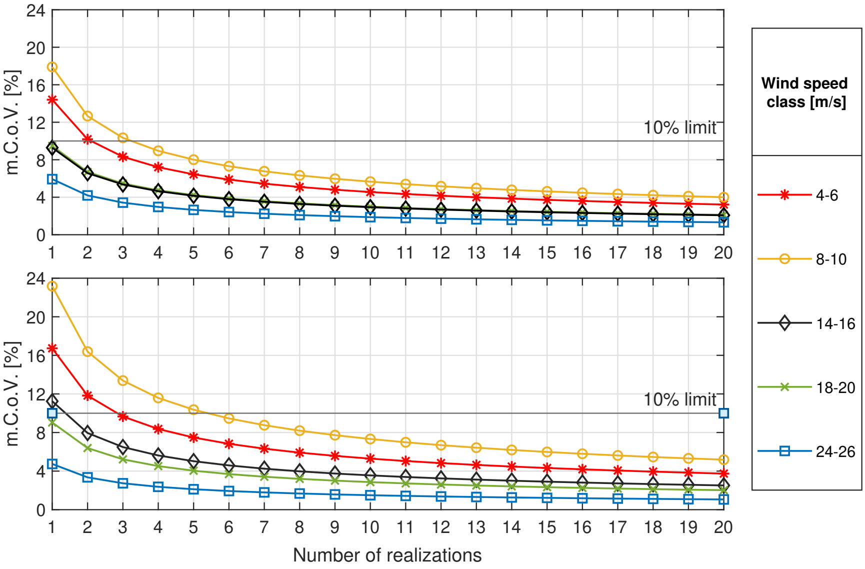

Figure 4.13: Statistical uncertainty of 1-hour damage as a function of number of realizations for the 10 MW OWT (Top: mudline - Bottom: tower base)

The fatigue damage was evaluated at the upwind position at both the mudline and tower base for the 10 MW OWT model. In Figure 4.13, the results for five wind classes are shown, indicating that the m.C.o.V varies between approximately 4.5% and 24% for a single simulation, and reduces gradually as more seeds are used. Higher stochastic variation was observed at the tower base, particularly for wind classes close to the rated speed. To achieve a reasonable compromise between accuracy and computational effort, an m.C.o.V cut-off limit of approximately 10% was set, and therefore five one-hour time-domain analyses were used for each lumped load case.

4.4 Lumping wind-sea and swell scatter diagrams

The previous sections described the damage-equivalent lumping method for co-directional scatter diagrams for the total sea representation. However, design standards [30] require multi-directional scatter diagrams for various DLCs, such as 1.2 (power production), 6.4 (idling due to wind speeds below cut-in or above cut-out) or 7.2 (parked within the operational range), where each wind class is divided into sectors with specified wind-wave direction. Furthermore, it is essential to consistently consider the individual contributions of wind-sea and swell components during FLS design. The following paragraphs outline the extension of the damage-equivalent lumping method to incorporate multi-directional scatter diagrams that include both wind-sea and swell components.

To establish multi-directional scatter diagrams, initially wind data and then wave data are split in $i_{\theta_u} = 1, ..., N_{\theta_u}$, and $i_{\theta_w} = 1, ..., N_{\theta_w}$ wind and wave directional sectors, respectively. Assuming wind-sea as the primary wave parameter, the probability of occurrence of a wind-sea sea state is given from Eq. 4.14,

$$P\left(H_{s,i}^{ws} \cap T_{p,j}^{ws} | U_k, \theta_{u,i_{\theta_u}}, \theta_{w,i_{\theta_w}}^{ws}\right) = \\ = P\left(H_{s,i}^{lb} \leq H_s^{ws} < H_{s,i}^{ub} \cap T_{p,j}^{lb} \leq T_p^{ws} < T_{p,j}^{ub} | U_k, \theta_{u,i_{\theta_u}}, \theta_{w,i_{\theta_w}}^{ws}\right). \tag{4.14}$$

Eq. 4.14 denotes the probability of occurrence of a wind-sea sea state $H_{s,i}^{ws} - T_{p,j}^{ws}$ in a scatter diagram that contains all occurrences under the concurrent conditions; wind speed $U \in [U_k^{lb}, U_k^{ub})$, wind direction $\theta_u \in [\theta_{u,i_{\theta_u}}^{lb}, \theta_{u,i_{\theta_u}}^{ub})$, and wave direction $\theta_w^{ws} \in [\theta_{w,i_{\theta_w}}^{lb}, \theta_{w,i_{\theta_w}}^{ub})$. The total probability of a wind-sea scatter diagram representative for a wind class k, wind direction class i_{θ_u}, and wind-sea direction class i_{θ_w} can be written in Eq. 4.15,

$$P_{SD_{k,\theta_u,\theta_{ws}}}^{ws} = \sum_{i=1}^{N_{H_s}} \sum_{j=1}^{N_{T_p}} P\left(H_{s,i}^{ws} \cap T_{p,j}^{ws} | U_k, \theta_{u,i_{\theta_u}}, \theta_{w,i_{\theta_w}}^{ws}\right). \tag{4.15}$$

Swell data are organized following the similar procedure, with an additional step to condition them with the wind-sea data. This is achieved by organizing the swell data in directional sectors for each wind-sea direction. As will be explained later, this will lead to consistently derived lumped load cases with unique probability of occurrence. The total probability of occurrence of swell scatter diagram can be expressed by Eq. 4.16,

$$P^{sw}_{SD_{k,\theta_u,\theta_{ws},\theta_{sw}}} = \sum_{i=1}^{N_{H_s}} \sum_{j=1}^{N_{T_p}} P\left(H^{sw}_{s,i} \cap T^{sw}_{p,j} | U_k, \theta_{u,i_{\theta_u}}, \theta^{ws}_{w,i_{\theta_w}}, \theta^{sw}_{w,i_{\theta_w}}\right). \quad (4.16)$$

Table 4.1: Organization of wind-sea and swell scatter diagrams for a wind class based on wind speed, wind, wind-sea, and swell direction.

θ_u	θ_u^{lb}	θ_u^{ub}	θ_w^{ws}	SD^{ws}	θ_w^{sw}	SD^{sw}
0	345	15	[0:30:330]	12	[0:30:330]	144
30	15	45	[0:30:330]	12	[0:30:330]	144
60	45	75	[0:30:330]	12	[0:30:330]	144
90	75	105	[0:30:330]	12	[0:30:330]	144
120	105	135	[0:30:330]	12	[0:30:330]	144
150	135	165	[0:30:330]	12	[0:30:330]	144
180	165	195	[0:30:330]	12	[0:30:330]	144
210	195	225	[0:30:330]	12	[0:30:330]	144
240	225	255	[0:30:330]	12	[0:30:330]	144
270	255	285	[0:30:330]	12	[0:30:330]	144
300	285	315	[0:30:330]	12	[0:30:330]	144
330	315	345	[0:30:330]	12	[0:30:330]	144

Assuming that the directional sectors are split in 30°, Table 4.1 demonstrates the organization of the relevant wind and wave parameters for one wind class in order to construct representative wind-sea and swell scatter diagrams for the lumping procedure. Within a given wind class and wind direction range, there are 12 wind-sea scatter diagrams (SD^{ws}) corresponding to specific direction ranges. Each scatter diagram represents wind-sea sea states within that particular direction range and has an associated total probability of occurrence $\left(P^{ws}_{SD_{k,\theta_u,\theta_{ws}}}\right)$.

Similarly, each wind-sea directional sector includes 12 swell scatter diagrams (SD^{sw}) representing swell sea states within specified direction ranges. These swell scatter diagrams are conditioned on the wind-sea direction. The damage-equivalent lumping method is applied for all non-zero wind-sea and swell scatter diagrams. The same procedure is followed as described in Sec. 4.3, except that the white noise wave excitation is applied with the required misalignment angle with respect to the uniform wind field, which is always applied in the fore-aft direction.

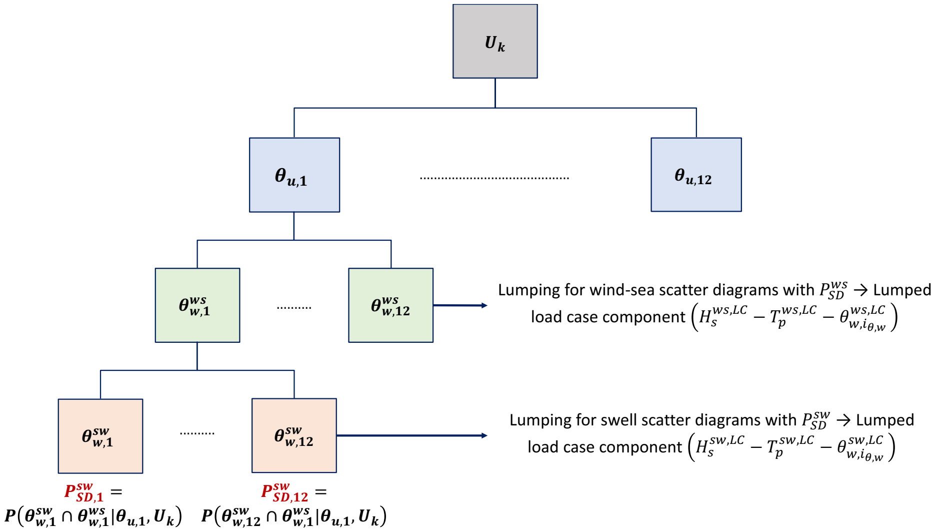

Figure 4.14: Organization wind-sea and swell data to derive representative lumped load cases for a wind class.

Figure 4.14 provides an illustration of how wind-sea and swell data are organized to perform the lumping process and derive representative lumped load cases comprising two wave components. The first component (C_1) represents the wind-sea scatter diagram with direction $\theta^{ws}_{w,i_{\theta_w}}$ and is defined by the sea state parameters $H_s^{ws,LC} - T_p^{ws,LC} - \theta^{ws}_{w,i_{\theta_w}}$. The second component ($C_2$) represents the swell scatter diagram with direction $\theta^{sw}_{w,i_{\theta_w}}$ and is defined by the sea state parameters $H_s^{sw,LC} - T_p^{sw,LC} - \theta^{sw}_{w,i_{\theta_w}}$.

The long-term fatigue damage, denoted as $D^{lumped}_{LT,SD}$, is calculated using Eq. 4.17, which incorporates the short-term damage $d^{TD}_{ST}(C_1, C_2)$ obtained from one realization in the aero-servo-hydro-elastic simulation tool. The short-term damage accounts for the two wave components (wind-sea and swell) with their representative sea-state parameters. The probability in Eq. 4.17 represents the joint probability of wind-sea data with direction $\theta^{ws}_{w,i_{\theta_w}}$ and swell data with direction $\theta^{sw}_{w,i_{\theta_w}}$, for a given wind speed (U_k) and wind direction $\left(\theta_{u,i_{\theta_u}}\right)$, as shown in Eq. 4.16.

$$D^{lumped}_{LT,SD} = N_y \cdot d^{TD}_{ST}(C_1, C_2) \cdot P^{sw}_{SD_{k,\theta_u,\theta_{ws},\theta_{sw}}} \tag{4.17}$$

Chapter 5

Results of lumping method for fatigue assessment

The chapter demonstrates the performance and validation of the damage-equivalent lumping method through comparison with full long-term fatigue assessment results. Initially, it shows the results for co-directional scatter diagrams of one wave component (combined sea), for the reference OWTs used in this thesis. Subsequently, the method's validation extends to wind-sea and swell components for a commercial project. The chapter also highlights the method's sensitivity across various aspects.

5.1 Results for co-directional scatter diagrams

Lumped load cases from damage-equivalent lumping method (DELM) were extracted using fully coupled and simplified models for the three OWTs. Then, the accuracy and computational time of the method were evaluated by comparing long-term fatigue damage estimates from lumped load cases and full long-term fatigue assessment (LTFA), using time-domain simulations.

The study considered wind classes ranging from 4 m/s to 30 m/s, with wind and waves acting in the fore-aft direction of the OWTs. The OWTs were operational for all wind classes, except for wind classes of 26-28 m/s and 28-30 m/s, where they were parked with their blades pitched at 90°. For each 1-hr simulation, a wind field was generated in TurbSim (Sec. 3.3.1.3), and a time-domain analysis with turbulent wind and irregular, long-crested waves was conducted in SIMA.

Random wind and wave seeds were used for each realization, and the first 400 s (transient response) were disregarded. Short-term damage from each time-domain simulation was calculated using rainflow counting method, as described in Sec. 3.3.1.5. Long-term damage was determined assuming Palmgren-Miner's linear damage accumulation rule. Table 5.1 summarizes the long-term fatigue assessment simulations for the two methods.

Table 5.1: Summary of long-term fatigue assessment for each OWT

	LTFA (Sec. 4.2)	DELM (Sec. 4.3)
Wind classes (13)	4-30 m/s	4-30 m/s
Wind/Wave direction	0°	0°
Sea state parameters	$H_{s,i} - T_{p,j}$	$H_s^{LC} - T_p^{LC}$
Simulations	~ 1020	13
Duration (excluding transient)	1h	1h
Random seeds per simulation	1	5

The wave kinematic theories and hydrodynamic load formulations used in the time-domain simulations are summarized in Table 5.2. The transition limits between the Airy linear theory and Stokes' 2$^{\text{nd}}$ order waves, as well as Morison's equation and MacCamy & Fuchs formulation, were determined by calculating wave loads on a rigid pile with a diameter of 9 m for various sea states. It was found that the Airy theory adequately represented wave loads for H_s up to 4.5 m. Additionally, by comparing the variance of the inertia loads calculated using Morison's equation were similar (approximately 5%) to those obtained using MacCamy & Fuchs formulation for peak wave periods T_p greater than 10 s. Based on Figure 2.7, which shows the inertia force coefficient as a function of frequency for the OWTs used in the thesis, the differences were negligible for T_p greater than 10 s (corresponding to f_p less than 0.1 Hz). Therefore, the same limits were assumed for all OWTs in the analysis.

Table 5.2: Load formulation and wave kinematics for simulations

	$T_p \leq 10$ s	$T_p > 10$ s
$H_s \leq 4.5$ m	MacCamy & Fuchs / Airy	Morison / Airy
$H_s > 4.5$ m	MacCamy & Fuchs / Airy	Morison / 2$^{\text{nd}}$ order

5.1.1 Observations from long-term fatigue assessment

The current section summarizes the results from LTFA, identifying the main response characteristics for each OWT. LTFA was performed by analyzing all sea state classes with a non-zero probability of occurrence in the scatter diagrams (Sec. 4.2). Figure 5.1 shows the long-term damage distribution at the mudline and tower base, over different wind classes.

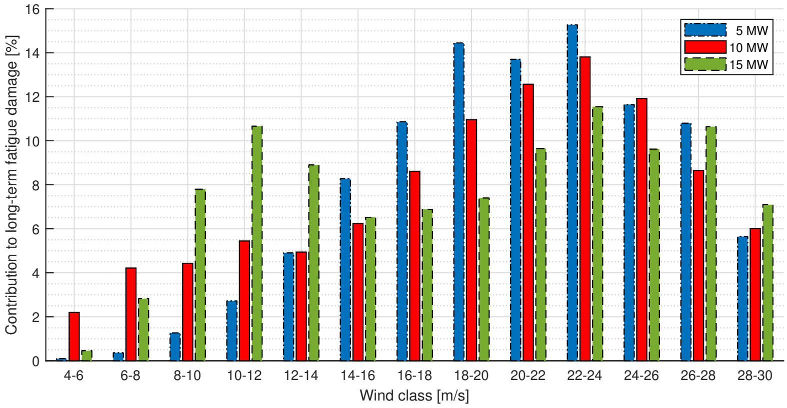

(a) Mudline

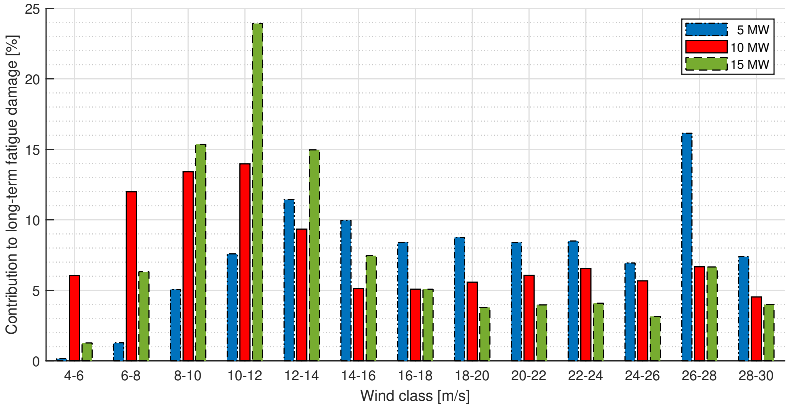

(b) Tower base

Figure 5.1: Long-term fatigue damage contribution over wind classes

The results show that wind classes near the rated speed contributed more to fatigue damage as the size of the turbine increases, indicating the higher importance of wind loads for larger OWTs. In particular, wind classes ranging from 8 m/s to 14 m/s contributed approximately 55% to the total fatigue damage at the tower base, while for the 10 MW and 5 MW turbines, the contributions were approximately 37% and 24%, respectively. The effect was less pronounced at the mudline, with relative contributions of approximately 27% (15 MW), 15% (10 MW), and 8% (5 MW) for the same wind classes. Figure 5.2 shows the axial stress spectra (grey lines) at the tower base for all sea states analyzed within the OWT scatter diagrams for wind class 8-10 m/s. The shaded area represents the range of peak frequencies of the sea states analyzed, and the vertical lines indicate the fore-aft first bending natural frequency, and the excitation frequencies from the operating rotor. For wind classes particularly in the vicinity of the rated speed, significant differences in slowly-varying wind-induced responses ($f \lesssim 0.05$ Hz) were observed for the 15 MW turbine. The variance (area) of the stress spectra for $f \lesssim 0.05$ Hz was calculated from the time-domain simulations for all wind classes to quantify this effect, and the results are shown in Figure 5.3. For the 15 MW turbine, the slowly varying wind process, which dominates the low-frequency components of the time series, is significantly higher than for the other turbines at the tower base, particularly around the rated speed, while minor differences are observed at the mudline. Similar results were observed for the 15 MW responses close to 3P excitation, although it is challenging to isolate the load processes at this frequency range.

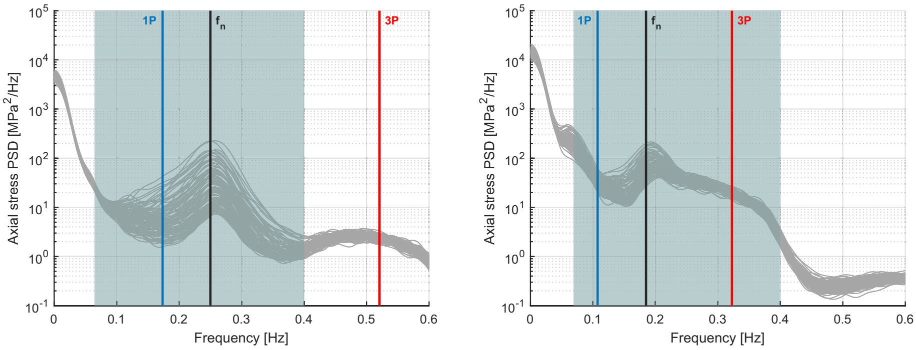

(a) 5 MW (b) 15 MW

Figure 5.2: Stress spectra (logarithmic scale) at tower base for all sea states analyzed within the scatter diagram for wind class 8-10 m/s. Shaded region represents the range of peak frequencies considered.

Figure 5.1 indicates a relatively high contribution of fatigue damage for the 10 MW turbine at wind speeds below 8 m/s. This is attributed to the operating characteristics of the 10 MW rotor, which operates at a constant frequency (1P) of 0.1 Hz (6 rpm) for these wind speeds. Consequently,

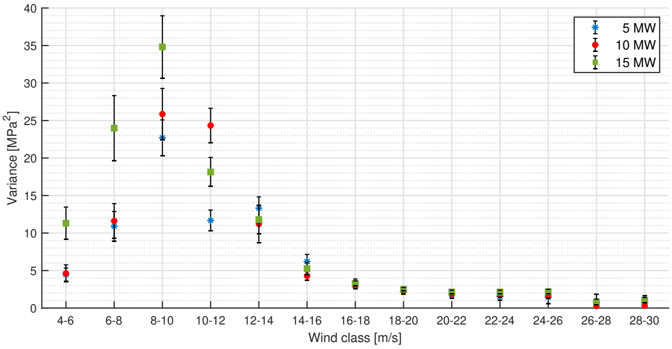

(a) Mudline

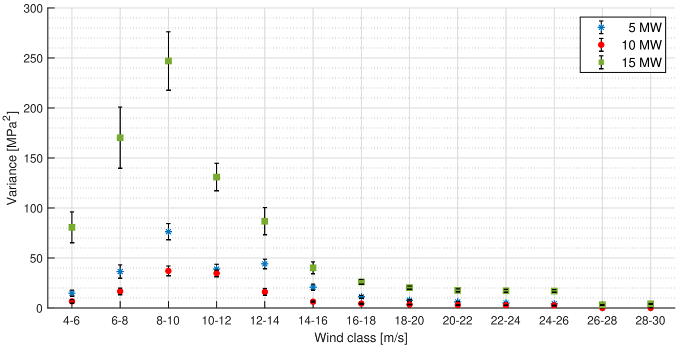

(b) Tower base

Figure 5.3: Variance (area) of the stress spectra for $f \lesssim 0.05$ Hz from the time-domain simulations for all wind classes.

the 3P excitation (0.3 Hz) is close to the first natural frequency of the support structure (0.28 Hz), causing resonance effects and contributing more to fatigue damage. This is depicted in Figure 5.4, which illustrates the axial stress spectra at the tower base for all sea states analyzed within the scatter diagrams for wind class 6-8 m/s. The high-frequency peaks due to the operating rotor are also evident.

Furthermore, Figure 5.1a reveals an increasing contribution of fatigue damage at the mudline for wind speeds ranging from 14 m/s to 24 m/s. The damage contribution increases from approximately 6-8% to 12-16% depending on the OWT. Higher wind speeds are associated with more severe sea states, leading to increased hydrodynamic loads and subsequent bending moments and stresses. As a result, wave loads gradually become more significant for lower cross-sections along the monopile due to the increased moment arm,

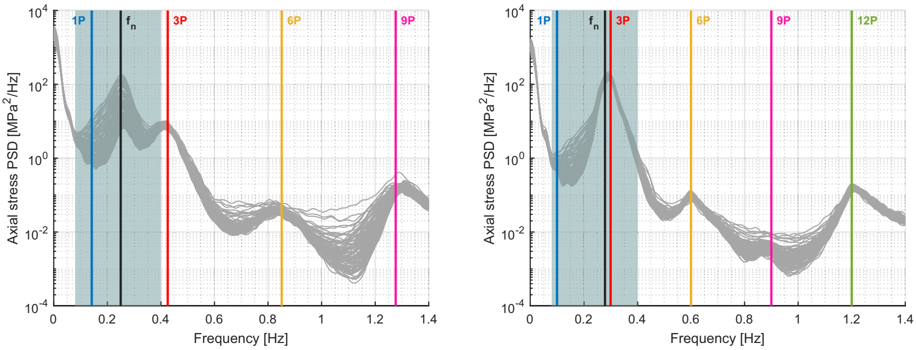

(a) 5 MW (b) 10 MW

Figure 5.4: Stress spectra (logarithmic scale) at tower base for all sea states analyzed within the scatter diagram for wind class 6-8 m/s. Shaded region represents the range of peak frequencies considered.

thereby dominating the fatigue responses. In contrast, for the tower base (Figure 5.1b), those classes contribute approximately 5-10% depending on the OWT, with no specific trend observed. For example, Figure 5.5 illustrates the sea states analyzed within the 20-22 m/s class of the 15 MW turbine. The stress responses at the mudline are primarily dominated by wave excitation frequencies, whereas the tower base primarily vibrates in the vicinity of the first natural frequency, with the peak responses varying depending on the severity of the sea state.

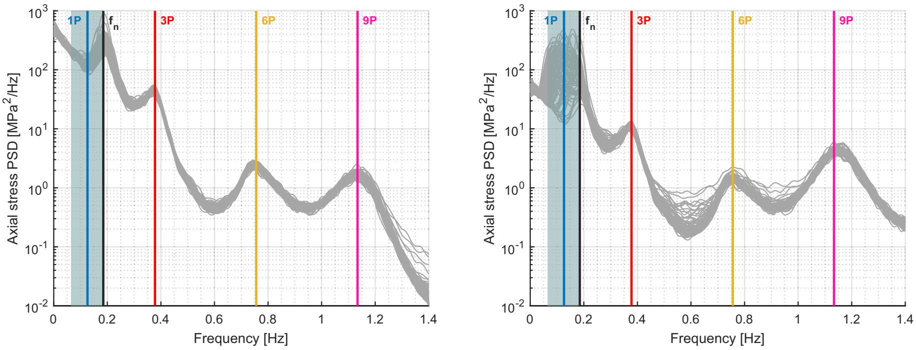

(a) Tower base (b) Mudline

Figure 5.5: Stress spectra (logarithmic scale) for all sea states analyzed within the scatter diagram for wind class 20-22 m/s (15 MW). Shaded region represents the range of peak frequencies considered.

For wind classes higher than 24 m/s, the low probability of occurrence dominates the contribution to the accumulated fatigue damage, and a decreasing trend is observed for all wind turbines. Nevertheless, despite the low probability, these wind classes still have a notable impact on long-term fatigue damage, particularly at the mudline, due to the relatively low or negligible aerodynamic damping above cut-out speed, combined with the severity of the sea states in those wind classes (most probable H_s classes within the wind class are between 4.5 m and 6 m). In these wind classes, vibrations around the natural frequency dominate the response at both locations along the OWT. At the mudline, responses in the wave excitation frequency also play a significant role. This is illustrated in Figure 5.6, which depicts the sea states analyzed within the 28-30 m/s wind class for the 10 MW turbine.

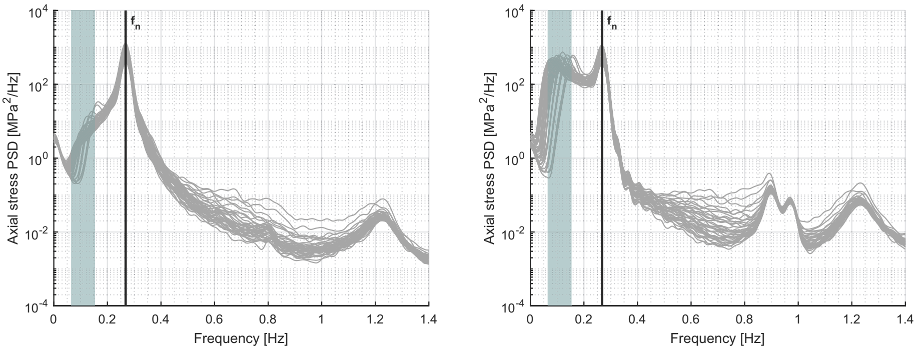

(a) Tower base

(b) Mudline

Figure 5.6: Stress spectra (logarithmic scale) for all sea states analyzed within the scatter diagram for wind class 28-30 m/s. Shaded region represents the range of peak frequencies considered.

5.1.2 Lumped load cases, accuracy, and computational time

The lumping method was applied to the three OWTs for co-directional scatter diagrams to generate lumped load cases representative for each wind class. The section summarizes the lumped load cases for each OWT model, and the accuracy of the fatigue damage obtained from the lumped load cases (DELM) compared to the full-scatter assessment (LTFA). The long-term damage estimates for different locations along the support structure are compared across the various wind classes for each OWT. Results are shown for the load cases extracted using fully-coupled and simplified models.

Figures 5.7 and 5.8 illustrate the sea state parameters (H_s^{LC}, T_p^{LC}) of the lumped load cases, as obtained using the fully coupled and simplified models. For each wind class, H_s^{LC}, and T_p^{LC} are shown together with the probability of occurrence of H_s and T_p classes, scaled to the total wind class probability. The colour and size of the markers represent the relative magnitude of the probabilities for each class.

Across all OWTs and wind classes, the H_s^{LC} was found in the proximity of the most probable H_s class, increasing from low to high wind speeds due to the larger probability of severe sea states. The H_s^{LC} values were similar for the three OWTs, with differences arising solely from the distribution of sea states in the scatter diagrams, which were based on the hub height wind speeds at 90 m (5 MW), 119 m (10 MW), and 150 m (15 MW). Specifically, the same wind speed at a lower hub height is associated with more severe sea states, resulting in scatter diagrams with relatively higher probabilities for higher H_s classes. This effect becomes pronounced for higher wind speeds, explaining the increasing H_s values from the 15 MW to the 5 MW OWTs.

The T_p^{LC} values generally follow a similar pattern, influenced by two factors. Firstly, for intermediate and high wind classes, where more severe sea states are present in the scatter diagrams (reflected in larger H_s^{LC} values), larger T_p values are observed. This leads to slightly larger T_p^{LC} values for the 5 MW model compared to the 10 MW and 15 MW models for the same reasons as given above. For the lower wind classes, the dynamic characteristics of the OWTs have a more significant impact on the resulting T_p^{LC} values. In particular, the peak period is about 1 s larger for the 15 MW model, attributed to its natural period being approximately 1.5 seconds longer, and thus affecting the distribution of scaled unit damage.

Comparing the load cases obtained using the fully coupled and simplified models, a strong agreement was observed for all OWTs. The differences in H_s^{LC} ranged from 0.05 m (4%) to 0.2 m (16%), while the differences in T_p^{LC} ranged from 0.1 s (2%) to 0.4 s (8%). The largest discrepancies were found for wind classes below and near the rated speed, particularly for the 15 MW model. This is due to the simplified representation of the control system, which becomes particularly significant for those wind classes.

Figures 5.9 (mudline) and 5.10 (tower base) show a comparison of the long-term fatigue damage between the full scatter assessment (LTFA) and the lumped load cases obtained using fully coupled and simplified models for the

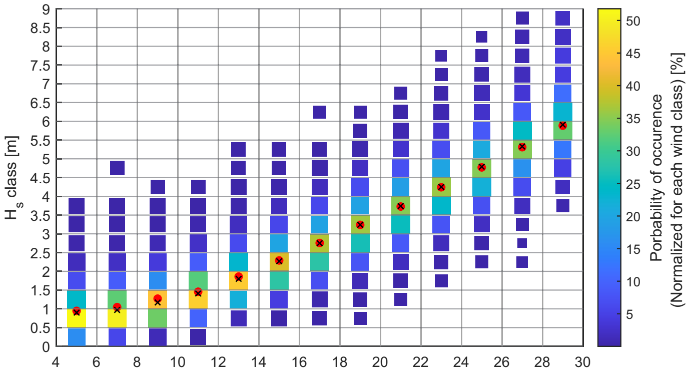

(a) 5 MW

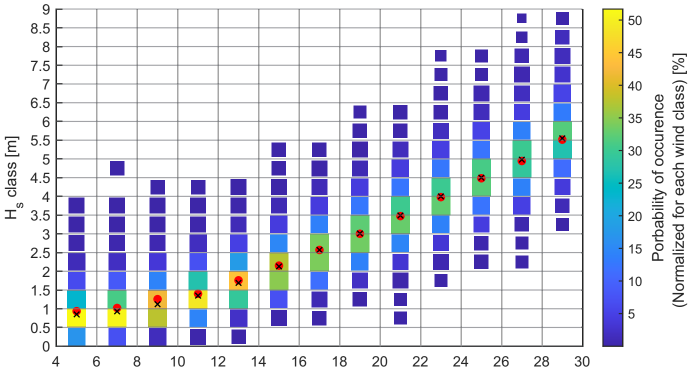

(b) 10 MW

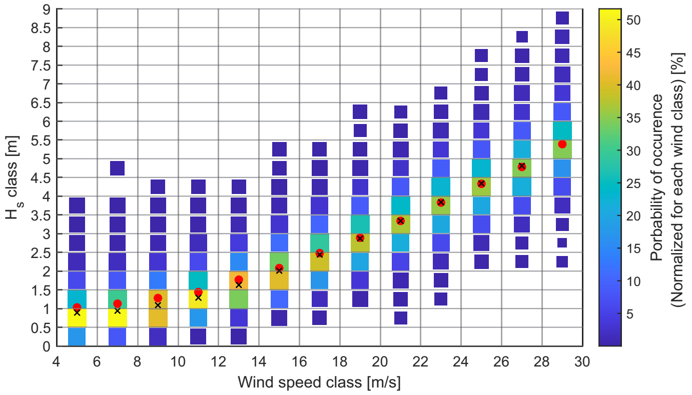

(c) 15 MW

Figure 5.7: H_s^{LC} as derived using fully coupled (red marker) and simplified (black marker) models, compared to the probability of occurrence of H_s classes within the scatter diagrams.

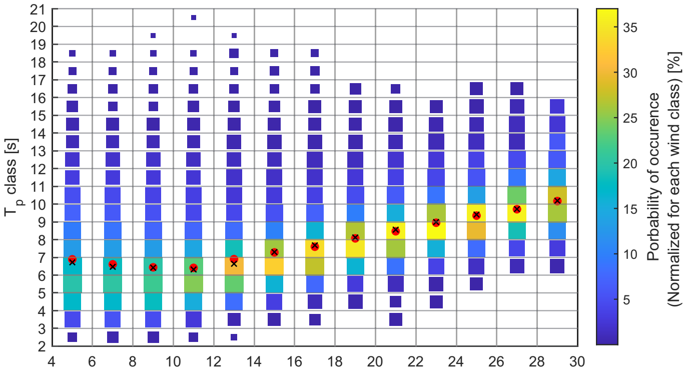

(a) 5 MW

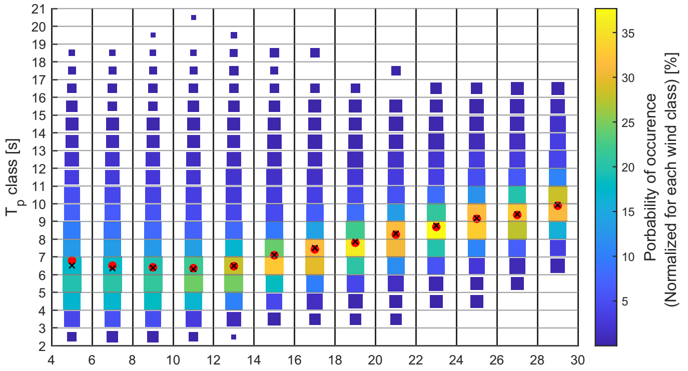

(b) 10 MW

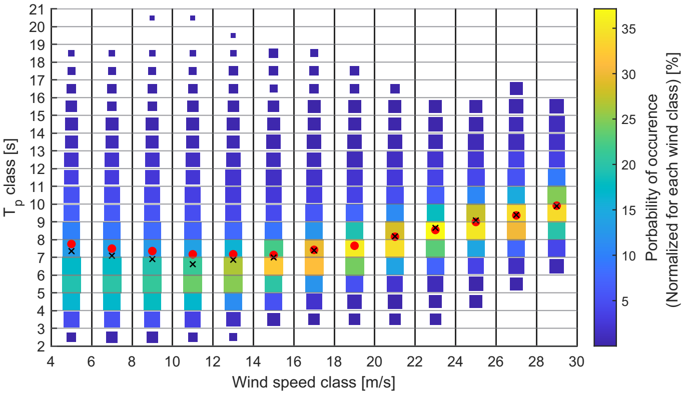

(c) 15 MW

Figure 5.8: T_p^{LC} as derived using fully coupled (red marker) and simplified (black marker) models, compared to the probability of occurrence of T_p classes within the scatter diagrams.

three OWTs. For the lumped load cases, each bar represents the mean long-term fatigue damage from the five time-domain realizations (see Sec. 4.3.3), and the error bars indicate the standard deviation. Fatigue values are normalized to the results from LTFA. Comparisons for the individual wind classes and the total (summation over the wind classes) are shown.

Overall, there was a generally good agreement between the lumped load cases and the full scatter results for individual wind classes, capturing the behaviour of long-term fatigue damage across different wind speeds. For all OWTs in the operational state, the relative differences between the lumped load cases and LTFA results mostly ranged between ±10-15%. The stochastic variability in the time-domain realizations of the lumped load cases, represented by the error bars, can explain most of the differences observed between DELM and LTFA. Additionally, the damage estimates for parked states were sensitive to the chosen wave kinematics model, which became increasingly important in the absence of aerodynamic damping. This effect was pronounced at the tower base and for locations close to SWL, and can be clearly seen in the comparisons in Figures 5.10a and 5.10b. Similar findings have been reported in previous studies [178, 179]. Specifically, for the parked states of the 5 MW OWT, the lumped load cases analyzed using 2$^{\text{nd}}$ order waves overestimated the damage by approximately 40%, while for the 10 MW OWT, the use of Airy theory underestimated significantly damage estimates by approximately 70%. The effect was also observed at the mudline, although to a lesser extent. For the total damage, differences between the results remained relatively stable. At the mudline, the variations were mostly within ±5%, falling within the range of stochastic variability.

Figure 5.11 provides an overview of the accuracy of damage estimates along the OWTs when comparing the results obtained from the lumped load cases to those from the full scatter assessment. The comparison includes the monopile location where the maximum damage occurs. A negative difference indicates that the damage calculated by the lumped load cases underestimates the actual damage, while a positive difference implies an overestimation. Below the mudline, the relative difference in long-term fatigue damage ranges from -6% to +1%, indicating that the lumped load cases generally underestimate or overestimate the damage by a small margin. These variations below the mudline are similar to those observed at the mudline.

The previous paragraphs primarily focused on damage comparisons for the tower base and the mudline. However, the objective of the DELM is to extract lumped load cases that can accurately determine the fatigue damage

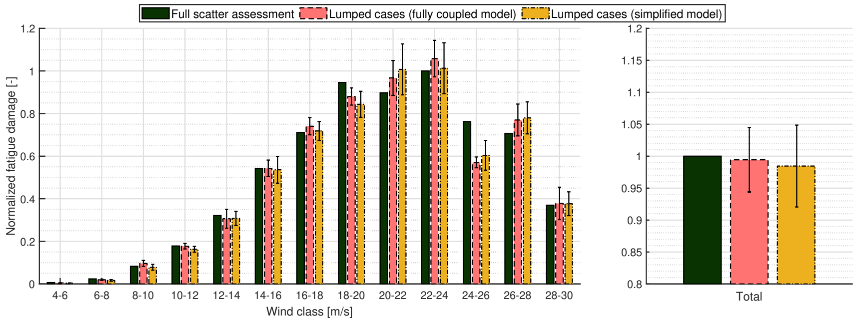

(a) 5 MW

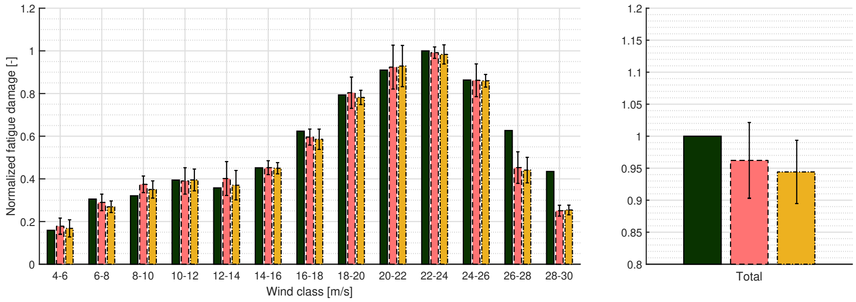

(b) 10 MW

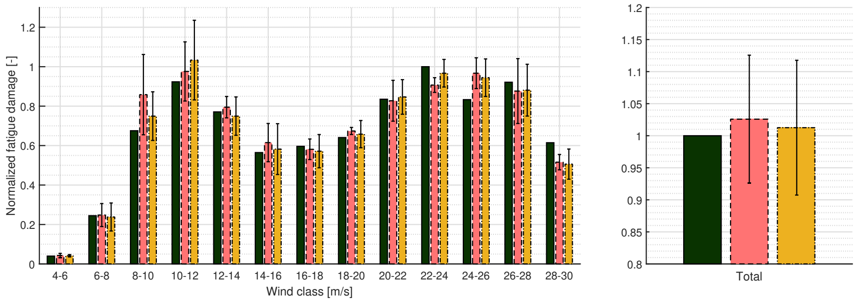

(c) 15 MW

Figure 5.9: Long-term fatigue damage comparison at mudline between full scatter assessment and lumped load cases obtained using fully coupled and simplified models

for the entire support structure. Figure 5.12 illustrates the total fatigue damage along the support structure for the three OWTs, with the values normalized to the maximum damage, confirming that the lumped load cases successfully capture the response characteristics along the OWTs. Moreover, similar results were observed for the damage estimated from the lumped load

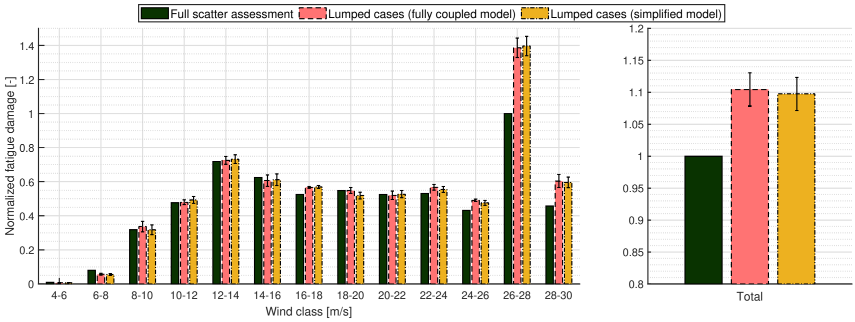

(a) 5 MW

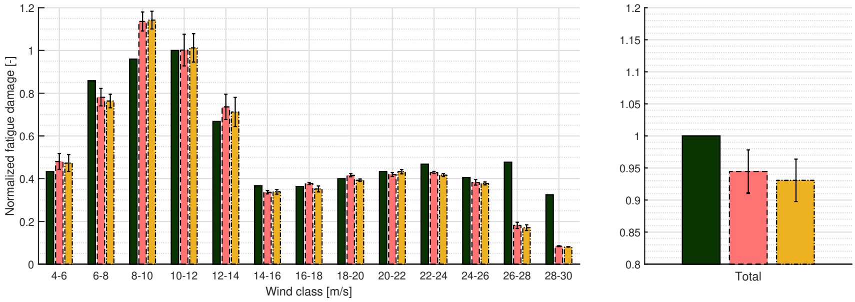

(b) 10 MW

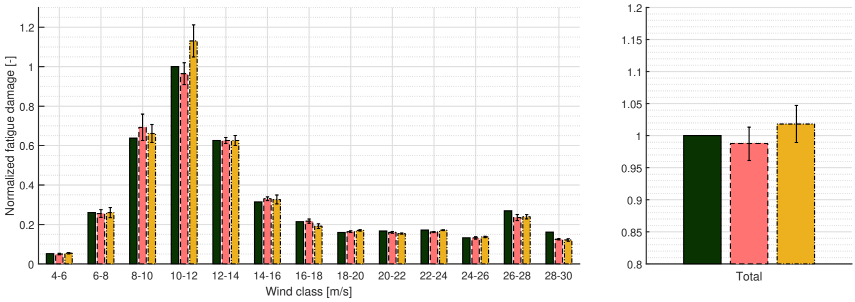

(c) 15 MW

Figure 5.10: Long-term fatigue damage comparison at tower base between full scatter assessment and lumped load cases obtained using fully coupled and simplified models

cases obtained using fully coupled and simplified models. Consequently, given that simplified models of reasonable accuracy are available, they can be used in conjunction with fully coupled time-domain models to apply the DELM and estimate long-term fatigue damage.

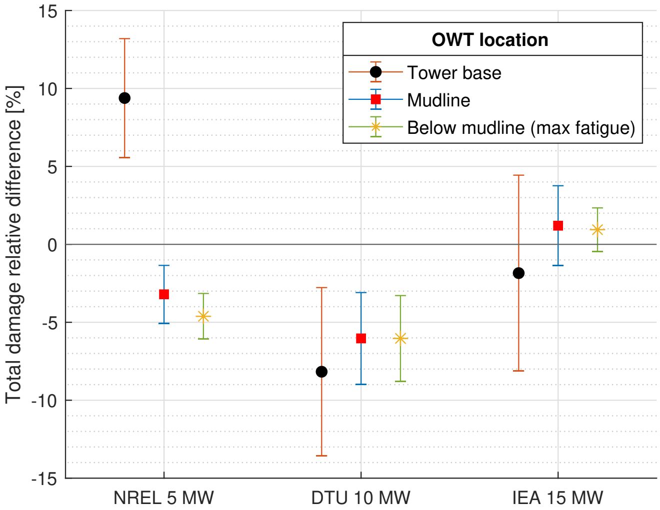

Figure 5.11: Total fatigue damage relative difference between DELM and LTFA for the three OWTs. Comparison at the angular position of the maximum damage around the circumference.

5.2 Sensitivity of lumped LCs to different factors

In the subsequent sections, variations in the dynamic characteristics of the structure and site-specific environmental conditions are examined to assess their impact on the derived lumped load cases. Additionally, the influence of the duration of white noise on the stress transfer functions and the resulting load cases is investigated.

5.2.1 Monopile design

The sensitivity of the lumped load cases to variations in monopile characteristics for the 10 MW OWT model was evaluated in this section. The primary parameters considered for monopile design are the embedded length, diameter, and thickness. To assess the sensitivity of the lumped load cases to different embedded lengths, five designs with different L_p/D_p ratios were tested. The diameter (D_p) and the thickness (t_p) were kept constant at 9 m, and 0.11 m. The lumping procedure was applied using fully-integrated time domain models. Figure 5.13 presents the first fore-aft natural frequencies and global damping ratios obtained from free decay tests. It is observed that higher load levels lead to lower natural frequencies due to the lower

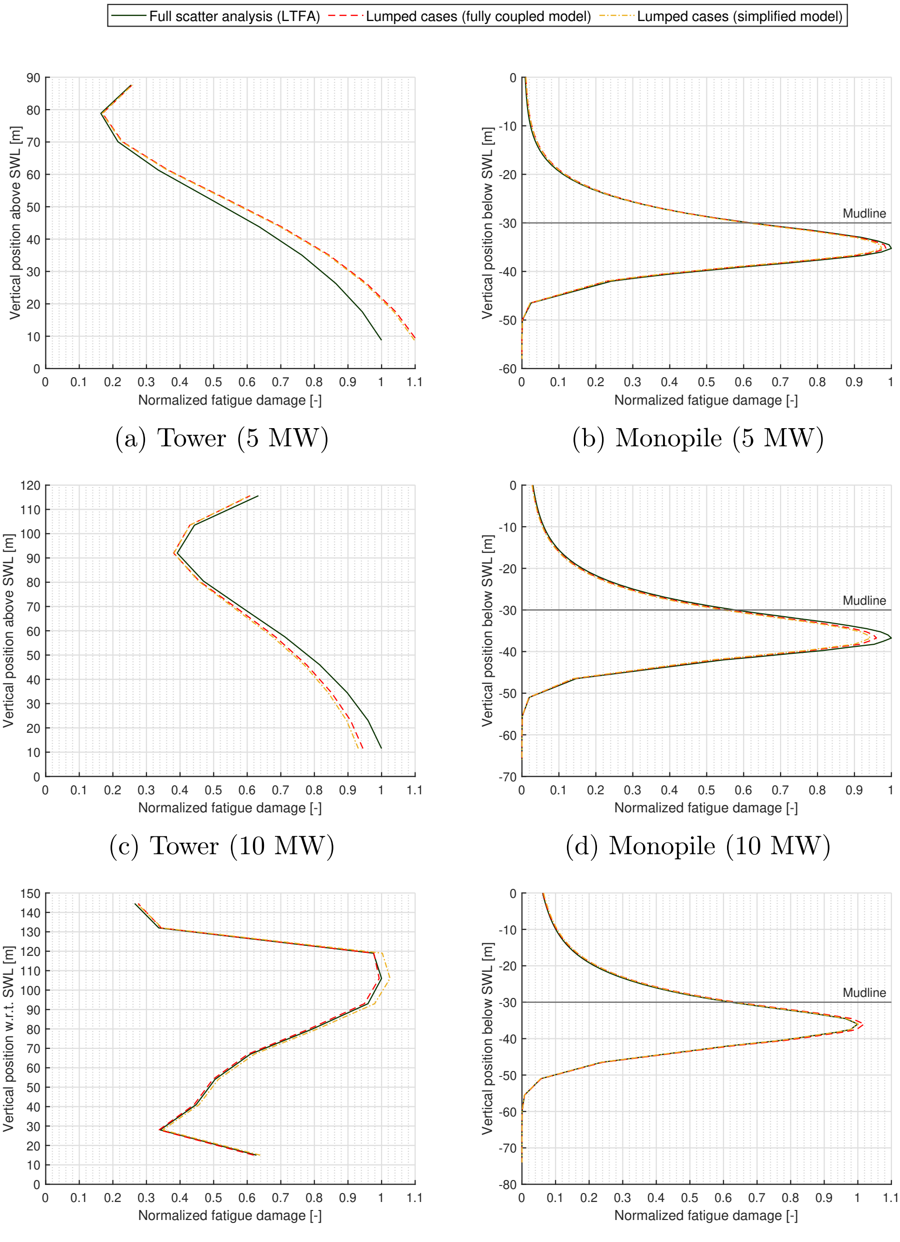

(a) Tower (5 MW)

(b) Monopile (5 MW)

(c) Tower (10 MW)

(d) Monopile (10 MW)

(e) Tower (15 MW)

(f) Monopile (15 MW)

Figure 5.12: Comparison of total long-term fatigue damage along the support structure between full scatter assessment and lumped load cases.

foundation stiffness, while larger global damping ratios result from the representation of hysteretic damping in the macro-element (further explained in Chapter 6).

Contour lines were similar for all the models, with slight variations in the region of the natural frequency, due to the differences in dynamic properties among the models. Lumped load cases with negligible variations were obtained for all wind classes within the operational range, as shown in Figure 5.14, indicating that the variations in the monopile embedded length had minimal impact on the derived lumped load cases.

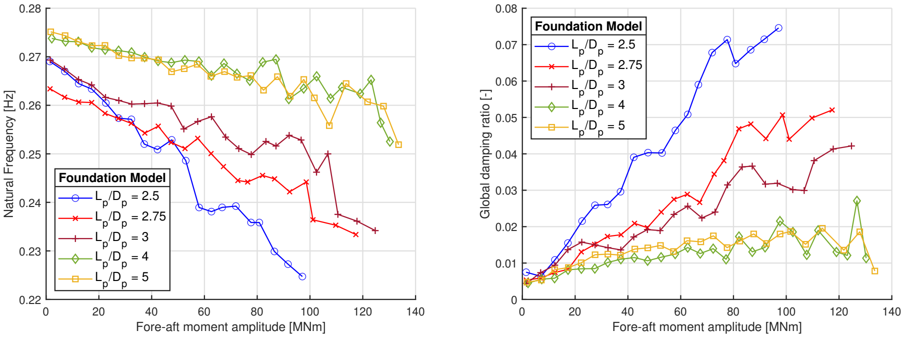

(a) Natural frequencies (b) Global damping ratios

Figure 5.13: Natural frequency and global damping ratio of the foundation models from free-vibration test [212]

To assess the sensitivity of the lumped load cases to variations in the monopile diameter (D_p) and thickness (t_p), the simplified model of the 10 MW OWT was used. To cover a range of frequencies within the soft-stiff design range of the turbine ($\sim 0.16 - 0.30$, Figure 1.12), different points were selected with a constant D_p/t_p ratio equal to 100, as illustrated in Figure 5.15. Table 5.3 summarizes the chosen points, and their natural frequency. It is noted that the soil stiffness is assumed to be the same for all the models and taken as the linear stiffness of the base case model (D_p =9 m t_p =0.11 m).

The different natural frequencies of the models were reflected in the contour lines obtained at the tower base, as shown in Figure 5.16 for wind class 10-12 m/s. The vertical lines represent the natural periods of the models. Figure 5.17 shows the lumped load cases for the various models across all wind classes. In terms of H_s^{LC}, similar values were observed for all the models, with variations ranging from 0.02 m to 0.18 m, without any specific

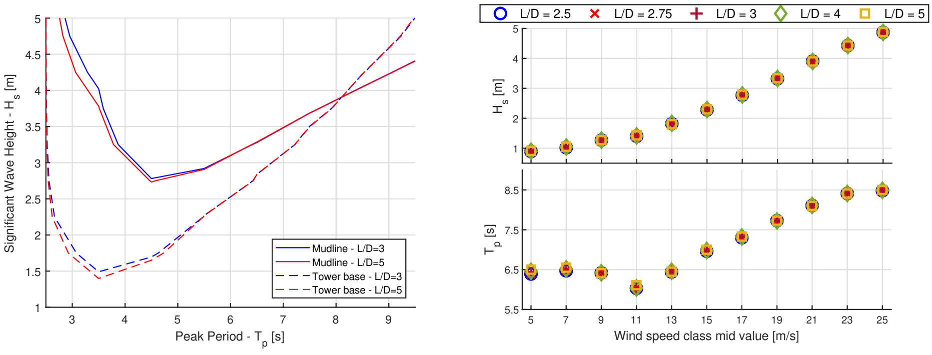

(a) Contour lines (b) Lumped $H_s - T_p$

Figure 5.14: (a) Contour lines of two foundation models for wind class 18-20 m/s (b) Lumped sea state parameters of each foundation model per wind class in operational range [212]

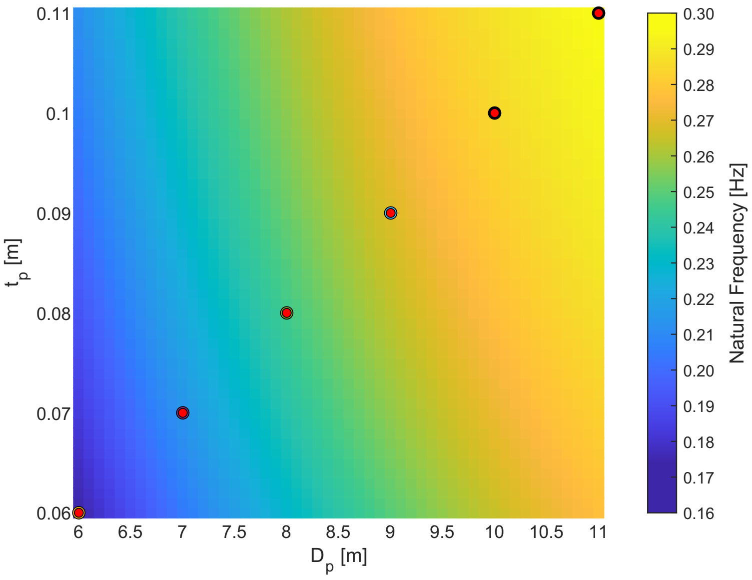

Figure 5.15: Variation of natural frequency with monopile diameter and thickness within the soft-stiff design range of 10 MW OWT

trend with respect to wind classes. T_p^{LC} varied between 0.04 s and 0.3 s between models M2-M6, while for model M1, differences from 0.2 s up to 0.75 s were found.

Table 5.3: Models to evaluate the sensitivity of the lumped load cases on variations of monopile diameter (D_p) and thickness (t_p)

Point -	D_p m	t_p m	Eigenfrequency Hz	Eigenperiod s
M1	6.0	0.06	0.1737	5.757
M2	7.0	0.07	0.2139	4.675
M3	8.0	0.08	0.2455	4.073
M4	9.0	0.09	0.2686	3.723
M5	10.0	0.10	0.2848	3.511
M6	11.0	0.11	0.2959	3.379

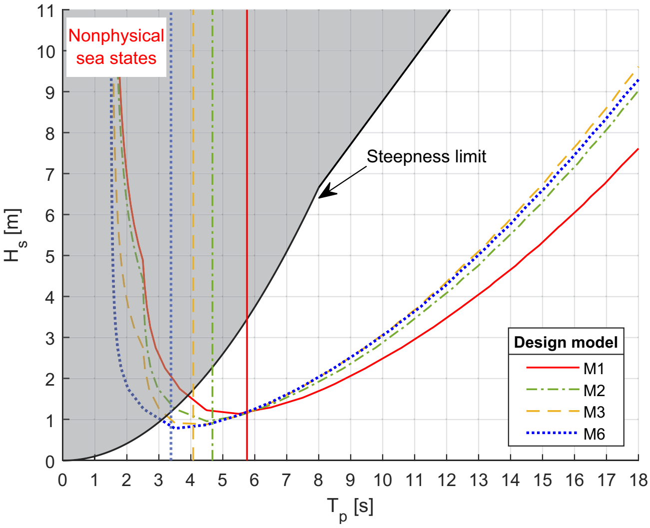

Figure 5.16: Contour lines at tower base for four models

It can be concluded that monopile design variations within the soft-stiff range, which can affect the natural period of the structure by approximately 1 s, will not significantly impact the derived T_p^{LC}. Therefore, similar lumped sea states can be used, especially in the early design phases, considering that the observed variations fall within this range. However, for more substantial differences, such as variations of up to 2.5 s (as seen in model M1), the dynamic characteristics of the structure gradually become more important, resulting in more notable changes in T_p^{LC}, and therefore it is recommended to update the lumped LCs to reflect the changes in design.

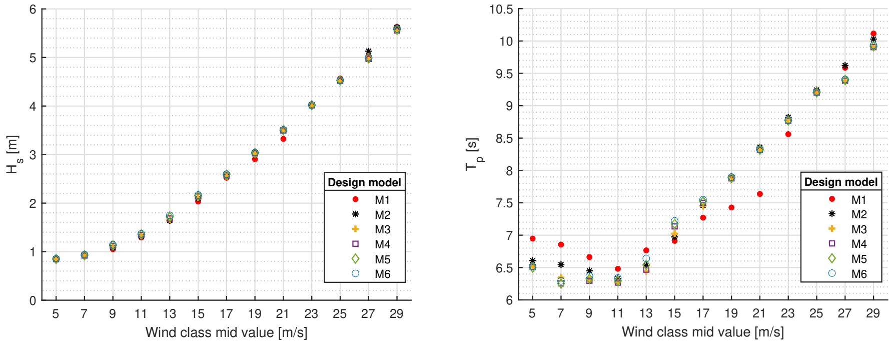

(a) H_s^{LC} (b) Lumped T_p^{LC}

Figure 5.17: Lumped load cases for the different design points (Table 5.3)

5.2.2 Environmental variability

Due to the inherent variability of the offshore environment, metocean conditions vary each year even for the same site, as shown in Figure 5.18 for the annual and 60-year empirical marginal distributions of U_{119}, H_s, and T_p. The lumping process takes into account this long-term variability by using scatter diagrams, and as a result, variations in the lumped load cases are expected. This section investigates how the lumped load cases vary using the annual scatter diagrams, each established from the annual data between 1958 and 2017, with the results illustrated in Figure 5.19.

A single white noise simulation was performed for each wind class, and the same stress transfer functions were used in the lumping process for all years. Therefore, the only parameter that varies is the distribution of sea states in the scatter diagrams, represented by $P(H_{s,i} \cap T_{p,j}|U_k)$, and the total probability of occurrence P_{SD} associated with a scatter diagram for a specific wind class. The metocean variability affects the calculation of $D_{LT,target}$ through the use of $P(H_{s,i} \cap T_{p,j}|U_k)$ in Eq. 4.10, and $D_{U,scale}$ through the use of P_{SD} in Eq. 4.11.

The variability in the metocean data leads to different lumped LCs, primarily driven by the distribution of sea states within the scatter diagrams. Generally, for most wind classes, H_s^{LC} varied between 0.15 m and 0.3 m, while larger variations (0.7 m to 1.5 m) were observed for higher wind speeds. Similarly, T_p^{LC} varied between 0.5 s and 1.5 s, with differences of up to 2 s for wind classes 26-28 m/s and 4 s for 28-30 m/s.

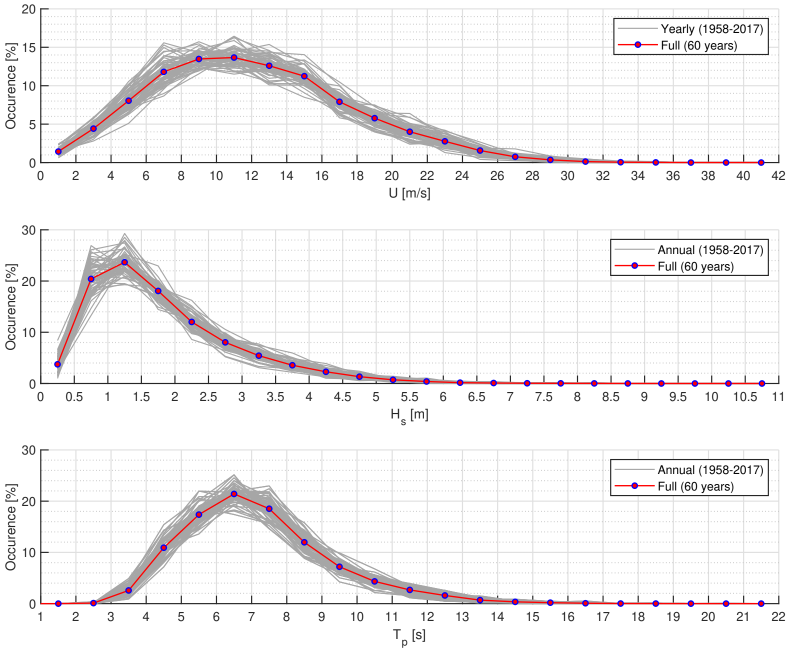

Figure 5.18: Annual and total (60 years) distributions of site-specific metocean conditions (NORA10 dataset)

The larger spread of the lumped LCs in these classes is due to the relatively small number of sea states present in the scatter diagrams, making it increasingly important how they are distributed within the scatter diagram for deriving the lumped sea states. Additionally, Figure 5.19 indicates a positive correlation between H_s^{LC} and T_p^{LC} for all wind classes, with correlation coefficients ranging from 0.85 to 0.95, which aligns with the physical behaviour of waves where larger wave heights are generally associated with longer periods. Results depict the high sensitivity to annual variation in offshore conditions conditions, highlighting the uncertainty in fatigue damage estimates using annual data.

5.2.3 Numerical variation

The damage-equivalent lumping method using fully-integrated time-domain models requires a white noise simulation to extract representative transfer functions (as discussed in Sec. 4.3.1). For the results presented in the thesis and the attached papers, a white noise simulation duration of 3 hours was

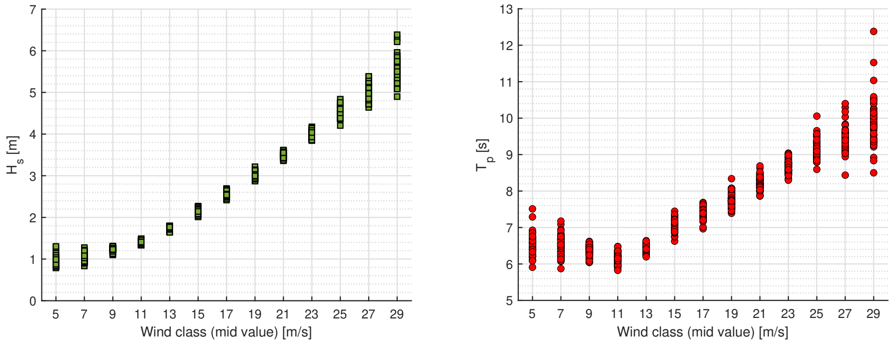

(a) Lumped H_s^{LC} (b) Lumped T_p^{LC}

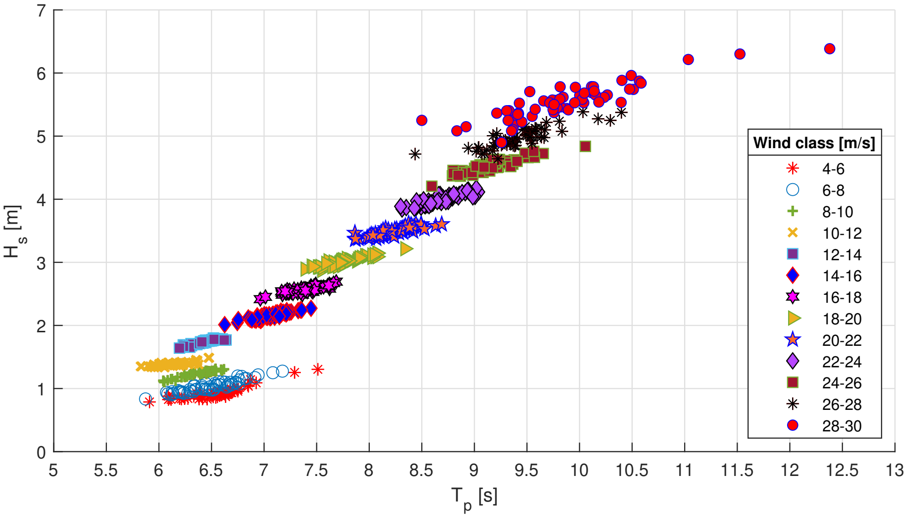

(c) Lumped load cases $H_s^{LC} - T_p^{LC}$ for different wind classes

Figure 5.19: Lumped sea state parameters and LCs from the annual scatter diagrams between 1958-2017

chosen. This duration ensures that the signal has approximately equal wave energy, i.e., constant power spectral density, over the frequency range.

The white noise simulation is computationally demanding, and therefore, reducing its duration without compromising the accuracy of the resulting lumped load cases would be highly beneficial. However, decreasing the duration of the white noise simulation leads to significant variations in the wave spectrum over the frequency range.

Figure 5.20 provides an example of wave spectra for a white noise signal with the same wave amplitude. Figure 5.20a demonstrates how the wave spectra vary with signals of different duration, while Figure 5.20b illustrates the variability of the wave spectra from four 10-minute white noise simulations with different random seeds. To evaluate the effect of the white noise duration on the stress transfer functions $H_{\zeta\sigma}$ and the resulting lumped load cases $H_s^{LC} - T_p^{LC}$, the lumping procedure was applied with different duration (1 min, 10 min, 1 hour, 3 hours, 6 hours) for three wind classes (8-10 m/s, 18-20 m/s, 26-28 m/s) using the 10 MW OWT model. Figure 5.21 shows the $H_{\zeta\sigma}$ obtained from the white noise simulations for the 18-20 m/s class.

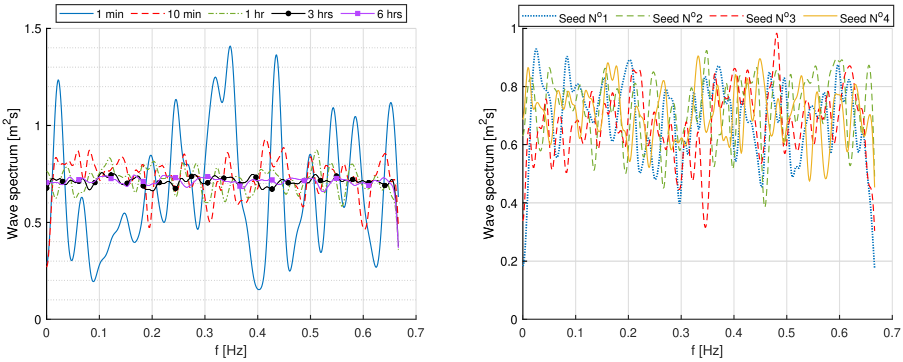

(a) Simulation duration

(b) Seed variability

Figure 5.20: White noise variation with (a) duration (b) seed variability (for 10 min duration)

For the 1-minute duration, 60 random seeds were analyzed, but the resulting $H_{\zeta\sigma}$ was found inadequate in capturing the dynamic response, particularly the wave response at mudline, due to high sensitivity to the wave spectrum dependency on the seed. The 10-minute simulations produced reasonable $H_{\zeta\sigma}$, accurately capturing the dynamic response at both locations along the OWT with slight variations. For longer simulation durations, the variability due to seed dependency became negligible. Similar results were also observed for the other wind classes.

Using the obtained $H_{\zeta\sigma}$, the lumped load cases $H_s^{LC} - T_p^{LC}$ were extracted for the three wind classes, as shown in Figure 5.22. In the 1-minute cases, a relatively large variation was observed in the lumped parameters, with a coefficient of variation ranging from 2% to 5% for H_s^{LC} and 1% to 3% for T_p^{LC}. Extending the white noise simulation duration to 10 minutes significantly reduced the variation of H_s^{LC} and T_p^{LC} to a range of 0-0.1 m and 0-0.1 s,

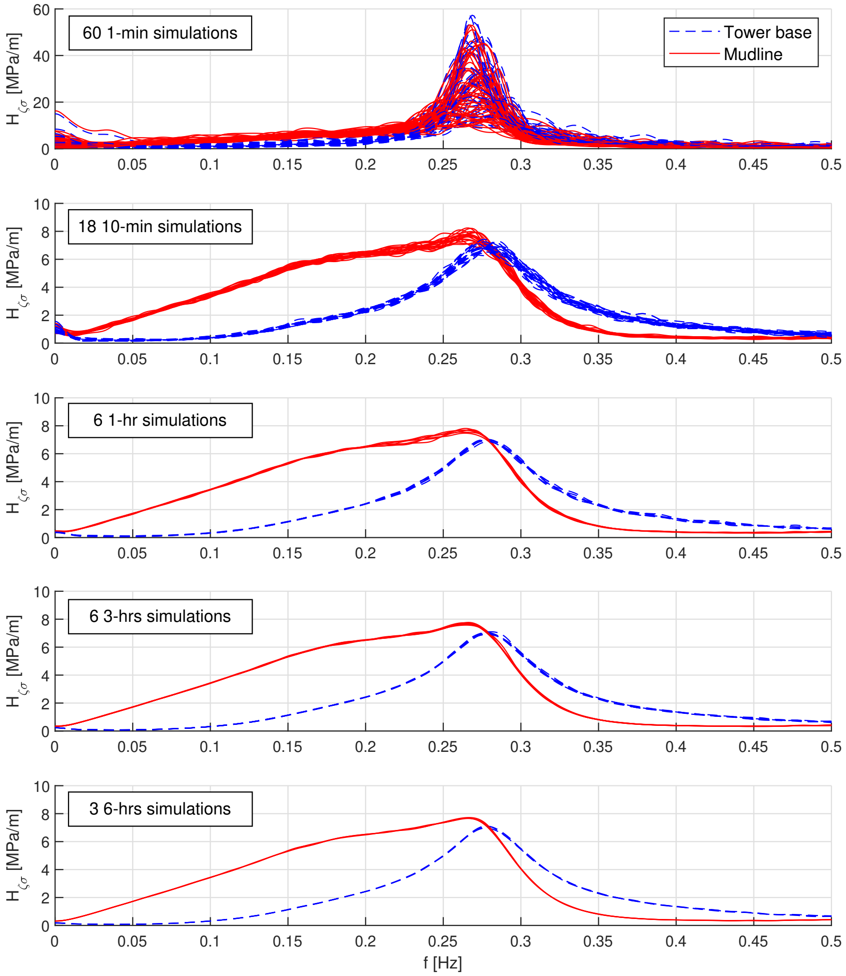

Figure 5.21: Stress transfer functions $H_{\zeta\sigma}$, as obtained from white noise simulations of different duration for wind class 18-20 m/s

respectively, across all wind classes. For longer durations, the variation became negligible, as indicated in the zoomed-in section of Figure 5.22a. The variations observed for the 10 min case are considered negligible, given the notable reduction of computation time from 3 hours to 10 min ($\sim 94\%$), and the inherent uncertainty in the fatigue damage estimates from time-domain simulations, and can be recommended when the method is applied using fully-coupled models for monopile foundations.

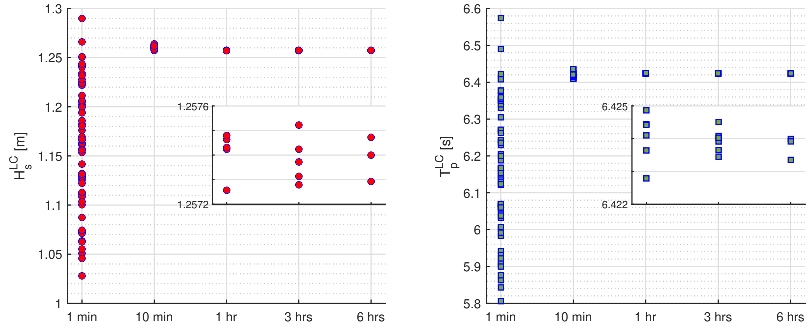

(a) 8-10 m/s

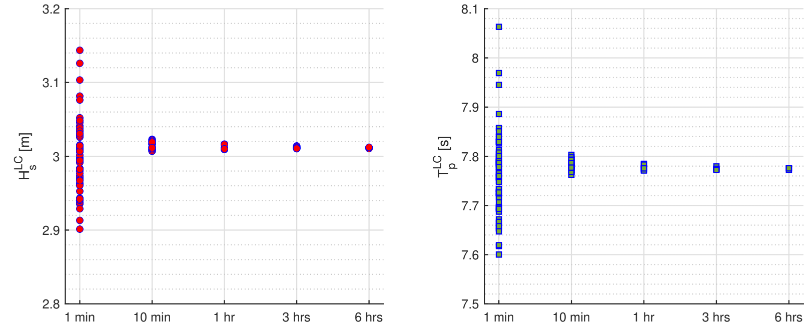

(b) 18-20 m/s

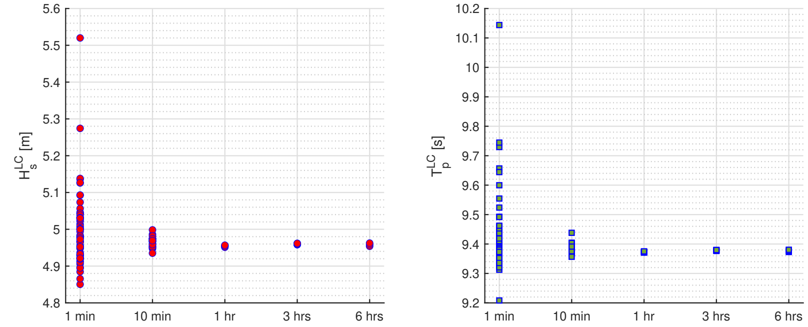

(c) 26-28 m/s

Figure 5.22: Variation of lumped load cases, with respect to white noise simulation time

5.3 Lumping of wind-sea and swell

5.3.1 Main project information

The accuracy of DELM was investigated for the Front End Engineering Design (FEED) stage of a monopile-based OWT project. Lumped LCs were derived based on the method described in Sec. 4.4 and used for the long-term fatigue assessment of the OWT, for the DLC 7.2 (parked within the operational range). The procedure involved defining one load case for each wind class, wind direction, wind-sea direction, and swell direction. In addition, an LTFA was carried out using hindcast data directly. Verification results are provided for three wind classes, allowing a comparison between the results obtained from the lumped LCs and the direct hindcast data analysis.

The SIMA software was employed to model the monopile-based OWT system, as illustrated in Figure 5.23. The monopile and tower were represented as beam elements with specified diameter and thickness, while the RNA was modelled as a SIMA body with defined mass and inertia. Soil-structure interaction was considered using $p - y$ curves. To determine the natural frequencies of the system's vibration modes, an eigenvalue analysis was performed. Table 5.4 provides a summary of the natural frequencies for the first and second fore-aft and side-side vibration modes.

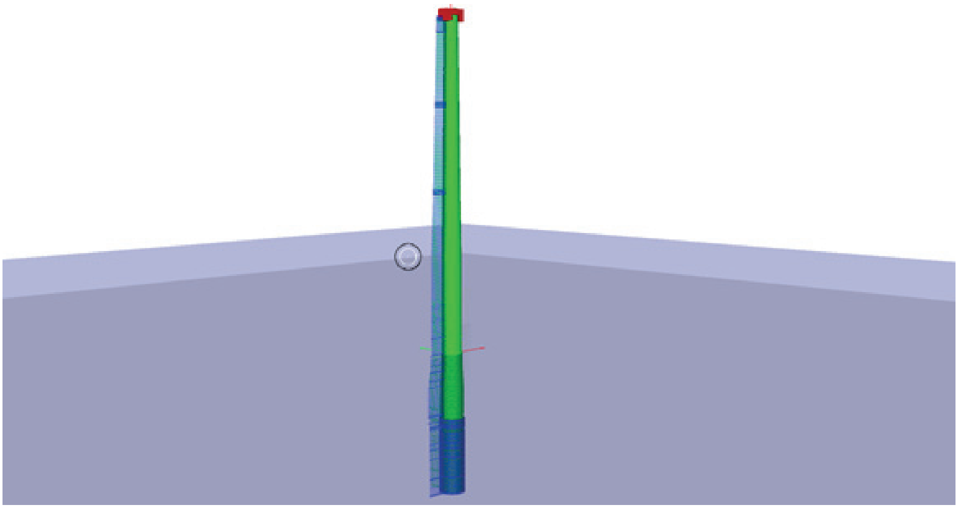

Figure 5.23: Numerical model in SIMA

Aerodynamic damping was represented by a dash-pot located at the RNA. Damping values related to the 1st side-side and fore-aft system modes for

Table 5.4: Natural frequencies-periods from the eigenvalue analysis

Vibration mode	Natural frequency [Hz]	Natural period [s]
1st Side-Side	0.16267	6.14
1st Fore-Aft	0.16439	6.08
2nd Side-Side	0.77607	1.29
2nd Fore-Aft	0.87865	1.14

different wind speeds were provided as percent of critical damping by the wind turbine manufacturer. The remaining sources of damping, i.e., hydrodynamic, soil, and structural, were represented by Rayleigh proportional damping, based on the first natural frequency, as obtained from the eigenvalue analysis.

The water depth of the site is 27.3 m. Hourly site-specific hindcast data for the continuous period from 2002 to 2019 were used to organize the metocean parameters. Figures 5.24 and 5.25 show the wind-sea and swell wave roses for H_s and T_p. Wind and wave directions are measured clockwise from North. It is observed that the wind-sea direction is predominantly from the southwest, following the general wind direction, while the swell component is independent and mainly originates from the southeast. The different characteristics of the two components are also observed by their $H_s - T_p$ parameters, where wind-sea is dominated by waves with T_p mainly between 3-7 s, while swell is dominated by waves between 6-11 s.

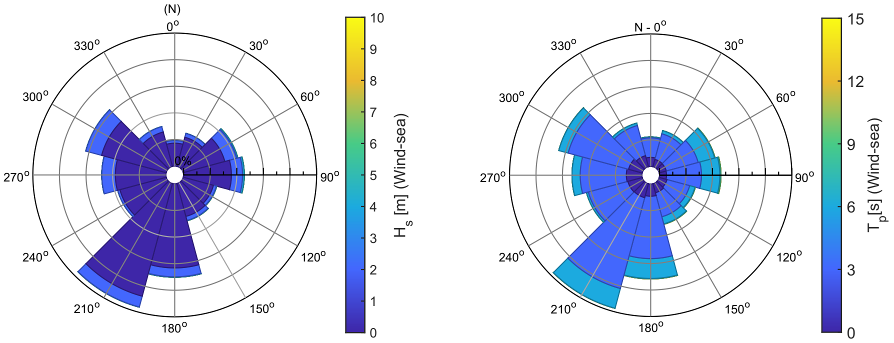

(a) H_s

(b) T_p

Figure 5.24: Wind-sea roses for the commercial FEED design

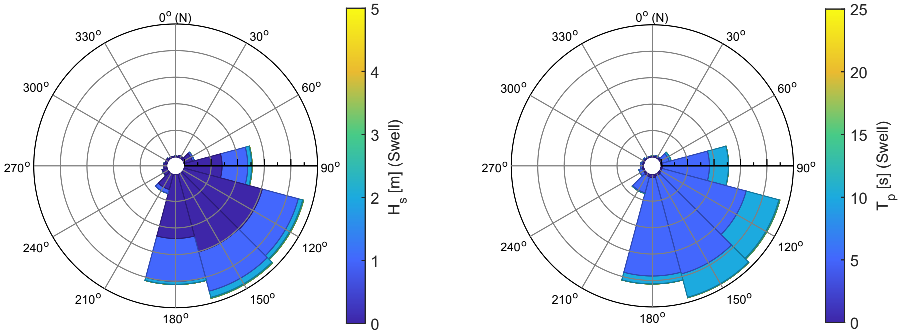

(a) H_s (b) T_p

Figure 5.25: Swell roses for the commercial FEED design

5.3.2 Lumped load cases

Representative lumped load cases (LCs) were derived for 29 wind classes, with wind speeds ranging from 3 m/s to 31 m/s in steps of 1 m/s. Considering the combination of all wind speeds, wind and wave directions in 30° increments from 0° to 330°, a total of 4176 wind-sea scatter diagrams were obtained. However, only around 2000 scatter diagrams had a non-zero probability of occurrence, as empty scatter diagrams were disregarded. Similarly, for the swell component, the total number of directional swell scatter diagrams was 50112. However, due to the limited range of swell directions, the non-zero scatter diagrams were around 4000 (92% reduction).

By coupling swell with wind-sea in the lumping process without crude simplifications, the total number of lumped LCs was found to be 4087, representing the total variability in wind speed, wind direction, wind-sea direction, and swell direction in the metocean database, which included 150283 occurrences.

The wind-wave environment was fully described using 4087 unique lumped load cases. Each load case consists of a wind-sea and a swell wave component, with representative sea-state parameters, as described in Sec. 4.4. Figure 5.26 shows the lumped LCs for wind-sea and swell for all wind speeds and wind directions, respectively, along with the hindcast data for the time considered. Each "dot" represents one wind-sea or swell scatter diagram, with the colour density indicating the total probability of occurrence for the wave scatter diagrams represented by the damage-equivalent lumped LCs.

While the lumped LCs generally follow the trend of the hindcast data as shown in Figure 5.26, it's important to note that they are derived based on damage equivalence and not solely on the distribution of sea states within the scatter diagrams. As a result, some variations can be expected between the exact distribution of the hindcast data and the lumped LCs, as shown in Figure 5.27.

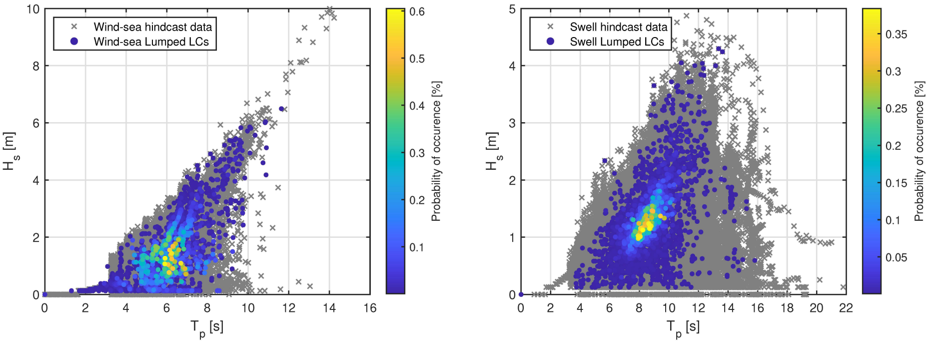

(a) Wind-sea (b) Swell

Figure 5.26: Lumped load cases for all wind speeds and wind directions

Figure 5.28 shows the $H_s - T_p$ values of the wind-sea and swell lumped load cases, along with their mean values, over the wind classes. For the wind-sea component, the sea state parameters gradually increase from low to high wind speeds. This is consistent with the fact that wind-sea severity is highly correlated with wind speed, with larger waves within the wind-sea scatter diagrams for higher wind speeds. This trend was also observed in the results presented in Sec. 5.1.2, where the combined wind-sea and swell scatter diagrams were used.

In contrast, for the swell component, the sea state parameters remain relatively constant across different wind speeds, with only a slight increase in $H_s - T_p$ for higher wind speeds. This behaviour is expected since swell waves are primarily generated by distant storms and are not strongly influenced by local wind conditions. Therefore, changes in wind speed have a lesser impact on swell characteristics compared to wind-sea. The spread in the lumped load cases for both wind-sea and swell components within each wind class is due to the inclusion of load cases from all scatter diagrams corresponding to different joint wind, wind-sea, and swell directions. Consequently, the expected variation in the distribution of sea states among scatter diagrams for different directions is also reflected in the resulting lumped load cases.

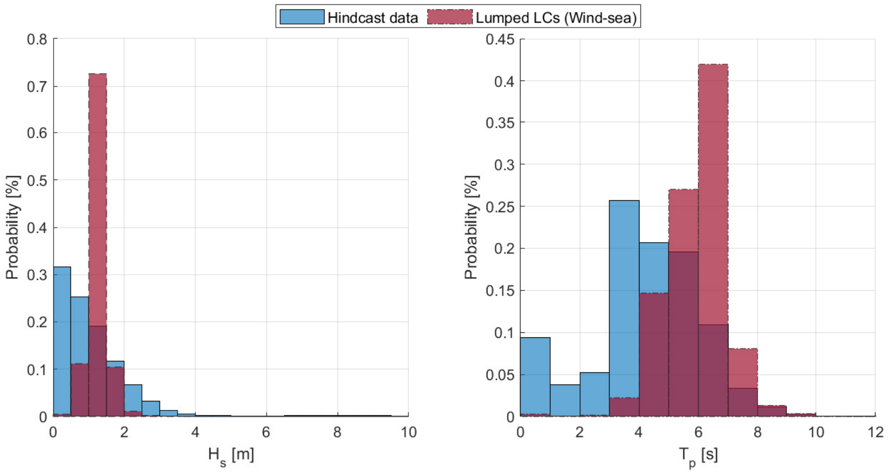

(a) Wind-sea

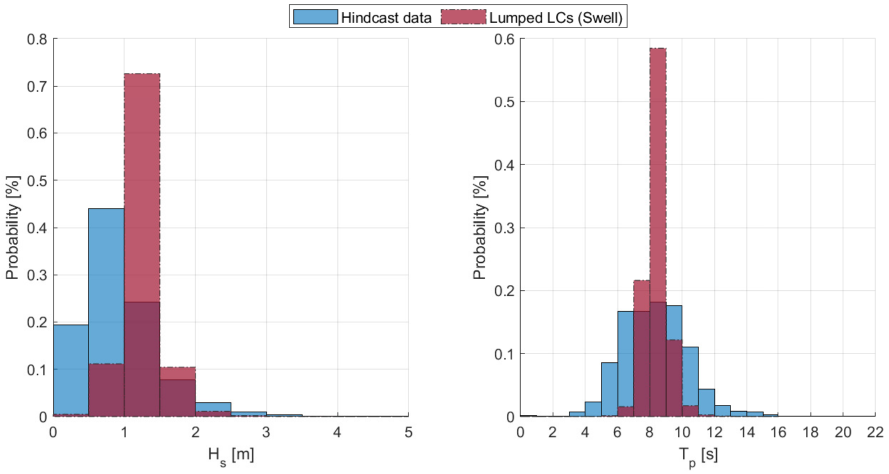

(b) Swell

Figure 5.27: $H_s - T_p$ histograms of wind-sea and swell hindcast data and lumped load cases

5.3.3 Verification of results

To verify the results, a full long-term assessment was conducted for three wind classes: 18 m/s, 21 m/s, and 24 m/s. The hourly wave occurrences for each wind class were selected from the hindcast data within the respective wind speed ranges: [17.5, 18.5) m/s, [20.5, 21.5) m/s, and [23.5, 24.5) m/s. For each occurrence, a representative load case was analyzed, consisting of both a wind-sea and swell component with their respective characteristics

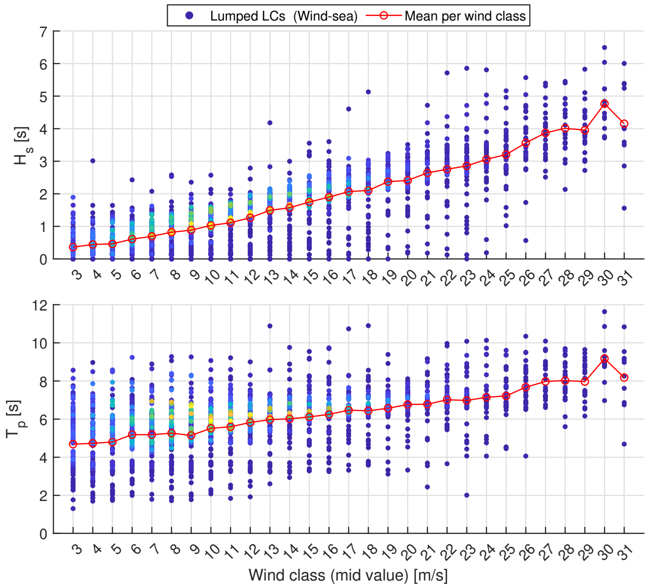

(a) Wind-sea

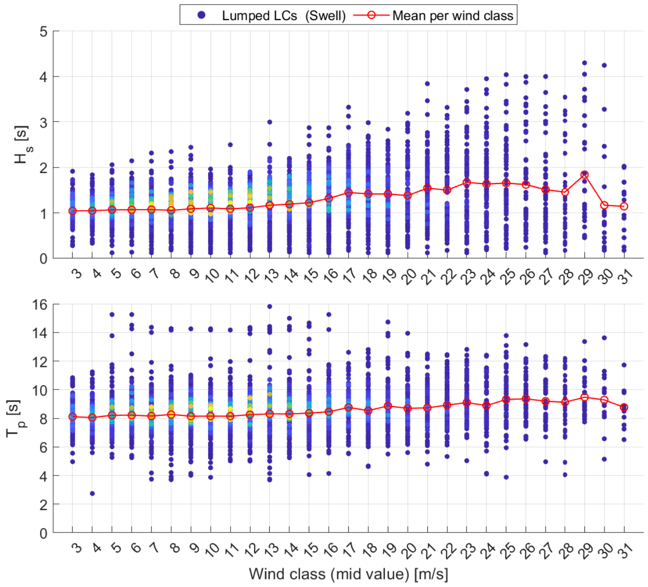

(b) Swell

Figure 5.28: Wind-sea and swell lumped load cases for each wind class

Table 5.5: Specifications for time domain analyses of lumped load cases

Turbine condition	Parked (DLC 7.2)
Wave kinematics	Airy wave theory
Wave kinematics at sea-surface	Wheeler stretching
Wave load model	MacCamy and Fuchs
Wave spectra	Single-peaked JONSWAP spectra for both wind-sea and swell
Wave spreading	No
Wind loads	Shear profile with exponent α=0.14 for heights between SWL and hub height

(H_s, T_p, θ_w) taken directly from the hindcast data. The short-term damage for each load case was calculated through 1-hour time-domain simulations in SIMA. The specifications for the analyses are summarized Table 5.5. The yearly damage was then determined using Eq. 4.17, with a probability of occurrence equal to 1/156307, where 156307 represents the total number of occurrences in the hindcast data for the considered period. Figures 5.29, 5.30, and 5.31 depict the hindcast data and the lumped load cases analyzed for the wind classes. Additionally, Table 5.6 provides the total number of analyses conducted for the hindcast data assessment, compared to the number of lumped load cases for the three wind classes.

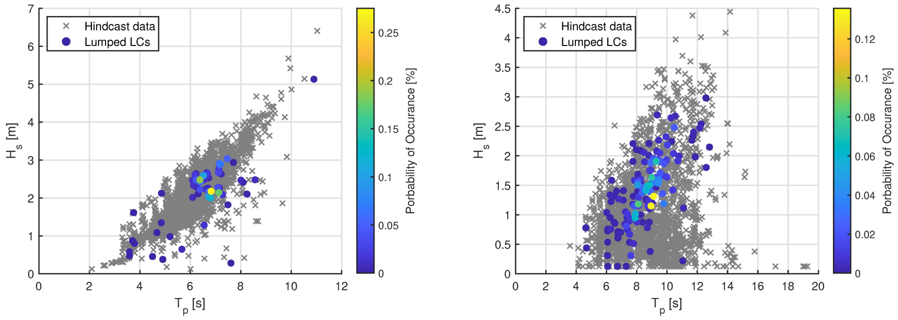

(a) Wind-sea

(b) Swell

Figure 5.29: Hindcast data and lumped load cases for [17.5, 18.5) m/s

In Figure 5.32, a comparison is shown between the yearly damage at the mudline obtained from the full long-term assessment using the hindcast data and the lumped load cases. The results depict that the lumped load cases are capable of capturing the damage distribution around the circumference and

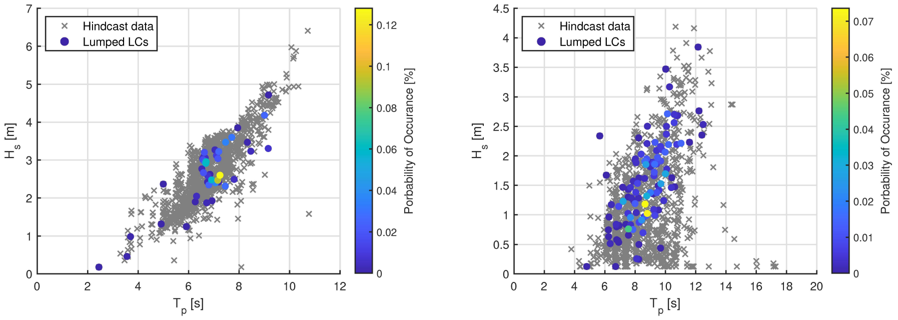

(a) Wind-sea (b) Swell

Figure 5.30: Hindcast data and lumped load cases for [20.5, 21.5) m/s

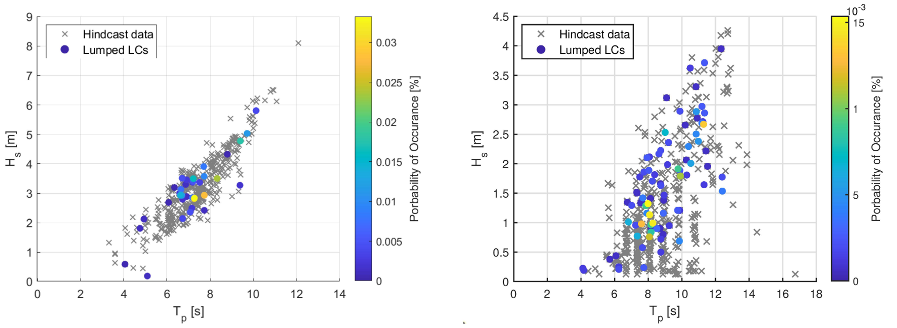

(a) Wind-sea (b) Swell

Figure 5.31: Hindcast data and lumped load cases for [23.5, 24.5) m/s

Table 5.6: Number of load cases used for verification

Wind class m/s	Hindcast data assessment -	Lumped DLCs -	Computational time reduction - %
18	2890	138	95.2
21	1272	107	91.5
24	436	84	80.7

accurately estimating the maximum fatigue damage. For the wind classes [17.5, 18.5) m/s and [23.5, 24.5) m/s, the lumped load cases underestimated the maximum damage, with deviations of -1.8% and -9.03% respectively, while for the wind class [20.5, 21.5) m/s, a slight overestimation of 0.37%

was observed. Considering the various uncertainties associated with the lumping process and fatigue calculation, these deviations in fatigue damage are relatively small. This is especially noteworthy considering the significant reduction in computational time achieved through the use of lumped load cases and the comprehensive representation of wind-sea and swell wave components in an integrated and consistent manner.

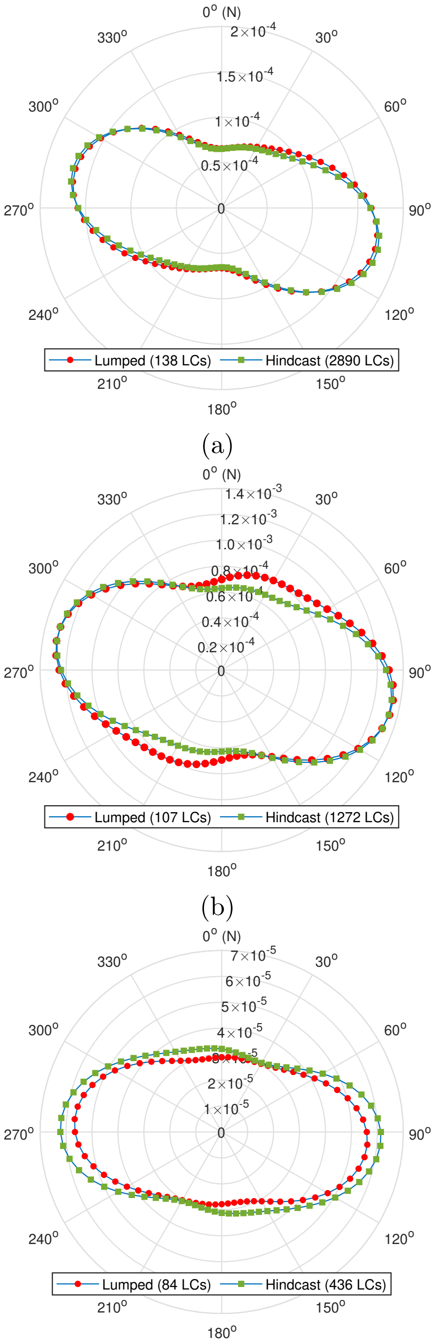

(a)

(b)

(c)

Figure 5.32: Yearly damage at mudline for lumped LCs and hindcast data for (a) [17.5, 18.5) m/s (b) [20.5, 21.5) m/s (c) [23.5, 24.5) m/s

Chapter 6

Soil-structure interaction effects on fatigue damage

This chapter evaluates the impact of foundation modelling on the dynamic behaviour and fatigue estimates of monopiles. Aspects such as hysteretic damping and different stiffness after load reversals incorporated into the macro-element model, which cannot be represented by the widely used approach of $p-y$ curves, are emphasized. Focus is given to conditions when aerodynamic damping is negligible in the response direction, such as parked states and wind-wave misalignment conditions.

6.1 Foundation damping and stiffness

In the time-domain simulation tool, the total damping includes aerodynamic, hydrodynamic, structural, and soil damping. Aerodynamic damping arises from the air drag on the rotating blades due to the relative motion between the rotor and the wind, and hydrodynamic viscous damping is approximated using the relative velocity between the structure and the fluid in the Morison equation. Hydrodynamic radiation damping was not modelled explicitly in the simulations.

Structural damping, which describes material damping due to friction and local strains, was represented by stiffness-proportional Rayleigh damping along the support structure. A structural damping ratio of ξ ≈1.0-1.1% of critical damping was used for all OWTs, based on the natural frequency of their first vibration mode. The value was based on published results using both full-scale measurements and simulations [220] and typical values adopted for reference wind turbines [191, 192]. The mass-proportional term in the definition of Rayleigh damping can introduce an artificial overdamping for low-frequency vibrations; therefore, it was not used.

Soil damping is inherently represented by the macro-element model, while for $p-y$ curves, it was represented by stiffness-proportional damping, where the stiffness-proportional coefficient β_d was defined based on a desired global damping ratio ξ, and the natural frequency of the first vibration mode for each OWT, as shown in Eq. 6.1,

$$\beta_d = \frac{\xi}{\pi f_1}. \tag{6.1}$$

To quantify the natural frequency and soil damping of each foundation model, free vibration tests with no wind and no waves were conducted for the three OWTs. The tests were performed by gradually applying the maximum thrust force for each OWT at the tower top and then releasing the force to allow the OWT to vibrate for 600 s. Aerodynamic damping was negligible during the decay test as the rotor was kept locked and the blades were pitched to feather by 90°. The global damping ratio ξ for each load cycle was then quantified based on the logarithmic decrement δ, which was calculated for multiple successive amplitudes (A_i, A_{i+1}) of the fore-aft bending moment at the mudline, as shown in Eq. 6.2,

$$\delta = \ln\left(\frac{A_i}{A_{i+1}}\right) = 2\pi\frac{\xi}{\sqrt{1-\xi^2}} \approx 2\pi\xi. \tag{6.2}$$

Figure 6.1 shows an example of free vibration analysis, where the bending moment at mudline is illustrated during the test. Free vibration tests were conducted for the macro-element and $p-y$ curve models. Figure 6.2 shows an example of the fore-aft bending moment at the mudline and the global damping ratio for the two foundation models, as obtained from the free-vibration test of the 15 MW OWT. The non-zero slope of the damping ratio with respect to response amplitude depicts the nonlinear soil (hysteretic) damping reproduced by the macro-element. Hysteretic damping cannot be reproduced by the stiffness-proportional Rayleigh damping, which provides similar damping over the range of response amplitudes.

Figure 6.3 shows the response from the decay test of the macro-element model alongside the $p-y$ curves, clearly depicting the hysteretic loops of the former, and the different soil stiffness formulation between the two models. In the $p-y$ curves, soil stiffness is represented as a nonlinear relationship between lateral soil resistance (p) and lateral displacement (y). As illustrated

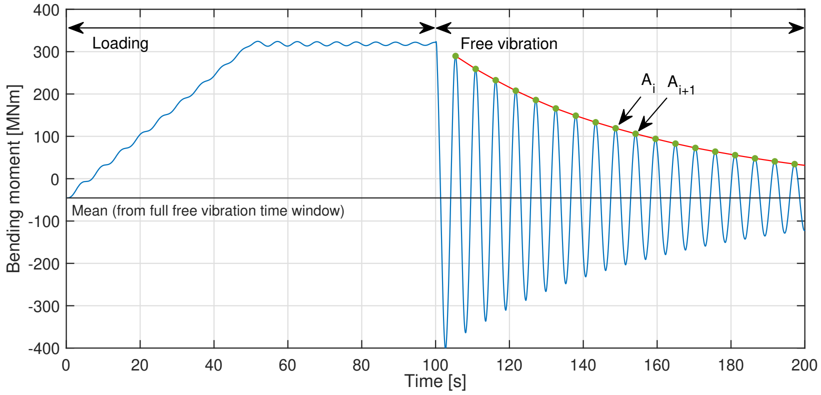

Figure 6.1: Example of free vibration analysis for 15 MW OWT (macro-element)

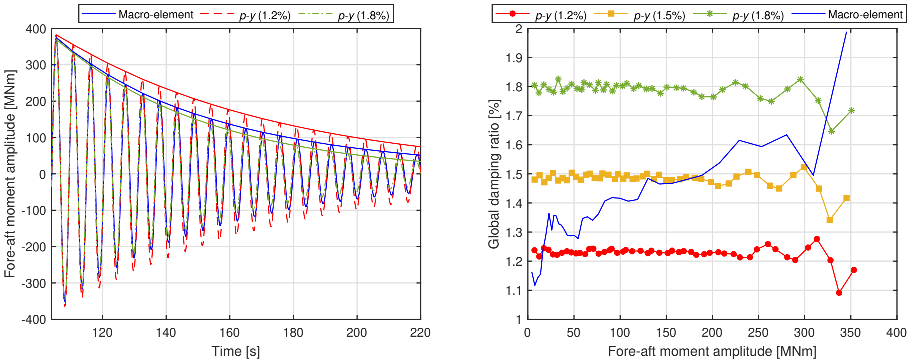

Figure 6.2: Decay test (left) and global damping ratio (right) for macro-element, and $p - y$ curves for different levels of soil damping (stiffness proportional)

in Figure 6.3, at low response levels, i.e., within the elastic region of the $p-y$ curve, the soil stiffness is typically linear, indicating that resistance increases proportionally with deflection, reflecting the initial stiffness of the soil. As lateral deflection increases, the $p-y$ curve transitions into a nonlinear region. Figure 6.4 presents the first fore-aft natural frequencies obtained from free decay tests for the macro-element and $p - y$ curves. It is observed that for higher load levels, the foundation stiffness is lower, leading to lower effective resonance frequencies.

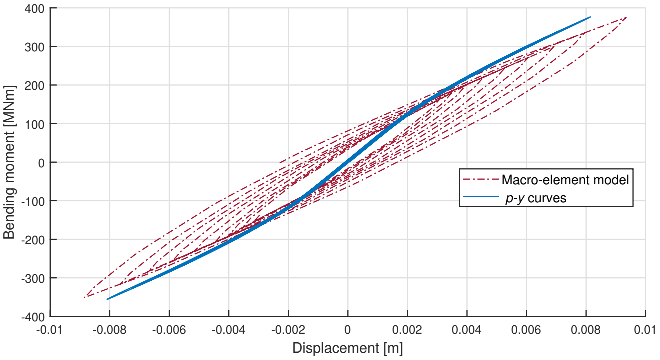

Figure 6.3: Response at mudline of macro-element and $p-y$ curve models from a decay test of the 15 MW OWT

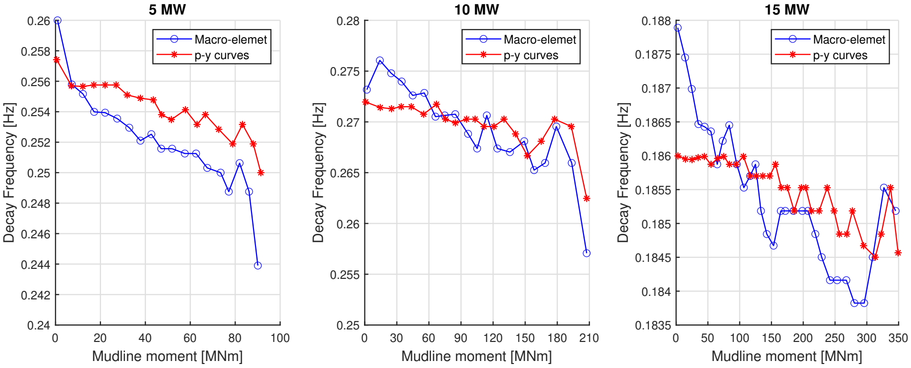

Figure 6.4: Decay frequency of macro-element and $p-y$ foundation models from free-vibration test

While the $p-y$ curves capture the overall nonlinear soil response, considering the cumulative effects of loading and unloading cycles, they fail to explicitly account for the different foundation stiffness between load reversals, which is captured by the macro-element model. In particular, Figure 6.3 demonstrates that during load reversals, when the load on the foundation reaches its maximum and is subsequently reversed, the soil surrounding the monopile unloads. Initially, the unloading is elastic, resulting in a stiffer response than before the reversal. As the load reversal magnitude gradually increases, the stiffness decreases due to plastic deformations in the soil. A similar pattern is observed during reloading. This behaviour creates a hysteresis loop, with the enclosed area representing the energy dissipated in the soil, which also corresponds to hysteretic damping at the foundation level. Higher load levels, which correspond to a larger enclosed area, are associated with increasing soil strains, resulting in a larger amount of hysteretic damping. In contrast, the $p-y$ curves follow the same elastic curve during load reversals, indicating no generation of hysteretic damping, as well as no variation in stiffness during load reversals.

6.2 Dynamic response and short-term fatigue

The impact of the foundation modelling on fatigue responses was assessed based on time-domain analyses using the fully coupled aero-hydro-servo-elasto-plastic simulation tool SIMA. The macro element model, which incorporates hysteretic damping and different stiffness after load reversals, was considered the baseline model and was compared to $p-y$ curves. Both models were calibrated to FEA results obtained from the same soil profile (Sec. 3.1.2). Their implementation in SIMA was discussed in Sec. 3.3.1.2. The next sections compare the $p-y$ curves to the macro-element. Firstly, the dynamic response obtained from time-domain simulations is compared for the two models, then the short-term damage estimates are assessed.

6.2.1 Effect of foundation modelling on dynamic response

OWTs respond across a wide range of frequencies as mentioned in previous sections (e.g., Sec. 1.4.3, Sec. 5.1.1), including slowly varying responses caused by wind loads, 1P-3P rotor operating frequencies, and wave frequencies. High-frequency vibrations, e.g., 2$^{\text{nd}}$ mode responses, are also present; however, their contribution to fatigue is negligible for monopile-based OWTs, considering also that stiffness-proportional Rayleigh damping, chosen based on the first vibration mode, dampens higher-frequency vibration modes to a great extent. Fatigue damage in OWTs, as obtained from time-domain simulations, is a result of various processes, any of which may dominate depending on the natural frequency of the OWT, its operational state (and wind speed), the sea state severity, and the location of interest along OWT.

Using the $p-y$ curves leads to distinct changes in the response compared to the macro-element. Firstly, the soil stiffness is generally reduced, leading to higher response amplitudes in the wave frequency range, as illustrated in Figure 6.5, which shows the fore-aft axial stress spectra ($S_{\sigma\sigma}$) at mudline for the two foundation models. The macro-element model reproduces the different foundation stiffness after load reversals, while the $p-y$ curves follow the same elastic curve. The lower soil stiffness of the $p-y$ models results in a lower resonance frequency that is also observed from the response spectra. The difference in soil stiffness was generally more pronounced for wind classes close to the rated speed with operating OWT, where the highest mean loads are applied due to the maximum thrust force.

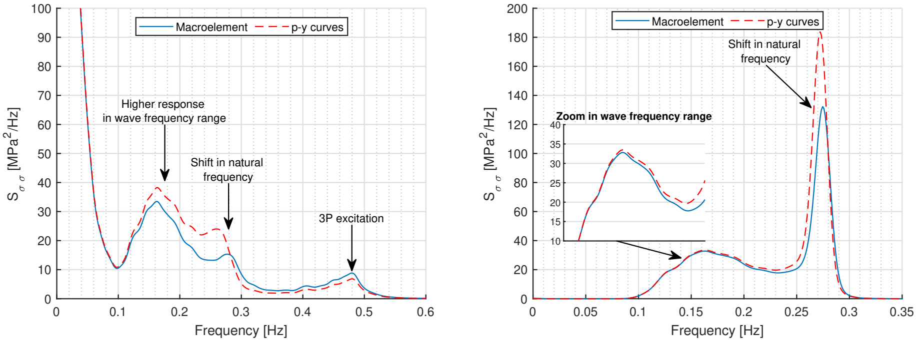

(a) Operation (b) Parked

Figure 6.5: Axial stress spectra at mudline (10 MW OWT) for a point aligned with the FA direction for $p-y$ curves and macro-element (U_{119}=11 m/s, H_s=1.39 m, T_p=6.37 s)

Soil damping particularly affects the response around the natural frequencies of the models. In operational states, aerodynamic damping dominates, so variations in soil damping included in the $p-y$ curves result in only minor differences in the overall response. However, in the parked state, the soil becomes the primary contributor to damping. This is evident in Figures 6.6 and 6.7, which demonstrate the impact of soil damping variation in the response, particularly for the parked states, at both the mudline and SWL.

Figures 6.6 and 6.7 compare the stress spectra for $p-y$ curves with soil damping corresponding to different global damping ratios. In the operational state, at the mudline, the response is dominated by the wave frequency range for that particular load case, while aerodynamic damping attenuates the response at the natural frequency. Variations in soil damping lead to only minor differences in the response spectra between the models. However, in the parked state, where aerodynamic damping is negligible, the resonant response becomes significantly more important. In this case, variations in soil damping have a considerable impact on the responses and subsequently on fatigue. Similar behaviour is observed at SWL, where the response close to SWL primarily occurs at the OWT natural frequency and the rotor operating frequencies, with negligible response due to wave excitation.

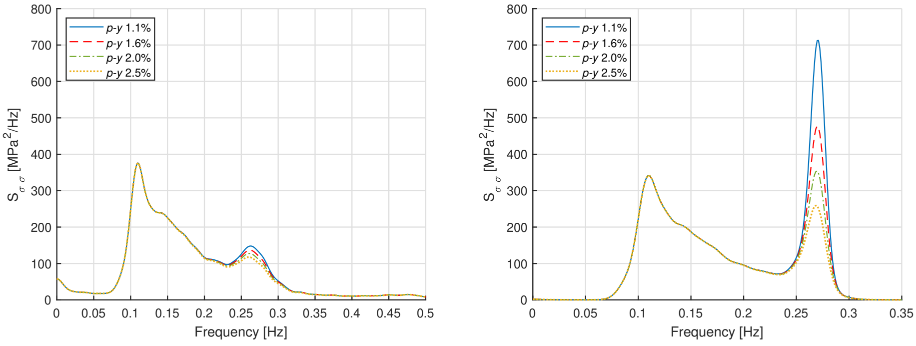

(a) Operation (b) Parked

Figure 6.6: Axial stress spectra at mudline (10 MW OWT) for a point aligned with the FA direction for $p-y$ curves with different levels of soil damping (U_{119}=25 m/s, H_s=4.48 m, T_p=9.15 s)

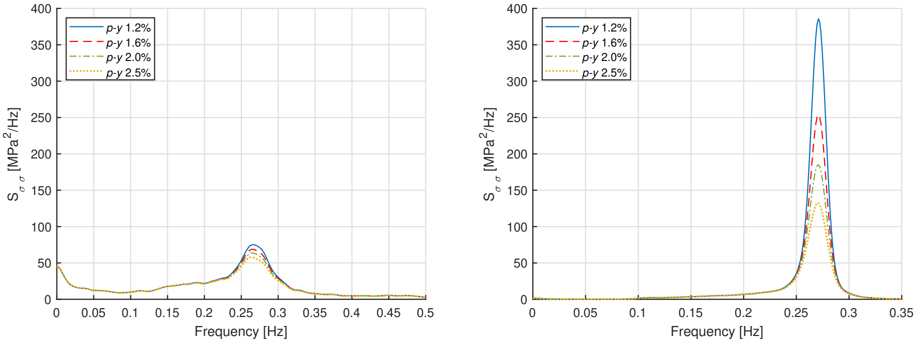

(a) Operation (b) Parked

Figure 6.7: Axial stress spectra at SWL (10 MW OWT) for a point aligned with the FA direction for $p-y$ curves with different levels of soil damping (U_{119}=25 m/s, H_s=4.48 m, T_p=9.15 s)

The stiffness-proportional term contributes damping that is linearly proportional to frequency. As only stiffness-proportional damping is used, with the coefficient determined based on the first natural frequency (as described in Eq. 6.1), any high-frequency response is strongly damped. This behaviour is illustrated in Figure 6.8, which compares the stress spectrum (log scale) at the mudline (parked condition) between macro-element and $p-y$ curves. While the $p-y$ closely approximate the macro-element response at the 1st natural frequency, responses in higher frequencies, such as the 2nd or

3rd vibration mode, are more heavily damped. This frequency dependency is an inherent limitation of the Rayleigh damping formulation. However, as Figure 6.8 shows, the energy content in the high-frequency range (e.g., above 3P) is negligible compared to the rest of the excitation frequencies when considering the fatigue of monopiles. Therefore this effect is assumed negligible for the resultant fatigue estimates. Finally, no differences in the response spectra were observed between the soil models in the low-frequency responses, i.e., for $f < 0.1$ Hz.

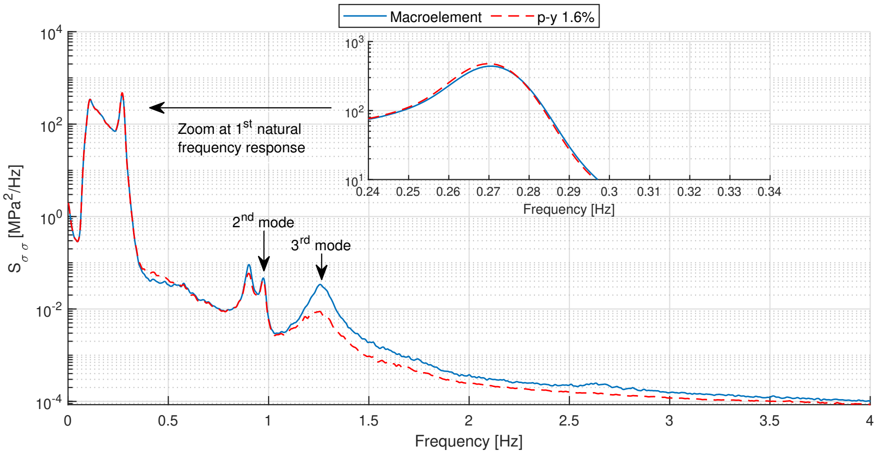

Figure 6.8: Effect of using Rayleigh formulation for soil damping on higher-order responses (U_{119}=25 m/s, H_s=4.48 m, T_p=9.15 s) - 10 MW

6.2.2 Short-term fatigue sensitivity to foundation modelling

To investigate the impact of foundation modelling on fatigue estimates, representative lumped load cases for four wind classes (obtained from Chapter 4) were tested for each OWT. For the $p-y$ curves, stiffness-proportional Rayleigh damping was employed to represent four levels of soil damping. The amount of soil damping, expressed as a percentage of critical damping, was selected for each OWT so that the total global damping ratio of the $p-y$ curves closely matched that of the macro-element model for low, intermediate, and high mean load levels at the mudline, as obtained from free-vibration tests. Figure 6.9 shows the global damping ratios used in the analyses for each OWT, using the macro-element model, and the $p-y$ curves with different levels of soil damping. The figure also shows the mean mudline moment for different wind classes, with black markers indicating the wind classes analyzed for each OWT.

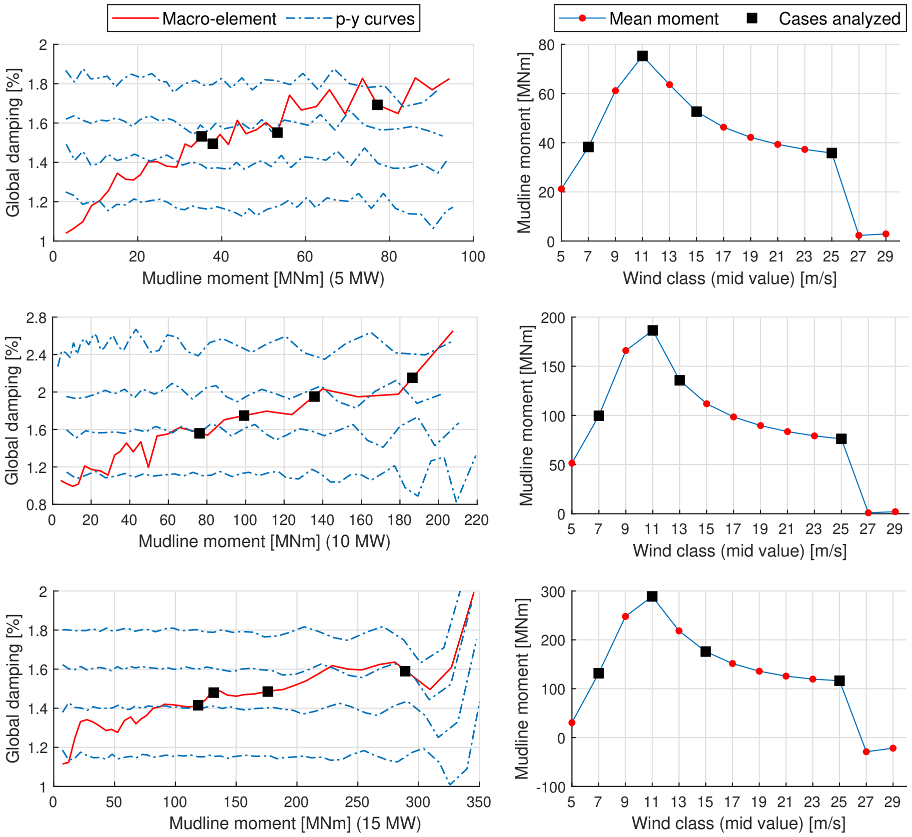

Figure 6.9: Left: Global damping ratio for macro-element, and $p - y$ curves for different levels of soil damping (stiffness proportional). Right: Mean bending moment mudline at different wind classes.

Table 6.1 summarizes the load cases analyzed for each OWT. Both operational and parked states were evaluated. For each load case, five 1-hour time-domain simulations were conducted with random wind and wave seeds, and the average fatigue damage was compared. The same seeds were used over the different operational states and soil models to eliminate the effect of statistical uncertainty from the simulations (see e.g., Figure 4.12).

Figures 6.10, 6.11, and 6.12 show the relative difference of 1-hour fatigue damage between the $p - y$ curves and the macro-element (reference) for the three OWTs, for operational and parked states. On the x-axis, the global damping ratio of the $p - y$ curves is shown (see Figure 6.9), corresponding

Table 6.1: Loading conditions analyzed for the different OWTs

5 MW			10 MW			15 MW		
U_{90} m/s	H_s m	T_p s	U_{119} m/s	H_s m	T_p s	U_{150} m/s	H_s m	T_p s
7	1.01	6.61	7	1.02	6.51	7	1.13	7.49
11	1.46	6.41	11	1.39	6.37	11	1.44	7.17
15	2.29	7.28	13	1.76	7.10	15	2.08	7.13
25	4.77	9.35	25	4.48	9.15	25	4.33	8.99

only to different amounts of soil damping included in the $p-y$ model. Positive (negative) deviation implies overestimation (underestimation) of $p-y$ curves compared to the macro-element. Results are shown for the monopile sections at mudline and still water level (SWL).

In operational states, the relative differences between the $p-y$ curves (with various damping levels) and the macro-element model mostly ranged from -5% to +15% for all OWTs. However, higher variations were observed for the 10 MW OWT in the wind class of 6-8 m/s. In this case, the $p-y$ curves underestimated the fatigue damage by 20% up to 50% for low and high soil damping levels, respectively. This discrepancy can be attributed to the resonance effects caused by the close proximity of the first natural frequency (0.28 Hz) to the mean 3P excitation frequency (0.3 Hz) of the turbine rotor, as mentioned in Sec. 5.1.1. The different stiffness formulation of the macro-element model results in the natural frequency being closer to the excitation frequency, resulting in relatively large differences in fatigue damage.

In parked conditions, significantly larger variations were observed between the models. At the tower, differences ranged from -80% to +120% for different OWTs, while at the mudline, differences were up to ±50%. These variations highlight the increased importance of foundation modelling and the inclusion of hysteretic damping effects in cases where aerodynamic damping is negligible, as expected from the response spectra (Figures 6.6b, 6.7b).

In operational states, for all OWTs, different soil damping levels (represented by Rayleigh damping) for each wind speed need to be applied in the $p-y$ curves model to closely approximate the fatigue responses obtained from the nonlinear elasto-plastic macro-element model. This can be observed, for example, by looking at Figures 6.11a and 6.9 for the 10 MW

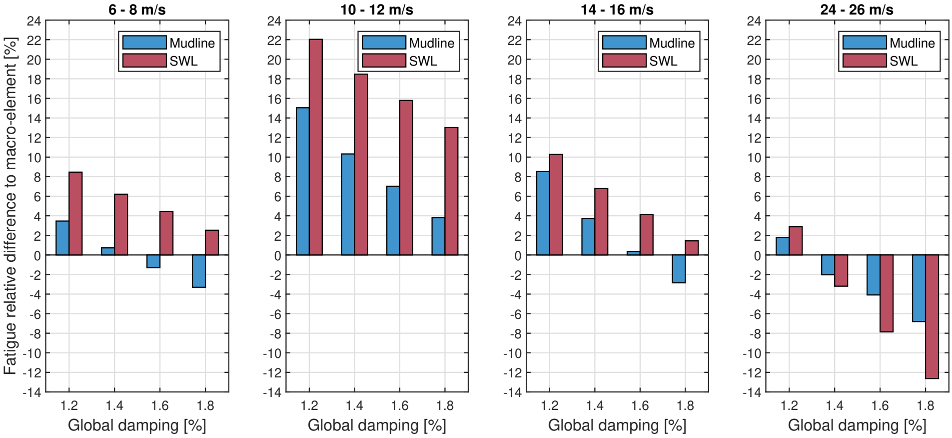

(a) Operational

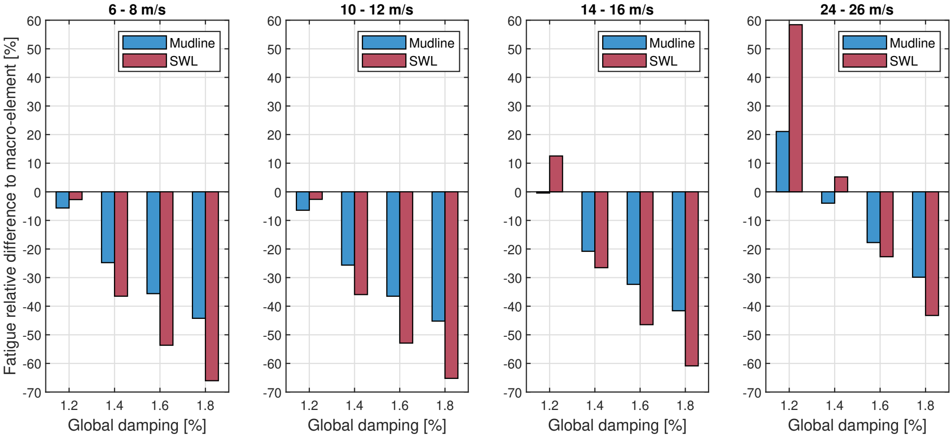

(b) Parked

Figure 6.10: Fatigue damage relative difference between $p-y$ curves and macro-element model for 5 MW model

model. At the rated speed, where maximum mean loads are experienced, the macro-element model exhibits maximum soil damping, resulting in a global damping ratio of approximately 2.4%. For higher wind classes (12-14 m/s and 24-26 m/s), where the mean loads gradually decrease to approximately 140 MNm and 80 MNm, respectively, the macro-element model exhibits decreasing global damping ratios of approximately 2.0% and 1.6%. Consequently, lower soil damping levels are required in the $p-y$ curves model to approximate the macro-element fatigue estimates, as shown in Figure 6.11a

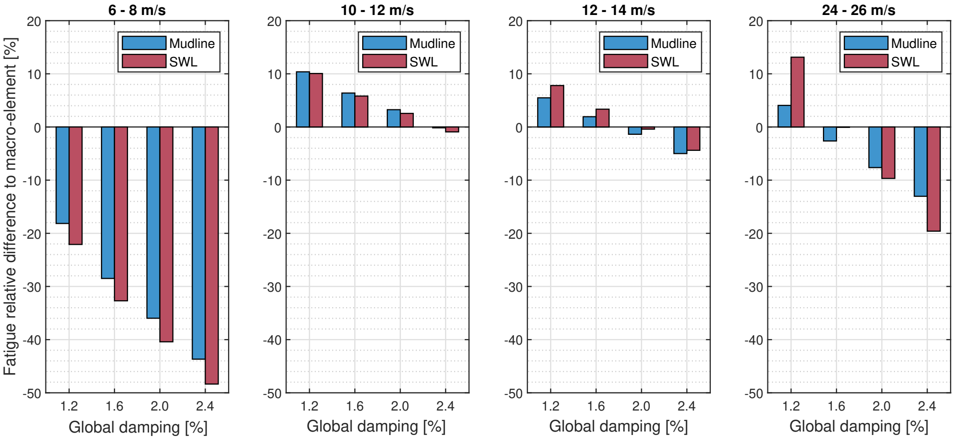

(a) Operational

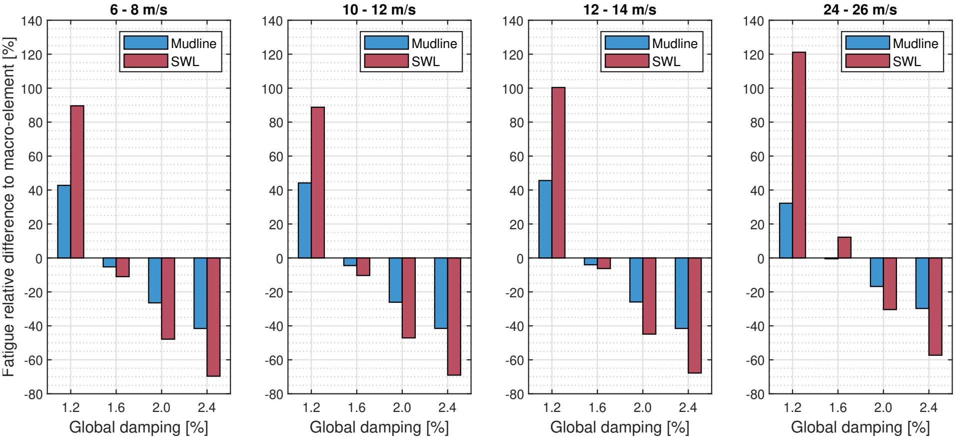

(b) Parked

Figure 6.11: Fatigue damage relative difference between $p-y$ curves and macro-element model for 10 MW model

for those wind classes. Similar behaviour is observed for other wind turbines, however it is generally challenging to isolate the effect of different processes on the resulting fatigue estimates, particularly in operational conditions where the differences between the models are small.

Contrary to operational states, in the parked state, the $p-y$ curves produced similar fatigue estimates to the macro-element model with an approximately constant soil damping level, regardless of the wind class. This was observed

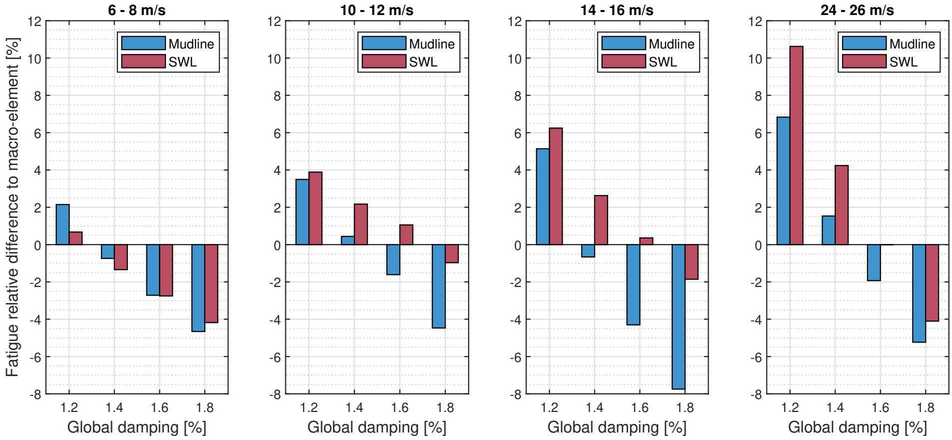

(a) Operational

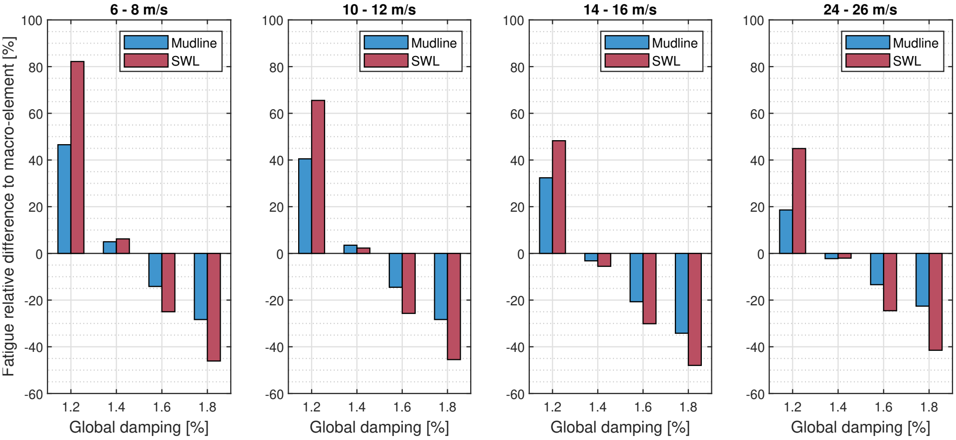

(b) Parked

Figure 6.12: Fatigue damage relative difference between $p-y$ curves and macro-element model for 15 MW model

for all OWTs, as depicted in Figures 6.10b, 6.11b, and 6.12b, respectively. Notably, for the 5 MW OWT, a soil damping level corresponding to a global damping ratio of 1.2% resulted in variations of 5-10% for all wind classes, except for the 24-26 m/s class where a model with a 1.4% damping value provided the best match to the fatigue estimates of the macro-element model. For the 10 MW and 15 MW models, the $p-y$ models with soil damping corresponding to a constant global damping ratio of 1.4% resulted in minor deviations from the macro-element model (±10%) for all wind classes.

6.3 Wind-wave misalignment

To understand the effect of foundation models on conditions with misaligned wind and waves, the general behavior of the OWTs is first analysed (Sec. 6.3.1) before comparing the macro and $p-y$ models (Sec. 6.3.2). The 10 MW OWT is used to demonstrate the effects of wind-wave misalignment. The results shown in this section are from publication P1 [221]. In all simulations the OWT is in operational state, and the rotor is facing the wind, meaning that the wind coincides with the fore-aft (FA) direction, and the side-to-side (SS) direction is perpendicular to the wind. The wind-wave misalignment is the angle between the wave and the FA direction. Table 6.2 summarizes the cases analyzed. The wave parameters were chosen as the mid values of the class that contributes the most to the long-term damage for the scatter diagram.

Table 6.2: Load cases analyzed for wind-wave misalignment

Load case	U_{119}	H_s	T_p	Wind-wave misalignment	Wave spectrum
-	m/s	m	s	°	-
LC1	5.06	0.75	5.5	[0°, 15°, 30°, 45°, 90°]	Pierson–Moskowitz
LC2	9.06	1.25	5.5	[0°, 15°, 30°, 45°, 90°]	Pierson–Moskowitz
LC3	14.94	2.25	6.5	[0°, 15°, 30°, 45°, 90°]	Torsethaugen
LC4	20.9	3.75	7.5	[0°, 15°, 30°, 45°, 90°]	JONSWAP

6.3.1 Maximum damage and dynamic response

Figures 6.13, 6.14, and 6.15 illustrate the short-term fatigue damage at the mudline around the circumference for three of the different load cases, each with varying wind-wave misalignment angles. For all cases, wind always comes from 0°, and waves come from 0° (left), 45° (middle), and 90° (right), as indicated by the black arrows.As shown, the point (angle) around the monopile circumference with largest fatigue damage changes, for different misalignment angles.

In LC1 (see Figure 6.13), the response is primarily dominated by the 3P excitation. As a result, the maximum fatigue damage occurs at a point around the circumference close to the wind direction, regardless of the wave direction. For misalignment angles up to 45°, the point of maximum damage slightly shifts towards the wave direction. However, as the misalignment

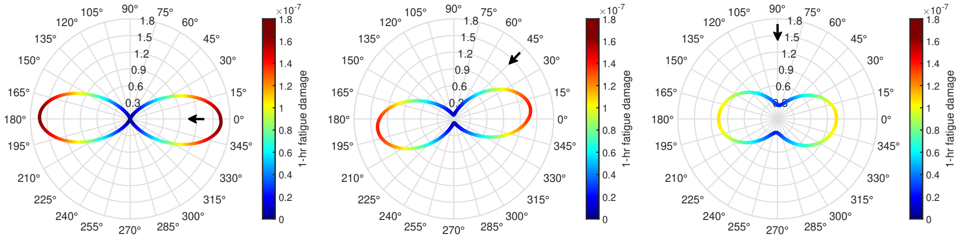

Figure 6.13: Fatigue damage at mudline around the circumference for LC1 (U_{119}=5 m/s) for different wind-wave misalignment angles.

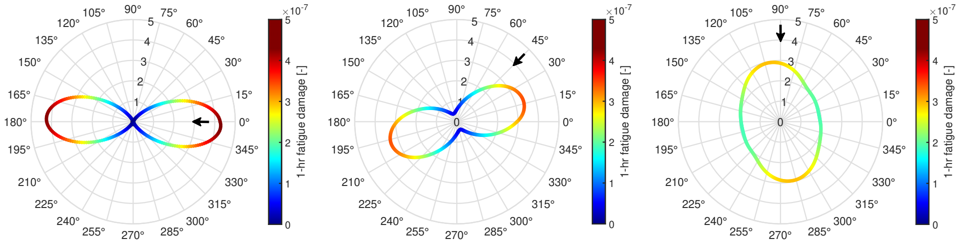

Figure 6.14: Fatigue damage at mudline around the circumference for LC2 (U_{119}=9 m/s) for different wind-wave misalignment angles.

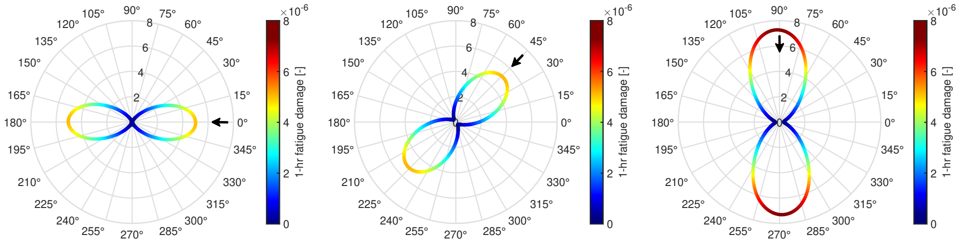

Figure 6.15: Fatigue damage at mudline around the circumference for LC4 (U_{119}=21 m/s) for different wind-wave misalignment angles.

angle between the wind and waves increases, the maximum fatigue damage decreases. Moreover, as the misalignment angle increases, the fatigue damage in the side-to-side direction due to waves also becomes noticeable. In LC2 (see Figure 6.14), which is close to the rated wind speed, a similar pattern is observed, with the maximum damage around the circumference decreasing as the misalignment angle increases. However, unlike LC1, the point of maximum damage aligns more closely with the wave direction. Furthermore, even for waves approaching from 90°, the aerodynamic loads at the rated speed in the fore-aft direction remain significant. For more severe wind and waves, such as LC4 (see Figure 6.15), dynamic responses due to waves become dominant. Larger misalignment angles between wind and waves lead to increased maximum fatigue damage. The point around the circumference experiencing the highest fatigue damage fully correlates with the wave direction.

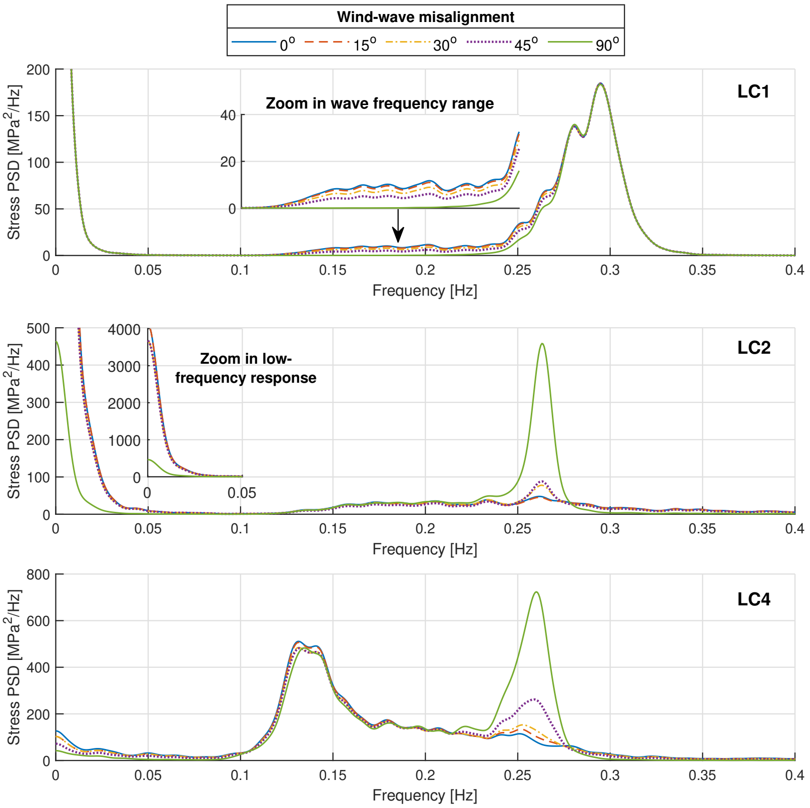

Figure 6.16: Axial stress PSD at mudline for the point of maximum fatigue damage for LC1, LC2, and LC4, for different misalignment angles

Figure 6.16 shows the axial stress spectra for three load cases (LC1, LC2, and LC4) at the mudline, at the point with the maximum fatigue damage, for different wind-wave misalignment angles. In the low-frequency range (below 0.05 - 0.1 Hz), for LC1 where the maximum damage occurs close to the wind direction (fore-aft), the responses remain the same for all misalignment angles. However, for LC2 and LC4, the responses gradually decrease as the misalignment angle increases, indicating that the maximum damage shifts from the wind direction to the wave direction (side-side). This shift is particularly noticeable for LC2 when operating close to the rated speed.

In the wave frequency range (0.1 – 0.2 Hz), the responses slightly decrease with larger misalignment angles. In unidirectional wind-waves, the soil experiences higher load levels due to the mean thrust force acting in the fore-aft direction. As a result, the soil softens, leading to slightly higher responses. For LC1, it is worth noting that at 90° misalignment, where the point of maximum damage is nonetheless in the fore-aft direction, the response in the wave frequency range is approximately zero.

In the resonance frequency range (0.25 – 0.27 Hz), for misalignment angles up to 30°, aerodynamic damping effectively attenuates the dynamic responses. However, for larger misalignment angles (45° and 90°), the contribution of aerodynamic damping becomes negligible in the wave excitation direction, and the soil becomes the primary source of damping. This is particularly significant for load cases where waves dominate the fatigue. Finally, the responses in the 3P frequency range dominate only for LC1, while for the other load cases, they decrease with larger misalignment angles. However, these responses have minor importance for these load cases.

6.3.2 Effect of foundation modelling

A comparison of the axial stress PSD between the macro-element and $p-y$ curves for different misalignment angles, indicates the importance of foundation modelling. Figure 6.17 shows LC4 in operational state with the different misalignment angles. As shown, for 0° and 15° there are negligible differences, due to the dominance of aerodynamic damping. For larger misalignment angles, the absence of aerodynamic damping in the wave excitation direction, where the maximum is found, makes foundation modelling essential for attenuating the response near the first natural frequency, with the macro-element providing with much lower stress amplitudes.

These effects are reflected in the fatigue damage relative differences between the macro-element and the $p-y$ curves, shown in Figure 6.18. Similarly as before, positive (negative) deviation implies overestimation (underestimation) of $p-y$ curves compared to the macro-element.

In LC1, relative differences between the models are negligible, because as mentioned before, the maximum fatigue damage is found in in fore-aft direction, where aerodynamic damping dominates. A similar behaviour is observed for LC2, with small differences in fatigue damage for all angles,

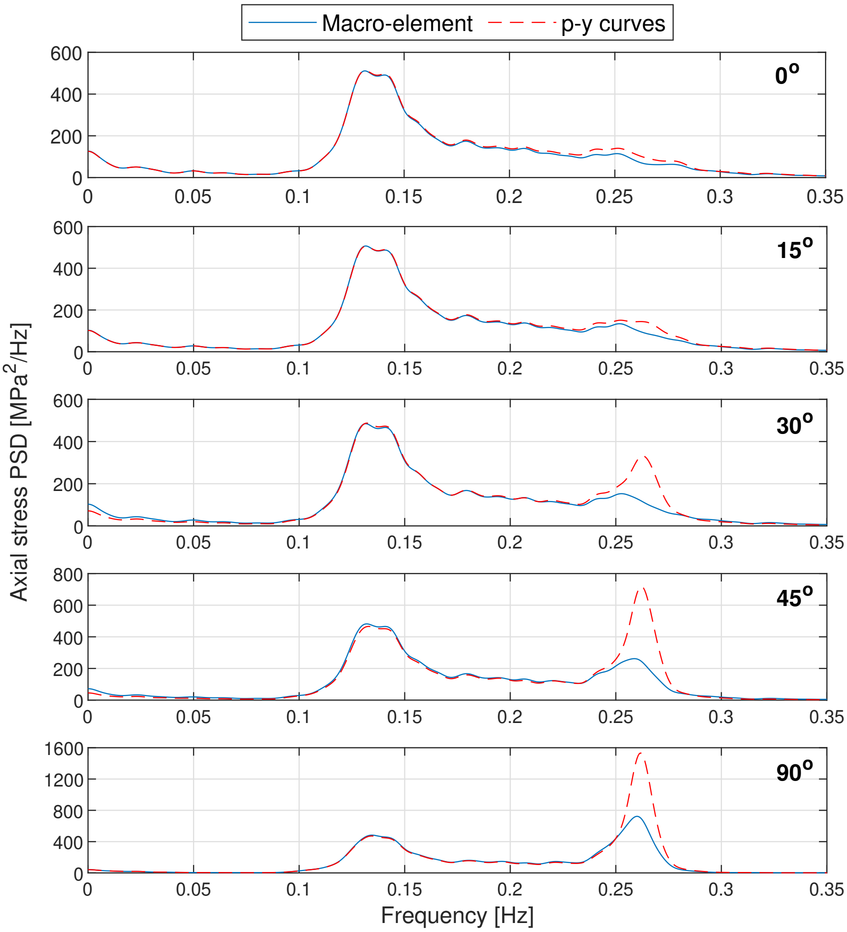

Figure 6.17: Axial stress PSD at mudline for LC4 for different misalignment angles, at the point around the circumference with the maximum fatigue damage.

except for the 90° case, where a difference about 180% was found, as the maximum damage is found close to side-side direction. For more severe LCs, for misalignment angles up to 30°, the relative difference in fatigue damage is comparable to the unidirectional wind-waves cases (aerodynamic damping is effective) with slight variations up to 20%, depending on the EC. However, for larger misalignment, the differences vary between 60% (EC4) 160% (EC3), indicating the importance of foundation modelling, in the lack of aerodynamic damping.

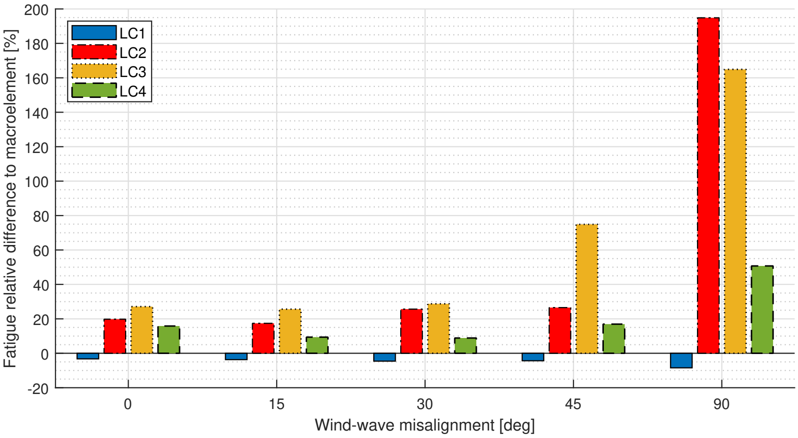

Figure 6.18: Relative difference in fatigue damage at mudline between macro-element and $p - y$ curves for different wind-wave misalignment

6.4 Effect of foundation model on long-term fatigue

The previous section focused on evaluating the impact of foundation modelling on the dynamic behaviour of of the OWTs, and the resultant short-term fatigue estimates. However, to determine the long-term effects, there are additional factors that need to be taken into account. These factors include site-specific long-term metocean conditions, the availability of individual OWTs throughout their entire lifespan, and potential long-term effects on the soil caused by OWT operation, such as soil degradation due to cyclic loading.

To investigate the impact of foundation modelling on long-term fatigue estimates, a sensitivity study was conducted using the elementary effects method, as explained in Paper 5 [222]. This study aimed to investigate various parameters, including foundation modelling, and their contribution to the uncertainty in long-term fatigue estimates. Among the different input choices considered in the time-domain load analyses, such as wave spectrum, wave spreading, turbulence model, and scour protection, it was found that foundation modelling was one of the most significant parameters influencing long-term fatigue estimates, especially for the monopile foundation up to the tower base.

Chapter 7

Extreme responses using environmental contours

The chapter investigates the effect of different statistical and load models on extreme responses of monopile-based offshore wind turbines using environmental contours. Focus is given on how using different probabilistic models for the metocean variables affects the resulting contours. Then, the effect of state-of-the-art soil and hydrodynamic models on extreme responses is identified for different operational states.

7.1 Full long-term assessment and contour method

The design of OWT foundations shall ensure that they can withstand extreme conditions. To achieve this, the Ultimate Limit State (ULS) design approach is used, which involves estimating long-term extreme responses based on characteristic values with a specified target return period [30, 59].

A commonly proposed method for estimating these long-term extreme responses is the full long-term analysis (FLTA) [58]. FLTA takes into account the variability in the environment and the short-term response, considering the contribution of all short-term conditions to the long-term response. Particularly, FLTA integrates the joint probability density function of a given environmental condition and the corresponding cumulative distribution function of the short-term extreme response. The full long-term cumulative distribution function of the structural response is obtained through this integration, shown in Eq. 7.1,

$$F_X^{LT}(\xi) = \int\int\int F_X^{ST}(\xi|u,h,t) f_{U_w,H_s,T_p}(u,h,t)\, du\, dh\, dt = 1 - P_f(\xi) \quad (7.1)$$

In Eq. 7.1, $F_X^{LT}(\xi)$ represents the long-term probability that the response X is less than or equal to ξ. $F_X^{ST}(\xi|u,h,t)$ is the short-term cumulative distribution function for $X=\xi$ for the corresponding probability density function $f_{U_w,H_s,T_p}(u,h,t)$ of environmental condition $U_w=u, H_s=h$, and $T_p=t$, and $P_f(\xi)$ is the failure probability for level ξ, typically found using FORM (First-Order Reliability Method). It's important to note that Eq. 7.1 is a common approximation used in practice, and a more complete formulation is obtained when ergodic averaging is used, see e.g. Giske et al. [133].

Eq. 7.1 provides a statistical distribution of the long-term response, considering the contributions of the short-term response under all possible environmental conditions. However, calculating this distribution requires computationally intensive time-domain simulations or model tests, which can be impractical for large numbers of conditions [86]. To address this, alternative approaches such as the environmental contour method are commonly used. In this thesis, contours are estimated using IFORM (Inverse FORM) [92], which involves solving the inverse problem of finding the characteristic response level ξ that corresponds to a given failure probability $P_f(\xi)$. Environmental contours represent the set of environmental conditions that are likely to result in a specific extreme response level, decoupling the structural response from the environment.

To establish N-year environmental contours, the target exceedance probability P_f is defined based on the desired return period T_N, expressed in hours of stationary sea states [96], and the duration of a stationary sea-state τ (e.g., 1 or 3 hours) in the hindcast data, as shown in Eq. 7.2,

$$P_f = \frac{\tau}{T_N}. \tag{7.2}$$

The reliability index β is then calculated using FORM theory from Eq. 7.3,

$$\beta = \Phi^{-1}\left(1-P_f\right) = \Phi^{-1}\left(1-\frac{\tau}{T_N}\right), \tag{7.3}$$

where $\Phi^{-1}(\cdot)$ denotes the inverse standard CDF. Given the reliability index, an environmental contour can be established based on a joint probabilistic model of metocean conditions using IFORM. The following sections describe the procedure and how using different probabilistic models for the metocean variables affects the resulting contours.

7.2 Joint environmental distribution

To establish environmental contours, a probabilistic model needs to be fitted to the metocean data. In this study, the conditional modelling approach was used [106, 108]. The joint probability distribution of the metocean variables was expressed as the product of their individual probability density functions. Specifically, the joint probability distribution is given by Eq. 7.4,

$$f_{U_{hub},H_s,T_p}(u,h,t) = f_{U_{hub}}(u) \cdot f_{H_s|U_{hub}}(h|u) \cdot f_{T_p|U_{hub},H_s}(t|u,h), \tag{7.4}$$

where $f_{U_{hub}}(u)$ represents the marginal distribution fitted for the wind speed data at hub height, $f_{H_s|U_{hub}}(h|u)$ is the conditional model fitted to H_s for a given wind speed, and $f_{T_p|U_{hub},H_s}(t|u,h)$ is the conditional model fitted to T_p for given wind speed and significant wave height.

The combined sea data, which includes both wind-sea and swell components, were used for fitting the probabilistic model. Fitting the joint distribution model poses additional challenges due to the different sea characteristics of the two components, which are particularly evident for lower and intermediate wind classes. These challenges also affect the shape of the resulting contours, which will be discussed further in Sec. 7.3.

The $H_s - T_p$ data were sampled based on the wind speed at hub height using the power law. As a result, the data contained within the same wind class may slightly differ between the 10 MW and 15 MW turbine models. Consequently, the fitted conditional distributions and resulting contours may also exhibit slight variations between the two models. However, similar conclusions can be applied to both cases. Therefore, the conditional distributions of H_s (Sec. 7.2.2) and T_p (Sec. 7.2.3) are only shown for the 10 MW OWT.

7.2.1 Wind speed marginal distribution

The 1-hour mean wind speed U_{hub} was calculated from the 10 m data using power law with exponent $\alpha = 0.14$, and was modelled using the Weibull distribution defined by Eq. 7.5,

$$f_{U_{hub}}(u) = \frac{\kappa_u}{A_u}\left(\frac{u-\gamma_u}{A_u}\right)^{\kappa_u - 1} \exp\left[-\left(\frac{u-\gamma_u}{A_u}\right)^{\kappa_u}\right]. \tag{7.5}$$

Parameters κ_u, A_u and γ_u denote the shape, scale and location parameters, respectively. Both a 2-parameter ($\gamma_u = 0$) that is more common in the literature, see e.g. [108–110], and a 3-parameter model were used. The maximum likelihood method was applied for the fitting. Figure 7.1 shows the histograms for wind speed data at 119 m and 150 m with the probability density functions and Weibull plots of U_{hub} marginal distributions.

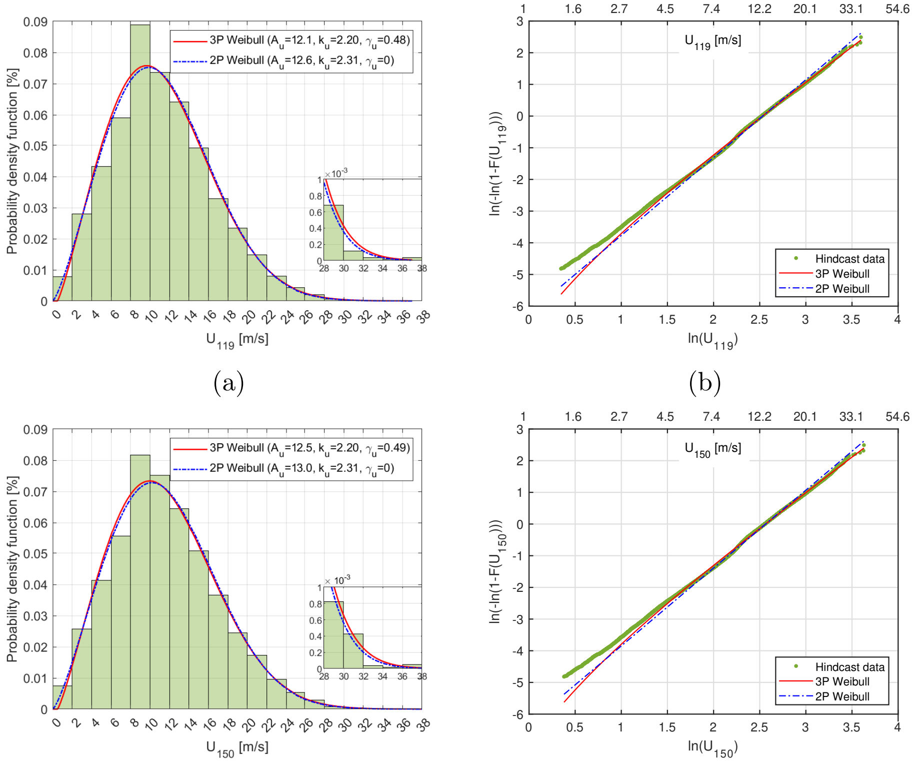

(a) (b)

(c) (d)

Figure 7.1: (a),(c) Probability density functions of U_{119} and U_{150} data. (b),(d) Weibull plots of U_{119} and U_{150} empirical and fitted distributions.

The fitted parameters are also indicated. Good agreement between the data and the fitting models was obtained, with negligible difference for wind speeds lower than 3.0 m/s, which are not considered important for the purposes of constructing environmental contours for extreme responses. In the upper tail, the 3-parameter distribution was slightly more conservative for both cases, and it was used for the rest of the study.

7.2.2 Significant wave height conditional distribution

Different distributions can be found in the literature for modelling H_s data. Previous studies have shown that H_s can be modelled reasonably well by 2-

or 3-parameter Weibull distributions, which have been used extensively in the literature [85, 101, 102, 107, 108, 110–115, 117]. Other distributions have been proposed, such as Ochi [223], generalized Gamma [223], 3-parameter beta [224] models. Finally, a hybrid model incorporating a log-normal and a Weibull distribution, usually called as LonoWe distribution was introduced by Haver et al. [103] and can be found in the literature [143].

7.2.2.1 Probabilistic models

In this study, four models were adopted for the conditional distribution of H_s given U_{hub}: a 2 parameter Weibull model, a 3-parameter Weibull model, where the fitted parameters were estimated using two different methods, and a LonoWe model. Wave data were sampled in wind classes with bin size of 2 m/s, associated with the mean wind speed at hub height, U_{hub}.

The 2-parameter Weibull distribution is given in Eq. 7.6,

$$f_{H_s|U_{hub}}(h|u) = \frac{\kappa_h^{2p}}{A_h^{2p}} \left(\frac{h}{A_h^{2p}}\right)^{\kappa_h^{2p}-1} \exp\left[-\left(\frac{h}{A_h^{2p}}\right)^{\kappa_h^{2p}}\right] \tag{7.6}$$

where κ_h^{2p}, A_h^{2p} are the shape and scale Weibull parameters, respectively.

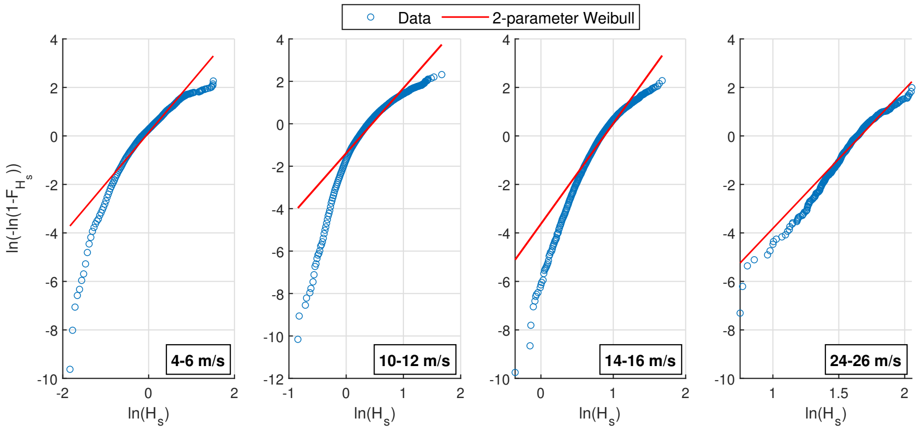

Figure 7.2: 2-parameter Weibull and empirical cumulative distributions for H_s within different wind classes

Figure 7.2 shows Weibull probability plots of the empirical data and the fitted 2-parameter Weibull cumulative distributions for different wind classes.

The plot highlights notable discrepancies between the analytical model and the hindcast data, particularly in the low and upper tails of the distribution. These findings are consistent with similar observations documented in the literature, e.g. [102, 143, 225], which also reported the insufficiency of 2-parameter distributions for H_s. The deviations were more pronounced in lower and intermediate wind classes, as the model was inadequate to capture the mixed nature of the data (wind-sea and swell) with distinct characteristics, making it challenging for the 2-parameter Weibull model to accurately capture the full range of variability in H_s. However, for higher wind classes where the sea states are predominantly wind-driven for the site considered, the 2-parameter Weibull model provided a more reasonable fit to the data.

A 3-parameter Weibull model was also employed to fit the data. The parameters were estimated using two methods: Maximum Likelihood Estimate (MLE) and Method of Moments (MoM). The conditional model fitted to H_s for a given wind class is given by Eq. 7.7:

$$f_{H_s|U_{hub}}(h|u) = \frac{\kappa_h^{3p}}{A_h^{3p}} \left(\frac{h-\gamma_h^{3p}}{A_h^{3p}}\right)^{\kappa_h^{3p}-1} \exp\left[-\left(\frac{h-\gamma_h^{3p}}{A_h^{3p}}\right)^{\kappa_h^{3p}}\right] \tag{7.7}$$

Here, κ_h^{3p}, A_h^{3p}, and γ_h^{3p} represent the shape, scale, and location parameters of the Weibull distribution, respectively. The parameters of $f_{H_s|U_{hub}}(h|u)$ were estimated using the Maximum Likelihood Estimate (MLE) by maximizing the log-likelihood function of the H_s sample data, see e.g. [140]. Using the MoM, the distribution parameters of $f_{H_s|U_{hub}}(h|u)$ were estimated to match the observed moments of the H_s data in the wind class. To estimate the parameters for the MoM method, the expected value (μ_{H_s}), the variance ($\sigma_{H_s}^2$) and the skewness coefficient (γ_{H_s}) - the first three moments - of H_s data for each wind class were estimated and then replaced in the Eqs 7.8, 7.9, and 7.10 respectively,

$$\mu_{H_s} = \gamma_{3p} + A_{3p}\Gamma\left(1+\frac{1}{\kappa_{3p}}\right) \tag{7.8}$$

$$\sigma_{H_s}^2 = A_{3p}^2\left[\Gamma\left(1+\frac{2}{\kappa_{3p}}\right) - \Gamma^2\left(1+\frac{1}{\kappa_{3p}}\right)\right] \tag{7.9}$$

$$\gamma_{H_s} = \frac{\Gamma\left(1+\frac{3}{\kappa_{3p}}\right) - 3\Gamma\left(1+\frac{1}{\kappa_{3p}}\right)\Gamma\left(1+\frac{2}{\kappa_{3p}}\right) + 2\Gamma^3\left(1+\frac{1}{\kappa_{3p}}\right)}{\left[\Gamma\left(1+\frac{2}{\kappa_{3p}}\right) - \Gamma^2\left(1+\frac{1}{\kappa_{3p}}\right)\right]^{3/2}} \tag{7.10}$$

Figure 7.3 shows the fitting of the 3-parameter Weibull model, along with the empirical cumulative distributions for H_s in different wind classes. Incorporating the additional (location) parameter in the 3-parameter Weibull model improves the fit to the data, particularly in capturing the low and upper tails of the distribution, compared to the 2-parameter Weibull model. However, its behaviour, especially in the lower and upper tails, depends on the method used to estimate the fitted parameters. When using the MLE method, the distribution parameters are primarily driven by the bulk of the data, with less emphasis on the tails. This results in non-conservative models, disregarding some severe sea states. This effect was particularly pronounced in lower and intermediate wind classes, where the dataset contains a large number of small or moderate sea states and only a few severe sea states, mainly originating from the swell component.

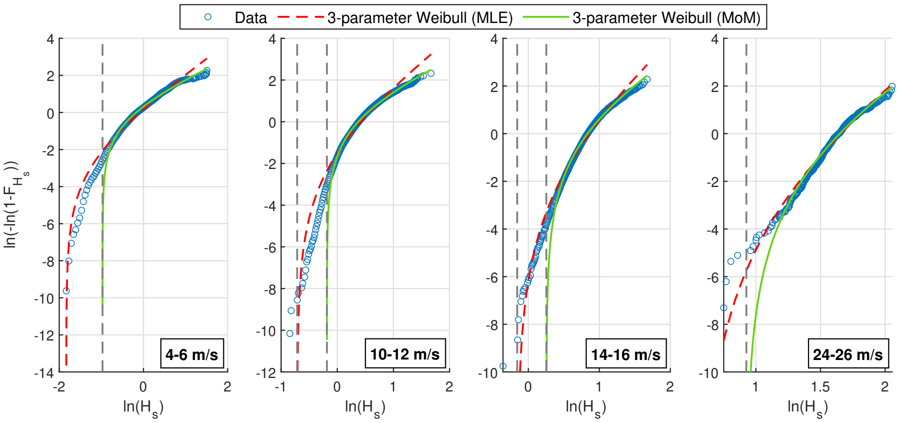

Figure 7.3: 3-parameter Weibull and empirical cumulative distributions for H_s within different wind classes. Vertical dashed lines indicate the location parameter of the fitted models.

In contrast, the Method of Moments (MoM) tends to capture the characteristics of the upper-tail behaviour of the data more accurately when estimating the distribution parameters. Consequently, MoM provided a better fit for the upper tail and resulted in more conservative models across all wind classes. The differences between the models, especially in the upper tail, were more significant in low and intermediate wind classes, whereas less variations were observed for high wind classes. It is important to emphasize that although the differences between the fitted models may appear small in the Weibull probability plot, they have a substantial impact on the resulting contours, as discussed in further detail in Sec. 7.3.1.

The LonoWe distribution was also employed to model the conditional distribution $f_{H_s|U_{hub}}(h|u)$ for each wind class. The LonoWe distribution was first introduced using a 2-parameter Weibull distribution. In the present study, the LonoWe model combines a Log-normal distribution for $h \leq \eta$ and a 3-parameter Weibull distribution for $h > \eta$, as described in Eq. 7.11.

$$f_{H_s|U_{hub}}(h|u) = \begin{cases} \frac{1}{\sqrt{2\pi}\sigma_h h} \exp\left[-\frac{(\ln(h)-\mu_h)^2}{2\sigma_h^2}\right], h \leq \eta \\ \frac{\kappa_h}{A_h}\left(\frac{h-\gamma_h}{A_h}\right)^{\kappa_h - 1} \exp\left[-\left(\frac{h-\gamma_h}{A_h}\right)^{\kappa_h}\right], h > \eta \end{cases} \tag{7.11}$$

The Log-normal distribution is characterized by its mean (μ_h) and variance (σ_h^2) of $\ln(h)$. The Weibull distribution is defined by its shape (κ_h), scale (A_h), and location (γ_h) parameters. The LonoWe model is relatively complex compared to the others. Firstly, more parameters need to be estimated, and secondly, there is no clear procedure to determine the transition point η between the two distributions, which is usually chosen arbitrarily.

To determine the transition point η between the two distributions, first, a Log-normal distribution was fitted to the data for $h \leq \eta$. Then, the Weibull parameters were estimated using the non-linear least square method by ensuring the continuity of the density function, $f_{H_s|U_{hub}}(h|u)$ and the cumulative distribution function, $F_{H_s|U_{hub}}(h|u)$, at $h = \eta$. The goal was to find the value of η that minimizes the root mean square error (RMSE) between the model and the data. The RMSE serves as a measure of the goodness-of-fit between the LonoWe model and the observed data for each wind class.

Different values of η were investigated for each wind class. Lower values of η imply that the majority of the H_s data within the wind class is modelled using the 3-parameter Weibull distribution, with only a small portion modelled using the Log-normal distribution. Conversely, higher values of η indicate a larger portion of the data being modelled with the Log-normal distribution. The specific value of η chosen for the LonoWe distribution was defined based on the minimum RMSE between the model and the data, ensuring the best overall fit for the given wind class.

Figure 7.4 shows the RMSE values between the fitted $f_{H_s|U_{hub}}(h|u)$ and the data for different values of η. The plot depicts that the RMSE is highest for lower values of η and gradually decreases as η increases. In some wind classes, such as 10-12 m/s, a minimum RMSE value is achieved at a specific η value. However, for other wind classes, like 14-16 m/s and 24-26 m/s, the

RMSE continues to decrease without reaching a clear minimum, indicating that the choice of η is not straightforward. Consequently, although RMSE provides a useful indication of the fitting quality of the LonoWe model, further investigation is needed to determine the optimal value for η.

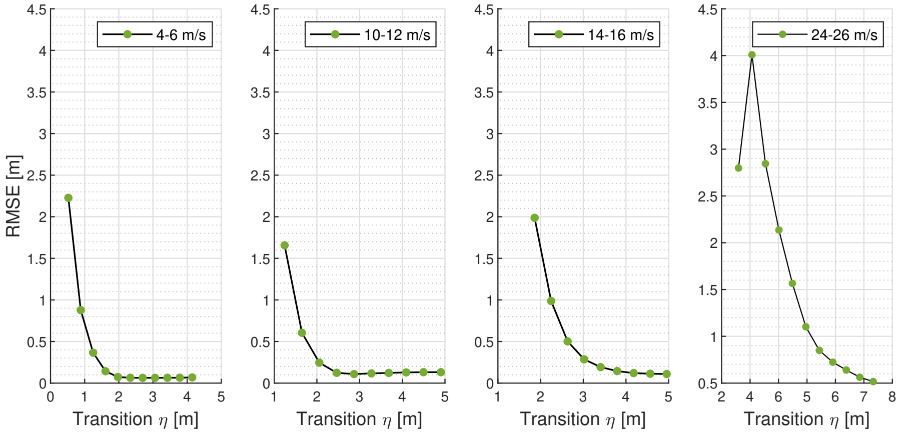

Figure 7.4: RMSE value between the LonoWe model and the data for various wind classes, using different transition points η.

Figure 7.5 shows the empirical and the fitted LonoWe cumulative distributions for two wind classes, considering different values of η. LonoWe had the same behaviour for all wind classes. For low values of η, the LonoWe model cannot capture the characteristics of the data, as indicated by the large RMSE values. As η increases, the model gradually improves, better capturing the behaviour of the lower and upper tails of the distribution.

However, with larger η, the amount of data used to fit the Weibull part of the LonoWe model decreases, leading to increased uncertainty in the fitted model. If an accurate probabilistic model for the whole range of H_s within a wind class is of interest, then it is essential to select a value for η that ensures an adequate amount of data is available for fitting both the Log-normal and Weibull distributions, avoiding extremely low or high values of η. When extreme responses are of interest, focus should be given on fitting only the high quantiles of H_s [226], omitting the bulk of the data, while η can be chosen based on a quantity that better indicates the quality of the fit at the upper tail, and not RMSE, which is a measure of fit to all observations.

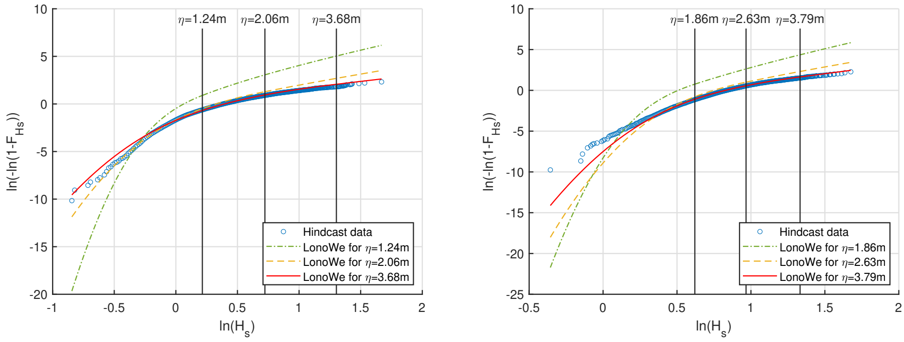

(a) 10-12 m/s (b) 14-16 m/s

Figure 7.5: LonoWe cumulative distributions for H_s for different transition η values between the Log-normal and Weibull distributions.

7.2.2.2 Dependence structure

The dependence structure used in this study is typically used in literature and recommended in the design standards [30, 59]. The dependence functions for the scale, shape, and location parameters for Weibull models were described by the power function given the wind speed data within a wind class, shown in Eq. 7.12,

$$\begin{aligned} A &= c_1 + c_2 \cdot u^{c_3} \\ k &= d_1 + d_2 \cdot u^{d_3} \\ \gamma &= e_1 + e_2 \cdot u^{e_3} \end{aligned} \tag{7.12}$$

where parameters $c_{i=1,2,3}, d_{i=1,2,3}, e_{i=1,2,3}$ were estimated using nonlinear curve-fitting based on least-squares, and u represents the wind speed data within each wind class. Figure 7.6 shows an example of the fitted parameters of the dependence function for the Weibull models. As shown, the MLE method resulted in larger shape and scale parameters for all wind classes, while the MoM predicted larger values for the location parameter (γ_h), also observed from Figure 7.3, leading to a worse fit at the lower tail of the data. The dependence functions for the Log-normal parameters of the LonoWe distribution are given in Eq. 7.13,

$$\begin{aligned} \mu_h &= m_1 + m_2 \cdot u^{m_3} \\ \sigma^2 &= s_1 + s_2 e^{(s_3 \cdot u)} \end{aligned} \tag{7.13}$$

where $m_{i=1,2,3}, s_{i=1,2,3}$ are the parameters of the power and exponential functions, respectively.

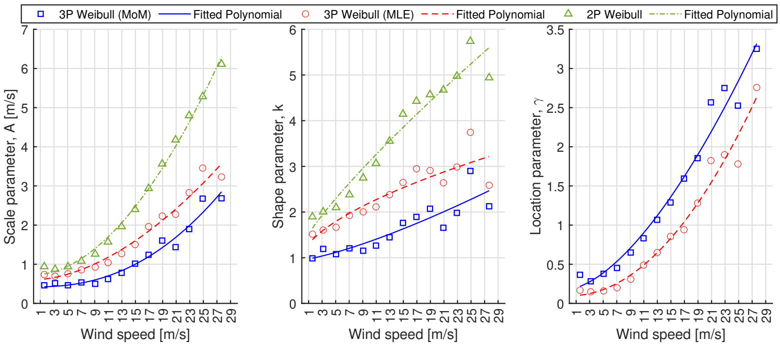

Figure 7.6: Weibull parameters and fitted polynomials for $f_{H_s|U_{hub}}(h|u)$ for Weibull models (10 MW - U_{hub}=119 m)

7.2.3 Peak period conditional distribution

In previous studies, it has been commonly assumed that the conditional distribution of T_p given H_s follows a log-normal distribution when considering only wave data [103, 106–108]. A method to establish the conditional distribution for T_p given U_{hub} and H_s was developed by Johannessen [227], and it has been used in other studies [113, 143]. However, as mentioned by Li et al. [143], the process of obtaining the distribution of T_p conditionally on both H_s and U_w is challenging following the methods described by Johannessen, as it is not straightforward to identify a reasonable relationship between the distribution parameters, and moreover, the raw data indicated that the dependency of the distribution parameters for T_p on U_w is limited. Therefore Johannessen's method was not employed in the thesis.

Two models were evaluated for the conditional distribution of T_p given U_{hub} and H_s: a log-normal, and a 3-parameter Weibull distribution shown in Equations 7.14, and 7.15, respectively,

$$f_{T_p|U_{hub},H_s}(t|u,h) = \frac{1}{\sqrt{2\pi}\,\sigma_t t}\exp\left[-\frac{(\ln(t)-\mu_t)^2}{2\sigma_t^2}\right], \tag{7.14}$$

$$f_{T_p|U_{hub},H_s}(t|u,h) = \frac{\kappa_t}{A_t}\left(\frac{t-\gamma_t}{A_t}\right)^{\kappa_t-1}\exp\left[-\left(\frac{t-\gamma_t}{A_t}\right)^{\kappa_t}\right] \tag{7.15}$$

In both equations, $f_{T_p|U_{hub},H_s}(t|u,h)$ represents the conditional probability density function of T_p given U_{hub} and H_s. In Eq. 7.14, μ_t and σ_t^2 are the mean and variance of $\ln(t)$ of the log-normal model and κ_t, A_t, γ_t denote the shape, scale and location Weibull parameters, respectively. The process of fitting the peak period (T_p) to the combined data is challenging due to the distinct characteristics of the wind-sea and swell components. Furthermore, there is usually a limited amount of T_p data available, particularly in the upper range of the period distribution, which poses an additional challenge for fitting the conditional distribution $f_{T_p|U_{hub},H_s}(t|u,h)$. Figure 7.7a shows the scatter density plots illustrating the site-specific hindcast data for the wind-driven and swell components. It is evident that swell is characterized by long wave periods and primarily consists of moderate sea states with H_s mostly below 6 m. On the contrary, the wind-sea component follows a different trend, closer to the wave steepness limit [59], with increasing severity for larger wind speeds.

Wave data characteristics for different wind speeds are also shown in colour density plots of H_s and T_p Figure 7.7b for low, intermediate, and high wind speeds. In the case of low and moderate wind speeds, there is a significant mixture of severe sea states originating from swell, while the wind-sea component consists of relatively small waves with short periods. As the wind speed increases, the wave steepness and the associated wave heights and periods gradually increase. For high wind speeds, severe sea states are primarily wind-driven. These observations highlight the distinct characteristics of wind-sea and swell components, indicating the challenges involved in accurately fitting the conditional distribution of T_p given U_{hub} and H_s.

7.2.3.1 Assessment of T_p probabilistic models and contours compared to wave steepness limit

While there is no distinct theoretical line defining a lower bound for the T_p as a function of H_s, there is a zone below which certain sea states cannot exist. This lower limit is typically described by empirical wave steepness limits [59], as Figure 7.7 depicts. The lower limit of wave steepness is affected by various factors such as wave breaking, the magnitude and duration of wind speeds, effective fetch length, and the combined nature of wind-sea and swell components. Wave breaking plays a crucial role in dissipating wave energy and setting a limit on the steepness of waves. For larger waves, the effects of wind and fetch length on the maximum steepness become more significant.

The physical limit of wave steepness is generally not considered during the establishment of probability distributions and environmental contours. Consequently, non-physical H_s-T_p combinations can be present in these contours, leading to unrealistic loading conditions. This may result from multiple reasons, such as that the marginal and conditional models may be misspecified,

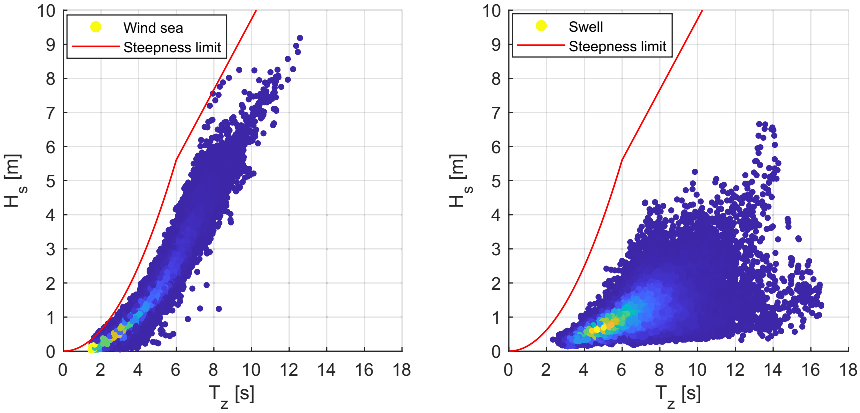

(a) Site-specific $H_s - T_z$ data for the wind-sea and swell components. Average steepness limiting values plotted for T_z [59]

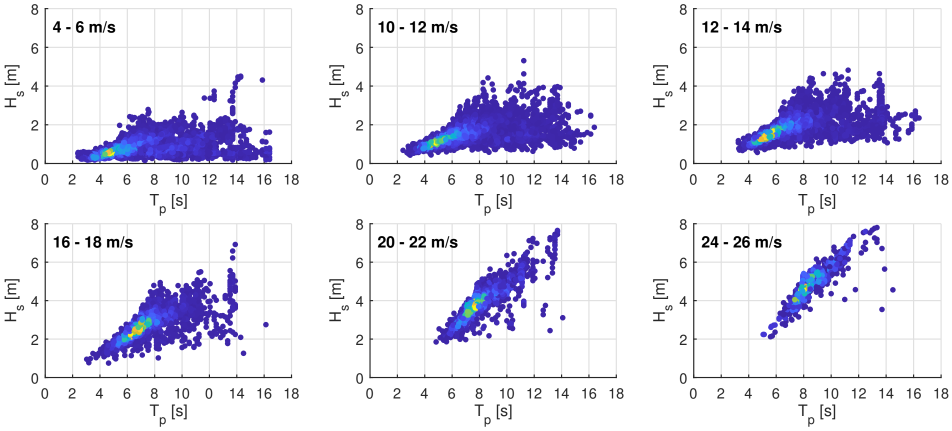

(b) $H_s - T_p$ colour density plots for different wind speeds

Figure 7.7: Wind-sea, swell, and combined sea data characteristics. Colour in the hindcast data indicates the density of points.

i.e. they are not an accurate fit for the data or the assumed dependence structure for conditional model parameters may not be appropriate. Furthermore, one reason is the uncertainty in parameter estimates due to finite sample size, particularly for cases with limited amount of data [228]. To address this concern, the IEC standard [30] recommends including the influence of a possible upper limit on H_s in the joint environmental model, or after establishing the contours to prevent excessively large values.

The average wave steepness for irregular sea states, denoted as S_p, is defined as the ratio of H_s to the peak wavelength (λ_p). The limiting values of wave steepness can be chosen as shown in Eq. 7.16, and linear interpolation can be used between the boundaries,

$$S_p = \begin{cases} 1/15, & \text{for } T_p \leq 8\ s \\ 1/25, & \text{for } T_p \geq 15\ s \end{cases} \tag{7.16}$$

Wave length can be calculated from the deep-water dispersion relation, shown in Eq. 7.17. However, due to the shallow depth of the location ($d = 30$ m), the deep-water wave length cannot be used directly, and the intermediate depth dispersion relation should be used to estimate the wave length λ_p, given in Eq. 7.18.

$$\lambda_p = \frac{g}{2\pi} \cdot T_p^2 \tag{7.17}$$

$$\left(\frac{2\pi}{T_p}\right)^2 = \frac{2\pi g}{\lambda_p} \tanh\left(\frac{2\pi d}{\lambda_p}\right) \tag{7.18}$$

Figure 7.8 illustrates $f_{T_p|U_{hub},H_s}(t|u,h)$ for two wind classes, namely 10-12 m/s and 24-26 m/s. Using a 3-parameter Weibull model for the conditional distribution of the peak period introduces a lower limit (the location parameter), generally capturing the lower limit of T_p for different H_s classes within each wind class. The challenge of fitting due to the limited amount of data, particularly for the case of the high wind class, can also be observed.

Additionally, Figure 7.9 displays the location parameter γ_t for all the 3-parameter Weibull distributions fitted to the T_p data across the wind classes. The steepness limit is also indicated in the plot. As shown, the lower values of the location parameter closely follow the trend of the steepness curve, capturing the behaviour of the hindcast data.

In Sec. 7.3.2, the resultant contours are compared to the steepness curves as obtained using the deep-water and intermediate wavelength relationship, to evaluate the adequacy of the T_p conditional Weibull and Log-normal models mainly at the steep side of contours, and ensure that subsequent design sea states remain within realistic ranges.

7.3 Environmental contours using IFORM

Having established the joint distribution of metocean parameters for each wind class, a contour corresponding to a given return period can be estab-

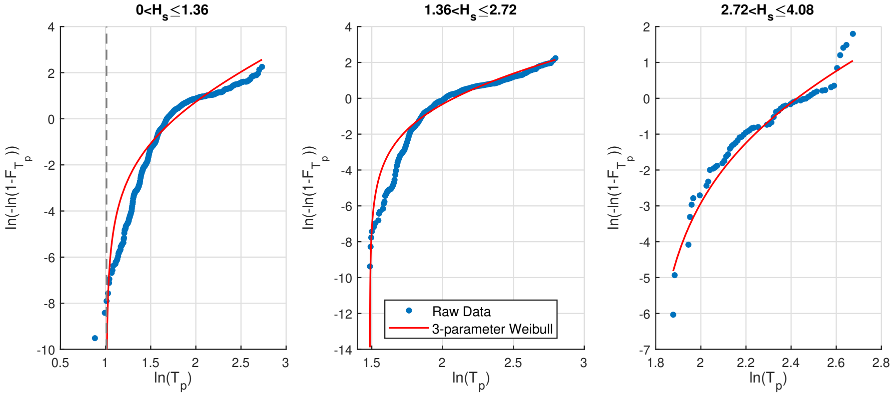

(a) 10-12 m/s

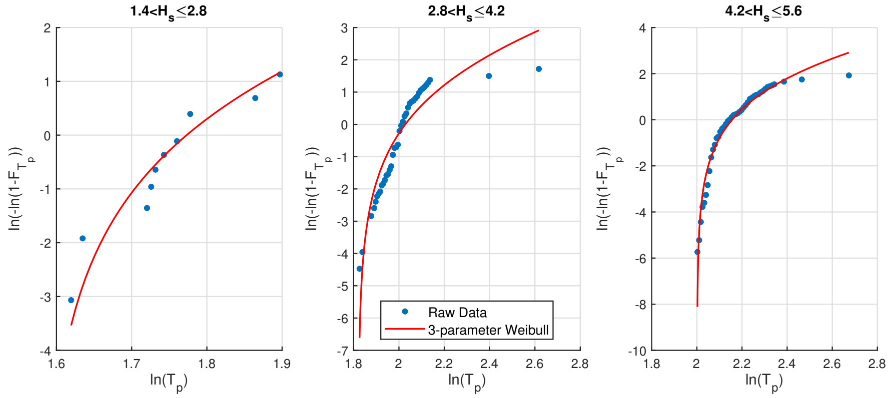

(b) 24-26 m/s

Figure 7.8: Hindcast data and 3-parameter Weibull conditional distribution for T_p

lished. The joint probability model in the physical space (X-space) is transformed to the standard Gaussian normalised U-space based on the Rosenblatt transformation [229]. This transformation maps the environmental variables in the physical space (U_{hub}, H_s, T_p) to uncorrelated normally distributed variables (U_1, U_2, U_3), based on Eq. 7.19:

$$\begin{aligned} \Phi\left(u_1\right) &= F_{U_{hub}}(u) \\ \Phi\left(u_2\right) &= F_{H_S|U_{hub}}(h|u) \\ \Phi\left(u_3\right) &= F_{T_p|U_{hub},H_s}(t|u,h) \end{aligned} \tag{7.19}$$

Here, $\Phi(\cdot)$ is the standard normal CDF, and $F(\cdot)$ denotes the CDFs of U_{hub},

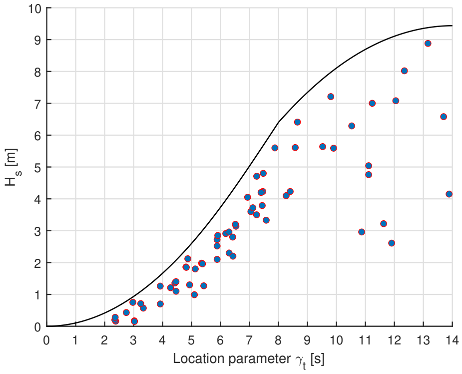

Figure 7.9: Location parameter γ_t for all the 3-parameter Weibull distributions fitted for T_p data. Steepness limit is also indicated.

H_s, T_p, respectively. Eq. 7.19 establishes a unique connection between variables (u, h, t) and (u_1, u_2, u_3), Consequently, the U-space variables can be back-transformed to the physical space using Eq. 7.20,

$$\begin{aligned} u &= F^{-1}_{U_{hub}}\left[\Phi\left(u_1\right)\right] \\ h &= F^{-1}_{H_s|U_{hub}}\left[\Phi\left(u_2\right)\right] \\ t &= F^{-1}_{T_p|U_{hub},H_s}\left[\Phi\left(u_3\right)\right]. \end{aligned} \tag{7.20}$$

In the Gaussian space, points with constant probability density define a sphere with a radius equal to the reliability index, β, as given in Eq. 7.21,

$$\beta = \sqrt{u_1^2 + u_2^2 + u_3^2}. \tag{7.21}$$

Based on Eq. 7.21, the $H_s - T_p$ contours for a wind class in the Gaussian space are slices of the sphere in the $U_2 - U_3$ plane. The lower and upper limits of these contours correspond to the limits of the wind class in the physical space. In the thesis, these slices for a wind class $k$were approximated by circles of radius r_k, using the mean value of the wind speed data, denoted as $\overline{u}_k$. Using Eq. 7.21 and the Rosenblatt transformation in Eq. 7.19, the radius r_k for a wind class is given in Eq. 7.22

$$r_k = u_2^2 + u_3^2 = \sqrt{\beta^2 - u_{1,k}^2} = \sqrt{\beta^2 - \left[\Phi^{-1}\left(F_{U_{hub}}\left(u = \overline{u}_k\right)\right)\right]^2} \tag{7.22}$$

Considering a sea-state event duration of $\tau = 1$ hour in the hindcast data and a return period of $T_N = 50$ years, the value of β is calculated as $\beta = 4.58$

using Eq. 7.21. Figure 7.10 illustrates the contour sphere with radius β and contour circles of radius r_k representing various wind classes k. Additionally, Figure 7.11 displays the contours for different target return periods T_N in both Gaussian and physical space, along with the class data.

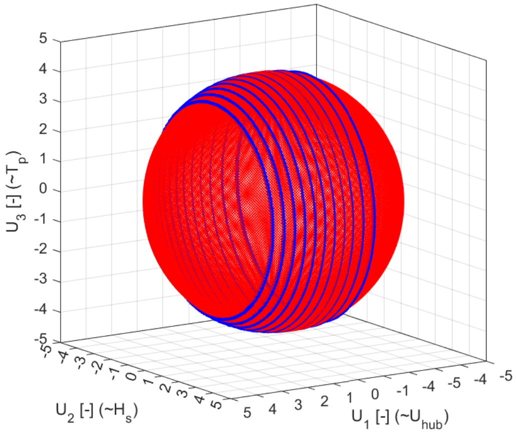

Figure 7.10: 50-year contour sphere with radius β and contour circles of radius r_k for various wind classes k in Gaussian U-space.

An alternative to using the mean value $\overline{u}$ in Eq. 7.22 would be to use the upper (U_k^{ub}) or the lower (U_k^{lb}) limit of the wind class. Figure 7.12 shows that the choice between these options has little effect on the resultant contours, for a 2 m/s width of the wind classes. A smaller width could be used, but that would reduce the number of observations in the wind classes, increasing the uncertainty in the fitting of the conditional distributions for H_s and T_p.

7.3.1 Effect of H_s conditional distributions on contours

Figures 7.13, 7.14, and 7.15 illustrate the impact of different conditional H_s models on the 50-year contours for different wind classes, for 10 MW and 15 MW models. The $H_s - T_p$ scatter density plots are shown, along with the steepness limits based on the deep- and intermediate-water depth dispersion relationships. The Weibull model is used for T_p in these plots.

The results demonstrate that the 2-parameter Weibull model results in significant discrepancies, as described in Sec. 7.2, leading to less conservative contours with inaccurate representation of the extreme sea states. The effect is pronounced for moderate wind classes characterized by mild sea states

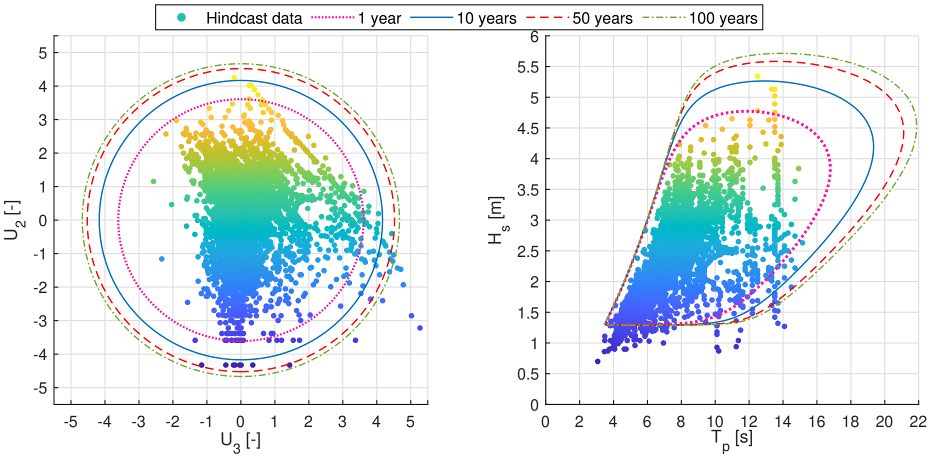

(a) 14-16 m/s

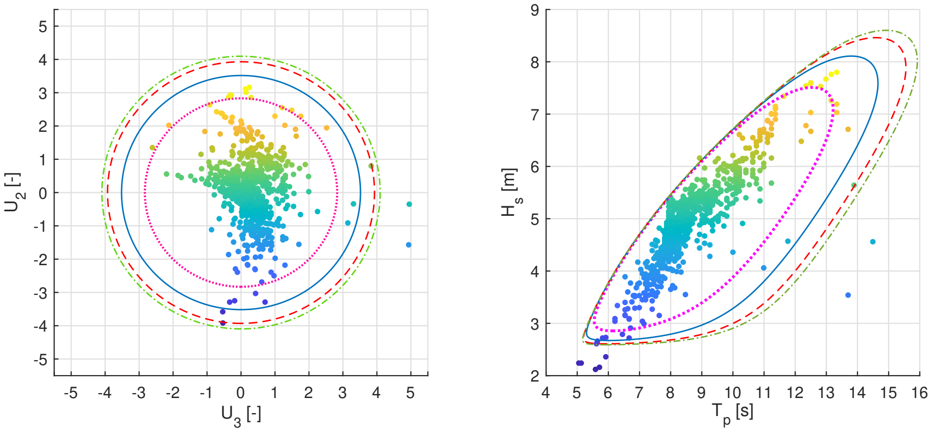

(b) 24-26 m/s

Figure 7.11: Contour circles in Gaussian and physical space for different return periods, for two wind classes.

with only a few severe observations originating from the swell. Similarly, the 3-parameter Weibull model using Maximum Likelihood Estimation (MLE) underestimates severe extreme sea states for these wind classes, as it estimates the model's parameters based on the entire data set within the wind class rather than specifically targeting the tail of the distribution. In contrast, the Method of Moments (MoM) approach for estimating the distribution parameters focuses on the upper tail of the data, resulting in more accurate contours for H_s that align well with the extreme wave heights

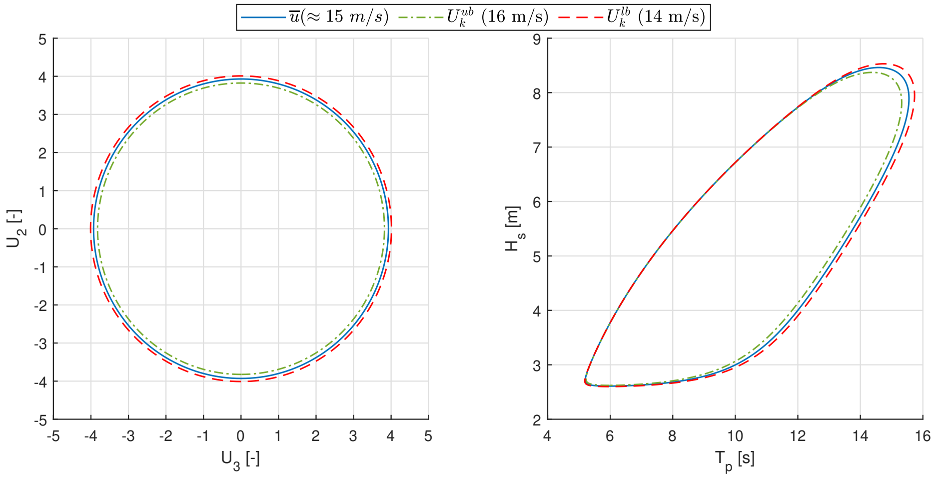

Figure 7.12: Contours in Gaussian and physical space for wind class 14-16 m/s, using different values of u (Eq. 7.22).

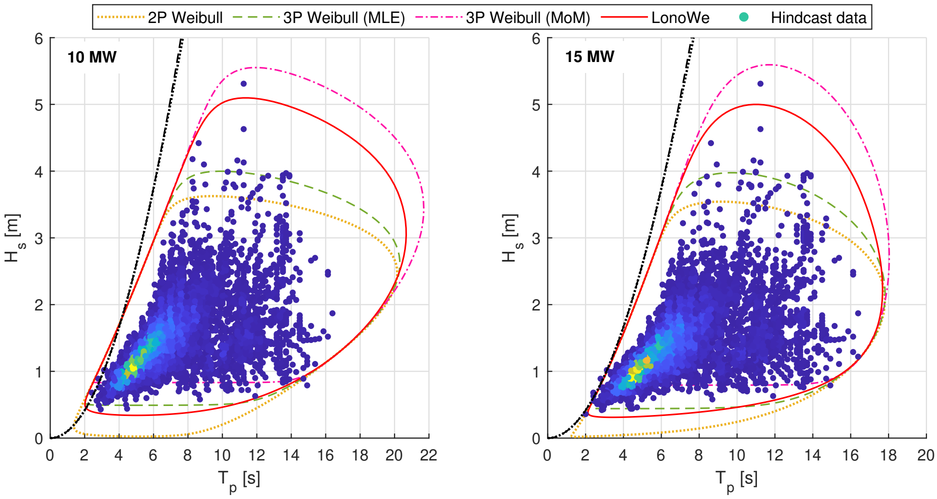

Figure 7.13: 50-year contours for wind class 10-12 m/s for 10 MW and 15 MW models

suggested by the hindcast data across all wind classes. The discrepancies between the different models are most notable for wind classes with moderate wind speeds due to the combined nature of sea states in these conditions. However, as wind speeds increase, the differences between the models become less significant.

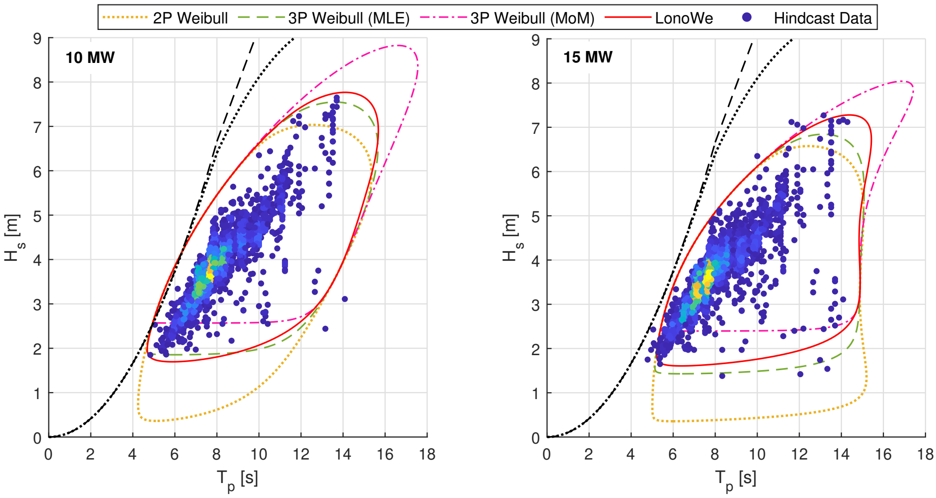

Figure 7.14: 50-year contours for wind class 20-22 m/s for 10 MW and 15 MW models

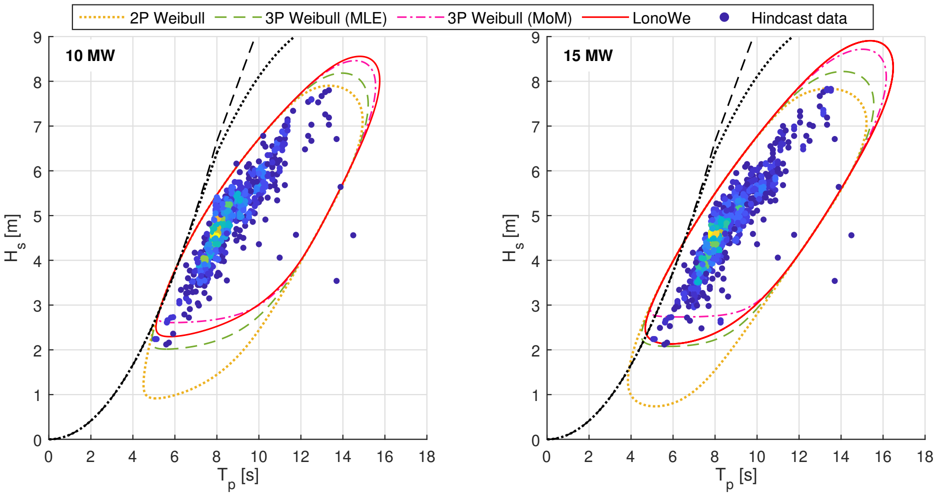

Figure 7.15: 50-year contours for wind class 24-26 m/s for 10 MW and 15 MW models

Additionally, the behaviour of the LonoWe model is sensitive to the selection of the transition point (η), as depicted in Figure 7.5. The accuracy of the resulting contours, particularly concerning extreme sea states, is noticeably affected by the choice of η. Figure 7.16 shows an example of two wind classes, where the LonoWe model leads to notably different contours depending on the transition point η, with some values of η leading to under-conservative contours that do not align well with the data within the wind classes.

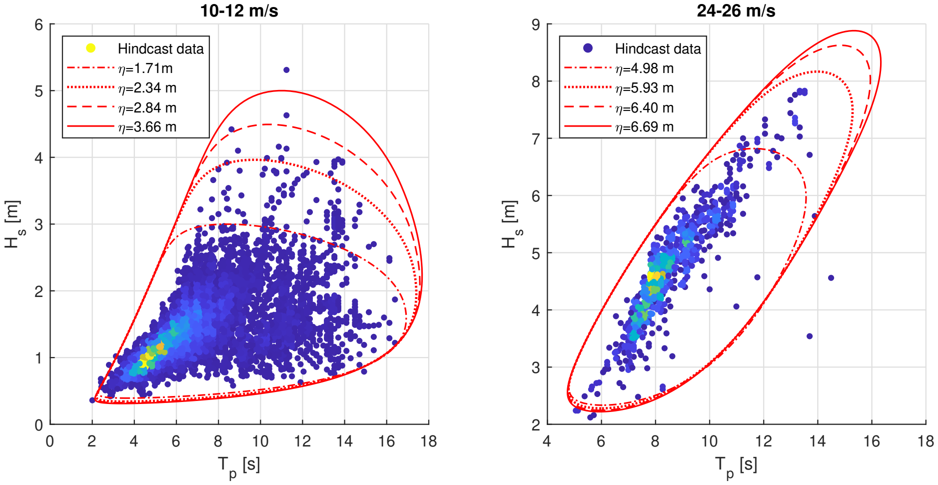

Figure 7.16: 50-year contours using LonoWe model with various values of the transition point η, between the Log-normal and Weibull models (15 MW OWT).

7.3.2 Effect of T_p conditional distributions on contours

Establishing the conditional distribution of peak period (T_p) is challenging due to the presence of wind-driven and swell components, which have distinct characteristics, as shown in the scatter density plots of site-specific hindcast data for different wind classes in Figure 7.7. For low and moderate wind speeds, the sea states are typically a combination of small wind-driven waves and swell, with the most severe sea states originating from swell. In contrast, for high wind speeds, the severe sea states are purely wind-driven. The dominance of different wave components at various wind speeds is also evident in the shape of the contours depicted in Figure 7.17. For low wind speeds, the contours are characterized by longer periods, primarily representing the swell and moderate wind-driven seas. As wind speeds increase, the contours gradually transform to represent the wind-driven severe sea states that dominate at high wind speeds.

Both the Log-normal and Weibull models provide reasonable fits to the wave peak period data, showing similar behaviour. Figure 7.18 illustrates the 50-year contours for three wind classes obtained using Weibull and Log-normal

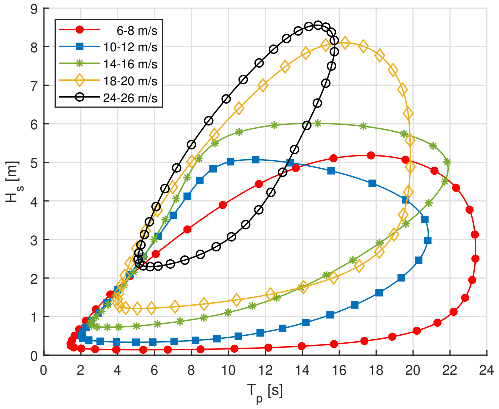

Figure 7.17: 50-year contours for different wind classes for 10 MW model

distributions for T_p, along with the steepness limits based on deep-water and intermediate-water depth dispersion relationships. The contours established using the Log-normal model do not align well with the data near the wave steepness limit, particularly for wind class 10-12 m/s and T_p values between 3-8 s. This discrepancy leads to relatively high H_s values above the steepness limit for a given peak period. Large-diameter monopile-based OWTs have a natural period within this range, and even moderate values of H_s can result in high dynamic excitation, potentially overestimating responses.

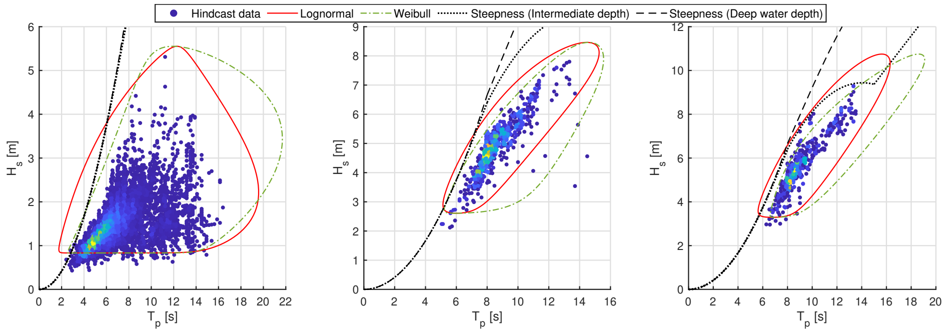

Figure 7.18: 50-year contour for three wind classes using a Log-normal and a Weibull model for the conditional T_p distribution. The wave steepness criteria are plotted. (Left:10-12 m/s Middle:24-26 m/s Right:26-38 m/s)

The Weibull distribution provides more realistic $H_s - T_p$ combinations, closely following the steepness limit for all wind classes. While the difference between the steepness criteria is negligible for wave periods lower than 8 s and water depths of 30 m, notable differences arise for peak periods larger than 8 s. This discrepancy becomes apparent in the wind class 26-38 m/s contour. The contours derived using the Log-normal distribution exhibit $H_s - T_p$ combinations that, although reasonable for deep-water depths, exceed the steepness limit when accounting for water depth effects.

7.4 Extremes for different statistical and load models

After establishing the 50-year contours, the next step is to estimate the 50-year response by analyzing different sea states along the contours and identifying the one that results in the largest maximum response. However, estimating extreme responses involves various sources of uncertainty. These uncertainties arise from statistical aspects, such as the choice of environmental contour used to estimate extremes, as well as the stochastic variation of response due to seed variability. Additionally, there are uncertainties associated with load modelling used in simulation tools.

The following sections focus on evaluating how extreme responses vary when using environmental contours derived from different probabilistic models for the joint distribution. The effect of seed variability on the stochastic variation of extreme responses is also investigated. Furthermore, physical models that better represent the load and response characteristics of large-diameter monopiles are compared to methods commonly used for smaller-diameter piles. Specifically, the impact of soil-structure interaction is assessed by comparing the macro-element model to $p - y$ curves. Additionally, the effect of diffraction on extreme loads is investigated by comparing the Morison equation with constant and frequency-dependent inertia coefficient (C_m).

To investigate the variation in extreme responses, two wind speeds were selected: the rated speed (10-12 m/s) and the cut-out speed (24-26 m/s) in both operational and parked states. These wind classes were chosen to represent scenarios where wind turbines experience maximum wind loads with moderately severe waves originating from swell (rated speed) and situations with lower thrust loads and more severe sea states (cut-out speed). The simulations consider long-crested waves, with wind and waves co-directional in the fore-aft direction of the wind turbines.

For all the subsequent aeroelastic simulations, TurbSim was used to generate the time series of turbulent wind. The mean wind speed was set to the mid-value of the rated and cut-out wind classes, i.e., 11 m/s and 25 m/s, respectively. Furthermore, 2$^{\text{nd}}$-order wave kinematics were used for all sea states. The quantity of interest compared between different statistical and load models is the fore-aft mudline bending moment.

7.4.1 Extremes along the contours

To analyze the variation in extreme responses along the established contours, 20 1-hour time-domain simulations were conducted for each selected sea state, with random wind and wave seeds. The number of simulations was chosen to reduce the stochastic variation of maximum response due to seed variability, and was considered a reasonable compromise between accuracy and computational effort for evaluating how responses vary along the contours. To ensure consistency, the same set of 20 seeds was used for each sea state analyzed along the contours, minimizing the effect of wind and wave seed variability between different sea states. The impact of seed variability on extreme response is discussed in Sec. 7.4.2.

The short-term global maxima of the fore-aft bending moment at the mudline for each sea state were fitted using the Gumbel distribution [230]. Eq. 7.23 shows the cumulative distribution function $F_M(x)$ of the short-term global maxima, characterized by the location, α_g, and scale, β_g, parameters. These parameters were estimated using the method of moments, based on the expected value and standard deviation of the Gumbel distributed variable as in Eq. 7.24,

$$F_M(x) = \exp\left[-\exp\left(-\frac{x-\alpha_g}{\beta_g} \right) \right] \tag{7.23}$$

$$\begin{aligned} \mu_M &= \alpha_g + \gamma \cdot \beta_g \\ \sigma_M &= \frac{\pi}{\sqrt{6}} \cdot \beta_g \end{aligned} \tag{7.24}$$

where $\gamma \approx 0.5772$ is the Euler–Mascheroni constant. The representative extreme response for a sea state (h_q, t_q) along a 50-year contour for a wind class associated with a mean wind speed u_q at hub height was then found by solving Eq. 7.25,

$$F_{M|U_{hub},H_s,T_p}(M_{p_g}|u_q,h_q,t_q) = p_g, \tag{7.25}$$

Here, p_g represents the percentile of the 1-hour extreme value distribution. Typically, percentiles in the range of 85% to 95% are used for most practical offshore problems dominated by wave loading, considering 3-hour extreme values [86, 95, 96] for 100-year return period. In this study, M_{p_g} is obtained from the extreme value distribution for $p_g = 90\%$ using Eq. 7.26. It is important to note that the selection of the specific percentile is based on representative values from previous studies, and the exact value should be validated through a full long-term assessment. However, for the purposes of this study, the precise value of the percentile is not expected to significantly affect the overall findings. The representative extreme response is denoted as $M_{90\%}$. Figure 7.19 shows examples of the Gumbel fit to the global maxima of the bending moment at the mudline obtained from 20 1-hour simulations for three sea states at the rated speed for the 15 MW model.

$$M_{p_g} = \alpha_g - \beta_g \cdot \ln\left[-\ln(p_g)\right] \tag{7.26}$$

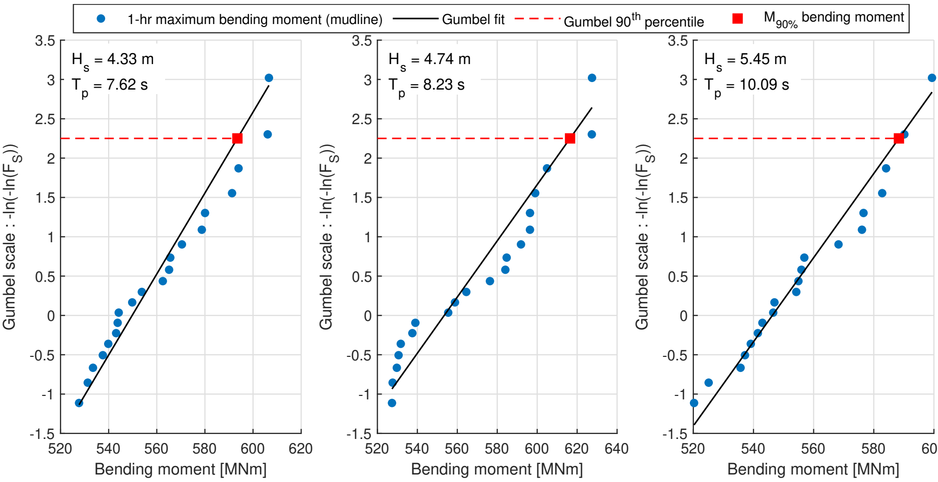

Figure 7.19: Gumbel distributions for the maximum mudline bending moment for 20 1-hr simulations for different sea states.

7.4.1.1 Rated speed

In the operational state, the extreme responses observed at the rated speed for both 10 MW and 15 MW OWTs were primarily caused by wind loads resulting from the maximum thrust force, combined with moderate yet steep waves that were close to the natural period of the structure. An example is shown in Figure 7.20, which displays two examples of time series spanning ±20 s, taken from the moment in time when the maximum mudline bending moment is observed during a 1-hour simulation. The examples correspond to a sea state with H_s of 4.74 m and T_p of 8.23 s for the 15 MW model. The plots also depict both the thrust force (including its mean value from the 1-hour time series) and the wave elevation. It is clearly observed that extreme responses occur under the combination of maximum thrust force and steep waves, and occur during the steep rise of the wave when wave particle acceleration is close to its maximum value.

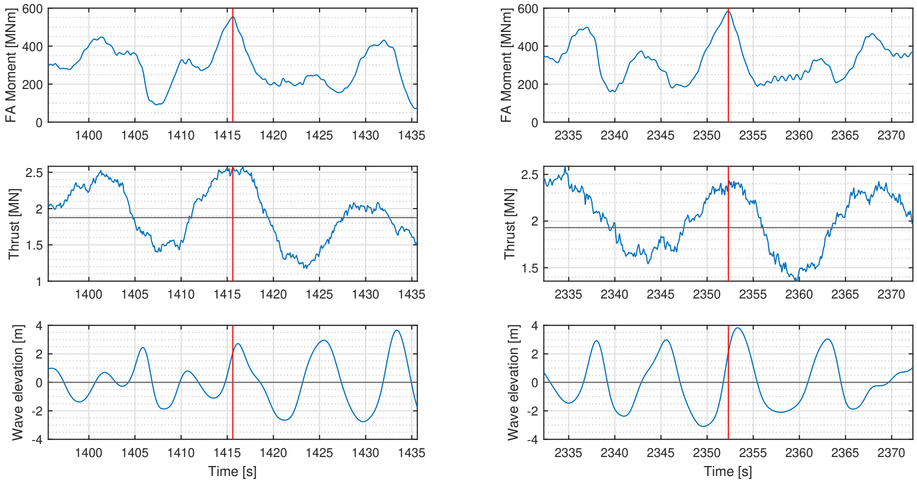

(a) Seed N°1

(b) Seed N°2

Figure 7.20: Examples of mudline bending moment, thrust, and wave elevation time series for the 15 MW OWT (H_s=4.74 m and T_p=8.23 s).

Figure 7.21 illustrates the environmental contours at the rated speed for different conditional H_s models, depicting the 90th percentile of the bending moment at the mudline for various sea states. Each dot on the contour represents a specific sea state that was analyzed along the contour using 20 simulations, and the colour scale reflects the extreme response magnitude for each sea state.

The extreme responses at the rated speed were influenced by the combined effect of wave height (H_s), wave steepness, and the natural period of the structure. Along the contours, the wave height gradually increases, but the waves become less steep, and the wave energy content around the natural period decreases. As a result, some relatively moderate sea states led to similar extreme responses as more severe sea states (in terms of wave height) that were less steep and not close to the natural period of the structure. For

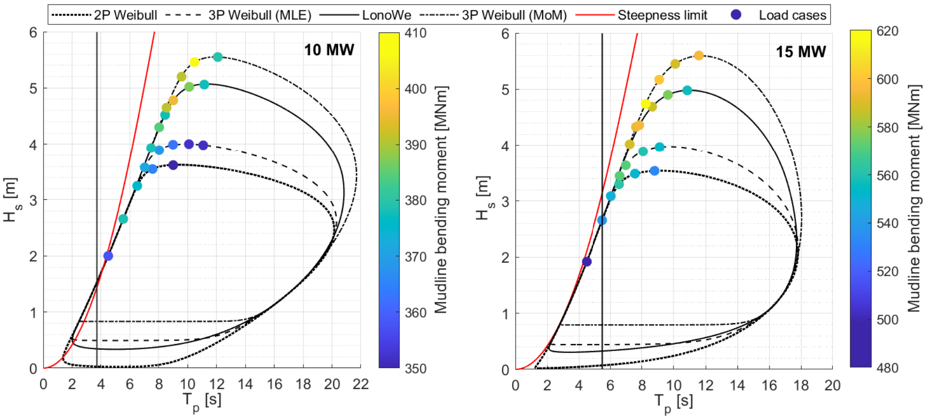

Figure 7.21: Environmental contours at rated speed for different conditional H_s models with the 90th percentile for various sea states.

instance, for the 10 MW model, a sea state with H_s =2.66 m and T_p =5.54 s resulted in a similar extreme response ($M_{90\%} \approx 378$ MNm) compared to a sea state with notably larger H_s (e.g., $H_s = 5.55$ m, $T_p = 12.09$ s).

Figure 7.22 illustrates individual wave events from the 20 1-hour simulations conducted for these two sea states. The red line indicates the natural period of the models and the black crosses the events that resulted in the largest mudline bending moment. The wave height (H) is defined as the crest-to-trough height, and the period (T) represents the time between two consecutive zero up-crossings. The wavelength of each wave event was calculated using Eq. 7.18, where the corresponding wave period was used instead of T_p. Subsequently, the wave steepness was calculated by the ratio of wave height to wavelength using $s = H/L$. It is important to note that wave steepness for certain events exceeds the theoretical limits defined by DNV and may lead to wave breaking in reality. However, wave breaking was not considered in this study. As observed, although the first sea state has much smaller waves, they are steeper and in the vicinity of the natural period of the structure, therefore causing similar extreme response $M_{90\%}$.

For the 10 MW OWT with a relatively small natural period of 3.7 s, the sea states in this range were not large enough to excite the structure to its highest extreme responses along the contour. Consequently, the highest response was found at the top of the contour for a sea state with H_s =5.46 m and T_p =10.48 s. A similar behaviour along the contours was observed for the

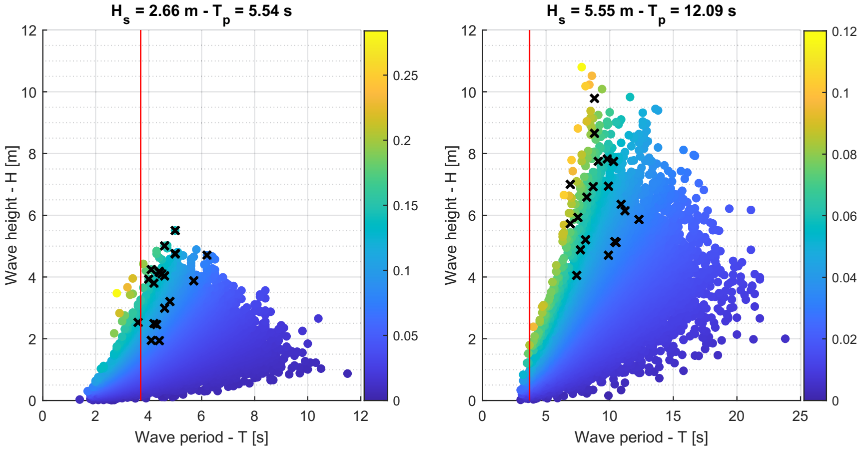

Figure 7.22: Wave events from 20 1-hr analyses for two sea states that resulted in the same $M_{90\%}$ (10 MW). Colorbar indicates wave steepness.

15 MW wind turbine model, as shown in Figure 7.23. However, the highest response was not found at the top, but on the left ridge of the contour for H_s=4.74 m and T_p=8.23 s. Due to its longer natural period (5.5 s), the 15 MW model is primarily affected by moderate but sufficiently large and steep wave events around the natural period, which induce high dynamic response, as it is observed by black crosses in Figure 7.23, which indicate the wave events that resulted in the highest mudline bending moment.

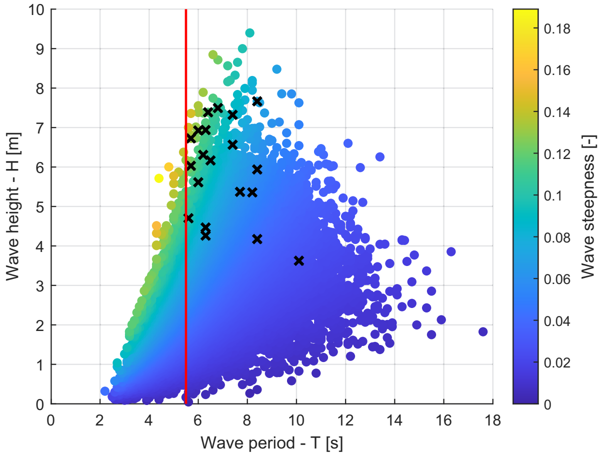

Figure 7.23: Wave events from 20 1-hr analyses for the worst sea state along the contour (15 MW). Black crosses indicate the events that resulted in the highest mudline bending moment at mudline.

As Figure 7.21 depicts, the choice of the conditional H_s model affected the estimated extreme responses. For the 10 MW OWT, the largest $M_{90\%}$ was obtained from the contour generated using the 3-parameter (MoM) model, with a value of approximately 406 MNm. Comparatively, the LonoWe model resulted in a slightly lower (2.7%) value, while for the 2-parameter and 3-parameter maximum likelihood estimation (MLE) Weibull models, the largest $M_{90\%}$ was 6.9% lower, for the same sea state.

The choice of conditional H_s model also influenced the estimated extreme responses for the 15 MW case. The largest extreme response was estimated along the contour obtained using the 3-parameter MoM model, with $M_{90\%}$ reaching 616 MNm. The LonoWe model resulted in a slightly lower (3.4%) extreme, while the 3-parameter MLE and 2-parameter Weibull models resulted in 7.3% and 8.7% lower values of $M_{90\%}$, respectively. It should be noted that wave steepness for some events exceeded theoretical limits and, in reality, wave breaking may occur; however, wave breaking was not considered in this study. Table 7.1 summarizes the largest $M_{90\%}$ response along the contours established using different conditional H_s models at rated speed.

Table 7.1: Worst sea state along the contours for different conditional H_s models and corresponding $M_{90\%}$ (rated speed)

	10 MW			15 MW		
Conditional H_s model	H_s m	T_p s	$M_{90\%}$ MNm	H_s m	T_p s	$M_{90\%}$ MNm
2P Weibull	2.66	5.54	378.6	3.30	6.56	562.1
3P Weibull (MLE)	2.66	5.54	378.6	3.45	6.59	571.7
3P Weibull (MoM)	5.46	10.48	406.1	4.74	8.23	616.5
LonoWe	4.78	9.01	395.3	4.36	7.83	595.1

7.4.1.2 Cut-out speed

At the cut-out speed, similar behaviour was observed for both the 10 MW and 15 MW models, as depicted in Figure 7.26. Extreme responses gradually increase along the contours, reaching the maximum values either at the top of the contour or for slightly smaller but steeper waves. Contrary to the rated speed, extreme responses occur as a result of severe wave events, while the thrust force contributes to a much lesser extent on the resultant extreme response. This is observed in Figure 7.24, which displays two examples of time series spanning ±20 s, taken from the moment in time when the maximum mudline bending moment is observed during a 1-hour simulation. The examples correspond to a sea state with H_s of 8.81 m and T_p of 14.5 s.

For the case N°1 (Figure 7.24a), Figure 7.25 shows how the total, inertia, and drag forces, calculated using Morison equation, are distributed along the monopile for that time window. As shown, inertia forces dominate, having the highest contribution to the total loading. The maximum mudline bending moment occurs between the wave zero up-crossing and wave crest, where the acceleration reaches its maximum values, and close to the wave crest, where the velocity gets larger, increasing the relative drag force contribution. The same observations were found also for the other cases.

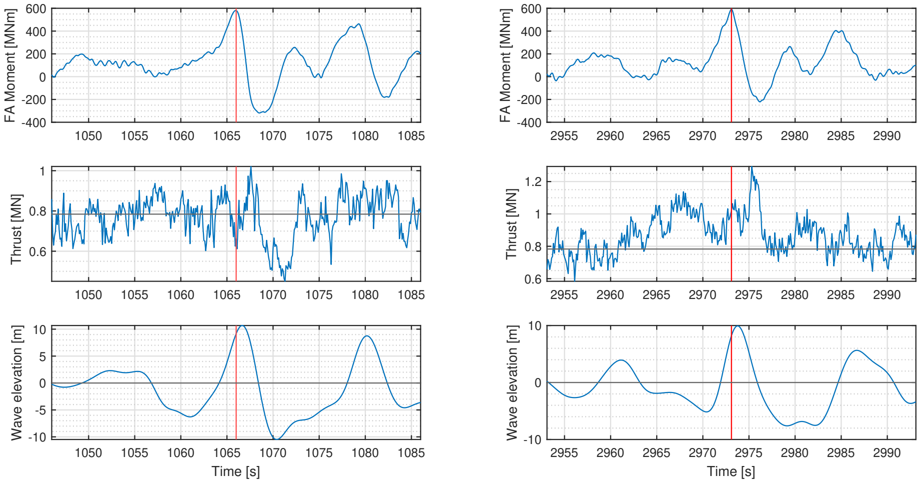

(a) Case N°1 (b) Case N°2

Figure 7.24: Examples of mudline bending moment, thrust, and wave elevation time series for the 15 MW OWT (H_s=8.81 m and T_p=14.5 s).

For the 10 MW model, the maximum response ($M_{90\%} \approx 457$ MNm) was obtained for a sea state with $H_s = 8.55$ m and $T_p = 14.94$ s, which was 11.1% larger than the largest $M_{90\%}$ observed at the rated speed. Similarly, for the 15 MW turbine, the load case with $H_s = 8.81$ m and $T_p = 14.5$ s resulted in the largest $M_{90\%} \approx 611$ MNm, which was lower than the largest $M_{90\%}$ at the rated speed (616 MNm). This suggests the significance of load cases at rated speed for larger capacity turbines with higher natural periods. The choice of conditional H_s model also influenced the estimated extreme

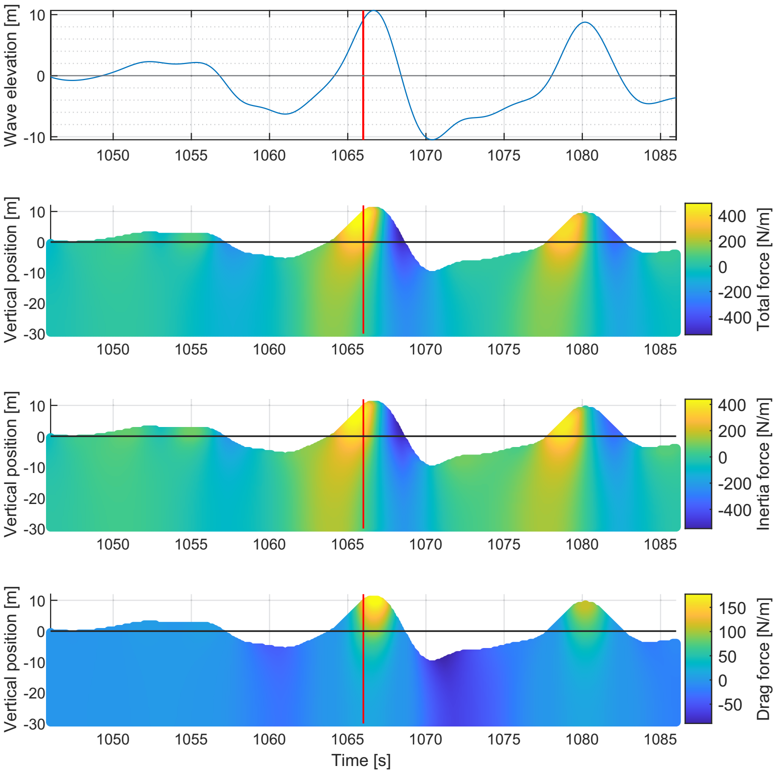

Figure 7.25: Total, inertia, and drag forces along monopile for the time window for case N°1

Table 7.2: Worst sea state along the contours for different conditional H_s models and corresponding $M_{90\%}$ (cut-out speed)

	10 MW			15 MW		
Conditional H_s model	H_s m	T_p s	$M_{90\%}$ MNm	H_s m	T_p s	$M_{90\%}$ MNm
2P Weibull	7.90	13.30	399.4	7.47	11.41	570.5
3P Weibull (MLE)	8.18	13.90	406.2	8.13	13.16	570.2
3P Weibull (MoM)	8.46	14.72	454.6	8.72	15.00	609.2
LonoWe	8.55	14.94	456.8	8.81	14.50	622.8

responses at the cut-out speed as shown in Figure 7.26 and Table 7.2. For the 10 MW turbine, the largest $M_{90\%}$ was obtained using the LonoWe

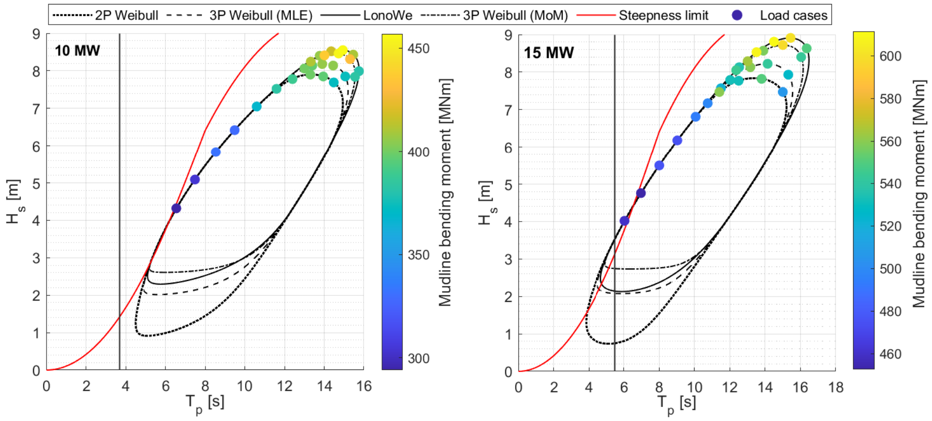

Figure 7.26: Environmental contours at cut-out speed for different conditional H_s models with the 90th percentile for various sea states.

model. The 3-parameter model (MoM) resulted in a slightly lower (0.4%) extreme response, indicating negligible differences between the contours of the two models. On the other hand, the 3-parameter (MLE) and 2-parameter Weibull models underestimated the extreme responses by 11.1% and 12.7% respectively due to slightly less severe sea states for the two models. Similarly, for the 15 MW wind turbine, the LonoWe model resulted in the largest $M_{90\%} \approx 611$ MNm, with the 3-parameter model (MoM) resulting in a slightly lower (2.2%) estimate. Meanwhile, the 3-parameter (MLE) and 2-parameter Weibull models resulted in similar $M_{90\%}$ (8.5% lower) for two different sea states, respectively.

7.4.2 Stochastic variation due to seed variability

The 90th percentile of the response for each sea state in Sec. 7.4.1 was based on the global maxima from 20 simulations with random wind and wave seeds. Although 20 simulations can provide a reasonable estimate of maximum response, there is still some uncertainty in quantile estimates as a function of number of samples due to seed variability. To evaluate the effect, the most severe load cases for the two OWTs for rated and cut-out wind speed were analyzed with 100 random seeds. Then, using the sample size of 100 global maxima, a Gumbel distribution was fitted and the scale and location parameters were estimated. Tables 7.3 and 7.4 summarize the load cases used for the study, the bending moment 90th percentile $M_{90\%}$ at mudline, and the corresponding Gumbel scale (β_g) and location (α_g) parameters.

Table 7.3: Load cases and Gumbel parameters (10 MW)

	U_{119} m/s	H_s m	T_p s	$M_{90\%}$ MNm	a_g MNm	b_g MNm
LC1	11	5.46	10.48	404.2	366.6	16.7
LC2	25	8.55	14.94	427.4	343.4	37.3

Table 7.4: Load cases and Gumbel parameters (15 MW)

	U_{150} m/s	H_s m	T_p s	$M_{90\%}$ MNm	a_g MNm	b_g MNm
LC1	11	4.74	8.23	591.5	547.9	19.4
LC2	25	8.81	14.5	572.7	482.3	40.2

The uncertainty of quantile estimation was evaluated using Monte Carlo simulations. Synthetic data samples of different sizes (between 3 and 100) were generated for a random variable Z that is assumed to follow a Gumbel distribution, with location and scale parameters μ_Z=0 and β_Z=1, respectively. Then, the 90$^{\text{th}}$ quantile estimate for each set of the synthetic samples was determined. The procedure was repeated ten thousands times to create a distribution of quantile estimates, and the 2.5.% - 97.5% confidence intervals were estimated. Then the confidence intervals of the distributed variable M_{p_g} for each load case were simply scaled following $M_{p_g} = a_g + \beta_g \cdot Z$. Figure 7.27 shows the results from the study. The top plots illustrate the 100 global maxima from the simulations, and the corresponding Gumbel fits. In the plots below, the blue/green markers for N=1 show the global maxima from each simulation, and the red cross marker shows the $M_{90\%}$ as estimated using all (N=100) global maxima, which is used as the reference value. The shaded area indicates the 2.5% and 97.5% confidence intervals.

As Figure 7.27 shows, short-term maxima from 1-hr simulations have a notable spread. In both OWTs and for both load cases, the uncertainty gradually decreased as more global maxima were used to estimate $M_{90\%}$, which is expected. Higher variability was observed for the more severe sea states (LC2), at the cut-out speed for both turbines. This is also supported by the ratio between the scale (β_g) and location (α_g) parameters, which is related to the coefficient of variation (CV). The relatively lower CV for the load cases at rated speed, indicates that β_g is relatively smaller than α_g, leading to a narrower spread relatively to the mode of the distribution. The results

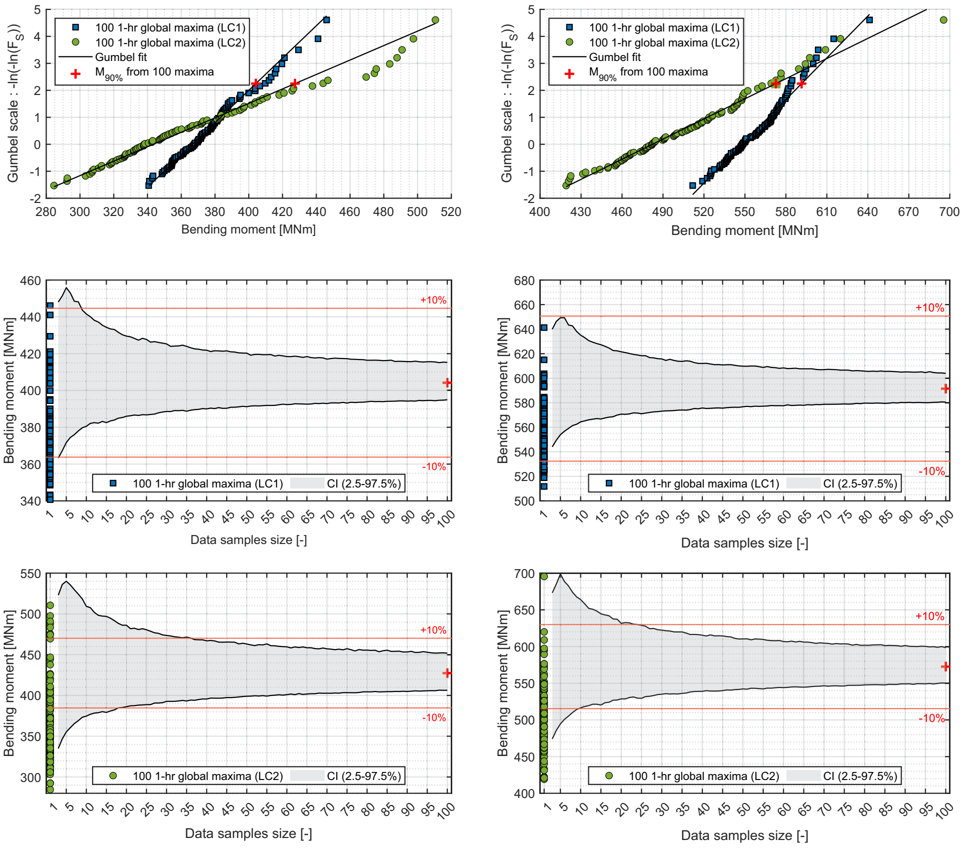

(a) 10 MW (b) 15 MW

Figure 7.27: Variation of extreme response due to seed variability. The confidence intervals are scaled from Monte Carlo simulations of a synthetic Gumbel distribution.

here are based on estimating the short-term extreme response distribution only using the global maximum from each simulation. Other methods can be used such as peaks-over-threshold (POT) [85] or the Naess-Gaidai ACER method [231], which consider a larger number of extremes from a given time series, resulting in better definition of distribution tails, and therefore smaller uncertainties. It is worth noting that for both OWTs, the $M_{90\%}$ values at the rated and the cut-out speeds were comparable, with a difference ranging from 3.7% to 5.5%. Nevertheless, the results for the 15 MW OWT indicated the increasing importance of evaluating load cases also at the rated speed for larger turbines, as higher extremes can be obtained compared to cut-out.

7.4.3 Impact of load models on extremes

7.4.3.1 Foundation modelling

As noted in Sec. 6.1, the total damping in OWT models consists of aerodynamic, hydrodynamic, structural, and soil damping. To account for structural damping, stiffness-proportional Rayleigh damping was applied along the support structure, with a damping ratio (ξ) of approximately 1.0-1.1% of critical damping for the first natural frequency of each turbine. In the case of the $p-y$ curves, soil damping was incorporated using stiffness-proportional Rayleigh damping at four different levels (Figure 6.9). The amount of soil damping, expressed as a percentage of critical damping, was chosen so the total global damping ratio of the $p-y$ curves closely matched the damping ratio of the macro-element model for different mean load levels.

To compare the macro-element model with the $p-y$ curves, the most severe sea states for each wind turbine at rated and cut-out speeds were considered. As explained in the previous section, twenty simulations were conducted for each sea state, and the 90th percentile of the bending moment at the mudline was estimated. The effect of foundation modelling was investigated for both an operational state, where aerodynamic damping dominates, and a parked state, where soil damping is the main contributor to damping in the system. The same 20 seeds were used to eliminate the effect of stochastic variation in the extremes due to seed variability.

Tables 7.5 and 7.6 summarize the extreme responses obtained from both the macro-element and the $p-y$ curves for different load cases, operational states, and damping levels, for 10 MW and 15 MW turbines, respectively. Additionally, Figure 7.28 depicts the relative differences between the macro-element model (used as reference) and $p-y$ models and for the various damping cases.

In operational states where aerodynamic damping dominates, the use of $p-y$ curves led to only slight differences in extreme responses compared to the macro-element model. Furthermore, varying the soil damping in the $p-y$ curves had a minor effect on the results. For the 10 MW turbine, the $p-y$ curves overestimated $M_{90\%}$ by approximately 1.6-2.6% for LC1 and 2.4-2.8% for LC2, when comparing the highest and lowest soil damping levels. Similarly, for the 15 MW wind turbine, the relative differences between the $p-y$ curves and the macro-element model were around 1.0% for LC1 and below 0.5% for LC2.

Table 7.5: $M_{90\%}$ for different foundation models and OWT states (10 MW)

<table>
<tr><th colspan="7">$M_{90\%}$ [MNm] (Mudline)</th></tr>
<tr><td></td><td colspan="3">LC1</td><td colspan="3">LC2</td></tr>
<tr><td></td><td>U_{119}</td><td>H_s</td><td>T_p</td><td>U_{119}</td><td>H_s</td><td>T_p</td></tr>
<tr><td></td><td>m/s</td><td>m</td><td>s</td><td>m/s</td><td>m</td><td>s</td></tr>
<tr><td></td><td>11</td><td>5.46</td><td>10.48</td><td>25</td><td>8.55</td><td>14.94</td></tr>
<tr><td>Model</td><td>Operation</td><td colspan="2">Parked</td><td>Operation</td><td colspan="2">Parked</td></tr>
<tr><td>Macro-element</td><td>406.1</td><td colspan="2">285.4</td><td>456.8</td><td colspan="2">504.5</td></tr>
<tr><td>$p-y$ (1.2%)</td><td>416.8</td><td colspan="2">315.2</td><td>469.7</td><td colspan="2">536.5</td></tr>
<tr><td>$p-y$ (1.6%)</td><td>415.3</td><td colspan="2">294.1</td><td>469.0</td><td colspan="2">525.8</td></tr>
<tr><td>$p-y$ (2.0%)</td><td>414.0</td><td colspan="2">283.3</td><td>468.5</td><td colspan="2">518.5</td></tr>
<tr><td>$p-y$ (2.4%)</td><td>412.7</td><td colspan="2">274.9</td><td>467.9</td><td colspan="2">510.2</td></tr>
</table>

Table 7.6: $M_{90\%}$ for different foundation models and OWT states (15 MW)

<table>
<tr><th colspan="7">$M_{90\%}$ [MNm] (Mudline)</th></tr>
<tr><td></td><td>U_{150}</td><td>H_s</td><td>T_p</td><td>U_{119}</td><td>H_s</td><td>T_p</td></tr>
<tr><td></td><td>m/s</td><td>m</td><td>s</td><td>m/s</td><td>m</td><td>s</td></tr>
<tr><td></td><td>11</td><td>4.74</td><td>8.23</td><td>25</td><td>8.81</td><td>14.50</td></tr>
<tr><td>Model</td><td>Operation</td><td colspan="2">Parked</td><td>Operation</td><td colspan="2">Parked</td></tr>
<tr><td>Macro-element</td><td>616.4</td><td colspan="2">400.9</td><td>611.1</td><td colspan="2">523.5</td></tr>
<tr><td>$p-y$ (1.2%)</td><td>623.0</td><td colspan="2">422.3</td><td>612.2</td><td colspan="2">549.7</td></tr>
<tr><td>$p-y$ (1.4%)</td><td>621.9</td><td colspan="2">404.6</td><td>611.8</td><td colspan="2">542.2</td></tr>
<tr><td>$p-y$ (1.6%)</td><td>621.2</td><td colspan="2">392.6</td><td>611.6</td><td colspan="2">536.9</td></tr>
<tr><td>$p-y$ (1.8%)</td><td>620.5</td><td colspan="2">381.2</td><td>611.1</td><td colspan="2">528.8</td></tr>
</table>

In parked conditions, where the minimum values of soil damping in the $p-y$ curves were used (corresponding to approximately 1.2% global damping for both turbines), the extreme responses were overestimated. The overestimation ranged from 6.3% (LC2) to 10.4% (LC1) for the 10 MW turbine, and around 5.1% for both LCs for the 15 MW wind turbine. Increasing the amount of soil damping in the $p-y$ curves gradually decreased the extreme responses for both load cases. For both OWTs, a more significant effect was observed for LC1 (rated), as these cases include wave events closer to resonant period, with responses being sensitive to damping variations.

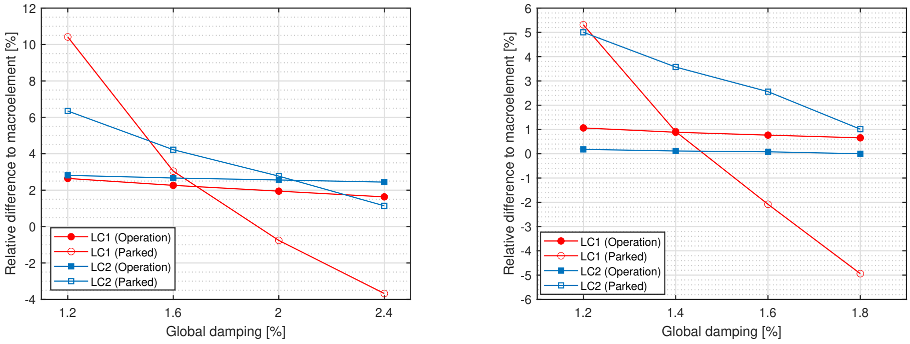

(a) 10 MW (b) 15 MW

Figure 7.28: Relative difference of $M_{90\%}$ between $p-y$ curves and macroelement for the load cases shown in Tables 7.5 -7.6

Figure 7.29 shows the global maxima obtained from 20 simulations, along with the corresponding Gumbel plots for the macro-element and $p-y$ curves for LC1 of the 15 MW OWT. For the operational state, the variation in soil damping within the $p-y$ curves leads to only minor differences in the extreme responses, and as a result, the variations in the 90th percentile of the bending moment are negligible. Contrary, for the parked state, the individual extreme values range from -13.2% to 8.3% in comparison to the macro-element. This relatively wider range of individual global maxima contributes to the higher variations observed in the 90th percentile results for the parked state. Similar observations were found for the other cases.

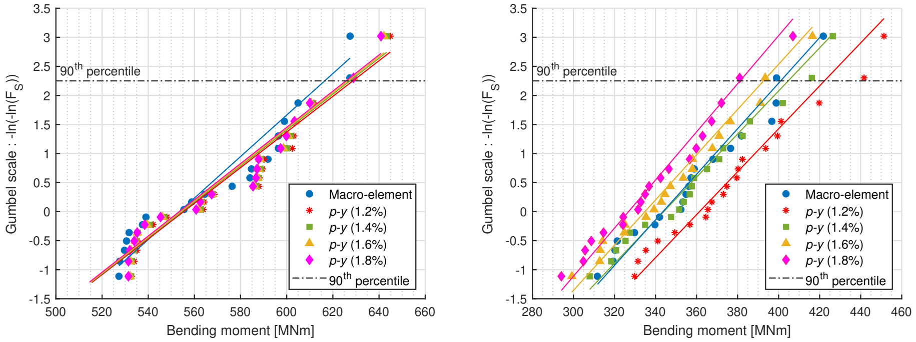

(a) Operation (b) Parked

Figure 7.29: Gumbel distributions for the maximum mudline bending moment (LC1 - 15 MW OWT) for the different soil models.

7.4.3.2 Hydrodynamic modelling

Morison's equation (Eq. 2.1) is recommended by the design standards [30, 59] and remains the most commonly used approach for monopile-based OWTs. It is based on the assumption of a slender structure, i.e. the cylinder diameter is small compared to the wavelength of the incident wave. To account for the diffraction of long-crested waves incident on vertical piles, which can be important when the dimension of the structure is large compared to the wavelength, i.e., $D > 0.2\lambda$, design standards [30] recommend using MacCamy and Fuchs [177] analytical solution.

Maximum loads relevant to ULS design are generally dominated by nonlinearities caused by wave steepness, particularly for intermediate and shallow water depths, and higher-order wave kinematics and wave load models are required. Morison's equation can be used with wave kinematics from different theories. On the contrary, MacCamy and Fuchs model is strictly only applicable with linear waves, and current engineering models do not account for diffraction effects when higher wave kinematic theories are used.

As diffraction becomes increasingly important with larger diameters, a new load model was developed and validated against experimental results for irregular severe sea states [232]. The model combines the conventional Morison's formulation for slender bodies with a frequency-dependent mass coefficient based on formulation from MacCamy and Fuchs. For a given sea state, the undisturbed incoming fluid particle acceleration time-series using 2^{nd}-order waves is transformed to frequency domain using Fourier transform. Assuming that the inertia force per unit length can be represented as a linear composition of N Fourier components from the nonlinear acceleration signal, it is given as,

$$dF_{inertia} = \pi\rho\frac{D_p^2}{4}\sum_{n=1}^{N} C_{m_n}\dot{u}_n \tag{7.27}$$

where $\dot{u}_n$ is the n^{th} Fourier component of the acceleration signal and C_{m_n} is the corresponding frequency-dependent mass coefficient. C_{m_n} is estimated from MacCamy-Fuchs diffraction theory from Eq. 7.28

$$C_{m_n} = \frac{4A(k_n\alpha)}{\pi(k_n\alpha)^2} \tag{7.28}$$

where $A(k_n\alpha) = \left[J_1'^2(k_n\alpha)+Y_1'^2(k_n\alpha)\right]^{-1/2}$ and $\alpha = \tan^{-1}\left[J_1'(k_n\alpha)/Y_1'(k_n\alpha)\right]$, where J_1', Y_1' are the first and second kind Bessel functions of first order, respectively, with the prime denoting the derivative with respect to the argument, $\alpha = D_p/2$ is the monopile radius, and k_n is the wave number. For a Fourier component at frequency ω_n, k_n is the positive real solution calculated from the linear dispersion relation for water depth h, Eq. 7.29,

$$k_n \cdot g \cdot \tanh(k_n h) = \omega_n^2. \tag{7.29}$$

This engineering model effectively applies a first order diffraction correction for both linear and nonlinear wave particle acceleration components. To evaluate the effect of diffraction on the extreme response estimates, the sea states for each OWT at rated and cut-out speed were analyzed, with operational OWTs. For each sea state, twenty simulations were conducted, and the 90^{th} percentile of the mudline bending moment was compared. The load cases were analyzed using the macro-element model and turbulent wind.

For each 1-hour time-domain simulation with 2^{nd} order wave kinematics, the velocity, and acceleration at each time instant were extracted from mudline to instantaneous surface elevation η, at nodal positions with dz=0.5 m. Dynamic nodal forces were applied using the Morison equation with constant and frequency-dependent C_m (Eq. 2.1), using the extracted kinematics. The wave kinematics were assumed to be valid ± 0.25 m for each nodal position (half of the element below and above). The nodal positions along the monopile were compared to the instantaneous surface elevation at each instant, and the nodal forces were applied accordingly, considering if the node - corresponding element - is fully or partially submerged. A simplified illustration is shown in Figure 7.30.

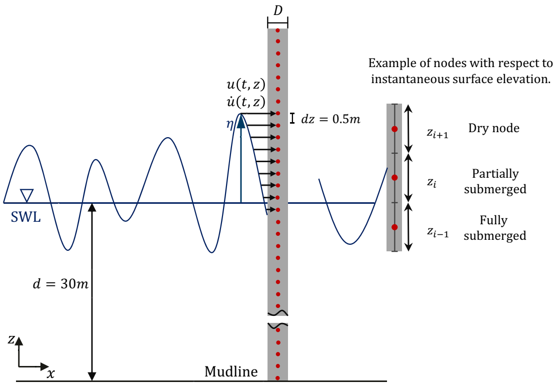

Figure 7.30: Illustration of nodal forces approach with dry, partially and fully submerged nodes with respect to instantaneous surface elevation η.

The nodal forces approach, as described, was tested against SIMA with constant C_m. Figure 7.31 shows an example of the mudline bending moment as obtained from SIMA, and using Morison equation with the wave kinematics from the time-domain simulation. The differences in the global maxima were underestimated by 1.0-2.5%, mainly due to the interpolation of the kinematics and the drag term in SIMA that includes the relative velocity, while the nodal forces formulation includes only the wave-particle velocity. For a consistent comparison, and to avoid differences in results due to i.e. interpolation of wave kinematics within the software, the global maxima using the nodal forces approach with constant and frequency-dependent C_m were compared.

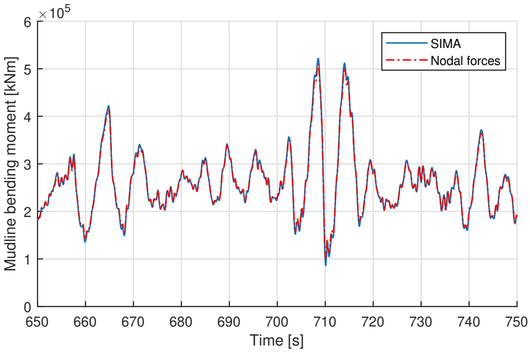

Figure 7.31: Comparison of mudline response as obtained from SIMA and using the nodal forces approach

Tables 7.7 and 7.8 summarize the $M_{90\%}$ at mudline, for the load cases analyzed. Figures 7.32 and 7.33 show the global maxima obtained from 20 simulations, along with the corresponding Gumbel plots using constant and frequency-dependent C_m, for 10 MW and 15 MW OWT, respectively.

For both OWTs, the load cases at the rated speed are mostly dominated by waves with shorter periods, where frequency-dependent C_m is lower than 2, resulting in lower extreme loads, and therefore in lower responses, as indicated in Figures 7.32a and 7.33a. For the 10 MW OWT, $M_{90\%}$ was reduced by 1.8% while for the 15 MW OWT by 4.3%. The effect is more apparent for the 15 MW model due to the combined effect of its larger diameter, and the sea state with a lower peak period.

On the contrary, at the cut-out speed, longer waves dominate extreme responses, where the theoretical C_m obtained from MacCamy-Fuchs is close

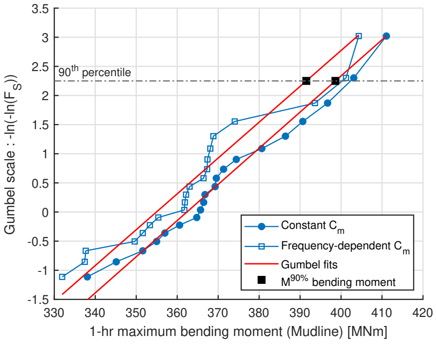

(a) Rated (LC1)

(b) Cut-out (LC2)

Figure 7.32: Gumbel distributions for the maximum mudline bending moment for 10 MW OWT using constant and frequency-dependent C_m, operational turbine

to 2. Consequently, extreme responses were similar using both methods. Slight differences in the individual maxima, as observed from Figures 7.32b and 7.33b, resulted in 0.5-1.6% difference in $M_{90\%}$ between the two models, for the two OWTs.

Table 7.7: $M_{90\%}$ using constant and frequency-dependent C_m (10 MW)

	U_{119}	H_s	T_p	$M_{90\%}$ Constant C_m	$M_{90\%}$ Frequency-dependent C_m
-	m/s	m	s	MNm	MNm
LC1	11	5.46	10.48	398.6	391.5
LC2	25	8.55	14.94	445.8	448.4

Table 7.8: $M_{90\%}$ using constant and frequency-dependent C_m (15 MW)

	U_{150}	H_s	T_p	$M_{90\%}$ Constant C_m	$M_{90\%}$ Frequency-dependent C_m
-	m/s	m	s	MNm	MNm
LC1	11	4.74	8.23	603.8	578.1
LC2	25	8.81	14.50	590.9	581.4

Figure 7.34 shows an example of mudline response spectra from one simulation for each of the load cases for the 15 MW OWT, using constant and

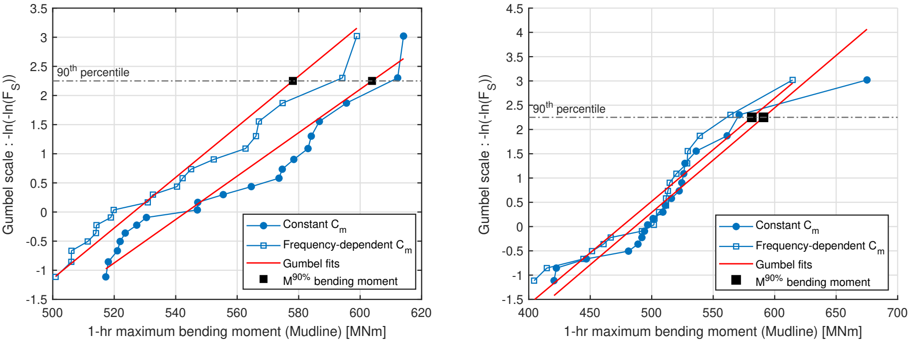

(a) Rated (LC1) (b) Cut-out (LC2)

Figure 7.33: Gumbel distributions for the maximum mudline bending moment for 15 MW OWT using constant and frequency-dependent C_m, operational turbine

frequency-dependent C_m. The frequency variation of C_m is also included. As shown, for the load case at rated speed, relatively short waves can result in large responses, where C_m values are expected to be lower than 2. As a result, more notable differences are observed also in the response spectra between the two approaches. The same effect is also seen for the load case at the cut-out speed, nevertheless in that case lower frequency waves dominate, where C_m from MacCamy-Fuchs theory is similar to 2, and consequently diffraction is less important.

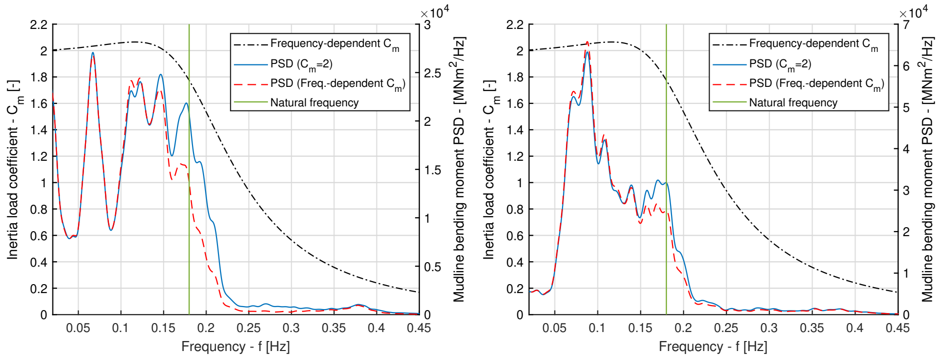

(a) H_s=4.74 m - T_p=8.23 s (rated) (b) H_s=8.81 m - T_p=14.50 s (cut-out)

Figure 7.34: Mudline response spectra from one simulation representative for LC1 (rated) and LC2 (cut-out) for 15 MW (operational). Frequency-dependent inertia load coefficient (for D_p=11 m) is also plotted.

Chapter 8

Conclusions and Recommendations

The motivation for this thesis originated from the challenges posed by the growing size of monopile foundations for offshore wind turbines (OWTs). It aimed to evaluate and improve commonly used design methods and investigate the effect of improved load models on long-term fatigue and extreme response predictions for three OWTs. This chapter summarizes the contributions of this thesis, as introduced in Sec. 1.6, to the scientific community and engineering practitioners. Recommendations for future studies are also made based on the author's views, and the limitations and the challenges encountered in the current work.

8.1 Environmental lumping for fatigue assessment

A novel lumping method was developed as an alternative to full long-term fatigue assessment for the FLS design of monopile-based OWTs. Lumped load cases (LCs) for scatter diagrams associated with different wind classes were derived using the damage-equivalent lumping method (DELM). The observed differences compared to full long-term fatigue assessment are considered acceptable, given the substantial improvement in computational efficiency (more than 95%). Moreover, the method was further developed to incorporate wind-sea and swell components in an integrated and consistent manner, and the sensitivity of the lumped LCs was evaluated.

- As the size of OWTs increases, wind classes near the rated speed contribute more to fatigue damage, highlighting the importance of wind loads for larger OWTs. This observation was also supported by the stress spectra, which showed a notable increase in slowly varying wind-induced responses for the 15 MW OWT. The impact was pronounced at the tower base but also observed at the mudline. It should be noted that the controllers used in the thesis for all OWTs are open-source controllers, and the impact of controller tuning or optimization have not been investigated on the results.

- At the mudline, fatigue damage increases for higher wind speeds, as those are associated with more severe sea states, which result in increased hydrodynamic loads, subsequent bending moments, and stresses on the structure. Sea states above cut-out speed (parked OWT) still have a notable impact on long-term fatigue due to their severity and the low or negligible aerodynamic damping, despite their low probability of occurrence.

- The relative differences between the lumped LCs and the scatter assessment mostly ranged between ±10-15% for individual wind classes, with statistical uncertainty due to seed variability accounting for most of the discrepancies. The total damage estimates from the lumped LCs ranged from -6% to +1% compared to the LTFA results at and below the mudline. Slightly higher variations (±10%) were observed at the tower base, primarily attributed to the sensitivity of damage estimates close to SWL on the wave kinematics model for parked states.

- Lumped LCs obtained using fully coupled and simplified models strongly agreed. Therefore, when simplified models of reasonable accuracy are available, they can be used to extract the lumped LCs, and then combined with fully coupled time-domain models to estimate the damage, can further reduce the computational effort.

- Considering lumping of wind-sea and swell-sea components, a reduction of 97.6% of computational effort compared to the original dataset, was achieved. Validation with fatigue assessment results using hindcast data for individual wind classes provided accuracy levels above 90% for long-term damage estimates. The lumped LCs followed the trends observed in the hindcast data, with the severity of the wind-sea component increasing with higher wind speeds, while the swell component remained relatively constant across different speeds.

- Variations in monopile design characteristics such as embedded length, diameter, and thickness showed that only changes that greatly impact the OWT dynamic characteristics, can lead to notable changes in the derived lumped LCs. Monopile diameter was found to be the most influential in this regard.

- The sensitivity of lumped LCs to inherent variability of metocean conditions was investigated by using scatter diagrams from annual data. Variations in the lumped LCs were primarily affected by the distribution of sea states within the scatter diagrams. Moreover, positive correlations were observed between lumped sea state parameters.
- A simulation duration of 10 minutes was sufficient to obtain transfer functions that accurately capture the dynamic response of the support structure over the , with negligible variations of the lumped LCs. Extending the duration did not reduce the observed variations.

8.2 Effect of foundation modelling on fatigue

The thesis evaluated the impact of foundation modelling on the dynamic behaviour and fatigue estimates of monopiles. It focused on the aspects of hysteretic damping and different stiffness after load reversals incorporated into the macro-element model, which cannot be represented by the widely used approach of $p-y$ curves combined with stiffness proportional Rayleigh damping.

In operational states, $p-y$ curves require varying soil damping levels to approximate the fatigue estimates of macro-element model, while in parked conditions, the $p-y$ curves produce similar fatigue estimates to the macro-element model with a nearly constant soil damping level.

Discrepancies in fatigue estimates between the models are relatively small in operational states, but significantly larger in parked states due to negligible aerodynamic damping. This leads to overestimation or underestimation of fatigue damage by $p-y$ curves based on the level of soil damping used. Similarly, when wind-wave misalignment is larger than 30°, there is negligible aerodynamic damping in the wave excitation direction, and important differences between the foundation models can be observed.

8.3 Environmental contours and extreme responses

Variations in extreme fore-aft bending moment responses at the mudline due to statistical and physical load modelling aspects were investigated for

10 MW and 15 MW turbines. The environmental contour method was employed to investigate the effects of different conditional probability distributions for H_s and T_p on the resulting contours for representative wind classes. Then, variations in extreme responses were investigated using different contours, and different hydrodynamic-soil models.

- Four statistical models were employed for the conditional distribution of H_s given wind speed. Despite the challenge of capturing the tail behaviour when fitting global hierarchical models to all observations, the 3-parameter Weibull model using the MoM to estimate distribution parameters provided the best fit for H_s across all wind classes, as it focuses on the upper tail of the data. The 3-parameter Weibull model using MLE resulted in less conservative contours compared to the MoM model, particularly in moderate wind classes, leading to less severe sea states. The 2-parameter Weibull model yielded significant discrepancies compared to the observations, while the LonoWe model proved challenging to fit, being sensitive to the transition point between Log-normal and Weibull distributions. The differences between statistical models were more apparent in intermediate wind classes, attributed to their inadequacy to capture the combined nature of moderate wind-sea states and a few severe sea states originating from swell.

- For the conditional distribution of T_p, the Log-normal and 3-parameter Weibull models were adopted. The Log-normal model deviated from the data trend near the wave steepness limit, particularly in intermediate wind classes, resulting in relatively high H_s values in the range of the turbines' natural periods. The Weibull model proved sensitive to the H_s class size, affecting T_p distributions and the resulting contours. Nonetheless, it provided a more accurate fit near the steepness limit, and it can be considered as an alternative to the commonly used Log-normal model. The importance of using the appropriate steepness curve was also evident to avoid unrealistic severe sea states.

- The 3-parameter Weibull (MoM) and LonoWe models captured the behaviour of the hindcast data in the upper tail, leading to more reasonable contours and resulting in higher extreme response predictions. Differences in the largest $M_{90\%}$ values between these models were found to range from approximately 0.5% to 3.5%, reflecting slight variations in the contours. Conversely, the 2-parameter and 3-parameter Weibull (MLE) models yielded the least conservative contours, with $M_{90\%}$ values being approximately 7.0% to 12.7% lower, depending on the OWT and wind class.

- The statistical uncertainty of $M_{90\%}$ values due to seed variability was investigated, by analyzing the effect of seed variability and the number of simulations. The results demonstrated a higher variability for the sea states at cut-out speed, with variations up to 15% when using 20 1-hr simulations. For the larger turbine, it was found that evaluating load cases at the rated speed became increasingly important, as it resulted in larger $M_{90\%}$ values than the ones at the cut-out speed.

- A comparison was made between a macro-element model incorporating hysteretic damping and nonlinear stiffness during load reversals, and the conventional $p - y$ curves. The differences in extreme responses between the models were within the range of approximately $\pm 2\%$ in operational states, while in parked states, variations between -5% and 11% were observed, highlighting the importance of soil in the absence of aerodynamic damping. Accounting for diffraction effects using frequency-dependent C_m becomes increasingly important for larger diameter and shorter sea states. Nevertheless, variations in estimated extremes compared to conventional Morison with constant C_m did not exceed 4.5%.

8.4 Recommendations for further work

Based on the conclusions drawn from the study, several recommendations for further work can be made to enhance the understanding and application of the lumping method for long-term fatigue damage estimation in offshore wind turbines (OWTs):

- Its applicability and performance for different sites and a broader range of OWT support structures, such as jacket, gravity-based, and floating foundations, should be studied. The different characteristics of those structures compared to the monopiles, i.e., the effect of mean stresses for gravity-based structures, the more complex geometry and local effects for jackets, and the effect of 2^{nd} order low-frequency motions of floating OWTs, may require adjustments of the proposed method. Furthermore, the method's accuracy for sites with different metocean characteristics should be further investigated.

- When the method is applied to different offshore structures, it is recommended to investigate the effect on the lumped LCs when using structural locations with different response characteristics, e.g., the mooring lines and the tower base of a floating OWT. Furthermore, when fully coupled models are used in the lumping process, the white noise simulation time should be evaluated, particularly for structures with longer natural periods than the ones studied in the thesis.

- By employing the lumping method for wind-sea and swell, representative DLCs considering the full variability of metocean parameters used for fatigue design can be extracted with reasonable computational effort. Initial validation studies within the thesis with results obtained from hindcast data fatigue assessment, revealed promising results for the proposed method. Nevertheless, further validation for different support structures and sites is recommended. Such work can potentially result in a new procedure, replacing the standard computationally demanding load case table setup, currently recommended by the design standards, accounting also for the effect of bimodal sea states, which is not currently addressed.

- Conducting comparative studies between the proposed fatigue lumping method with other existing methods used in practice, can help to further benchmark its performance, advantages, and limitations, for both OWTs and other offshore structures. Finally, potential use of the lumping method for optimizing foundation design within a wind farm should be investigated.

Furthermore, based on the conclusions and limitations of the current study the following recommendations are proposed to more accurately predict long-term extreme responses using environmental contours:

- Conclusions regarding the conditional models for wave height and period are based on the site-dependent hindcast data. Further studies for sites with different metocean characteristics can offer additional insights into the accuracy of the different statistical models and their impact on the environmental contours, and subsequent extreme responses. Preferably, data covering a larger period than 10 years (as used in the study) should be used.

- The LonoWe model can be a reasonable choice, when the whole range of H_s data within the wind class needs to be modelled reasonably well. However, a clear procedure should be developed for choosing the transition point between Log-normal and Weibull models. Furthermore, the behaviour of the Log-normal model for the wave period with respect to the wave steepness limit should be further investigated by introducing a lower limit to the model. Finally, the Weibull model for the peak period was strongly sensitive to the H_s class size within a wind class, affecting the resultant contours, and therefore further research is suggested.

- The dependence structure for the metocean parameters used in the thesis to establish the environmental contours was based on the recommendations of the current design standards. Nevertheless, it does not provide a physical interpretation, as it is mostly based on experience. Further work is recommended on investigating other dependence structures/functions, which can potentially include physical relations and limitations between the metocean parameters, e.g. steepness limit.
- The results of the current study for extreme responses were extracted using numerical simulations, with 2^{nd} order wave kinematics. Further research is recommended using fully nonlinear wave kinematics, to provide a more comprehensive understanding of highly-nonlinear breaking waves on extreme loads and responses of OWTs, also considering load cases above cut-out speed. To capture the combined effect of wind and wave loads, studies should also include the effect of wind loads that becomes increasingly important for larger turbines, through e.g., hybrid model tests or using fully nonlinear wave kinematics (extracted from model tests or potential flow theory codes) in the aero-servo-hydro-elastic simulation tools.
- The environmental contour method is a probabilistic approach, and the choice of percentile depends on the level of conservatism required for the design. In the current study, the percentile (90%) was chosen based on previous studies and established experience from other types of offshore structures, corresponding to 100-year extreme responses. Further work including full long-term assessment is required to verify the appropriate percentile that corresponds to 50-year extreme responses of monopile-based OWTs for different wind classes and operational conditions, when the contour method is used.
- The present work focused on the importance of foundation and hydrodynamic load modelling. Further research is recommended to investigate the impact of other aspects such as wave directionality, wave spreading, and different turbulence models in the incoming wind on extreme responses. Finally, as steep sea states induce high structural responses for monopile-based OWTs, it is essential to also investigate further the long-term distribution of the wave steepness and physical parameters related to steep wave events.

Appendices

Appendix A

Structural formulation for state-space models

In this appendix, elemental stiffness and mass matrices of a straight beam are provided. Furthermore, the generalized mass, stiffness, and damping matrices are given. The formulations were used for the simplified OWT state-space models.

A.1 Elemental matrices for an Euler–Bernoulli beam element

As in Euler–Bernoulli beam theory, the rotatory inertia matrix is neglected, only the mass matrix associated with transnational inertia was used, given in Eq. A.1, as follows

$$M_{el} = \frac{m_{el}L_{el}}{420}\begin{bmatrix} 156 & 22L_{el} & 54 & -13L_{el} \\ 22L_{el} & 4L_{el}^2 & 13L_{el} & -3L_{el}^2 \\ 54 & 13L_{el} & 156 & -22L_{el} \\ -13L_{el} & -3L_{el}^2 & -22L_{el} & 4L_{el}^2 \end{bmatrix} \tag{A.1}$$

where L_{el} is the beam element length, and m_{el} is the elemental mass. The elemental bending ($[\boldsymbol{K_{el,b}}]$) and geometric ($[\boldsymbol{K_{el,g}}]$) stiffness matrices, for an Euler-Bernoulli straight beam are given by Eq. A.2, and Eq. A.3 respectively, as follows,

$$K_{el,b} = \frac{EI_{el}}{L_{el}^3}\begin{bmatrix} 12 & 6L_{el} & -12 & 6L_{el} \\ 6L_{el} & 4L_{el}^2 & -6L_{el} & 2L_{el}^2 \\ -12 & -6L_{el} & 12 & -6L_{el} \\ 6L_{el} & 2L_{el}^2 & -6L_{el} & 4L_{el}^2 \end{bmatrix} \tag{A.2}$$

$$K_{el,g} = P\begin{bmatrix} 6L_{el}/5 & 1/10 & -6L_{el}/5 & 1/10 \\ 1/10 & 2L_{el}/15 & -1/10 & -L_{el}/30 \\ -6L_{el}/5 & -1/10 & 6L_{el}/5 & -1/10 \\ 1/10 & L_{el}/30 & -1/10 & 2L_{el}/15 \end{bmatrix} \tag{A.3}$$

where I_{el} is the area moment of inertia for a hollow cylindrical cross section, P is the axial force acting on the element.

A.2 Generalized structural matrices

The generalized mass matrix is expressed by Eq. A.4, as follows

$$\begin{aligned} \boldsymbol{M_\chi} = \underbrace{\int_L m_{el}(z)\boldsymbol{\psi}(z)\boldsymbol{\psi}^\top(z)\mathrm{d}z}_{\text{Integrated mass}} + \underbrace{\sum M(z_i)\boldsymbol{\psi}(z_i)\boldsymbol{\psi}^\top(z_i)}_{\text{Discrete masses}} + \\ + \underbrace{\sum I(z_i)\boldsymbol{\psi_z}(z_i)\boldsymbol{\psi_z}^\top(z_i)}_{\text{Discrete inertias}} \end{aligned} \tag{A.4}$$

where $m_{el}(z)$ is elemental mass, $M(z_i)$, $I(z_i)$ represent discrete masses, and inertias respectively located at position z_i along the support structure. The first term in Eq. A.4 is decomposed in two parts, below and above the SWL, as shown in Eq. A.5,

$$\begin{aligned}\int\limits_L m_{el}(z)\boldsymbol{\psi}(z)\boldsymbol{\psi}^\top(z) = \\ \int_{-L}^{0}[m_{el}(z)+a_{11}(z)]\boldsymbol{\psi}(z)\boldsymbol{\psi}^\top(z)\mathrm{d}z + \int_{0}^{z_{top}} m_{el}(z)\boldsymbol{\psi}(z)\boldsymbol{\psi}^\top(z)\mathrm{d}z\end{aligned} \tag{A.5}$$

where the first term includes the water mass, additionally to the structural mass, and it is added the transverse added mass per unit length, based on the analytical expression for a 2D circular cylinder of diameter D_p [233], given by Eq. A.6,

$$a_{11}(z) = \rho\pi D_p^2(z)/4 \tag{A.6}$$

where ρ_w is the water density, and D_p is the monopile diameter. The generalized stiffness matrix is expressed by Eq. A.7, as follows,

$$\begin{aligned}\boldsymbol{K_\chi} = \underbrace{\int_L EI_{el}(z)\boldsymbol{\psi_{zz}}(z)\boldsymbol{\psi}^\top_{\boldsymbol{zz}}(z)\mathrm{d}z}_{\text{Integrated bending stiffness}} + \underbrace{\int_L P(z)\boldsymbol{\psi_z}(z)\boldsymbol{\psi}^\top_{\boldsymbol{z}}(z)\mathrm{d}z}_{\text{Integrated axial stiffness}} + \\ + \underbrace{K(z_s)\boldsymbol{\psi_z}(z_s)\boldsymbol{\psi}^\top_{\boldsymbol{z}}(z_s)}_{\text{Soil stiffness}}\end{aligned} \tag{A.7}$$

where $EI_{el}(z)$ is the elemental bending stiffness, $P(z)$ is the elemental axial force, and $K(z_i)$ represents the soil stiffness, at mudline (z_s=-30 m). The generalized damping matrix consists of two terms as shown in Eq. A.8,

$$\boldsymbol{C_\chi} = \underbrace{\beta\int\limits_L EI_{el}(z)\boldsymbol{\psi_{zz}}(z)\boldsymbol{\psi}^\top_{\boldsymbol{zz}}(z)\mathrm{d}z}_{\text{Rayleigh damping}} + \underbrace{B(z_{top})\boldsymbol{\psi}(z_{top})\boldsymbol{\psi}^\top(z_{top})}_{\text{Aerodynamic damping}} \tag{A.8}$$

where the first term describes the structural, soil, and hydrodynamic damping represented by stiffness-proportional Rayleigh damping with stiffness-proportional coefficient β along the support structure. The second term describes the aerodynamic damping applied to the tower top, z_{top}.

References

[1] Allen L, O'Connell A, Kiermer V. How can we ensure visibility and diversity in research contributions? how the contributor role taxonomy (credit) is helping the shift from authorship to contributorship. *Learned Publishing* 2019; **32**(1):71–74. URL `https://doi.org/10.1002/leap.1210`.

[2] Masson-Delmotte V, Zhai P, H-O P, Roberts D, Skea J, Shukla P, Pirani A, Moufouma-Okia W, Péan C, Pidcock R, *et al.*. IPCC, 2018: Global warming of 1.5°C. An IPCC special report on the impacts of global warming of 1.5°C above pre-industrial levels and related global greenhouse gas emission pathways, in the context of strengthening the global response to the threat of climate change, sustainable development, and efforts to eradicate poverty. In Press. *Technical report*, Intergovernmental Panel on Climate Change (IPCC) 2018.

[3] Paris agreement 12 2015. URL `https://treaties.un.org/pages/ViewDetails.aspx?src=TREATY&mtdsg_no=XXVII-7-d&chapter=27&clang=_en`.

[4] Masson-Delmotte V, Zhai P, A P, Connors S, Péan C, Skea J, Shukla P, Pirani A, Berger S, Caud N, *et al.*. IPCC, climate change 2021: The physical science basis. contribution of working group i to the sixth assessment report of the intergovernmental panel on climate change. cambridge university press. In Press. *Technical report*, Intergovernmental Panel on Climate Change (IPCC) 2021.

[5] Hansen J, Sato M, Russell G, Kharecha P. Climate sensitivity, sea level, and atmospheric CO_2. *Philosophical transactions. Series A, Mathematical, physical, and engineering sciences* 10 2013; **371**:20120 294, doi: 10.1098/rsta.2012.0294.

[6] Global Wind Report, Global Wind Energy Council,. *Technical report*, Global Wind Energy Council 2021.

[7] IRENA (2018), Global Energy Transformation: A roadmap to 2050, Abu Dhabi,. *Technical report*, International Renewable Energy Agency 2018.

[8] Oh KY, Nam W, Ryu MS, Kim JY, Epureanu BI. A review of foundations of offshore wind energy convertors: Current status and future perspectives. *Renewable and Sustainable Energy Reviews* 2018; **88**:16–36. URL https://doi.org/10.1016/j.rser.2018.02.005.

[9] Lizet R, Fraile D, Brindley G. Offshore Wind in Europe - Key trends and statistics. *Technical Report*, Wind Europe 2020.

[10] Hermans JM, Peeringa KW. Future XL monopile foundation design for a 10 MW wind turbine in deep water. *Technical Report*, ECN (Energy research Centre of the Netherlands) 2016.

[11] Tong W. *Wind Power Generation and Wind Turbine Design*. WIT Press, 2010. URL https://books.google.no/books?id=wU9bgvrl4rQC.

[12] Gottlieb, Magnus Hornø and Nymark, Anders Holst and Grann, Emil Damgaard and Bøggild, Johannes. Making green energy affordable : How the offshore wind energy industry matured – and what we can learn from it. *Technical Report*, Ørsted 2019.

[13] IRENA (2020), Renewable Power Generation Costs in 2019, Abu Dhabi,. *Technical report*, International Renewable Energy Agency, 2020.

[14] Oh KY, Kim JY, Lee JS, Ryu KW. Wind resource assessment around korean peninsula for feasibility study on 100 MW class offshore wind farm. *International Symposium on Low Carbon and Renewable Energy Technology 2010 (ISLCT 2010)*, vol. 42, 2012; 217–226. URL https://doi.org/10.1016/j.renene.2011.08.012.

[15] Oh KY, Kim JY, Lee JK, Ryu MS, Lee JS. An assessment of wind energy potential at the demonstration offshore wind farm in korea. *Energy* 2012; **46**(1):555–563. URL https://doi.org/10.1016/j.energy.2012.07.056.

[16] IRENA (2019d), Renewable capacity statistics,. *Technical report*, International Renewable Energy Agency, Abu Dhabi, 2019.

[17] IRENA (2019a), Global Energy Transformation: A roadmap to 2050 (2019 edition), Abu Dhabi,. *Technical report*, International Renewable Energy Agency, 2019.

[18] IRENA (2021), Offshore Renewables: An action agenda for deployment. *Technical report*, International Renewable Energy Agency (IRENA) 2021.

[19] Gonzalez-Rodriguez AG. Review of offshore wind farm cost components. *Energy for Sustainable Development* 2017; **37**:10–19. URL https://www.sciencedirect.com/science/article/pii/S0973082616303647.

[20] Guide to an offshore wind farm updated and extended. BVG Associates, Published on behalf of The Crown Estate and the Offshore Renewable Energy Catapult. *Technical report*, BVG Associates 2019.

[21] Offshore wind cost reduction pathways. BVG Associates,. *Technical report*, BVG Associates 2012.

[22] Offshore Wind Cost Reductions - Pathways Study. The Crown Estate,. *Technical report*, The Crown Estate 2012.

[23] Future Renewable Energy cost - Offshore Wind. BVG Associates,. *Technical report*, KIC InnoEnergy 2014.

[24] Approaches to cost-reduction in offshore wind - a report for the Committee on Climate change. BVG Associates,. *Technical report*, BVG Associates 2015.

[25] Cost reduction options for offhsore wind in the Netherlands FID 2010-2020. TKI Wind op Zee,. *Technical report*, TKI Wind op Zee 2015.

[26] Future Renewable Energy Cost: Offshore Wind. 57 Technologies Innovations that will have great impact on reducing the cost of electricity from European offshore wind farms. KIC InnoEnergy,. *Technical report*, KIC InnoEnergy 2017.

[27] Offshore Wind Cost Reduction - Recent and future trends in the uk and europe, Catapult Offshore Renewable Energy,. *Technical report*, Catapult Offshore Renewable Energy 2016.

[28] BVG Associates: Ports and services for offshore wind in 2030; A vision of the future including their role in lcoe reduction, Offshore Wind Ports Platform. *Technical report*, Offshore Wind Ports Platform 2018.

[29] Pathways to potential cost reductions for offshore wind energy, TKI Wind op Zee,. *Technical report*, TKI Wind op Zee 2021.

[30] International Electrotechnical Commission (IEC). International Electrotechnical Commission, Wind turbine generator systems-Part 1: Safety requirements. 4th edition (IEC 61400-1) 2019.

[31] Kallehave D, Byrne B, Thilsted C, Mikkelsen K. Optimization of monopiles for offshore wind turbines. *Philosophical transactions. Series A, Mathematical, physical, and engineering sciences* 02 2015; **373**. URL `https://doi.org/10.1098/rsta.2003.1286`.

[32] Wu X, Hu Y, Li Y, Yang J, Duan L, Wang T, Adcock T, Jiang Z, Gao Z, Lin Z, *et al.*. Foundations of offshore wind turbines: A review. *Renewable and Sustainable Energy Reviews* 2019; **104**:379–393. URL `https://doi.org/10.1016/j.rser.2019.01.012`.

[33] ICF. 2021. Comparison of Environmental Effects from Different Offshore Wind Turbine Foundations. *Technical Report*, U.S. Dept. of the Interior, Bureau of Ocean Energy Management, Headquarters, Sterling, VA. OCS Study BOEM 2021-053. 48 pp. 2021.

[34] Malhotra S. Design and Construction Considerations for Offshore Wind Turbine Foundations. *The Robert Dean Symposium on Coastal and Ocean Engineering; Special Symposium on Offshore Renewable Energy, International Conference on Offshore Mechanics and Arctic Engineering*, vol. Volume 5: Ocean Space Utilization; Polar and Arctic Sciences and Technology, 2007; 635–647. URL `https://doi.org/10.1061/41095(365)155`.

[35] Carstens H, Nielsen H, Hansen H. Lowering costs by individual design of foundation structures. *European Wind Energy Conference (EWEC), 2004, London, UK*, 2004.

[36] Passon P, Branner K, Larsen SE, Hvenekær Rasmussen J. Offshore Wind Turbine Foundation Design. PhD Thesis, DTU Wind Energy PhD 2015.

[37] Seidel M. Design of support structures for offshore wind turbines – interfaces between project owner, turbine manufacturer, authorities and designer. *Stahlbau* 09 2010; **79**:631 – 636. URL `https://doi.org/10.1002/stab.201001362`.

[38] Van der Valk P, Voormeeren S, Valk P, Rixen D. Dynamic models for load calculation procedures of offshore wind turbine support structures: Overview, assessment and outlook. *Journal of Computational and Nonlinear Dynamics* 01 2014; **10**. URL 10.1115/1.4028136.

[39] DNV-GL. Det Norske Veritas - Germanischer Lloyd, Support structures for wind turbines (DNVGL-ST-0126) 2018.

[40] Seidel M, Mutius M, Steudel D. Design and load calculations for offshore foundations of a 5 MW turbine. *Proceedings of 5th German wind energy conference, DEWEC*, 2004. URL https://api.semanticscholar.org/CorpusID:162174015.

[41] Seidel M, Mutius M, Rix P, Steudel D. Integrated analysis of wind and wave loading for complex support structures of offshore wind turbines. *Conference Proceedings Offshore Wind 2005, Copenhagen*, 2005.

[42] Robertson AN, Wendt F, Jonkman JM, Popko W, Borg M, Bredmose H, Schlutter F, Qvist J, Bergua R, Harries R, *et al.*. Oc5 project phase ib: Validation of hydrodynamic loading on a fixed, flexible cylinder for offshore wind applications. *Energy Procedia* 2016; **94**:82–101. URL https://www.sciencedirect.com/science/article/pii/S1876610216308700.

[43] Sørum SH, Horn JTH, Amdahl J. Comparison of numerical response predictions for a bottom-fixed offshore wind turbine. *Energy Procedia* 2017; **137**:89–99. URL https://www.sciencedirect.com/science/article/pii/S1876610217352979.

[44] Popko W, Huhn ML, Robertson A, Jonkman J, Wendt F, Müller K, Kretschmer M, Vorpahl F, Hagen TR, Galinos C, *et al.*. Verification of a Numerical Model of the Offshore Wind Turbine From the Alpha Ventus Wind Farm Within OC5 Phase III. 2018.

[45] Segeren MLA, Hermans KW. Experimental investigation of the dynamic installation of a slip joint connection between the monopile and tower of an offshore wind turbine. *Journal of Physics: Conference Series* jun 2014; **524**(1):012 080. URL https://dx.doi.org/10.1088/1742-6596/524/1/012080.

[46] GoBe Consultants Ltd. Thanet Extension Offshore Wind Farm - Environmental Statement Volume 2 Chapter 1: Project Description (Offshore). *Technical Report*, Vattenfall Wind Power Ltd 2018.

[47] Seidel M. Wave Induced Fatigue Loads on Monopiles - New Approaches for Lumping of Scatter Tables and Site Specific Interpolation of Fatigue Loads. *International Wind Engineering Conference (IWEC)*, vol. 83, 2014. URL `https://api.semanticscholar.org/CorpusID:109046867`.

[48] O'Kelly B, Arshad M. 20 - offshore wind turbine foundations – analysis and design. *Offshore Wind Farms*, Ng C, Ran L (eds.). Woodhead Publishing, 2016; 589–610. URL `https://doi.org/10.1016/B978-0-08-100779-2.00020-9`.

[49] van der Tempel J, Molenaar DP. Wind turbine structural dynamics – a review of the principles for modern power generation, onshore and offshore. *Wind Engineering* 2002; **26**(4):211–222. URL `https://doi.org/10.1260/030952402321039412`.

[50] Bhattacharya S, Cox JA, Lombardi D, Muir Wood D. Dynamics of offshore wind turbines supported on two foundations. *Proceedings of the Institution of Civil Engineers - Geotechnical Engineering* 2013; **166**(2):159–169. URL `https://doi.org/10.1680/geng.11.00015`.

[51] Bhattacharya S. Challenges in design of foundations for offshore wind turbines. *Institution of Engineering and Technology* 10 2014; **1**. URL `10.1049/etr.2014.0041`.

[52] Arany L, Bhattacharya S, Macdonald J, Hogan S. Design of monopiles for offshore wind turbines in 10 steps. *Soil Dynamics and Earthquake Engineering* 2017; **92**:126–152. URL `https://doi.org/10.1016/j.soildyn.2016.09.024`.

[53] Nikitas G, Vimalan NJ, Bhattacharya S. An innovative cyclic loading device to study long term performance of offshore wind turbines. *Soil Dynamics and Earthquake Engineering* 2016; **82**:154–160. URL `https://doi.org/10.1016/j.soildyn.2015.12.008`.

[54] Devaney L. Breaking wave loads and stress analysis of jacket structures supporting offshore wind turbines. PhD Thesis, UK 2012. URL `https://pure.manchester.ac.uk/ws/portalfiles/portal/54519118/FULL_TEXT.PDF`.

[55] Amar Bouzid D, Bhattacharya S, Otsmane L. Assessment of natural frequency of installed offshore wind turbines using nonlinear finite element model considering soil-monopile interaction. *Journal of Rock*

Mechanics and Geotechnical Engineering 2018; **10**(2):333–346. URL https://doi.org/10.1016/j.jrmge.2017.11.010.

[56] Reistad M, Breivik O, Haakenstad H, Aarnes OJ, Furevik BR, Bidlot JR. A high-resolution hindcast of wind and waves for the north sea, the norwegian sea, and the barents sea. *Journal of Geophysical Research: Oceans* 2011; **116**(C5). URL https://agupubs.onlinelibrary.wiley.com/doi/abs/10.1029/2010JC006402.

[57] Aarnes OJ, Øyvind Breivik, Reistad M. Wave extremes in the northeast atlantic. *Journal of Climate* 01 Mar 2012; **25**(5):1529 – 1543. URL 10.1175/JCLI-D-11-00132.1.

[58] Naess A, Moan T. *Stochastic Dynamics of Marine Structures*. Cambridge University Press, 2012. URL 10.1017/CBO9781139021364.

[59] DNV-GL (Det Norske Veritas - Germanischer Lloyd). Environmental conditions and environmental loads (DNVGL-RP-C205) September, 2019.

[60] Bureau Veritas. Guidance for Long-term Hydro-structure Calculations February, 2019.

[61] Schaumann P, Böker C. Can tripods and jackets compete the monopiles? *Contribution to Copenhagen Offshore Wind, 26-28 October*, 2005.

[62] ABS (American Bureau of Shipping). Guide For The Fatigue Assessment Of Offshore Structures 2014.

[63] DNV-GL (Det Norske Veritas - Germanischer Lloyd). Fatigue design of offshore steel structures (DNVGL-RP-C203).

[64] API. API Recommended Practice 2A-WSD; Planning, Designing, and Constructing Fixed Offshore Platforms Working Stress Design; 22 Edition 2014.

[65] Matsuishi M, Endo T. Fatigue of metals subjected to varying stress. *Proceedings of the Kyushu Branch of Japan Society of Mechanics Engineering* 1968; :37–40URL https://api.semanticscholar.org/CorpusID:134952923.

[66] Seidel M, Voormeeren S, van der Steen JB. State-of-the-art design processes for offshore wind turbine support structures. *Stahlbau* 2016; **85**(9):583–590. URL https://doi.org/10.1002/stab.201610404.

[67] Sheehan JM, Grealish FW, Harte AM, Smith RJ. Characterizing the Wave Environment in the Fatigue Analysis of Flexible Risers. *Journal of Offshore Mechanics and Arctic Engineering* 11 2005; **128**(2):108–118. URL https://doi.org/10.1115/1.2185129.

[68] Low YM, Cheung SH. On the long-term fatigue assessment of mooring and riser systems. *Ocean Engineering* 2012; **53**:60–71. URL https://doi.org/10.1016/j.oceaneng.2012.06.017.

[69] Du J, Chang A, Wang S, Li H. A Novel Lumping Block Method for Fatigue Damage Assessment of Mooring Chain. *Proceedings of the Twenty-fourth (2014) International Ocean and Polar Engineering Conference*, Korea, 2014.

[70] Hou HM, Dong GH, Xu TJ. An improved lumping block equivalent method for predicting fatigue damage of mooring system for fish cage. *Ocean Engineering* 2019; **193**:106 567. URL https://doi.org/10.1016/j.oceaneng.2019.106567.

[71] Kühn M. Dynamics and design optimisation of offshore wind energy Conversion systems. PhD Thesis 2001. URL http://resolver.tudelft.nl/uuid:adc3b032-3dde-4e32-84c3-7b8e181e5263.

[72] Seidel M. Wave induced fatigue loads - insights from frequency domain calculations. *Stahlbau* 08 2014; **83**. URL https://doi.org/10.1002/stab.201001362.

[73] Passon P, Branner K. Condensation of long-term wave climates for the fatigue design of hydrodynamically sensitive offshore wind turbine support structures. *Ships and Offshore Structures* 2014; **Vol. 11**:142–166. URL https://doi.org/10.1080/17445302.2014.967994.

[74] Passon P. Damage equivalent wind-wave correlations on basis of damage contour lines for the fatigue design of offshore wind turbines. *Renewable Energy* 2015; **Vol. 81**:723–736. URL https://doi.org/10.1016/j.renene.2015.03.070.

[75] Song X, Du J, Wang S, Li H, Chang A. An innovative block partition and equivalence method of the wave scatter diagram for offshore structural fatigue assessment. *Applied Ocean Research* 2016; **60**:12–28. URL https://doi.org/10.1016/j.apor.2016.08.005.

[76] Song X, Wang S. A novel spectral moments equivalence based lumping block method for efficient estimation of offshore structural fatigue

damage. *International Journal of Fatigue* 2019; **118**:162–175. URL https://doi.org/10.1016/j.ijfatigue.2018.09.016.

[77] Jia J. An efficient nonlinear dynamic approach for calculating wave induced fatigue damage of offshore structures and its industrial applications for lifetime extension. *Applied Ocean Research* 2008; **30**(3):189–198. URL https://doi.org/10.1016/j.apor.2008.09.003.

[78] DNV-GL (Det Norske Veritas - Germanischer Lloyd). Riser fatigue (DNVGL-RP-F204) 2017.

[79] Burton T, Jenkins N, Sharpe D, Bossanyi E. *Wind Energy Handbook*. John Wiley & Sons, Ltd, 2011. URL https://onlinelibrary.wiley.com/doi/book/10.1002/9781119992714.

[80] International Electrotechnical Commission (IEC). International standard 61400-3, wind turbines, part 3: Design requirements for offshore wind turbines 2009.

[81] DNV-GL (Det Norske Veritas - Germanischer Lloyd). Support structures for wind turbines (DNVGL-ST-0126) 2016.

[82] Agarwal P, Manuel L. Simulation of offshore wind turbine response for long-term extreme load prediction. *Engineering Structures* 2009; **31**(10):2236–2246. URL https://www.sciencedirect.com/science/article/pii/S0141029609001436.

[83] de Hauteclocque G, Mackay E, Vanem E. Quantitative comparison of environmental contour approaches. *Ocean Engineering* 2022; **245**:110 374. URL https://www.sciencedirect.com/science/article/pii/S0029801821016693.

[84] Mackay E, de Hauteclocque G, Vanem E, Jonathan P. The effect of serial correlation in environmental conditions on estimates of extreme events. *Ocean Engineering* 2021; **242**:110 092. URL https://www.sciencedirect.com/science/article/pii/S0029801821014189.

[85] Velarde J, Vanem E, Kramhøft C, Sørensen J. Probabilistic analysis of offshore wind turbines under extreme resonant response: Application of environmental contour method. *Applied Ocean Research* 12 2019; **93**:101 947. URL https://doi.org/10.1016/j.apor.2019.101947.

[86] Baarholm GS, Haver S, Økland OD. Combining contours of significant wave height and peak period with platform response distributions

for predicting design response. *Marine Structures* 2010; **23**(2):147–163. URL https://www.sciencedirect.com/science/article/pii/S0951833910000171.

[87] Li Q, Gao Z, Moan T. Modified environmental contour method for predicting long-term extreme responses of bottom-fixed offshore wind turbines. *Marine Structures* 2016; **48**:15–32. URL https://www.sciencedirect.com/science/article/pii/S0951833916300181.

[88] Li L, Yuan ZM, Gao Y, Zhang X, Tezdogan T. Investigation on long-term extreme response of an integrated offshore renewable energy device with a modified environmental contour method. *Renewable Energy* 2019; **132**:33–42. URL https://www.sciencedirect.com/science/article/pii/S0960148118309352.

[89] Haselsteiner AF, Frieling M, Mackay E, Sander A, Thoben KD. Long-term extreme response of an offshore turbine: How accurate are contour-based estimates? *Renewable Energy* 2022; **181**:945–965. URL https://www.sciencedirect.com/science/article/pii/S0960148121013975.

[90] Giske FIG, Leira BJ, Øiseth O. Full long-term extreme response analysis of marine structures using inverse form. *Probabilistic Engineering Mechanics* 2017; **50**:1–8. URL https://www.sciencedirect.com/science/article/pii/S0266892017300760.

[91] Videiro PM, Sagrilo LVS. Efficient Evaluation of Long-Term Response for Design of Components of Offshore Structures. 2017. URL https://doi.org/10.1115/OMAE2017-61444.

[92] Winterstein SR, Ude TC, Cornell CA, Bjerager P, Haver S. Environmental Parameters for Extreme Response: Inverse FORM with Omission Factors. *Proceedings of the 6th International conference on structural safety and reliability (ICOSSAR-93)*, Austria 9-13 August, 1993.

[93] Vanem E. A comparison study on the estimation of extreme structural response from different environmental contour methods. *Marine Structures* 2017; **56**:137–162. URL https://www.sciencedirect.com/science/article/pii/S0951833916303100.

[94] Haselsteiner AF, Coe RG, Manuel L, Chai W, Leira B, Clarindo G, Guedes Soares C, Ásta Hannesdóttir, Dimitrov N, Sander A, *et al.*. A benchmarking exercise for environmental contours. *Ocean Engineering*

2021; **236**:109 504. URL https://www.sciencedirect.com/science/article/pii/S0029801821009033.

[95] Haver S, Sagli G, Gran T. Long Term Response Analysis of Fixed and Floating Structures. *Symposium on Ocean Wave Kinematics, Dynamics and Loads on Structures*, 1998.

[96] Kleiven G, Haver S. Met-Ocean Contour Lines for Design; Correction for Omitted Variability in the Response Process. *International Offshore and Polar Engineering Conference (ISOPE)*, France, 2004.

[97] Muliawan MJ, Gao Z, Moan T. Application of the Contour Line Method for Estimating Extreme Response in Mooring Lines of a Two-Body Floating Wave Energy Converter. 2012; 429–439. URL https://doi.org/10.1115/OMAE2012-83370.

[98] Saranyasoontorn K, Manuel L. Design Loads for Wind Turbines Using the Environmental Contour Method. *Journal of Solar Energy Engineering* 07 2006; **128**(4):554–561, doi: 10.1115/1.2346700. URL https://doi.org/10.1115/1.2346700.

[99] NORSOK. Standard N-003; Action and action effects, third edition 2017.

[100] Derbanne Q, de Hauteclocque G, Dumont M. How to Account for Short-Term and Long-Term Variability in the Prediction of the 100 Years Response? 2017. URL https://doi.org/10.1115/OMAE2017-61701.

[101] Battjes JA. Long-term wave height distributions at seven stations around the british isles. *Deutsche Hydrografische Zeitschrift* 1972; **25**(1):71–74. URL https://doi.org/10.1007/BF02312702.

[102] Ochi MK, Whalen JE. Prediction of the severest significant wave height. *Coastal Engineering 1980* ; :587–599URL https://ascelibrary.org/doi/abs/10.1061/9780872622647.036.

[103] Haver S. Wave climate off northern norway. *Applied Ocean Research* 1985; **7**(2):85–92. URL https://www.sciencedirect.com/science/article/pii/0141118785900380.

[104] Haver S, Nyhus KA. A Wave Climate Description For Long Term Response Calculations. *International Offshore Mechanics and Arctic Engineering Symposium*, vol. Vol. IV, ASME, 1986. URL https://api.semanticscholar.org/CorpusID:127887895.

[105] Haver S. On the joint distribution of heights and periods of sea waves. *Ocean Engineering* 1987; **14**(5):359–376. URL https://www.sciencedirect.com/science/article/pii/0029801887900503.

[106] Bitner-Gregersen EM, Haver S. Joint Long Term Description of Environmental Parameters for Structural Response Calculations. *International Workshop on Wave Hindcasting and Forecasting, 1989*, 1989.

[107] Mathisen J, Bitner-Gregersen E. Joint distributions for significant wave height and wave zero-up-crossing period. *Applied Ocean Research* 1990; **12**(2):93–103. URL https://www.sciencedirect.com/science/article/pii/S0141118705800331.

[108] Bitner-Gregersen EM, Haver S. Joint Environmental Model for Reliability Calculations. *Proceedings of the first International Offshore and Polar Engineering Conference (ISOPE)*, vol. I, 1991.

[109] Bitner-Gregersen EM. Joint Probabilistic Description for Combined Seas. 2005; 169–180. URL https://doi.org/10.1115/OMAE2005-67382.

[110] Bitner-Gregersen EM. Joint met-ocean description for design and operations of marine structures. *Applied Ocean Research* 2015; **Vol. 51**:279–292. URL https://doi.org/10.1016/j.apor.2015.01.007.

[111] Vanem E. Uncertainties in extreme value modelling of wave data in a climate change perspective. *Journal of Ocean Engineering and Marine Energy* 2015; **1**:339–359. URL https://doi.org/10.1007/s40722-015-0025-3.

[112] Giske FIG, Kvåle KA, Leira BJ, Øiseth O. Long-term extreme response analysis of a long-span pontoon bridge. *Marine Structures* 2018; **58**:154–171. URL https://www.sciencedirect.com/science/article/pii/S0951833917303386.

[113] Horn JT, Bitner-Gregersen EM, Krokstad J, Leira B, Amdahl J. A new combination of conditional environmental distributions. *Applied Ocean Research* 2018; **Vol. 73**:17–26. URL https://doi.org/10.1016/j.apor.2018.01.010.

[114] Orimolade AP, Haver S, Gudmestad OT. Estimation of extreme significant wave heights and the associated uncertainties: A case study using nora10 hindcast data for the barents sea. *Marine Structures* 2016;

49:1–17. URL https://www.sciencedirect.com/science/article/pii/S0951833916300697.

[115] Bitner-Gregersen EM. Comparison of wind and wave climate in open sea and coastal waters. *Ocean Engineering* 2018; **170**:199–208. URL https://www.sciencedirect.com/science/article/pii/S0029801818319759.

[116] Velarde J, Vanem E, Kramhøft C, Sørensen JD. Probabilistic analysis of offshore wind turbines under extreme resonant response: Application of environmental contour method. *Applied Ocean Research* 2019; **93**:101 947. URL https://www.sciencedirect.com/science/article/pii/S0141118719304328.

[117] Vanem E. Joint statistical models for significant wave height and wave period in a changing climate. *Marine Structures* 2016; **49**:180–205. URL https://www.sciencedirect.com/science/article/pii/S095183391630106X.

[118] Zhang Y, Kim CW, Beer M, Dai H, Soares CG. Modeling multivariate ocean data using asymmetric copulas. *Coastal Engineering* 2018; **135**:91–111. URL https://www.sciencedirect.com/science/article/pii/S0378383916302812.

[119] Fazeres-Ferradosa T, Taveira-Pinto F, Vanem E, Reis MT, das Neves L. Asymmetric copula–based distribution models for met-ocean data in offshore wind engineering applications. *Wind Engineering* 2018; **42**(4):304–334. URL https://doi.org/10.1177/0309524X18777323.

[120] Lin Y, Dong S, Tao S. Modelling long-term joint distribution of significant wave height and mean zero-crossing wave period using a copula mixture. *Ocean Engineering* 2020; **197**:106 856. URL https://www.sciencedirect.com/science/article/pii/S0029801819309473.

[121] Ferreira J, Guedes Soares C. Modelling bivariate distributions of significant wave height and mean wave period. *Applied Ocean Research* 2002; **24**(1):31–45. URL https://www.sciencedirect.com/science/article/pii/S0141118702000068.

[122] Eckert-Gallup A, Martin N. Kernel density estimation (KDE) with adaptive bandwidth selection for environmental contours of extreme sea states. *OCEANS 2016 MTS/IEEE Monterey*, 2016; 1–5. URL https://ieeexplore.ieee.org/document/7761150.

[123] Haselsteiner AF, Ohlendorf JH, Wosniok W, Thoben KD. Deriving environmental contours from highest density regions. *Coastal Engineering* 2017; **123**:42–51. URL https://www.sciencedirect.com/science/article/pii/S0378383916304446.

[124] Mackay EBL, Jonathan P. Estimation of Environmental Contours Using a Block Resampling Method. 2020. URL https://doi.org/10.1115/OMAE2020-18308.

[125] Jonathan P, Flynn J, Ewans K. Joint modelling of wave spectral parameters for extreme sea states. *Ocean Engineering* 2010; **37**(11):1070–1080. URL https://www.sciencedirect.com/science/article/pii/S0029801810001022.

[126] Jonathan P, Ewans K, Flynn J. On the Estimation of Ocean Engineering Design Contours. *Journal of Offshore Mechanics and Arctic Engineering* 07 2014; **136**(4). URL https://doi.org/10.1115/1.4027645.

[127] Haselsteiner AF, Sander A, Ohlendorf JH, Thoben KD. Global Hierarchical Models for Wind and Wave Contours: Physical Interpretations of the Dependence Functions. 2020; V02AT02A047. URL 10.1115/OMAE2020-18668.

[128] Haver S, Winterstein S. Environmental contour lines: a method for estimating long term extremes by a short term analysis. *Transactions - Society of Naval Architects and Marine Engineers* 2009; :116–127URL https://www.researchgate.net/publication/242315833_Environmental_Contour_Lines_A_Method_for_Estimating_Long_Term_Extremes_by_a_Short_Term_Analysis.

[129] Bang Huseby A, Vanem E, Natvig B. A new approach to environmental contours for ocean engineering applications based on direct monte carlo simulations. *Ocean Engineering* 2013; **60**:124–135. URL https://www.sciencedirect.com/science/article/pii/S0029801812004532.

[130] Huseby AB, Vanem E, Natvig B. Alternative environmental contours for structural reliability analysis. *Structural Safety* 2015; **54**:32–45. URL https://www.sciencedirect.com/science/article/pii/S0167473014001143.

[131] Vanem E. 3-dimensional environmental contours based on a direct sampling method for structural reliability analysis of ships and off-

shore structures. *Ships and Offshore Structures* 2019; **14**(1):74–85. URL https://doi.org/10.1080/17445302.2018.1478377.

[132] Chai W, Leira BJ. Environmental contours based on inverse sorm. *Marine Structures* 2018; **60**:34–51. URL https://www.sciencedirect.com/science/article/pii/S0951833917304707.

[133] Giske FIG, Leira BJ, Øiseth O. Long-Term Extreme Response Analysis of Marine Structures Using Inverse SORM. *Journal of Offshore Mechanics and Arctic Engineering* 05 2018; **140**(5). URL https://doi.org/10.1115/1.4039718.

[134] Mackay E, Haselsteiner AF. Marginal and total exceedance probabilities of environmental contours. *Marine Structures* 2021; **75**:102 863. URL https://www.sciencedirect.com/science/article/pii/S0951833920301568.

[135] Silva-González F, Heredia-Zavoni E, Montes-Iturrizaga R. Development of environmental contours using nataf distribution model. *Ocean Engineering* 2013; **58**:27–34. URL https://www.sciencedirect.com/science/article/pii/S0029801812003241.

[136] Derbanne Q, de Hauteclocque G. A New Approach for Environmental Contour and Multivariate De-Clustering. 2019; V003T02A030. URL https://doi.org/10.1115/OMAE2019-95993.

[137] Mackay E, de Hauteclocque G. Model-free environmental contours in higher dimensions. *Ocean Engineering* 2023; **273**:113 959. URL https://www.sciencedirect.com/science/article/pii/S0029801823003438.

[138] Ross E, Astrup OC, Bitner-Gregersen E, Bunn N, Feld G, Gouldby B, Huseby A, Liu Y, Randell D, Vanem E, *et al.*. On environmental contours for marine and coastal design. *Ocean Engineering* 2020; **195**:106 194. URL http://www.sciencedirect.com/science/article/pii/S0029801819303798.

[139] Silva-González F, Vázquez-Hernández A, Sagrilo L, Cuamatzi R. The effect of some uncertainties associated to the environmental contour lines definition on the extreme response of an fpso under hurricane conditions. *Applied Ocean Research* 2015; **53**:190–199. URL https://www.sciencedirect.com/science/article/pii/S0141118715001194.

[140] Vanem E, Gramstad O, Bitner-Gregersen EM. A simulation study on the uncertainty of environmental contours due to sampling variability for different estimation methods. *Applied Ocean Research* 2019; **91**:101 870. URL `https://www.sciencedirect.com/science/article/pii/S0141118719302676`.

[141] Coe RG, Manuel L, Haselsteiner AF. On limiting the influence of serial correlation in metocean data for prediction of extreme return levels and environmental contours. *Ocean Engineering* 2022; **266**:113 032. URL `https://www.sciencedirect.com/science/article/pii/S0029801822023150`.

[142] Valamanesh V, Myers A, Arwade S. Multivariate analysis of extreme metocean conditions for offshore wind turbines. *Structural Safety* 2015; **55**:60–69. URL `https://www.sciencedirect.com/science/article/pii/S0167473015000296`.

[143] Li L, Gao Z, Moan T. Joint Distribution of Environmental Condition at Five European Offshore Sites for Design of Combined Wind and Wave Energy Devices. *Journal of Offshore Mechanics and Arctic Engineering* 06 2015; **137**(3). URL `https://doi.org/10.1115/1.4029842`.

[144] Horn JT, Winterstein SR. Extreme response estimation of offshore wind turbines with an extended contour-line method. *Journal of Physics: Conference Series* oct 2018; **1104**:012 031. URL `https://doi.org/10.1088/1742-6596/1104/1/012031`.

[145] Saranyasoontorn K, Manuel L. On Assessing the Accuracy of Offshore Wind Turbine Reliability-Based Design Loads From the Environmental Contour Method. 2004. URL `https://onepetro.org/ISOPEIOPEC/proceedings-pdf/ISOPE04/All-ISOPE04/ISOPE-I-04-030/1859916/isope-i-04-030.pdf`.

[146] Li Q, Gao Z, Moan T. Modified environmental contour method to determine the long-term extreme responses of a semi-submersible wind turbine. *Ocean Engineering* 2017; **142**:563–576. URL `https://www.sciencedirect.com/science/article/pii/S0029801817304109`.

[147] El Beshbichi O, Rødstøl H, Xing Y, Ong MC. Prediction of long-term extreme response of two-rotor floating wind turbine concept using the modified environmental contour method. *Renewable Energy* 2022; **189**:1133–1144. URL `https://www.sciencedirect.com/science/article/pii/S0960148122002683`.

[148] Reese L, Matlock H. Non-dimensional solutions for laterally-loaded piles with soil modulus assumed proportional to depth. *Proceedings of 8th Texas Conference SMFE 7/1-41, University of Texas, Austin*, 1956.

[149] LEBLANC C, HOULSBY G, BYRNE B. Response of stiff piles in sand to long-term cyclic lateral loading. *Géotechnique* 2010; **60**(2):79–90. URL https://doi.org/10.1680/geot.7.00196.

[150] Doherty P, Gavin K. Laterally loaded monopile design for offshore wind farms. *Proceedings of the ICE - Energy, 165 (1):7-17*, 2012. URL https://doi.org/10.1680/ener.11.00003.

[151] Byrne B, Houlsby G. Foundations for offshore wind turbines. *Philosophical transactions. Series A, Mathematical, physical, and engineering sciences* 01 2004; **361**:2909–30. URL https://doi.org/10.1098/rsta.2003.1286.

[152] Lombardi D, Bhattacharya S, Muir Wood D. Dynamic soil–structure interaction of monopile supported wind turbines in cohesive soil. *Soil Dynamics and Earthquake Engineering* 2013; **49**:165–180. URL https://doi.org/10.1016/j.soildyn.2013.01.015.

[153] Bhattacharya S. *Design of Foundations for Offshore Wind Turbines*. John Wiley & Sons, Ltd, 2019. URL https://onlinelibrary.wiley.com/doi/abs/10.1002/9781119128137.

[154] Kallehave D, Thilsted C, Troya A, Meyer V. Observed variations of monopile foundation stiffness. *Frontiers in Offshore Geotechnics III* 2015; :717–722URL 10.1201/b18442-98.

[155] Damgaard M, Ibsen L, Andersen L, Andersen J. Cross-wind modal properties of offshore wind turbines identified by full scale testing. *Journal of Wind Engineering and Industrial Aerodynamics* 05 2014; **116**:94–108. URL https://www.sciencedirect.com/science/article/pii/S0167610513000603?via%3Dihub.

[156] Arany L, Bhattacharya S, Macdonald JH, Hogan SJ. Closed form solution of eigen frequency of monopile supported offshore wind turbines in deeper waters incorporating stiffness of substructure and ssi. *Soil Dynamics and Earthquake Engineering* 2016; **83**:18–32. URL https://www.sciencedirect.com/science/article/pii/S0267726115003206.

[157] Bhattacharya S, Nikitas N, Garnsey J, Alexander N, Cox J, Lombardi D, Muir Wood D, Nash D. Observed dynamic soil–structure interaction in scale testing of offshore wind turbine foundations. *Soil Dynamics and Earthquake Engineering* 2013; **54**:47–60. URL `https://www.sciencedirect.com/science/article/pii/S026772611300167X`.

[158] Guo Z, Yu L, Wang L, Bhattacharya S, Nikitas G, Xing Y. Model Tests on the Long-Term Dynamic Performance of Offshore Wind Turbines Founded on Monopiles in Sand. *Journal of Offshore Mechanics and Arctic Engineering* 08 2015; **137**(4). URL `https://doi.org/10.1115/1.4030682`.

[159] Page A, Schafhirt S, Eiksund G, Skau K, Jostad HP, Sturm H. Alternative Numerical Pile Foundation Models for Integrated Analyses of Monopile-based Offshore Wind Turbines. *Twenty-sixth International Ocean and Polar Engineering Conference*, 2016.

[160] Page AM, Skau KS, Jostad HP, Eiksund GR. A new foundation model for integrated analyses of monopile-based offshore wind turbines. *Energy Procedia* 2017; **137**:100–107. URL `https://www.sciencedirect.com/science/article/pii/S1876610217352980`.

[161] Roscoe K, Schofield HN. The stability of short pier foundations on sand, discussion. *Br. Welding Journal* 1957; :12–19.

[162] Bienen B, Byrne BW, Houlsby GT, Cassidy MJ. Investigating six-degree-of-freedom loading of shallow foundations on sand. *Géotechnique* 2006; **56**(6):367–379. URL `https://doi.org/10.1680/geot.2006.56.6.367`.

[163] Correia A. A Pile-head Macro-element Approach to Seismic Design of monoshaft supported bridges. PhD Thesis, European School for Advanced Studies in Reduction of Seismic Risk, ROSE School, Pavia, Italy 2011.

[164] Houlsby GT, Cassidy MJ. A plasticity model for the behaviour of footings on sand under combined loading. *Géotechnique* 2002; **52**(2):117–129. URL `https://doi.org/10.1680/geot.2002.52.2.117`.

[165] Skau KS, Grimstad G, Page AM, Eiksund GR, Jostad HP. A macro-element for integrated time domain analyses representing bucket foundations for offshore wind turbines. *Marine Structures* 2017; **Vol. 59**:158–178. URL `https://doi.org/10.1016/j.marstruc.2018.01.011`.

[166] Tistel J, Grimstad G, Eiksund G. A macro model for shallow foundations on granular soils describing non-linear foundation behavior. *Computers & Structures* 08 2017; **232**. URL https://doi.org/10.1016/j.compstruc.2017.07.018.

[167] Iwan WD. On a class of models for the yielding behavior of continuous and composite systems. *Journal of Applied Mechanics* 1967; **Vol. 34**.

[168] Arnkjell Løkke. REDWIN - Reducing cost of offshore wind by integrated structural and geotechnical design - Adaptation for practitioners. *Technical Report*, Norwegian Geotechnical Institute (NGI) 2018.

[169] Page AM, Grimstad G, Eiksund GR, Jostad HP. A macro-element pile foundation model for integrated analyses of monopile-based offshore wind turbines. *Ocean Engineering* 2018; **167**:23–35. URL https://www.sciencedirect.com/science/article/pii/S0029801818315142.

[170] Page A, Grimstad G, Eiksund G, Jostad HP. A macro-element model for multidirectional cyclic lateral loading of monopiles in clay. *Computers and Geotechnics* 2018; **Vol. 106**:314–326. URL https://doi.org/10.1016/j.compgeo.2018.11.007.

[171] Page AM, Næss V, De Vaal JB, Eiksund GR, Nygaard TA. Impact of foundation modelling in offshore wind turbines: Comparison between simulations and field data. *Marine Structures* 2019; **64**:379–400. URL https://www.sciencedirect.com/science/article/pii/S0951833918301485.

[172] Schafhirt S, Page A, Eiksund G, Muskulus M. Influence of soil parameters on the fatigue lifetime of offshore wind turbines with monopile support structure. *Energy Procedia* 09 2016; **94**:347–356. URL https://doi.org/10.1016/j.egypro.2016.09.194.

[173] Damgaard M, Andersen L, Ibsen L. Dynamic response sensitivity of an offshore wind turbine for varying subsoil conditions. *Ocean Engineering* 2015; **101**:227–234. URL https://www.sciencedirect.com/science/article/pii/S0029801815001201.

[174] Aasen S, Page A, Skau K, Nygaard T. Effect of foundation modelling on the fatigue lifetime of a monopile-based offshore wind turbine. *Wind Energy Science* 07 2017; **2**:361–376. URL https://wes.copernicus.org/articles/2/361/2017/.

[175] Carswell W, Johansson J, Løvholt F, Arwade SR, DeGroot DJ, Myers AT. Foundation damping and the dynamics of offshore wind turbine monopiles. *Renewable Energy* 2015; **Vol. 80**:724–736. URL https://www.sciencedirect.com/science/article/pii/S0960148115001743.

[176] Morison J, Johnson J, Schaaf S. The Force Exerted by Surface Waves on Piles. *Journal of Petroleum Technology* 05 1950; **2**(05):149–154. URL https://doi.org/10.2118/950149-G.

[177] MacCamy RC, Fuchs R A. Wave Forces on Piles: A Diffraction Theory. *Technical Report*, Office of Naval Research, U. S. Department of the Navy 1954.

[178] van der Meulen M, Ashuri T, van Bussel G, Molenaar D. Influence of nonlinear irregular waves on the fatigue loads of an offshore wind turbine. *The Sixteenth International Offshore and Polar Engineering Conference*, 2012; The Science of Making Torque from Wind; 4th scientific conference, Oldenburg (Germany). URL https://repository.tudelft.nl/islandora/object/uuid%3A8ae3eea4-fcf9-45f3-8cd9-e8f0adbef1b3.

[179] Schløer S, Bredmose H, Bingham H, Larsen T. Effects from fully nonlinear irregular wave forcing on the fatigue life of an offshore wind turbine and its monopile foundation. 2012. URL https://doi.org/10.1115/OMAE2012-83477.

[180] Pierella F, Bredmose H, Vaal JBD, Eliassen L, Krokstad J, Nygaard TA, Oggiano L, Stenbro R. The dimensioning sea loads (DIMSELO) project. *Journal of Physics: Conference Series* oct 2018; **1104**:012 037. URL https://doi.org/10.1088/1742-6596/1104/1/012037.

[181] Pierella F, Lindberg O, Bredmose H, Bingham HB, Read RW, Engsig-Karup AP. The derisk database: Extreme design waves for offshore wind turbines. *Marine Structures* 2021; **80**:103 046. URL https://www.sciencedirect.com/science/article/pii/S0951833921001015.

[182] Suja-Thauvin L. Response of monopile wind turbines to higher order wave loads. PhD Thesis, Norwegian University of Science and Technology, Norway 2019. URL http://hdl.handle.net/11250/2641679.

[183] Rainey RCT. A new equation for calculating wave loads on offshore structures. *Journal of Fluid Mechanics* 1989; **204**:295–324, doi: 10.1017/S002211208900176X.

[184] Faltinsen OM, Newman JN, Vinje T. Nonlinear wave loads on a slender vertical cylinder. *Journal of Fluid Mechanics* 1995; **289**:179–198. URL `10.1017/S0022112095001297`.

[185] Malenica S, Molin B. Third-harmonic wave diffraction by a vertical cylinder. *Journal of Fluid Mechanics* 1995; **302**:203–229. URL `10.1017/S0022112095004071`.

[186] Kristiansen T, Faltinsen OM. Higher harmonic wave loads on a vertical cylinder in finite water depth. *Journal of Fluid Mechanics* 2017; **833**:773–805. URL `10.1017/jfm.2017.702`.

[187] Bredmose H, Mariegaard J, Paulsen B, Jensen B, Schløer S, Larsen T, Kim T, Hansen A. *The Wave Loads project*. No. 0045 in DTU Wind Energy E, DTU Wind Energy: Denmark, 2013.

[188] Bruserud K, Haver S. Comparison of wave and current measurements to NORA10 and NoNoCur hindcast data in the northern North Sea. *Ocean Dynamics* Jul 2016; **66**(6-7):823–838. URL `https://doi.org/10.1007/s10236-016-0953-z`.

[189] Grimstad G, Andresen L, Jostad HP. NGI-ADP: Anisotropic shear strength model for clay. *International Journal for Numerical and Analytical Methods in Geomechanics* 2012; **36**(4):483–497. URL `https://doi.org/10.1002/nag.1016`.

[190] Jonkman J, Butterfield S, Musial W, Scott G. Definition of a 5 MW reference wind turbine for offshore system development. *Report*, National Renewable Energy Laboratory (NREL), Denver, CO, US 2009. URL `https://www.osti.gov/biblio/947422`.

[191] Bak C, Zahle F, Bitsche R, Kim T, Yde A, Henriksen LC, Natarajan A, Hansen MH. Description of the DTU 10 MW reference wind turbine. *Report*, DTU Wind Energy, Kgs. Lyngby, DK 2013.

[192] Gaertner E, Rinker J, Sethuraman L, Zahle F, Anderson B, Barter G, Abbas N, Meng F, Bortolotti P, Skrzypinski W, *et al.*. Definition of the IEA 15-megawatt offshore reference wind turbine. *Technical Report*, International Energy Agency, Denver, CO, US 2020. URL `https://www.osti.gov/biblio/947422`.

[193] Hansen MH, Henriksen LC. Basic DTU wind energy controller. *Report*, DTU Wind Energy, Roskilde, Denmark 2013.

[194] NREL. ROSCO. Version 2.2.0. https://github.com/NREL/rosco.

[195] Velarde J. Design of Monopile Foundations to Support the DTU 10 MW Offshore Wind Turbine 2015. URL http://hdl.handle.net/11250/2397147.

[196] Jonkman J, Musial W. Offshore code comparison collaboration (OC3) for IEA task 23 offshore wind technology and deployment. *Report*, NREL, Golden, Colorado, USA 2010.

[197] Velarde J, Bachynski EE. Design and fatigue analysis of monopile foundations to support the DTU 10 MW offshore wind turbine. *Energy Procedia* 2017; **137**:3–13. URL https://www.sciencedirect.com/science/article/pii/S1876610217352906, 14th Deep Sea Offshore Wind R&D Conference, EERA DeepWind'2017.

[198] SIMO 4.10.3 user guide. *Technical Report*, SINTEF Ocean 2017.

[199] RIFLEX 4.10.3 user guide. *Technical Report*, SINTEF Ocean 2017.

[200] Bachynski EE, Kristiansen T, Thys M. Experimental and numerical investigations of monopile ringing in irregular finite-depth water waves. *Applied Ocean Research* 2017; **68**:154–170. URL https://www.sciencedirect.com/science/article/pii/S0141118716305284.

[201] Klinkvort RT, Sturm H, Page AM, Zhang Y, Jostad HP. A consistent, rigorous and super-fast monopile design approach. *Proceedings of the 4th International Symposium on Frontiers in Offshore Geotechnics*, American Society of Civil Engineers: Austin, Texas, US, August 28–31, 2022.

[202] Jonkman BJ. TurbSim user's guide: Version 1.50, Technical Report. *Technical Report*, National Renewable Energy Lab (NREL) 2009.

[203] Bachynski E, Ormberg H. Comparison of engineering models for the aerodynamic load distribution along a wind turbine blade. *Proceedings of the twenty-fifth International Ocean and Polar Engineering Conference - ISOPE 2015.*, vol. 2015, 2015; 561–567.

[204] Brodtkorb P, Johannesson P, Lindgren G, Rychlik I, Ryden J, Sjo E. WAFO—A MATLAB Toolbox for the Analysis of Random Waves and

Loads. *10th International Offshore and Polar Engineering Conference (ISOPE)*, vol. 3, 2000; 343–350.

[205] Hegseth JM. Efficient modelling and design optimization of large floating wind turbines 2020. URL https://hdl.handle.net/11250/2688280.

[206] Borgman LE. Ocean wave simulation for engineering design. *Journal of the Waterways and Harbors Division* 1969; **95**(4):557–586. URL https://doi.org/10.1061/JWHEAU.0000665.

[207] Ning SA. A simple solution method for the blade element momentum equations with guaranteed convergence. *Wind Energy* 2014; **17**(9):1327–1345. URL https://onlinelibrary.wiley.com/doi/abs/10.1002/we.1636.

[208] Halfpenny A. Dynamic analysis of both on and offshore wind turbines in the frequency domain. PhD Thesis, University College London, Department of Mechanical Engineering 1998. URL https://discovery.ucl.ac.uk/id/eprint/1317858.

[209] Hegseth JM, Bachynski EE, Martins JRRA. Integrated design optimization of spar floating wind turbines. *Marine Structures* 2020; **72**. URL https://doi.org/10.1016/j.marstruc.2020.102771.

[210] Katsikogiannis G, Hegseth JM, Bachynski-Polić EE. Application of a lumping method for fatigue design of monopile-based wind turbines using fully coupled and simplified models. *Applied Ocean Research* 2022; **120**:102 998. URL https://www.sciencedirect.com/science/article/pii/S0141118721004600.

[211] Gao Z. Stochastic response analysis of mooring systems with emphasis on frequency-domain analysis of fatigue due to wide-band response processes. PhD Thesis, Norwegian University of Science and Technology 2008. URL http://hdl.handle.net/11250/237629.

[212] Katsikogiannis G, Sørum SH, Bachynski EE, Amdahl J. Environmental lumping for efficient fatigue assessment of large-diameter monopile wind turbines. *Marine Structures* 2021; **77**:102 939. URL https://www.sciencedirect.com/science/article/pii/S0951833921000071.

[213] Wirsching PH, Shehata AM. Fatigue Under Wide Band Random Stresses Using the Rain-Flow Method. *Journal of Engineering Materials and Technology* 07 1977; **99**(3):205–211. URL https://doi.org/10.1115/1.3443520.

[214] Zhao W, Baker MJ. On the probability density function of rainflow stress range for stationary Gaussian processes. *International Journal of Fatigue* 1992; **14**(2):121–135. URL https://doi.org/10.1016/0142-1123(92)90088-T.

[215] Dirlik T. Application of computers in fatigue analysis. Phd thesis, University of Warwick 1985. URL http://wrap.warwick.ac.uk/2949/.

[216] Tovo R. Cycle distribution and fatigue damage under broad-band random loading. *International Journal of Fatigue* 2002; **24**(11):1137–1147. URL https://doi.org/10.1016/S0142-1123(02)00032-4.

[217] Benasciutti D, Tovo R. Spectral methods for lifetime prediction under wide-band stationary random processes. *International Journal of Fatigue* 2005; **27**(8):867–877. URL https://doi.org/10.1016/j.ijfatigue.2004.10.007.

[218] Gao Z, Moan T. Frequency-domain fatigue analysis of wide-band stationary gaussian processes using a trimodal spectral formulation. *International Journal of Fatigue* 2008; **30**(10):1944–1955. URL https://www.sciencedirect.com/science/article/pii/S0142112308000182.

[219] Benasciutti D, Tovo R. Comparison of spectral methods for fatigue analysis of broad-band gaussian random processes. *Probabilistic Engineering Mechanics* 2006; **21**(4):287–299. URL https://www.sciencedirect.com/science/article/pii/S0266892005000718.

[220] Shirzadeh R, Devriendt C, Bidakhvidi M, Guillaume P. Experimental and computational damping estimation of an offshore wind turbine on a monopile foundation. *Journal of Wind Engineering and Industrial Aerodynamics* 2013; **120**:96–106. URL https://www.sciencedirect.com/science/article/pii/S0167610513001359.

[221] Katsikogiannis G, Bachynski EE, Page AM. Fatigue sensitivity to foundation modelling in different operational states for the dtu 10 MW monopile-based offshore wind turbine. *Journal of Physics: Conference Series* oct 2019; **1356**(1):012019. URL https://dx.doi.org/10.1088/1742-6596/1356/1/012019.

[222] Sørum SH, Katsikogiannis G, Bachynski-Polić EE, Amdahl J, Page AM, Klinkvort RT. Fatigue design sensitivities of large monopile offshore wind turbines. *Wind Energy* 2022; **25**(10):1684–1709. URL `https://onlinelibrary.wiley.com/doi/abs/10.1002/we.2755`.

[223] Ochi MK. New approach for estimating the severest sea state from statistical data. *Coastal Engineering 1992* ; :512–525URL `https://ascelibrary.org/doi/abs/10.1061/9780872629332.038`.

[224] Ferreira J, Guedes Soares C. Modelling the long-term distribution of significant wave height with the beta and gamma models. *Ocean Engineering* 1999; **26**(8):713–725. URL `https://www.sciencedirect.com/science/article/pii/S0029801898000225`.

[225] Haselsteiner AF, Thoben KD. Predicting wave heights for marine design by prioritizing extreme events in a global model. *Renewable Energy* 2020; **156**:1146–1157. URL `https://www.sciencedirect.com/science/article/pii/S0960148120306443`.

[226] Haselsteiner AF, Thoben KD. Predicting wave heights for marine design by prioritizing extreme events in a global model. *Renewable Energy* 2020; **156**:1146–1157. URL `https://www.sciencedirect.com/science/article/pii/S0960148120306443`.

[227] Johannessen K, Meling TS, Haver S. Joint Distribution For Wind And Waves In the Northern North Sea. *International Journal of Offshore and Polar Engineering* 03 2002; **12**(01). URL `https://onepetro.org/IJOPE/article-pdf/2181647/isope-02-12-1-001.pdf`.

[228] Cheng Z, Svangstu E, Moan T, Gao Z. Long-term joint distribution of environmental conditions in a Norwegian fjord for design of floating bridges. *Ocean Engineering* 2019; **191**:106 472. URL `https://doi.org/10.1016/j.oceaneng.2019.106472`.

[229] Rosenblatt M. Remarks on a multivariate transformation. *Ann. Math. Statist.* 09 1952; **23**(3):470–472. URL `https://doi.org/10.1214/aoms/1177729394`.

[230] Bury KV. *Statistical Models in Applied Science*. John Wiley & Sons, Ltd, 1975. URL `https://doi.org/10.1002/nme.1620120617`.

[231] Naess A, Gaidai O. Estimation of extreme values from sampled time series. *Structural Safety* 2009; **31**(4):325–334. URL `https://www.sciencedirect.com/science/article/pii/S0167473008000829`.

[232] Fatemeh H Dadmarzi CP Erin E Bachynski-Polić, Thys M. Validation of a frequency-dependent Morison force formulation for a large monopile in severe irregular seas. *Ocean Engineering* ; .

[233] Newman JN. *Marine Hydrodynamics*. The MIT Press, 1977. URL `https://home.hvl.no/ansatte/gste/ftp/MarinLab_files/Litteratur/Marine_Hydrodynamics_Newman_2018.pdf`.

Previous PhD theses published at the Department of Marine Technology (earlier: Faculty of Marine Technology)
NORWEGIAN UNIVERSITY OF SCIENCE AND TECHNOLOGY

Report No.	Author	Title
	Kavlie, Dag	Optimization of Plane Elastic Grillages, 1967
	Hansen, Hans R.	Man-Machine Communication and Data-Storage Methods in Ship Structural Design, 1971
	Gisvold, Kaare M.	A Method for non-linear mixed -integer programming and its Application to Design Problems, 1971
	Lund, Sverre	Tanker Frame Optimalization by means of SUMT-Transformation and Behaviour Models, 1971
	Vinje, Tor	On Vibration of Spherical Shells Interacting with Fluid, 1972
	Lorentz, Jan D.	Tank Arrangement for Crude Oil Carriers in Accordance with the new Anti-Pollution Regulations, 1975
	Carlsen, Carl A.	Computer-Aided Design of Tanker Structures, 1975
	Larsen, Carl M.	Static and Dynamic Analysis of Offshore Pipelines during Installation, 1976
UR-79-01	Brigt Hatlestad, MK	The finite element method used in a fatigue evaluation of fixed offshore platforms. (Dr.Ing. Thesis)
UR-79-02	Erik Pettersen, MK	Analysis and design of cellular structures. (Dr.Ing. Thesis)
UR-79-03	Sverre Valsgård, MK	Finite difference and finite element methods applied to nonlinear analysis of plated structures. (Dr.Ing. Thesis)
UR-79-04	Nils T. Nordsve, MK	Finite element collapse analysis of structural members considering imperfections and stresses due to fabrication. (Dr.Ing. Thesis)
UR-79-05	Ivar J. Fylling, MK	Analysis of towline forces in ocean towing systems. (Dr.Ing. Thesis)
UR-79- x	Finn Gunnar Nielsen, MH	Hydrodynamic problems related to oil barriers for offshore application
UR-80-06	Nils Sandsmark, MM	Analysis of Stationary and Transient Heat Conduction by the Use of the Finite Element Method. (Dr.Ing. Thesis)
UR-80-09	Sverre Haver, MK	Analysis of uncertainties related to the stochastic modeling of ocean waves. (Dr.Ing. Thesis)

UR-81-15	Odland, Jonas	On the Strength of welded Ring stiffened cylindrical Shells primarily subjected to axial Compression
UR-82-17	Engesvik, Knut	Analysis of Uncertainties in the fatigue Capacity of Welded Joints
UR-82-18	Rye, Henrik	Ocean wave groups
UR-83-30	Eide, Oddvar Inge	On Cumulative Fatigue Damage in Steel Welded Joints
UR-83-33	Mo, Olav	Stochastic Time Domain Analysis of Slender Offshore Structures
UR-83-34	Amdahl, Jørgen	Energy absorption in Ship-platform impacts
UR-84-37	Mørch, Morten	Motions and mooring forces of semi submersibles as determined by full-scale measurements and theoretical analysis
UR-84-38	Soares, C. Guedes	Probabilistic models for load effects in ship structures
UR-84-39	Aarsnes, Jan V.	Current forces on ships
UR-84-40	Czujko, Jerzy	Collapse Analysis of Plates subjected to Biaxial Compression and Lateral Load
UR-85-46	Alf G. Engseth, MK	Finite element collapse analysis of tubular steel offshore structures. (Dr.Ing. Thesis)
UR-86-47	Dengody Sheshappa, MP	A Computer Design Model for Optimizing Fishing Vessel Designs Based on Techno-Economic Analysis. (Dr.Ing. Thesis)
UR-86-48	Vidar Aanesland, MH	A Theoretical and Numerical Study of Ship Wave Resistance. (Dr.Ing. Thesis)
UR-86-49	Heinz-Joachim Wessel, MK	Fracture Mechanics Analysis of Crack Growth in Plate Girders. (Dr.Ing. Thesis)
UR-86-50	Jon Taby, MK	Ultimate and Post-ultimate Strength of Dented Tubular Members. (Dr.Ing. Thesis)
UR-86-51	Walter Lian, MH	A Numerical Study of Two-Dimensional Separated Flow Past Bluff Bodies at Moderate KC-Numbers. (Dr.Ing. Thesis)
UR-86-52	Bjørn Sortland, MH	Force Measurements in Oscillating Flow on Ship Sections and Circular Cylinders in a U-Tube Water Tank. (Dr.Ing. Thesis)
UR-86-53	Kurt Strand, MM	A System Dynamic Approach to One-dimensional Fluid Flow. (Dr.Ing. Thesis)
UR-86-54	Arne Edvin Løken, MH	Three Dimensional Second Order Hydrodynamic Effects on Ocean Structures in Waves. (Dr.Ing. Thesis)
UR-86-55	Sigurd Falch, MH	A Numerical Study of Slamming of Two-

		Dimensional Bodies. (Dr.Ing. Thesis)
UR-87-56	Arne Braathen, MH	Application of a Vortex Tracking Method to the Prediction of Roll Damping of a Two-Dimension Floating Body. (Dr.Ing. Thesis)
UR-87-57	Bernt Leira, MK	Gaussian Vector Processes for Reliability Analysis involving Wave-Induced Load Effects. (Dr.Ing. Thesis)
UR-87-58	Magnus Småvik, MM	Thermal Load and Process Characteristics in a Two-Stroke Diesel Engine with Thermal Barriers (in Norwegian). (Dr.Ing. Thesis)
MTA-88-59	Bernt Arild Bremdal, MP	An Investigation of Marine Installation Processes – A Knowledge - Based Planning Approach. (Dr.Ing. Thesis)
MTA-88-60	Xu Jun, MK	Non-linear Dynamic Analysis of Space-framed Offshore Structures. (Dr.Ing. Thesis)
MTA-89-61	Gang Miao, MH	Hydrodynamic Forces and Dynamic Responses of Circular Cylinders in Wave Zones. (Dr.Ing. Thesis)
MTA-89-62	Martin Greenhow, MH	Linear and Non-Linear Studies of Waves and Floating Bodies. Part I and Part II. (Dr.Techn. Thesis)
MTA-89-63	Chang Li, MH	Force Coefficients of Spheres and Cubes in Oscillatory Flow with and without Current. (Dr.Ing. Thesis
MTA-89-64	Hu Ying, MP	A Study of Marketing and Design in Development of Marine Transport Systems. (Dr.Ing. Thesis)
MTA-89-65	Arild Jæger, MH	Seakeeping, Dynamic Stability and Performance of a Wedge Shaped Planing Hull. (Dr.Ing. Thesis)
MTA-89-66	Chan Siu Hung, MM	The dynamic characteristics of tilting-pad bearings
MTA-89-67	Kim Wikstrøm, MP	Analysis av projekteringen for ett offshore projekt. (Licenciat-avhandling)
MTA-89-68	Jiao Guoyang, MK	Reliability Analysis of Crack Growth under Random Loading, considering Model Updating. (Dr.Ing. Thesis)
MTA-89-69	Arnt Olufsen, MK	Uncertainty and Reliability Analysis of Fixed Offshore Structures. (Dr.Ing. Thesis)
MTA-89-70	Wu Yu-Lin, MR	System Reliability Analyses of Offshore Structures using improved Truss and Beam Models. (Dr.Ing. Thesis)
MTA-90-71	Jan Roger Hoff, MH	Three-dimensional Green function of a vessel with forward speed in waves. (Dr.Ing. Thesis)
MTA-90-72	Rong Zhao, MH	Slow-Drift Motions of a Moored Two-Dimensional Body in Irregular Waves. (Dr.Ing. Thesis)
MTA-90-73	Atle Minsaas, MP	Economical Risk Analysis. (Dr.Ing. Thesis)

MTA-90-74	Knut-Aril Farnes, MK	Long-term Statistics of Response in Non-linear Marine Structures. (Dr.Ing. Thesis)
MTA-90-75	Torbjørn Sotberg, MK	Application of Reliability Methods for Safety Assessment of Submarine Pipelines. (Dr.Ing. Thesis)
MTA-90-76	Zeuthen, Steffen, MP	SEAMAID. A computational model of the design process in a constraint-based logic programming environment. An example from the offshore domain. (Dr.Ing. Thesis)
MTA-91-77	Haagensen, Sven, MM	Fuel Dependant Cyclic Variability in a Spark Ignition Engine - An Optical Approach. (Dr.Ing. Thesis)
MTA-91-78	Løland, Geir, MH	Current forces on and flow through fish farms. (Dr.Ing. Thesis)
MTA-91-79	Hoen, Christopher, MK	System Identification of Structures Excited by Stochastic Load Processes. (Dr.Ing. Thesis)
MTA-91-80	Haugen, Stein, MK	Probabilistic Evaluation of Frequency of Collision between Ships and Offshore Platforms. (Dr.Ing. Thesis)
MTA-91-81	Sødahl, Nils, MK	Methods for Design and Analysis of Flexible Risers. (Dr.Ing. Thesis)
MTA-91-82	Ormberg, Harald, MK	Non-linear Response Analysis of Floating Fish Farm Systems. (Dr.Ing. Thesis)
MTA-91-83	Marley, Mark J., MK	Time Variant Reliability under Fatigue Degradation. (Dr.Ing. Thesis)
MTA-91-84	Krokstad, Jørgen R., MH	Second-order Loads in Multidirectional Seas. (Dr.Ing. Thesis)
MTA-91-85	Molteberg, Gunnar A., MM	The Application of System Identification Techniques to Performance Monitoring of Four Stroke Turbocharged Diesel Engines. (Dr.Ing. Thesis)
MTA-92-86	Mørch, Hans Jørgen Bjelke, MH	Aspects of Hydrofoil Design: with Emphasis on Hydrofoil Interaction in Calm Water. (Dr.Ing. Thesis)
MTA-92-87	Chan Siu Hung, MM	Nonlinear Analysis of Rotordynamic Instabilities in Highspeed Turbomachinery. (Dr.Ing. Thesis)
MTA-92-88	Bessason, Bjarni, MK	Assessment of Earthquake Loading and Response of Seismically Isolated Bridges. (Dr.Ing. Thesis)
MTA-92-89	Langli, Geir, MP	Improving Operational Safety through exploitation of Design Knowledge - an investigation of offshore platform safety. (Dr.Ing. Thesis)
MTA-92-90	Sævik, Svein, MK	On Stresses and Fatigue in Flexible Pipes. (Dr.Ing. Thesis)
MTA-92-91	Ask, Tor Ø., MM	Ignition and Flame Growth in Lean Gas-Air Mixtures. An Experimental Study with a Schlieren

		System. (Dr.Ing. Thesis)
MTA-86-92	Hessen, Gunnar, MK	Fracture Mechanics Analysis of Stiffened Tubular Members. (Dr.Ing. Thesis)
MTA-93-93	Steinebach, Christian, MM	Knowledge Based Systems for Diagnosis of Rotating Machinery. (Dr.Ing. Thesis)
MTA-93-94	Dalane, Jan Inge, MK	System Reliability in Design and Maintenance of Fixed Offshore Structures. (Dr.Ing. Thesis)
MTA-93-95	Steen, Sverre, MH	Cobblestone Effect on SES. (Dr.Ing. Thesis)
MTA-93-96	Karunakaran, Daniel, MK	Nonlinear Dynamic Response and Reliability Analysis of Drag-dominated Offshore Platforms. (Dr.Ing. Thesis)
MTA-93-97	Hagen, Arnulf, MP	The Framework of a Design Process Language. (Dr.Ing. Thesis)
MTA-93-98	Nordrik, Rune, MM	Investigation of Spark Ignition and Autoignition in Methane and Air Using Computational Fluid Dynamics and Chemical Reaction Kinetics. A Numerical Study of Ignition Processes in Internal Combustion Engines. (Dr.Ing. Thesis)
MTA-94-99	Passano, Elizabeth, MK	Efficient Analysis of Nonlinear Slender Marine Structures. (Dr.Ing. Thesis)
MTA-94-100	Kvålsvold, Jan, MH	Hydroelastic Modelling of Wetdeck Slamming on Multihull Vessels. (Dr.Ing. Thesis)
MTA-94-102	Bech, Sidsel M., MK	Experimental and Numerical Determination of Stiffness and Strength of GRP/PVC Sandwich Structures. (Dr.Ing. Thesis)
MTA-95-103	Paulsen, Hallvard, MM	A Study of Transient Jet and Spray using a Schlieren Method and Digital Image Processing. (Dr.Ing. Thesis)
MTA-95-104	Hovde, Geir Olav, MK	Fatigue and Overload Reliability of Offshore Structural Systems, Considering the Effect of Inspection and Repair. (Dr.Ing. Thesis)
MTA-95-105	Wang, Xiaozhi, MK	Reliability Analysis of Production Ships with Emphasis on Load Combination and Ultimate Strength. (Dr.Ing. Thesis)
MTA-95-106	Ulstein, Tore, MH	Nonlinear Effects of a Flexible Stern Seal Bag on Cobblestone Oscillations of an SES. (Dr.Ing. Thesis)
MTA-95-107	Solaas, Frøydis, MH	Analytical and Numerical Studies of Sloshing in Tanks. (Dr.Ing. Thesis)
MTA-95-108	Hellan, Øyvind, MK	Nonlinear Pushover and Cyclic Analyses in Ultimate Limit State Design and Reassessment of Tubular Steel Offshore Structures. (Dr.Ing. Thesis)
MTA-95-109	Hermundstad, Ole A., MK	Theoretical and Experimental Hydroelastic Analysis of High Speed Vessels. (Dr.Ing. Thesis)

MTA-96-110	Bratland, Anne K., MH	Wave-Current Interaction Effects on Large-Volume Bodies in Water of Finite Depth. (Dr.Ing. Thesis)
MTA-96-111	Herfjord, Kjell, MH	A Study of Two-dimensional Separated Flow by a Combination of the Finite Element Method and Navier-Stokes Equations. (Dr.Ing. Thesis)
MTA-96-112	Æsøy, Vilmar, MM	Hot Surface Assisted Compression Ignition in a Direct Injection Natural Gas Engine. (Dr.Ing. Thesis)
MTA-96-113	Eknes, Monika L., MK	Escalation Scenarios Initiated by Gas Explosions on Offshore Installations. (Dr.Ing. Thesis)
MTA-96-114	Erikstad, Stein O., MP	A Decision Support Model for Preliminary Ship Design. (Dr.Ing. Thesis)
MTA-96-115	Pedersen, Egil, MH	A Nautical Study of Towed Marine Seismic Streamer Cable Configurations. (Dr.Ing. Thesis)
MTA-97-116	Moksnes, Paul O., MM	Modelling Two-Phase Thermo-Fluid Systems Using Bond Graphs. (Dr.Ing. Thesis)
MTA-97-117	Halse, Karl H., MK	On Vortex Shedding and Prediction of Vortex-Induced Vibrations of Circular Cylinders. (Dr.Ing. Thesis)
MTA-97-118	Igland, Ragnar T., MK	Reliability Analysis of Pipelines during Laying, considering Ultimate Strength under Combined Loads. (Dr.Ing. Thesis)
MTA-97-119	Pedersen, Hans-P., MP	Levendefiskteknologi for fiskefartøy. (Dr.Ing. Thesis)
MTA-98-120	Vikestad, Kyrre, MK	Multi-Frequency Response of a Cylinder Subjected to Vortex Shedding and Support Motions. (Dr.Ing. Thesis)
MTA-98-121	Azadi, Mohammad R. E., MK	Analysis of Static and Dynamic Pile-Soil-Jacket Behaviour. (Dr.Ing. Thesis)
MTA-98-122	Ulltang, Terje, MP	A Communication Model for Product Information. (Dr.Ing. Thesis)
MTA-98-123	Torbergsen, Erik, MM	Impeller/Diffuser Interaction Forces in Centrifugal Pumps. (Dr.Ing. Thesis)
MTA-98-124	Hansen, Edmond, MH	A Discrete Element Model to Study Marginal Ice Zone Dynamics and the Behaviour of Vessels Moored in Broken Ice. (Dr.Ing. Thesis)
MTA-98-125	Videiro, Paulo M., MK	Reliability Based Design of Marine Structures. (Dr.Ing. Thesis)
MTA-99-126	Mainçon, Philippe, MK	Fatigue Reliability of Long Welds Application to Titanium Risers. (Dr.Ing. Thesis)
MTA-99-127	Haugen, Elin M., MH	Hydroelastic Analysis of Slamming on Stiffened Plates with Application to Catamaran Wetdecks. (Dr.Ing. Thesis)
MTA-99-	Langhelle, Nina K., MK	Experimental Validation and Calibration of

128		Nonlinear Finite Element Models for Use in Design of Aluminium Structures Exposed to Fire. (Dr.Ing. Thesis)
MTA-99-129	Berstad, Are J., MK	Calculation of Fatigue Damage in Ship Structures. (Dr.Ing. Thesis)
MTA-99-130	Andersen, Trond M., MM	Short Term Maintenance Planning. (Dr.Ing. Thesis)
MTA-99-131	Tveiten, Bård Wathne, MK	Fatigue Assessment of Welded Aluminium Ship Details. (Dr.Ing. Thesis)
MTA-99-132	Søreide, Fredrik, MP	Applications of underwater technology in deep water archaeology. Principles and practice. (Dr.Ing. Thesis)
MTA-99-133	Tønnessen, Rune, MH	A Finite Element Method Applied to Unsteady Viscous Flow Around 2D Blunt Bodies With Sharp Corners. (Dr.Ing. Thesis)
MTA-99-134	Elvekrok, Dag R., MP	Engineering Integration in Field Development Projects in the Norwegian Oil and Gas Industry. The Supplier Management of Norne. (Dr.Ing. Thesis)
MTA-99-135	Fagerholt, Kjetil, MP	Optimeringsbaserte Metoder for Ruteplanlegging innen skipsfart. (Dr.Ing. Thesis)
MTA-99-136	Bysveen, Marie, MM	Visualization in Two Directions on a Dynamic Combustion Rig for Studies of Fuel Quality. (Dr.Ing. Thesis)
MTA-2000-137	Storteig, Eskild, MM	Dynamic characteristics and leakage performance of liquid annular seals in centrifugal pumps. (Dr.Ing. Thesis)
MTA-2000-138	Sagli, Gro, MK	Model uncertainty and simplified estimates of long term extremes of hull girder loads in ships. (Dr.Ing. Thesis)
MTA-2000-139	Tronstad, Harald, MK	Nonlinear analysis and design of cable net structures like fishing gear based on the finite element method. (Dr.Ing. Thesis)
MTA-2000-140	Kroneberg, André, MP	Innovation in shipping by using scenarios. (Dr.Ing. Thesis)
MTA-2000-141	Haslum, Herbjørn Alf, MH	Simplified methods applied to nonlinear motion of spar platforms. (Dr.Ing. Thesis)
MTA-2001-142	Samdal, Ole Johan, MM	Modelling of Degradation Mechanisms and Stressor Interaction on Static Mechanical Equipment Residual Lifetime. (Dr.Ing. Thesis)
MTA-2001-143	Baarholm, Rolf Jarle, MH	Theoretical and experimental studies of wave impact underneath decks of offshore platforms. (Dr.Ing. Thesis)
MTA-2001-144	Wang, Lihua, MK	Probabilistic Analysis of Nonlinear Wave-induced Loads on Ships. (Dr.Ing. Thesis)
MTA-2001-145	Kristensen, Odd H. Holt, MK	Ultimate Capacity of Aluminium Plates under Multiple Loads, Considering HAZ Properties.

		(Dr.Ing. Thesis)
MTA-2001-146	Greco, Marilena, MH	A Two-Dimensional Study of Green-Water Loading. (Dr.Ing. Thesis)
MTA-2001-147	Heggelund, Svein E., MK	Calculation of Global Design Loads and Load Effects in Large High Speed Catamarans. (Dr.Ing. Thesis)
MTA-2001-148	Babalola, Olusegun T., MK	Fatigue Strength of Titanium Risers – Defect Sensitivity. (Dr.Ing. Thesis)
MTA-2001-149	Mohammed, Abuu K., MK	Nonlinear Shell Finite Elements for Ultimate Strength and Collapse Analysis of Ship Structures. (Dr.Ing. Thesis)
MTA-2002-150	Holmedal, Lars E., MH	Wave-current interactions in the vicinity of the sea bed. (Dr.Ing. Thesis)
MTA-2002-151	Rognebakke, Olav F., MH	Sloshing in rectangular tanks and interaction with ship motions. (Dr.Ing. Thesis)
MTA-2002-152	Lader, Pål Furset, MH	Geometry and Kinematics of Breaking Waves. (Dr.Ing. Thesis)
MTA-2002-153	Yang, Qinzheng, MH	Wash and wave resistance of ships in finite water depth. (Dr.Ing. Thesis)
MTA-2002-154	Melhus, Øyvin, MM	Utilization of VOC in Diesel Engines. Ignition and combustion of VOC released by crude oil tankers. (Dr.Ing. Thesis)
MTA-2002-155	Ronæss, Marit, MH	Wave Induced Motions of Two Ships Advancing on Parallel Course. (Dr.Ing. Thesis)
MTA-2002-156	Økland, Ole D., MK	Numerical and experimental investigation of whipping in twin hull vessels exposed to severe wet deck slamming. (Dr.Ing. Thesis)
MTA-2002-157	Ge, Chunhua, MK	Global Hydroelastic Response of Catamarans due to Wet Deck Slamming. (Dr.Ing. Thesis)
MTA-2002-158	Byklum, Eirik, MK	Nonlinear Shell Finite Elements for Ultimate Strength and Collapse Analysis of Ship Structures. (Dr.Ing. Thesis)
IMT-2003-1	Chen, Haibo, MK	Probabilistic Evaluation of FPSO-Tanker Collision in Tandem Offloading Operation. (Dr.Ing. Thesis)
IMT-2003-2	Skaugset, Kjetil Bjørn, MK	On the Suppression of Vortex Induced Vibrations of Circular Cylinders by Radial Water Jets. (Dr.Ing. Thesis)
IMT-2003-3	Chezhian, Muthu	Three-Dimensional Analysis of Slamming. (Dr.Ing. Thesis)
IMT-2003-4	Buhaug, Øyvind	Deposit Formation on Cylinder Liner Surfaces in Medium Speed Engines. (Dr.Ing. Thesis)
IMT-2003-5	Tregde, Vidar	Aspects of Ship Design: Optimization of Aft Hull with Inverse Geometry Design. (Dr.Ing. Thesis)

IMT-2003-6	Wist, Hanne Therese	Statistical Properties of Successive Ocean Wave Parameters. (Dr.Ing. Thesis)
IMT-2004-7	Ransau, Samuel	Numerical Methods for Flows with Evolving Interfaces. (Dr.Ing. Thesis)
IMT-2004-8	Soma, Torkel	Blue-Chip or Sub-Standard. A data interrogation approach of identity safety characteristics of shipping organization. (Dr.Ing. Thesis)
IMT-2004-9	Ersdal, Svein	An experimental study of hydrodynamic forces on cylinders and cables in near axial flow. (Dr.Ing. Thesis)
IMT-2005-10	Brodtkorb, Per Andreas	The Probability of Occurrence of Dangerous Wave Situations at Sea. (Dr.Ing. Thesis)
IMT-2005-11	Yttervik, Rune	Ocean current variability in relation to offshore engineering. (Dr.Ing. Thesis)
IMT-2005-12	Fredheim, Arne	Current Forces on Net-Structures. (Dr.Ing. Thesis)
IMT-2005-13	Heggernes, Kjetil	Flow around marine structures. (Dr.Ing. Thesis
IMT-2005-14	Fouques, Sebastien	Lagrangian Modelling of Ocean Surface Waves and Synthetic Aperture Radar Wave Measurements. (Dr.Ing. Thesis)
IMT-2006-15	Holm, Håvard	Numerical calculation of viscous free surface flow around marine structures. (Dr.Ing. Thesis)
IMT-2006-16	Bjørheim, Lars G.	Failure Assessment of Long Through Thickness Fatigue Cracks in Ship Hulls. (Dr.Ing. Thesis)
IMT-2006-17	Hansson, Lisbeth	Safety Management for Prevention of Occupational Accidents. (Dr.Ing. Thesis)
IMT-2006-18	Zhu, Xinying	Application of the CIP Method to Strongly Nonlinear Wave-Body Interaction Problems. (Dr.Ing. Thesis)
IMT-2006-19	Reite, Karl Johan	Modelling and Control of Trawl Systems. (Dr.Ing. Thesis)
IMT-2006-20	Smogeli, Øyvind Notland	Control of Marine Propellers. From Normal to Extreme Conditions. (Dr.Ing. Thesis)
IMT-2007-21	Storhaug, Gaute	Experimental Investigation of Wave Induced Vibrations and Their Effect on the Fatigue Loading of Ships. (Dr.Ing. Thesis)
IMT-2007-22	Sun, Hui	A Boundary Element Method Applied to Strongly Nonlinear Wave-Body Interaction Problems. (PhD Thesis, CeSOS)
IMT-2007-23	Rustad, Anne Marthine	Modelling and Control of Top Tensioned Risers. (PhD Thesis, CeSOS)
IMT-2007-24	Johansen, Vegar	Modelling flexible slender system for real-time

		simulations and control applications
IMT-2007-25	Wroldsen, Anders Sunde	Modelling and control of tensegrity structures. (PhD Thesis, CeSOS)
IMT-2007-26	Aronsen, Kristoffer Høye	An experimental investigation of in-line and combined inline and cross flow vortex induced vibrations. (Dr. avhandling, IMT)
IMT-2007-27	Gao, Zhen	Stochastic Response Analysis of Mooring Systems with Emphasis on Frequency-domain Analysis of Fatigue due to Wide-band Response Processes (PhD Thesis, CeSOS)
IMT-2007-28	Thorstensen, Tom Anders	Lifetime Profit Modelling of Ageing Systems Utilizing Information about Technical Condition. (Dr.ing. thesis, IMT)
IMT-2008-29	Refsnes, Jon Erling Gorset	Nonlinear Model-Based Control of Slender Body AUVs (PhD Thesis, IMT)
IMT-2008-30	Berntsen, Per Ivar B.	Structural Reliability Based Position Mooring. (PhD-Thesis, IMT)
IMT-2008-31	Ye, Naiquan	Fatigue Assessment of Aluminium Welded Box-stiffener Joints in Ships (Dr.ing. thesis, IMT)
IMT-2008-32	Radan, Damir	Integrated Control of Marine Electrical Power Systems. (PhD-Thesis, IMT)
IMT-2008-33	Thomassen, Paul	Methods for Dynamic Response Analysis and Fatigue Life Estimation of Floating Fish Cages. (Dr.ing. thesis, IMT)
IMT-2008-34	Pákozdi, Csaba	A Smoothed Particle Hydrodynamics Study of Two-dimensional Nonlinear Sloshing in Rectangular Tanks. (Dr.ing.thesis, IMT/ CeSOS)
IMT-2007-35	Grytøyr, Guttorm	A Higher-Order Boundary Element Method and Applications to Marine Hydrodynamics. (Dr.ing.thesis, IMT)
IMT-2008-36	Drummen, Ingo	Experimental and Numerical Investigation of Nonlinear Wave-Induced Load Effects in Containerships considering Hydroelasticity. (PhD thesis, CeSOS)
IMT-2008-37	Skejic, Renato	Maneuvering and Seakeeping of a Singel Ship and of Two Ships in Interaction. (PhD-Thesis, CeSOS)
IMT-2008-38	Harlem, Alf	An Age-Based Replacement Model for Repairable Systems with Attention to High-Speed Marine Diesel Engines. (PhD-Thesis, IMT)
IMT-2008-39	Alsos, Hagbart S.	Ship Grounding. Analysis of Ductile Fracture, Bottom Damage and Hull Girder Response. (PhD-thesis, IMT)
IMT-2008-40	Graczyk, Mateusz	Experimental Investigation of Sloshing Loading and Load Effects in Membrane LNG Tanks Subjected to Random Excitation. (PhD-thesis, CeSOS)

IMT-2008-41	Taghipour, Reza	Efficient Prediction of Dynamic Response for Flexible amd Multi-body Marine Structures. (PhD-thesis, CeSOS)
IMT-2008-42	Ruth, Eivind	Propulsion control and thrust allocation on marine vessels. (PhD thesis, CeSOS)
IMT-2008-43	Nystad, Bent Helge	Technical Condition Indexes and Remaining Useful Life of Aggregated Systems. PhD thesis, IMT
IMT-2008-44	Soni, Prashant Kumar	Hydrodynamic Coefficients for Vortex Induced Vibrations of Flexible Beams, PhD thesis, CeSOS
IMT-2009-45	Amlashi, Hadi K.K.	Ultimate Strength and Reliability-based Design of Ship Hulls with Emphasis on Combined Global and Local Loads. PhD Thesis, IMT
IMT-2009-46	Pedersen, Tom Arne	Bond Graph Modelling of Marine Power Systems. PhD Thesis, IMT
IMT-2009-47	Kristiansen, Trygve	Two-Dimensional Numerical and Experimental Studies of Piston-Mode Resonance. PhD-Thesis, CeSOS
IMT-2009-48	Ong, Muk Chen	Applications of a Standard High Reynolds Number Model and a Stochastic Scour Prediction Model for Marine Structures. PhD-thesis, IMT
IMT-2009-49	Hong, Lin	Simplified Analysis and Design of Ships subjected to Collision and Grounding. PhD-thesis, IMT
IMT-2009-50	Koushan, Kamran	Vortex Induced Vibrations of Free Span Pipelines, PhD thesis, IMT
IMT-2009-51	Korsvik, Jarl Eirik	Heuristic Methods for Ship Routing and Scheduling. PhD-thesis, IMT
IMT-2009-52	Lee, Jihoon	Experimental Investigation and Numerical in Analyzing the Ocean Current Displacement of Longlines. Ph.d.-Thesis, IMT.
IMT-2009-53	Vestbøstad, Tone Gran	A Numerical Study of Wave-in-Deck Impact usin a Two-Dimensional Constrained Interpolation Profile Method, Ph.d.thesis, CeSOS.
IMT-2009-54	Bruun, Kristine	Bond Graph Modelling of Fuel Cells for Marine Power Plants. Ph.d.-thesis, IMT
IMT 2009-55	Holstad, Anders	Numerical Investigation of Turbulence in a Sekwed Three-Dimensional Channel Flow, Ph.d.-thesis, IMT.
IMT 2009-56	Ayala-Uraga, Efren	Reliability-Based Assessment of Deteriorating Ship-shaped Offshore Structures, Ph.d.-thesis, IMT
IMT 2009-57	Kong, Xiangjun	A Numerical Study of a Damaged Ship in Beam Sea Waves. Ph.d.-thesis, IMT/CeSOS.
IMT 2010-58	Kristiansen, David	Wave Induced Effects on Floaters of Aquaculture Plants, Ph.d.-thesis, CeSOS.

IMT 2010-59	Ludvigsen, Martin	An ROV-Toolbox for Optical and Acoustic Scientific Seabed Investigation. Ph.d.-thesis IMT.
IMT 2010-60	Hals, Jørgen	Modelling and Phase Control of Wave-Energy Converters. Ph.d.thesis, CeSOS.
IMT 2010- 61	Shu, Zhi	Uncertainty Assessment of Wave Loads and Ultimate Strength of Tankers and Bulk Carriers in a Reliability Framework. Ph.d. Thesis, IMT/ CeSOS
IMT 2010-62	Shao, Yanlin	Numerical Potential-Flow Studies on Weakly-Nonlinear Wave-Body Interactions with/without Small Forward Speed, Ph.d.thesis,CeSOS.
IMT 2010-63	Califano, Andrea	Dynamic Loads on Marine Propellers due to Intermittent Ventilation. Ph.d.thesis, IMT.
IMT 2010-64	El Khoury, George	Numerical Simulations of Massively Separated Turbulent Flows, Ph.d.-thesis, IMT
IMT 2010-65	Seim, Knut Sponheim	Mixing Process in Dense Overflows with Emphasis on the Faroe Bank Channel Overflow. Ph.d.thesis, IMT
IMT 2010-66	Jia, Huirong	Structural Analysis of Intect and Damaged Ships in a Collission Risk Analysis Perspective. Ph.d.thesis CeSoS.
IMT 2010-67	Jiao, Linlin	Wave-Induced Effects on a Pontoon-type Very Large Floating Structures (VLFS). Ph.D.-thesis, CeSOS.
IMT 2010-68	Abrahamsen, Bjørn Christian	Sloshing Induced Tank Roof with Entrapped Air Pocket. Ph.d.thesis, CeSOS.
IMT 2011-69	Karimirad, Madjid	Stochastic Dynamic Response Analysis of Spar-Type Wind Turbines with Catenary or Taut Mooring Systems. Ph.d.-thesis, CeSOS.
IMT - 2011-70	Erlend Meland	Condition Monitoring of Safety Critical Valves. Ph.d.-thesis, IMT.
IMT – 2011-71	Yang, Limin	Stochastic Dynamic System Analysis of Wave Energy Converter with Hydraulic Power Take-Off, with Particular Reference to Wear Damage Analysis, Ph.d. Thesis, CeSOS.
IMT – 2011-72	Visscher, Jan	Application of Particla Image Velocimetry on Turbulent Marine Flows, Ph.d.Thesis, IMT.
IMT – 2011-73	Su, Biao	Numerical Predictions of Global and Local Ice Loads on Ships. Ph.d.Thesis, CeSOS.
IMT – 2011-74	Liu, Zhenhui	Analytical and Numerical Analysis of Iceberg Collision with Ship Structures. Ph.d.Thesis, IMT.
IMT – 2011-75	Aarsæther, Karl Gunnar	Modeling and Analysis of Ship Traffic by Observation and Numerical Simulation. Ph.d.Thesis, IMT.

Imt – 2011-76	Wu, Jie	Hydrodynamic Force Identification from Stochastic Vortex Induced Vibration Experiments with Slender Beams. Ph.d.Thesis, IMT.
Imt – 2011-77	Amini, Hamid	Azimuth Propulsors in Off-design Conditions. Ph.d.Thesis, IMT.
IMT – 2011-78	Nguyen, Tan-Hoi	Toward a System of Real-Time Prediction and Monitoring of Bottom Damage Conditions During Ship Grounding. Ph.d.thesis, IMT.
IMT- 2011-79	Tavakoli, Mohammad T.	Assessment of Oil Spill in Ship Collision and Grounding, Ph.d.thesis, IMT.
IMT- 2011-80	Guo, Bingjie	Numerical and Experimental Investigation of Added Resistance in Waves. Ph.d.Thesis, IMT.
IMT- 2011-81	Chen, Qiaofeng	Ultimate Strength of Aluminium Panels, considering HAZ Effects, IMT
IMT- 2012-82	Kota, Ravikiran S.	Wave Loads on Decks of Offshore Structures in Random Seas, CeSOS.
IMT- 2012-83	Sten, Ronny	Dynamic Simulation of Deep Water Drilling Risers with Heave Compensating System, IMT.
IMT- 2012-84	Berle, Øyvind	Risk and resilience in global maritime supply chains, IMT.
IMT- 2012-85	Fang, Shaoji	Fault Tolerant Position Mooring Control Based on Structural Reliability, CeSOS.
IMT- 2012-86	You, Jikun	Numerical studies on wave forces and moored ship motions in intermediate and shallow water, CeSOS.
IMT- 2012-87	Xiang ,Xu	Maneuvering of two interacting ships in waves, CeSOS
IMT- 2012-88	Dong, Wenbin	Time-domain fatigue response and reliability analysis of offshore wind turbines with emphasis on welded tubular joints and gear components, CeSOS
IMT- 2012-89	Zhu, Suji	Investigation of Wave-Induced Nonlinear Load Effects in Open Ships considering Hull Girder Vibrations in Bending and Torsion, CeSOS
IMT- 2012-90	Zhou, Li	Numerical and Experimental Investigation of Station-keeping in Level Ice, CeSOS
IMT- 2012-91	Ushakov, Sergey	Particulate matter emission characteristics from diesel enignes operating on conventional and alternative marine fuels, IMT
IMT- 2013-1	Yin, Decao	Experimental and Numerical Analysis of Combined In-line and Cross-flow Vortex Induced Vibrations, CeSOS

IMT-2013-2	Kurniawan, Adi	Modelling and geometry optimisation of wave energy converters, CeSOS
IMT-2013-3	Al Ryati, Nabil	Technical condition indexes doe auxiliary marine diesel engines, IMT
IMT-2013-4	Firoozkoohi, Reza	Experimental, numerical and analytical investigation of the effect of screens on sloshing, CeSOS
IMT-2013-5	Ommani, Babak	Potential-Flow Predictions of a Semi-Displacement Vessel Including Applications to Calm Water Broaching, CeSOS
IMT-2013-6	Xing, Yihan	Modelling and analysis of the gearbox in a floating spar-type wind turbine, CeSOS
IMT-7-2013	Balland, Océane	Optimization models for reducing air emissions from ships, IMT
IMT-8-2013	Yang, Dan	Transitional wake flow behind an inclined flat plate-----Computation and analysis, IMT
IMT-9-2013	Abdillah, Suyuthi	Prediction of Extreme Loads and Fatigue Damage for a Ship Hull due to Ice Action, IMT
IMT-10-2013	Ramìrez, Pedro Agustìn Pèrez	Ageing management and life extension of technical systems- Concepts and methods applied to oil and gas facilities, IMT
IMT-11-2013	Chuang, Zhenju	Experimental and Numerical Investigation of Speed Loss due to Seakeeping and Maneuvering. IMT
IMT-12-2013	Etemaddar, Mahmoud	Load and Response Analysis of Wind Turbines under Atmospheric Icing and Controller System Faults with Emphasis on Spar Type Floating Wind Turbines, IMT
IMT-13-2013	Lindstad, Haakon	Strategies and measures for reducing maritime CO2 emissons, IMT
IMT-14-2013	Haris, Sabril	Damage interaction analysis of ship collisions, IMT
IMT-15-2013	Shainee, Mohamed	Conceptual Design, Numerical and Experimental Investigation of a SPM Cage Concept for Offshore Mariculture, IMT
IMT-16-2013	Gansel, Lars	Flow past porous cylinders and effects of biofouling and fish behavior on the flow in and around Atlantic salmon net cages, IMT
IMT-17-2013	Gaspar, Henrique	Handling Aspects of Complexity in Conceptual Ship Design, IMT
IMT-18-2013	Thys, Maxime	Theoretical and Experimental Investigation of a Free Running Fishing Vessel at Small Frequency of Encounter, CeSOS
IMT-19-2013	Aglen, Ida	VIV in Free Spanning Pipelines, CeSOS

IMT-1-2014	Song, An	Theoretical and experimental studies of wave diffraction and radiation loads on a horizontally submerged perforated plate, CeSOS
IMT-2-2014	Rogne, Øyvind Ygre	Numerical and Experimental Investigation of a Hinged 5-body Wave Energy Converter, CeSOS
IMT-3-2014	Dai, Lijuan	Safe and efficient operation and maintenance of offshore wind farms ,IMT
IMT-4-2014	Bachynski, Erin Elizabeth	Design and Dynamic Analysis of Tension Leg Platform Wind Turbines, CeSOS
IMT-5-2014	Wang, Jingbo	Water Entry of Freefall Wedged – Wedge motions and Cavity Dynamics, CeSOS
IMT-6-2014	Kim, Ekaterina	Experimental and numerical studies related to the coupled behavior of ice mass and steel structures during accidental collisions, IMT
IMT-7-2014	Tan, Xiang	Numerical investigation of ship's continuous- mode icebreaking in leverl ice, CeSOS
IMT-8-2014	Muliawan, Made Jaya	Design and Analysis of Combined Floating Wave and Wind Power Facilities, with Emphasis on Extreme Load Effects of the Mooring System, CeSOS
IMT-9-2014	Jiang, Zhiyu	Long-term response analysis of wind turbines with an emphasis on fault and shutdown conditions, IMT
IMT-10-2014	Dukan, Fredrik	ROV Motion Control Systems, IMT
IMT-11-2014	Grimsmo, Nils I.	Dynamic simulations of hydraulic cylinder for heave compensation of deep water drilling risers, IMT
IMT-12-2014	Kvittem, Marit I.	Modelling and response analysis for fatigue design of a semisubmersible wind turbine, CeSOS
IMT-13-2014	Akhtar, Juned	The Effects of Human Fatigue on Risk at Sea, IMT
IMT-14-2014	Syahroni, Nur	Fatigue Assessment of Welded Joints Taking into Account Effects of Residual Stress, IMT
IMT-1-2015	Bøckmann, Eirik	Wave Propulsion of ships, IMT
IMT-2-2015	Wang, Kai	Modelling and dynamic analysis of a semi-submersible floating vertical axis wind turbine, CeSOS
IMT-3-2015	Fredriksen, Arnt Gunvald	A numerical and experimental study of a two-dimensional body with moonpool in waves and current, CeSOS
IMT-4-2015	Jose Patricio Gallardo Canabes	Numerical studies of viscous flow around bluff bodies, IMT

IMT-5-2015	Vegard Longva	Formulation and application of finite element techniques for slender marine structures subjected to contact interactions, IMT
IMT-6-2015	Jacobus De Vaal	Aerodynamic modelling of floating wind turbines, CeSOS
IMT-7-2015	Fachri Nasution	Fatigue Performance of Copper Power Conductors, IMT
IMT-8-2015	Oleh I Karpa	Development of bivariate extreme value distributions for applications in marine technology,CeSOS
IMT-9-2015	Daniel de Almeida Fernandes	An output feedback motion control system for ROVs, AMOS
IMT-10-2015	Bo Zhao	Particle Filter for Fault Diagnosis: Application to Dynamic Positioning Vessel and Underwater Robotics, CeSOS
IMT-11-2015	Wenting Zhu	Impact of emission allocation in maritime transportation, IMT
IMT-12-2015	Amir Rasekhi Nejad	Dynamic Analysis and Design of Gearboxes in Offshore Wind Turbines in a Structural Reliability Perspective, CeSOS
IMT-13-2015	Arturo Jesùs Ortega Malca	Dynamic Response of Flexibles Risers due to Unsteady Slug Flow, CeSOS
IMT-14-2015	Dagfinn Husjord	Guidance and decision-support system for safe navigation of ships operating in close proximity, IMT
IMT-15-2015	Anirban Bhattacharyya	Ducted Propellers: Behaviour in Waves and Scale Effects, IMT
IMT-16-2015	Qin Zhang	Image Processing for Ice Parameter Identification in Ice Management, IMT
IMT-1-2016	Vincentius Rumawas	Human Factors in Ship Design and Operation: An Experiential Learning, IMT
IMT-2-2016	Martin Storheim	Structural response in ship-platform and ship-ice collisions, IMT
IMT-3-2016	Mia Abrahamsen Prsic	Numerical Simulations of the Flow around single and Tandem Circular Cylinders Close to a Plane Wall, IMT
IMT-4-2016	Tufan Arslan	Large-eddy simulations of cross-flow around ship sections, IMT

IMT-5-2016	Pierre Yves-Henry	Parametrisation of aquatic vegetation in hydraulic and coastal research,IMT
IMT-6-2016	Lin Li	Dynamic Analysis of the Instalation of Monopiles for Offshore Wind Turbines, CeSOS
IMT-7-2016	Øivind Kåre Kjerstad	Dynamic Positioning of Marine Vessels in Ice, IMT
IMT-8-2016	Xiaopeng Wu	Numerical Analysis of Anchor Handling and Fish Trawling Operations in a Safety Perspective, CeSOS
IMT-9-2016	Zhengshun Cheng	Integrated Dynamic Analysis of Floating Vertical Axis Wind Turbines, CeSOS
IMT-10-2016	Ling Wan	Experimental and Numerical Study of a Combined Offshore Wind and Wave Energy Converter Concept
IMT-11-2016	Wei Chai	Stochastic dynamic analysis and reliability evaluation of the roll motion for ships in random seas, CeSOS
IMT-12-2016	Øyvind Selnes Patricksson	Decision support for conceptual ship design with focus on a changing life cycle and future uncertainty, IMT
IMT-13-2016	Mats Jørgen Thorsen	Time domain analysis of vortex-induced vibrations, IMT
IMT-14-2016	Edgar McGuinness	Safety in the Norwegian Fishing Fleet – Analysis and measures for improvement, IMT
IMT-15-2016	Sepideh Jafarzadeh	Energy effiency and emission abatement in the fishing fleet, IMT
IMT-16-2016	Wilson Ivan Guachamin Acero	Assessment of marine operations for offshore wind turbine installation with emphasis on response-based operational limits, IMT
IMT-17-2016	Mauro Candeloro	Tools and Methods for Autonomous Operations on Seabed and Water Coumn using Underwater Vehicles, IMT
IMT-18-2016	Valentin Chabaud	Real-Time Hybrid Model Testing of Floating Wind Tubines, IMT
IMT-1-2017	Mohammad Saud Afzal	Three-dimensional streaming in a sea bed boundary layer
IMT-2-2017	Peng Li	A Theoretical and Experimental Study of Wave-induced Hydroelastic Response of a Circular Floating Collar
IMT-3-2017	Martin Bergström	A simulation-based design method for arctic maritime transport systems

IMT-4-2017	Bhushan Taskar	The effect of waves on marine propellers and propulsion
IMT-5-2017	Mohsen Bardestani	A two-dimensional numerical and experimental study of a floater with net and sinker tube in waves and current
IMT-6-2017	Fatemeh Hoseini Dadmarzi	Direct Numerical Simualtion of turbulent wakes behind different plate configurations
IMT-7-2017	Michel R. Miyazaki	Modeling and control of hybrid marine power plants
IMT-8-2017	Giri Rajasekhar Gunnu	Safety and effiency enhancement of anchor handling operations with particular emphasis on the stability of anchor handling vessels
IMT-9-2017	Kevin Koosup Yum	Transient Performance and Emissions of a Turbocharged Diesel Engine for Marine Power Plants
IMT-10-2017	Zhaolong Yu	Hydrodynamic and structural aspects of ship collisions
IMT-11-2017	Martin Hassel	Risk Analysis and Modelling of Allisions between Passing Vessels and Offshore Installations
IMT-12-2017	Astrid H. Brodtkorb	Hybrid Control of Marine Vessels – Dynamic Positioning in Varying Conditions
IMT-13-2017	Kjersti Bruserud	Simultaneous stochastic model of waves and current for prediction of structural design loads
IMT-14-2017	Finn-Idar Grøtta Giske	Long-Term Extreme Response Analysis of Marine Structures Using Inverse Reliability Methods
IMT-15-2017	Stian Skjong	Modeling and Simulation of Maritime Systems and Operations for Virtual Prototyping using co-Simulations
IMT-1-2018	Yingguang Chu	Virtual Prototyping for Marine Crane Design and Operations
IMT-2-2018	Sergey Gavrilin	Validation of ship manoeuvring simulation models
IMT-3-2018	Jeevith Hegde	Tools and methods to manage risk in autonomous subsea inspection,maintenance and repair operations
IMT-4-2018	Ida M. Strand	Sea Loads on Closed Flexible Fish Cages
IMT-5-2018	Erlend Kvinge Jørgensen	Navigation and Control of Underwater Robotic Vehicles

IMT-6-2018	Bård Stovner	Aided Intertial Navigation of Underwater Vehicles
IMT-7-2018	Erlend Liavåg Grotle	Thermodynamic Response Enhanced by Sloshing in Marine LNG Fuel Tanks
IMT-8-2018	Børge Rokseth	Safety and Verification of Advanced Maritime Vessels
IMT-9-2018	Jan Vidar Ulveseter	Advances in Semi-Empirical Time Domain Modelling of Vortex-Induced Vibrations
IMT-10-2018	Chenyu Luan	Design and analysis for a steel braceless semi-submersible hull for supporting a 5-MW horizontal axis wind turbine
IMT-11-2018	Carl Fredrik Rehn	Ship Design under Uncertainty
IMT-12-2018	Øyvind Ødegård	Towards Autonomous Operations and Systems in Marine Archaeology
IMT-13-2018	Stein Melvær Nornes	Guidance and Control of Marine Robotics for Ocean Mapping and Monitoring
IMT-14-2018	Petter Norgren	Autonomous Underwater Vehicles in Arctic Marine Operations: Arctic marine research and ice monitoring
IMT-15-2018	Minjoo Choi	Modular Adaptable Ship Design for Handling Uncertainty in the Future Operating Context
MT-16-2018	Ole Alexander Eidsvik	Dynamics of Remotely Operated Underwater Vehicle Systems
IMT-17-2018	Mahdi Ghane	Fault Diagnosis of Floating Wind Turbine Drivetrain- Methodologies and Applications
IMT-18-2018	Christoph Alexander Thieme	Risk Analysis and Modelling of Autonomous Marine Systems
IMT-19-2018	Yugao Shen	Operational limits for floating-collar fish farms in waves and current, without and with well-boat presence
IMT-20-2018	Tianjiao Dai	Investigations of Shear Interaction and Stresses in Flexible Pipes and Umbilicals
IMT-21-2018	Sigurd Solheim Pettersen	Resilience by Latent Capabilities in Marine Systems
IMT-22-2018	Thomas Sauder	Fidelity of Cyber-physical Empirical Methods. Application to the Active Truncation of Slender Marine Structures
IMT-23-2018	Jan-Tore Horn	Statistical and Modelling Uncertainties in the Design of Offshore Wind Turbines

IMT-24-2018	Anna Swider	Data Mining Methods for the Analysis of Power Systems of Vessels
IMT-1-2019	Zhao He	Hydrodynamic study of a moored fish farming cage with fish influence
IMT-2-2019	Isar Ghamari	Numerical and Experimental Study on the Ship Parametric Roll Resonance and the Effect of Anti-Roll Tank
IMT-3-2019	Håkon Strandenes	Turbulent Flow Simulations at Higher Reynolds Numbers
IMT-4-2019	Siri Mariane Holen	Safety in Norwegian Fish Farming – Concepts and Methods for Improvement
IMT-5-2019	Ping Fu	Reliability Analysis of Wake-Induced Riser Collision
IMT-6-2019	Vladimir Krivopolianskii	Experimental Investigation of Injection and Combustion Processes in Marine Gas Engines using Constant Volume Rig
IMT-7-2019	Anna Maria Kozlowska	Hydrodynamic Loads on Marine Propellers Subject to Ventilation and out of Water Condition.
IMT-8-2019	Hans-Martin Heyn	Motion Sensing on Vessels Operating in Sea Ice: A Local Ice Monitoring System for Transit and Stationkeeping Operations under the Influence of Sea Ice
IMT-9-2019|	Stefan Vilsen	Method for Real-Time Hybrid Model Testing of Ocean Structures – Case on Slender Marine Systems
IMT-10-2019	Finn-Christian W. Hanssen	Non-Linear Wave-Body Interaction in Severe Waves
IMT-11-2019	Trygve Olav Fossum	Adaptive Sampling for Marine Robotics
IMT-12-2019	Jørgen Bremnes Nielsen	Modeling and Simulation for Design Evaluation
IMT-13-2019	Yuna Zhao	Numerical modelling and dyncamic analysis of offshore wind turbine blade installation
IMT-14-2019	Daniela Myland	Experimental and Theoretical Investigations on the Ship Resistance in Level Ice
IMT-15-2019	Zhengru Ren	Advanced control algorithms to support automated offshore wind turbine installation
IMT-16-2019	Drazen Polic	Ice-propeller impact analysis using an inverse propulsion machinery simulation approach
IMT-17-2019	Endre Sandvik	Sea passage scenario simulation for ship system performance evaluation

IMT-18-2019	Loup Suja-Thauvin	Response of Monopile Wind Turbines to Higher Order Wave Loads
IMT-19-2019	Emil Smilden	Structural control of offshore wind turbines – Increasing the role of control design in offshore wind farm development
IMT-20-2019	Aleksandar-Sasa Milakovic	On equivalent ice thickness and machine learning in ship ice transit simulations
IMT-1-2020	Amrit Shankar Verma	Modelling, Analysis and Response-based Operability Assessment of Offshore Wind Turbine Blade Installation with Emphasis on Impact Damages
IMT-2-2020	Bent Oddvar Arnesen Haugaløkken	Autonomous Technology for Inspection, Maintenance and Repair Operations in the Norwegian Aquaculture
IMT-3-2020	Seongpil Cho	Model-based fault detection and diagnosis of a blade pitch system in floating wind turbines
IMT-4-2020	Jose Jorge Garcia Agis	Effectiveness in Decision-Making in Ship Design under Uncertainty
IMT-5-2020	Thomas H. Viuff	Uncertainty Assessment of Wave-and Current-induced Global Response of Floating Bridges
IMT-6-2020	Fredrik Mentzoni	Hydrodynamic Loads on Complex Structures in the Wave Zone
IMT-7-2020	Senthuran Ravinthrakumar	Numerical and Experimental Studies of Resonant Flow in Moonpools in Operational Conditions
IMT-8-2020	Stian Skaalvik Sandøy	Acoustic-based Probabilistic Localization and Mapping using Unmanned Underwater Vehicles for Aquaculture Operations
IMT-9-2020	Kun Xu	Design and Analysis of Mooring System for Semi-submersible Floating Wind Turbine in Shallow Water
IMT-10-2020	Jianxun Zhu	Cavity Flows and Wake Behind an Elliptic Cylinder Translating Above the Wall
IMT-11-2020	Sandra Hogenboom	Decision-making within Dynamic Positioning Operations in the Offshore Industry – A Human Factors based Approach
IMT-12-2020	Woongshik Nam	Structural Resistance of Ship and Offshore Structures Exposed to the Risk of Brittle Failure
IMT-13-2020	Svenn Are Tutturen Værnø	Transient Performance in Dynamic Positioning of Ships: Investigation of Residual Load Models and Control Methods for Effective Compensation
IMT-14-2020	Mohd Atif Siddiqui	Experimental and Numerical Hydrodynamic Analysis of a Damaged Ship in Waves
IMT-15-2020	John Marius Hegseth	Efficient Modelling and Design Optimization of Large Floating Wind Turbines

IMT-16-2020	Asle Natskår	Reliability-based Assessment of Marine Operations with Emphasis on Sea Transport on Barges
IMT-17-2020	Shi Deng	Experimental and Numerical Study of Hydrodynamic Responses of a Twin-Tube Submerged Floating Tunnel Considering Vortex-Induced Vibration
IMT-18-2020	Jone Torsvik	Dynamic Analysis in Design and Operation of Large Floating Offshore Wind Turbine Drivetrains
IMT-1-2021	Ali Ebrahimi	Handling Complexity to Improve Ship Design Competitiveness
IMT-2-2021	Davide Proserpio	Isogeometric Phase-Field Methods for Modeling Fracture in Shell Structures
IMT-3-2021	Cai Tian	Numerical Studies of Viscous Flow Around Step Cylinders
IMT-4-2021	Farid Khazaeli Moghadam	Vibration-based Condition Monitoring of Large Offshore Wind Turbines in a Digital Twin Perspective
IMT-5-2021	Shuaishuai Wang	Design and Dynamic Analysis of a 10-MW Medium-Speed Drivetrain in Offshore Wind Turbines
IMT-6-2021	Sadi Tavakoli	Ship Propulsion Dynamics and Emissions
IMT-7-2021	Haoran Li	Nonlinear wave loads, and resulting global response statistics of a semi-submersible wind turbine platform with heave plates
IMT-8-2021	Einar Skiftestad Ueland	Load Control for Real-Time Hybrid Model Testing using Cable-Driven Parallel Robots
IMT-9-2021	Mengning Wu	Uncertainty of machine learning-based methods for wave forecast and its effect on installation of offshore wind turbines
IMT-10-2021	Xu Han	Onboard Tuning and Uncertainty Estimation of Vessel Seakeeping Model Parameters
IMT-01-2022	Ingunn Marie Holmen	Safety in Exposed Aquacultrue Operations
IMT-02-2022	Prateek Gupta	Ship Performance Monitoring using In-service Measurements and Big Data Analysis Methods
IMT-03-2022	Sangwoo Kim	Non-linear time domain analysis of deepwater riser vortex-induced vibrations
IMT-04-2022	Jarle Vinje Kramer	Hydrodynamic Aspects of Sail-Assisted Merchant Vessels
IMT-05-2022	Øyvind Rabliås	Numerical and Expermental Studies of Maneuvering in Regular and Irregular Waves

IMT-06-2022	Pramod Ghimire	Simulation-Based Ship Hybrid Power System Conspet Studies and Performance Analyses
IMT-07-2022	Carlos Eduardo Silva de Souza	Structural modelling, coupled dynamics, and design of large floating wind turbines
IMT-08-2022	Lorenzo Balestra	Design of hybrid fuel cell & battery systems for maritime vessels
IMT-09-2022	Sharmin Sultana	Process safety and risk management using system perspectives – A contribution to the chemical process and petroleum industry
IMT-10-2022	Øystein Sture	Autonomous Exploration for Marine Minerals
IMT-11-2022	Tiantian Zhu	Information and Decision-making for Major Accident Prevention – A concept of information-based strategies for accident prevention
IMT-12-2022	Siamak Karimi	Shore-to-Ship Charging Systems for Battery-Electric Ships
IMT-01-2023	Huili Xu	Fish-inspired Propulsion Study: Numerical Hydrodynamics of Rigid/Flexible/Morphing Foils and Observations on Real Fish
IMT-02-2023	Chana Sinsabvarodom	Probabilistic Modelling of Ice-drift and Ice Loading on Fixed and Floating Offshore Structures
IMT-03-2023	Martin Skaldebø	Intelligent low-cost solutions for underwater intervention using computer vision and machine learning
IMT-04-2023	Hans Tobias Slette	Vessel operations in exposed aquaculture – Achieving safe and efficient operation of vessel fleets in fish farm systems experiencing challenging metocean conditions
IMT-05-2023	Ruochen Yang	Methods and models for analyzing and controlling the safety in operations of autonomous marine systems
IMT-06-2023	Tobias Rye Torben	Formal Approaches to Design and Verification of Safe Control Systems for Autonomous Vessels
IMT-07-2023	YoungRong Kim	Modeling Operational Performance for the Global Fleet & Application of an Energy Saving Measure
IMT-08-2023	Henrik Schmidt-Didlaukies	Modeling and Hybrid Feedback Control of Underwater Vehicles
IMT-09-2023	Ehsan Esmailian	Optimal Ship Design for Operating in Real Sea States
IMT-10-2023	Astrid Vamråk Solheim	Exploring the performance of conceptual offshore production systems for deep-sea mining
IMT-11-2023	Benjamin Lagemann	Conceptual design of low-emission ships

IMT-12-2023	Erling Neerland Lone	Fatigue reliability of offshore Mooring chains under influence of mean load and corrosion
IMT-13-2023	Kamyar Malekibagherabadi	Simulator Approach to Concept Analysis and Optimization of Marine Power Plants
IMT-14-2023	Håvard Snefjellås Løvås	Optical Techniques for Hyperspectral Imaging of the Seafloor
IMT-15-2023	Stian Høegh Sørum	Uncertainties in the Design of Monopile Offshore Wind Turbines
IMT-16-2023	Nathalie Ramos	Mechanical and thermal simulations of 3D printed structures and the 3D printing process
IMT-17-2023	Daeseong Park	Model-Based Design of Marine Hybrid Power Systems
IMT-18-2023	Chuanqi Guo	Analysis and modeling of risk of an autonomous ferry for safer design and operation
IMT-01-2024	Dennis David Langer	Hyperspectral Push-broom Systems: Operations, Software Development, and Spatial Resolution
IMT-02-2024	Jens Einar Bremnes	Safe Autonomy in Marine Robotics
IMT-03-2024	George Katsikogiannis	Estimation of Long-Term Fatigue and Extreme Responses of Large-Diameter Monopiles for Offshore Wind Turbines